

Wenhua Chen · Karun Rawat  
Fadhel M. Ghannouchi

# Multiband RF Circuits and Techniques for Wireless Transmitters

 Springer

# Multiband RF Circuits and Techniques for Wireless Transmitters

Wenhua Chen · Karun Rawat  
Fadhel M. Ghannouchi

# Multiband RF Circuits and Techniques for Wireless Transmitters

 Springer

Wenhua Chen  
Tsinghua University  
Beijing  
China

Fadhel M. Ghannouchi  
University of Calgary  
Calgary, AB  
Canada

Karun Rawat  
Indian Institute of Technology Roorkee  
Roorkee  
India

ISBN 978-3-662-50438-3      ISBN 978-3-662-50440-6 (eBook)  
DOI 10.1007/978-3-662-50440-6

Library of Congress Control Number: 2016940120

© Springer-Verlag Berlin Heidelberg 2016

This work is subject to copyright. All rights are reserved by the Publisher, whether the whole or part of the material is concerned, specifically the rights of translation, reprinting, reuse of illustrations, recitation, broadcasting, reproduction on microfilms or in any other physical way, and transmission or information storage and retrieval, electronic adaptation, computer software, or by similar or dissimilar methodology now known or hereafter developed.

The use of general descriptive names, registered names, trademarks, service marks, etc. in this publication does not imply, even in the absence of a specific statement, that such names are exempt from the relevant protective laws and regulations and therefore free for general use.

The publisher, the authors and the editors are safe to assume that the advice and information in this book are believed to be true and accurate at the date of publication. Neither the publisher nor the authors or the editors give a warranty, express or implied, with respect to the material contained herein or for any errors or omissions that may have been made.

Printed on acid-free paper

This Springer imprint is published by Springer Nature  
The registered company is Springer-Verlag GmbH Berlin Heidelberg



*We would like to dedicate our efforts  
to our family who inspired and  
supported us through everything.  
We would also like to acknowledge  
all of our students and colleagues  
for their support.*

# Contents

<b>1</b>	<b>RF Amplifier Design and Architectures</b>	<b>1</b>
1.1	Introduction	1
1.2	Small-Signal Amplifier Design	2
1.2.1	Types of Transistor Amplifier Power Gains	2
1.2.2	Transistor Amplifier Stability	4
1.2.3	Single-Stage Transistor Amplifier Design	4
1.3	Large-Signal Amplifier Design	7
1.3.1	PA Analytical Modeling and Figures of Merits	7
1.3.2	PA Classes of Operations (A, B, AB, and C)	16
1.3.3	Current and Voltage Waveforms	19
1.3.4	Harmonic Impedance-Controlled Amplifiers	20
1.3.5	Continuous-Mode PAs	23
	References	28
<b>2</b>	<b>Dual-Branch RF Amplifier Design and Architectures</b>	<b>29</b>
2.1	Introduction	29
2.2	Balanced Amplifiers	30
2.3	Push–Pull Amplifiers	32
2.3.1	Push–Pull Amplifier with Bipolar Transistors	34
2.3.2	Push–Pull Amplifier with Baluns	35
2.4	Doherty Amplifiers	36
2.4.1	Doherty Amplifier Architecture	36
2.4.2	Efficiency Calculation and Optimization of Doherty Amplifier	37
2.5	Pulsed-Load-Modulated Amplifier	39
2.5.1	Load Modulation in Switched Resonators	40
2.5.2	PAs with Pulsed-Load Modulation	41
2.6	Linc Amplifiers	45
2.6.1	LINC Amplifier Architecture	45
2.6.2	Case of Matched and Isolated Combiner	47
2.6.3	Case of Nonmatched Combiners (Chireix Combiners)	49

2.7	Delta-Sigma-Based Transmitters . . . . .	51
2.7.1	Delta-Sigma Modulation . . . . .	51
2.7.2	DSM-Based Transmitter. . . . .	54
2.7.3	Efficiency Calculation of DSM Transmitter. . . . .	54
2.7.4	Cartesian Delta-Sigma Transmitter. . . . .	56
2.7.5	Polar Delta-Sigma Transmitter . . . . .	57
	References . . . . .	58
<b>3</b>	<b>Multiband RF Transmitters . . . . .</b>	<b>59</b>
3.1	Introduction . . . . .	59
3.2	RF Transmitters . . . . .	59
3.2.1	Conventional Single-Band Transmitter . . . . .	59
3.2.2	Multiband Transmitter . . . . .	60
3.3	Multiband Transmitter Architectures . . . . .	61
3.3.1	Multiband Doherty Transmitter . . . . .	61
3.3.2	Multiband Envelope-Tracking Transmitter . . . . .	64
3.3.3	Multiband Outphasing Transmitter. . . . .	67
3.3.4	Multiband Delta-Sigma Transmitter . . . . .	68
3.4	Multiband RF Transmitter Circuits. . . . .	69
3.4.1	Reconfigurable Multiband Transmitter . . . . .	69
3.4.2	Concurrent Multiband PA . . . . .	71
	References . . . . .	78
<b>4</b>	<b>Multiband RF Passive Circuits . . . . .</b>	<b>81</b>
4.1	Introduction . . . . .	81
4.2	Fundamentals of Network Theory . . . . .	81
4.2.1	Introduction to Some Important Network Parameters Designs . . . . .	82
4.2.2	Properties of RF Networks in Terms of Network Parameters . . . . .	85
4.2.3	Image Parameters and Design of RF Networks Using ABCD Matrix . . . . .	86
4.2.4	Transmission-Line Equivalence with Image Parameters . . . . .	87
4.3	Multiband RF Transformers . . . . .	90
4.3.1	Stub-Loaded (T-Shape and Pi-Shape) Transformers . . . . .	90
4.3.2	Multisection Non-quarter-Wave Impedance Transformer . . . . .	93
4.3.3	Coupled-Line-Based Impedance Transformer . . . . .	96
4.4	Multiband Power Divider and Hybrid Design . . . . .	98
4.4.1	Multiband Wilkinson Power Divider . . . . .	98
4.4.2	Multiband Hybrid Couplers . . . . .	100
4.4.3	Multiband Frequency-Dependent Power Dividers . . . . .	106
4.5	Planar Slow-Wave Structures and Miniaturization . . . . .	113

- 4.6 Multiband Filters . . . . . 119
  - 4.6.1 Fundamentals of RF Filter Design . . . . . 120
  - 4.6.2 Lowpass Prototype Design . . . . . 122
  - 4.6.3 Filter Design from Lowpass Prototype (Scaling and Frequency Transformation). . . . . 125
  - 4.6.4 Distributed-Element Filter Realization . . . . . 132
  - 4.6.5 Multiband Lumped-Element Filter Design . . . . . 135
  - 4.6.6 Multiband Filter Design Using Coupling Matrix . . . . . 138
  - 4.6.7 Reconfigurable Band Pass Filter Design . . . . . 146
- References . . . . . 154
- 5 Multiband Power Amplifier Design.** . . . . . 157
  - 5.1 Introduction . . . . . 157
  - 5.2 Multiband Power Amplifier Matching . . . . . 157
    - 5.2.1 Concurrent Matching Techniques . . . . . 158
    - 5.2.2 Reconfigurable Matching Techniques. . . . . 169
  - 5.3 Multiband Power Amplifier Design . . . . . 172
    - 5.3.1 Multiband Class-AB Power Amplifier Design . . . . . 172
    - 5.3.2 Multiband Class-E Power Amplifier . . . . . 173
    - 5.3.3 Multiband Class-F Power Amplifier. . . . . 179
  - 5.4 Multiband Doherty Power Amplifier . . . . . 181
    - 5.4.1 Multiband Doherty Power Amplifier Design . . . . . 186
- References . . . . . 198
- 6 Digital Techniques for Multiband RF Transmitters** . . . . . 203
  - 6.1 Introduction . . . . . 203
  - 6.2 Nonlinearities of Multiband Transmitters . . . . . 203
  - 6.3 Two-Dimensional Digital Predistortion (2D-DPD) Technique . . . . . 207
    - 6.3.1 2D-DPD Behavioral Model . . . . . 207
    - 6.3.2 Model Evaluation and Results. . . . . 210
  - 6.4 Low-Complexity 2D-DPD Techniques . . . . . 212
    - 6.4.1 2D-Modified Memory Polynomial (2D-MMP) Model . . . . . 212
    - 6.4.2 Adaptive Pruning Method for 2D-DPD . . . . . 223
  - 6.5 Digital Techniques for Multiband Transmitters with Hardware Impairments . . . . . 226
    - 6.5.1 Time-Misalignment Tolerant (TMT) Behavioral Model . . . . . 226
    - 6.5.2 Phase-Compensated Behavioral Model. . . . . 231
  - 6.6 Hardware Implementation for 2D-DPD with Subsampling Technique. . . . . 234
    - 6.6.1 Subsampling Feedback Architecture . . . . . 234
    - 6.6.2 Subsampling Frequencies Selection . . . . . 236
    - 6.6.3 Experimental Evaluation . . . . . 238
- References . . . . . 241

# Chapter 1

## RF Amplifier Design and Architectures

### 1.1 Introduction

An amplifier receives a signal from an input source and provides a scaled version of the signal to an output device such as an antenna or to another amplifier stage. In small-signal amplifiers, the main factors are usually linearity, gain, and efficiency. For small-signal analysis, the amount of power handling capacity and power efficiency are of little concern. Large-signal devices such as power amplifiers (PAs), on the other hand, primarily provide sufficient power to an output load to drive another device, typically a few watts to tens of watts.

In this chapter, we concentrate on those PA circuits that are typically used to handle large-voltage signals at moderate-to-high current levels. The main features of a large-signal PA are the power efficiency, the maximum amount of power that the circuit is capable of handling, and the linearity.

There has been considerable industrial interest in producing Radio Frequency (RF) PAs with good linearity and power efficiency. These two contradictory requirements can be composed by using external circuitry to linearize an efficient amplifier. Ideally, linearity is the ability of an amplifier to maintain equal gain for any input signal. But, this is not true in practice, especially for higher input power levels. PAs must be linear to minimize interference and spectral regrowth. However, PAs have an inherent nonlinear behavior and are considered the main reason of distortions in RF transmitters.

Moreover, researchers have been focusing on designing more efficient power amplification techniques. Efficiency is needed to minimize power consumption and operating costs of high-power RF transmitters. The trade-off between linearity and efficiency is well reported in the literature. The current state of the art is to design a PA with the highest possible efficiency and to implement a linearization technique to restore linearity.

## 1.2 Small-Signal Amplifier Design

For small-signal amplifiers, a linear analysis is applicable. Consequently, we can treat the transistor as a two-port network that is entirely defined by its measured scattering ( $S$ ) parameters or predicted using a small-signal linear-equivalent circuit model.

### 1.2.1 Types of Transistor Amplifier Power Gains

A generic two-port transistor identified by its  $S$  parameters (defined in a system having characteristic impedance  $Z_o$ ) connected to a voltage generator,  $V_s$ , having source impedance  $Z_s$  and loaded with an impedance  $Z_L$ , is shown in Fig. 1.1.

$(a_1, b_1)$  and  $(a_2, b_2)$  are the incident and reflected normalized voltage waves of the two-port circuit, respectively, which can be expressed as a function of the incident and reflected voltages at the two ports as follows:

$$a_1 = \frac{V_1^+}{\sqrt{Z_o}}, \quad b_1 = \frac{V_1^-}{\sqrt{Z_o}}, \quad a_2 = \frac{V_2^+}{\sqrt{Z_o}} \quad \text{and} \quad b_2 = \frac{V_2^-}{\sqrt{Z_o}} \quad (1.1)$$

where  $V_1^+$  and  $V_2^+$  are the incident voltages, and  $V_1^-$  and  $V_2^-$  are the reflected voltages at port 1 and port 2 of the transistor. The reflection coefficients associated with the source and load impedances can be expressed as follows:

$$\Gamma_s = \frac{Z_s - Z_o}{Z_s + Z_o} \quad \text{and} \quad \Gamma_L = \frac{Z_L - Z_o}{Z_L + Z_o} \quad (1.2)$$

The input and output reflection coefficients at the transistor terminals can be expressed thus:

$$\Gamma_{\text{out}} = \frac{b_1}{a_1} = S_{11} + \frac{S_{21}S_{12}\Gamma_L}{1 - S_{22}\Gamma_L} \quad \text{and} \quad \Gamma_{\text{in}} = \frac{b_2}{a_2} = S_{22} + \frac{S_{21}S_{12}\Gamma_s}{1 - S_{11}\Gamma_s} \quad (1.3)$$

There are three commonly used definitions for transistor amplifier power gain, which are as follows:

- **Transducer Gain,  $G_T$ :** This is the ratio of the time-average power dissipated in the load,  $P_L$ , to the time-average power available from the source,  $P_{av,s}$ . The analytical expression of  $G_T$  in terms of the  $S$  parameters of the network, as well

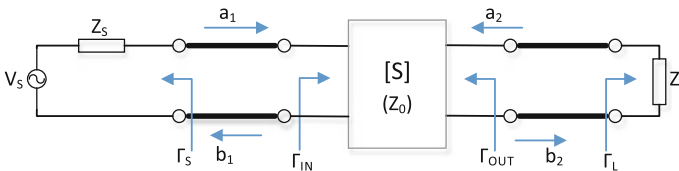


**Fig. 1.1** A two-port network with arbitrary source and load impedances

as the source and reflection coefficients  $\Gamma_S$  and  $\Gamma_L$ , respectively, can be demonstrated to be as follows:

$$G_T = \frac{P_L}{P_{av,S}} = \frac{1 - |\Gamma_S|^2}{|1 - \Gamma_{in}\Gamma_S|^2} |S_{21}|^2 \frac{1 - |\Gamma_L|^2}{|1 - S_{22}\Gamma_L|^2} \quad (1.4)$$

It can also be shown that  $G_T$  can be expressed as

$$G_T = \frac{P_L}{P_{av,S}} = \frac{1 - |\Gamma_S|^2}{|1 - S_{11}\Gamma_S|^2} |S_{21}|^2 \frac{1 - |\Gamma_L|^2}{|1 - \Gamma_{out}\Gamma_L|^2} \quad (1.5)$$

It is clear from the above equation that  $G_T = f(\Gamma_L, \Gamma_S, [S])$ .

- *Operating Power Gain,  $G_P$* : This is the ratio of the time-average power dissipated in a load,  $P_L$ , to the time-average power delivered to the input of the network,  $P_{in}$ . By assuming that the input is in a conjugate matched condition ( $\Gamma_{in} = \Gamma_S^*$ ), it can be easily demonstrated that the transducer power gain expression can be reduced to the operating power gain  $G_P$ , as follows:

$$G_P = \frac{P_L}{P_{in}} = \frac{1}{1 - |\Gamma_{in}|^2} |S_{21}|^2 \frac{1 - |\Gamma_L|^2}{|1 - S_{22}\Gamma_L|^2} = f(\Gamma_L, [S]) \quad (1.6)$$

- *Available Gain,  $G_A$* : This is the ratio of the maximally available time-average power from the network,  $P_{av,N}$ , to the time-average power available from the source,  $P_{av,S}$ . By assuming that the output is in a conjugate matched condition ( $\Gamma_{out} = \Gamma_L^*$ ), it can be easily demonstrated that the transducer power gain expression can be reduced to the operating power gain,  $G_A$ , as follows:

$$G_A = \frac{P_{av,N}}{P_{av,S}} = \frac{1 - |\Gamma_S|^2}{|1 - S_{11}\Gamma_S|^2} |S_{21}|^2 \frac{1}{1 - |\Gamma_{out}|^2} = f(\Gamma_S, [S]) \quad (1.7)$$

All of these gain expressions (1.4)–(1.7) are formed by the product of three factors. The first and third describe how the gain is reduced (or accentuated) by the matching source and load circuits, respectively. Moreover, it is apparent from (1.6) that  $G_P$  is not dependent on  $\Gamma_S$  (or  $Z_S$ ). Similarly, from (1.7) it is clear that  $G_A$  is not dependent on  $\Gamma_L$  (or  $Z_L$ ). However,  $G_T$  is dependent on both  $\Gamma_S$  and  $\Gamma_L$ . The design for a given value of the transducer power gain requires solving Eq. (1.5) in four-dimensional space, and for this reason,  $G_A$  or  $G_P$  are used instead of  $G_A$ , which require only solving (1.6) or (1.7) in two-dimensional space.

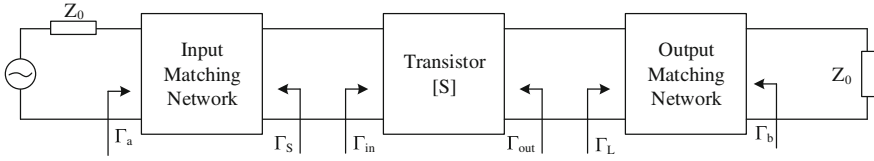


**Fig. 1.2** A general two-port transistor amplifier circuit

### 1.2.2 Transistor Amplifier Stability

In the two-port amplifier circuit of Fig. 1.2, oscillation occurs if either the input or output port impedance has a negative real part, which implies that  $|\Gamma_{in}| > 1$  or  $|\Gamma_{out}| > 1$ .

Because  $\Gamma_{in}$  and  $\Gamma_{out}$  depend on the load and the source matching networks, respectively, the stability of the amplifier, in turn, depends on  $\Gamma_s$  and  $\Gamma_L$  as presented by the matching networks. Thus, two types of stability can be defined:

- **Unconditional Stability:** The network is unconditionally stable if  $|\Gamma_{in}| < 1$  and  $|\Gamma_{out}| < 1$  for all passive source and load impedances (i.e.,  $|\Gamma_s| < 1$  and  $|\Gamma_L| < 1$ ).
- **Conditional Stability:** The network is conditionally stable (or potentially unstable) if  $|\Gamma_{in}| > 1$  or/and  $|\Gamma_{out}| > 1$  only for a certain range of passive source and load impedances.

Given the  $S$  parameters of the transistor, the condition for unconditional stability is given by the following equation:

$$\mu = \frac{1 - |S_{11}|^2}{|S_{22} - S_{11}^*(S_{11}S_{22} - S_{12}S_{21})| + |S_{12}S_{21}|} > 1 \quad (1.8)$$

Thus, if  $\mu < 1$ , the device is potentially unstable. Moreover, larger values of  $\mu$  imply greater stability.

### 1.2.3 Single-Stage Transistor Amplifier Design

After determining the stability of the active device, the input and output matching networks of the transistor amplifier can be designed. To realize maximum gain, a conjugate match between the amplifier source or load impedance and the transistor should be achieved. With reference to Fig. 1.2, maximum power transfer from the input matching network to the transistor will occur when



$$\Gamma_{\text{in}} = \Gamma_{\text{S}}^* \quad (1.9)$$

and maximum power transfer from the output matching network to the transistor will occur when

$$\Gamma_{\text{out}} = \Gamma_{\text{L}}^* \quad (1.10)$$

When (1.9) and (1.10) are fulfilled simultaneously, maximum transducer gain,  $G_{\text{T,max}}$ , will be obtained for the pair  $(\Gamma_{\text{MS}}, \Gamma_{\text{ML}})$ . The value of  $G_{\text{T,max}}$  is given by

$$G_{\text{T,max}} = \frac{1}{1 - |\Gamma_{\text{MS}}|^2} |S_{21}|^2 \frac{1 - |\Gamma_{\text{ML}}|^2}{|1 - S_{22}\Gamma_{\text{ML}}|^2} \quad (1.11)$$

Considering the  $\Gamma_{\text{in}}$  and  $\Gamma_{\text{out}}$  expressions,

$$\Gamma_{\text{in}} = S_{11} + \frac{S_{12}S_{21}\Gamma_{\text{ML}}}{1 - S_{22}\Gamma_{\text{ML}}} \quad (1.12)$$

$$\Gamma_{\text{out}} = S_{22} + \frac{S_{12}S_{21}\Gamma_{\text{MS}}}{1 - S_{11}\Gamma_{\text{MS}}} \quad (1.13)$$

Using (1.9) and (1.10), the above equations can be written as

$$\Gamma_{\text{MS}}^* = S_{11} + \frac{S_{12}S_{21}\Gamma_{\text{ML}}}{1 - S_{22}\Gamma_{\text{ML}}} \quad (1.14)$$

$$\Gamma_{\text{ML}}^* = S_{22} + \frac{S_{12}S_{21}\Gamma_{\text{MS}}}{1 - S_{11}\Gamma_{\text{MS}}} \quad (1.15)$$

This set of two equations can be solved for the two unknowns  $\Gamma_{\text{MS}}$  and  $\Gamma_{\text{ML}}$  that can be demonstrated to be

$$\Gamma_{\text{MS}} = \frac{B_1 \pm \sqrt{B_1^2 - 4|C_1|^2}}{2C_1} \quad (1.16)$$

$$\Gamma_{\text{ML}} = \frac{B_2 \pm \sqrt{B_2^2 - 4|C_2|^2}}{2C_2} \quad (1.17)$$

where

$$B_1 = 1 + |S_{11}|^2 - |S_{22}|^2 - |A|^2 \quad (1.18)$$

$$B_2 = 1 + |S_{22}|^2 - |S_{11}|^2 - |A|^2 \quad (1.19)$$

$$C_1 = S_{11} - S_{22}^* \Delta \quad (1.20)$$

$$C_2 = S_{22} - S_{11}^* \Delta \quad (1.21)$$

$$\Delta = S_{11}S_{22} - S_{12}S_{21} \quad (1.22)$$

These design equations will produce physically realizable matching networks, provided that the transistor is unconditionally stable (or has been stabilized). The conjugate matching conditions at the input and output of the transistors lead to perfect matching at the output of the amplifier with a voltage standing wave ratio (VSWR) equal to unity.

It may be preferable in some cases to design for less than the maximum achievable gain, either using  $G_T$ ,  $G_A$  or  $G_P$  in order to improve the bandwidth (BW), enhance the noise performance of the amplifier, aim at a trade-off between noise and gain, or obtain a specific value for the gain of the amplifier. The design procedure requires plotting sets of constant gain circles along with constant noise figure (NF) circles and constant VSWR circles on the input (source) and/or output (load) Smith charts to represent loci for  $\Gamma_S$  and  $\Gamma_L$  that give the targeted values of gain, noise or VSWR.

As shown in Fig. 1.2, it can be demonstrated that for nonconjugate matched conditions at the input and/or the output, the transistor and input and output VSWR expressions are

$$(\text{VSWR})_{\text{in}} = \frac{1 + |\Gamma_a|}{1 - |\Gamma_a|} \quad \text{and} \quad (\text{VSWR})_{\text{out}} = \frac{1 + |\Gamma_b|}{1 - |\Gamma_b|} \quad (1.23)$$

with

$$|\Gamma_a| = \left| \frac{\Gamma_{\text{in}} - \Gamma_s^*}{1 - \Gamma_{\text{in}}\Gamma_s} \right| \quad \text{and} \quad |\Gamma_b| = \left| \frac{\Gamma_{\text{out}} - \Gamma_L^*}{1 - \Gamma_{\text{out}}\Gamma_L} \right| \quad (1.24)$$

In such cases, the power delivered to the input of the transistor and the power absorbed by the load are

$$P_{\text{in}} = P_{\text{av,S}}(1 - |\Gamma_a|^2) \quad \text{and} \quad P_{\text{L}} = P_{\text{av,N}}(1 - |\Gamma_b|^2) \quad (1.25)$$

The analysis of the aforementioned small-signal-amplifier design concept is elaborated in [1].

## 1.3 Large-Signal Amplifier Design

So far we have considered only small-signal amplifiers, where the input signal is low enough such that the transistor can be assumed to operate linearly and can be represented and modeled by its  $S$  parameters. At high-input powers, however, transistors do not behave linearly. In this case, the performance of the PA will depend on the input power level. Moreover, the impedances seen at the input and output of the transistor are power dependent, which complicates the design of the PA.

### 1.3.1 PA Analytical Modeling and Figures of Merits

A general block diagram of a PA is shown in Fig. 1.3, which consists of a transistor with its biasing circuits and the input and matching networks. The required current and voltage to bias the transistors are provided by the biasing circuits. The input and output matching networks are designed to transfer the maximum power through the PA. The performance of a PA can be characterized by several figures of merits. A number of these are discussed in the following subsections.

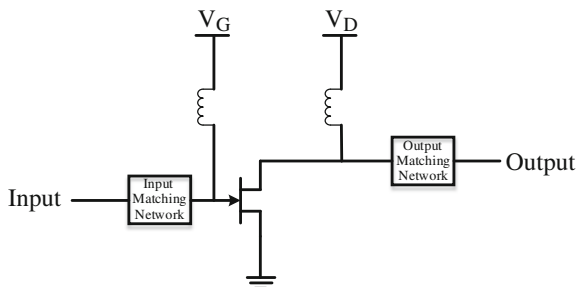
#### 1.3.1.1 Memoryless PA Modeling

A memoryless system is one in which the output of the system depends only on the present input and not the past values of input. Behavioral modeling of a device requires input and output characteristics of the device under test (DUT). PAs amplify the input signal such that the relation between the input  $x(t)$  and output signals  $y(t)$  can be written as the following Taylor series expansion:

$$y(t) = a_1x(t) + a_2x^2(t) + \dots + a_Nx^N(t) \quad (1.26)$$

The above equation provides a memoryless PA bandpass model with  $N$  as the maximum order of nonlinearity,  $a_i$ 's are the coefficients of the behavioral model and  $t$  is the time. However, the above model does not take into account the memory that is inherently present in practical systems. Hence, a better model would address the memory of the system.

**Fig. 1.3** A general block diagram of a PA



### 1.3.1.2 Saleh's Model

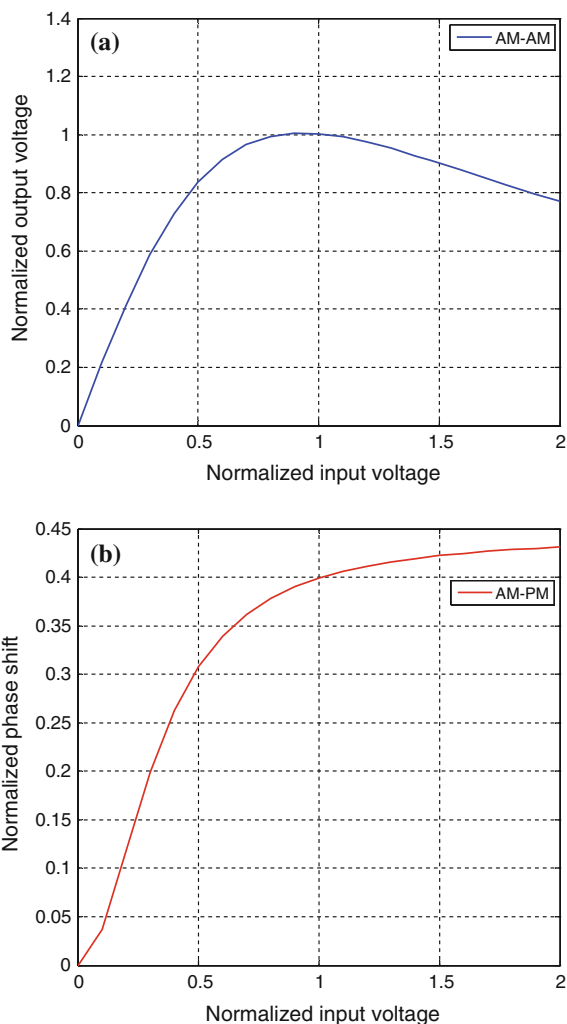
Saleh's model provides a simplified memoryless nonlinearity model for a PA. According to Saleh's model for an input amplitude and phase-modulated signal of the form

$$x(t) = A(t) \cos(2\pi f_c t + \phi(t)) \quad (1.27)$$

The output signal of the nonlinear device is given by Saleh [2]:

$$y(t) = F(x) \cos(2\pi f_c t + \phi(t) + \theta(x)) \quad (1.28)$$

**Fig. 1.4** AM/AM and AM/PM curves of travelling wave tube amplifiers (TWTA) using Saleh's model.  
**a** AM-AM characteristics,  
**b** AM-PM characteristics



$$F\{x\} = \frac{\alpha_F x}{1 + \beta_F x^2} \quad (1.29a)$$

$$\theta\{x\} = \frac{\alpha_\theta x^2}{1 + \beta_\theta x^2} \quad (1.29b)$$

with  $x = |A(t)|$  where  $F(x)$  is the AM/AM (amplitude modulation to amplitude modulation) characteristic and  $\theta(x)$  is the AM/PM (amplitude modulation to phase modulation) characteristic.  $A(t)$  and  $\phi(t)$  are the amplitude and phase of the input signal, transmitted at a carrier frequency of  $f_c$ , and both AM/AM and AM/PM characteristics are a function of the amplitude of input voltage,  $x$ , and not its phase. Figure 1.4 shows typical AM/AM and AM/PM curves of a nonlinear amplifiers model using Saleh's model with  $(\alpha_F = 2.1587; \beta_F = 1.1517; \alpha_\theta = 4.033; \beta_\theta = 9.1040)$ . The frequency-dependent Saleh's model is also presented in literature where the coefficients of the model are frequency dependent.

### 1.3.1.3 Memory Polynomial Model

The memory polynomial model (MPM), which is a simplified form of the Volterra series, considers the memory effects along with the nonlinearity of the PA. Hence, it is a more accurate model of a PA compared with the memoryless models. For a given time discrete input  $x(n)$ , the output of the MPM is given by

$$y(n) = \sum_{m=0}^M \sum_{k=0}^K a_{mk} \cdot x(n-m) \cdot |x(n-m)|^k \quad (1.30)$$

where  $a_{mk}$ 's are the coefficients of the model. Other polynomial models include envelope memory polynomial modes, generalized memory polynomial model, hybrid memory polynomial model, etc.

### 1.3.1.4 AM/AM and AM/PM Curves

AM/AM and AM/PM are of great significance in understanding the characteristics of a device, a nonlinear device in the case of PAs. These provide the output characteristics of the DUT with respect to the input characteristics. The AM/AM characteristics are the measure of the variation in the output voltage of the DUT with respect to the input voltage, while AM/PM is the measure of the variations in-phase at the output of the DUT, with respect to the change in the input voltage levels. Graphical representation of AM/AM and AM/PM characteristics is provided in Fig. 1.4.

### 1.3.1.5 Gain

The power gain of a PA is the ratio of output to input power, and is usually measured in decibels. The power gain of a PA in dB (decibel) is given by

$$G(\text{dB}) = 10 \log \left( \frac{P_{\text{out}}}{P_{\text{in}}} \right) \quad (1.31)$$

where  $P_{\text{in}}$  is the input power and  $P_{\text{out}}$  is the output power.

### 1.3.1.6 Bandwidth

The BW of an amplifier is the range of frequencies for which the amplifier delivers acceptable performance. A well-accepted metric for acceptable performance is the half power points (i.e., frequencies where the power is half of its peak value) on the output. Hence, the BW can be defined as the difference between the lower and upper half power points of the gain transfer function of the system as illustrated in Fig. 1.5. This BW is also called the 3-dB BW.

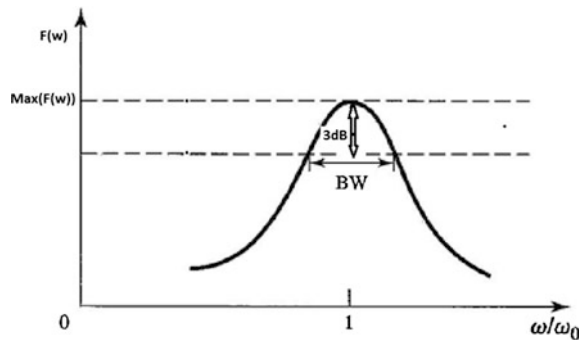
### 1.3.1.7 Noise Figure

The noise factor ( $F$ ) is a metric that gives an indication of noise added by the circuit. The noise factor is defined as the input signal-to-noise ratio ( $\text{SNR}_{\text{in}}$ ) divided by the output SNR ( $\text{SNR}_{\text{out}}$ ), which is given by

$$F = \frac{\text{SNR}_{\text{in}}}{\text{SNR}_{\text{out}}} \quad (1.32)$$

Since noise is inevitable, the SNR at the output is less than that at the input, and therefore, the noise factor is always greater than unity.

**Fig. 1.5** 3 dB bandwidth illustration of the frequency dispersive system



If the noise factor is expressed in dB, it is called the NF for the circuit, which is obtained as

$$\text{NF} = 10\log(F) = \text{SNR}_{\text{in,dB}} - \text{SNR}_{\text{out,dB}} \quad (1.33)$$

### 1.3.1.8 Power Efficiency

Power efficiency in PAs is a metric to quantify the amplifier's ability to transform the given input power to useful RF output power. There are two forms of input power to the PA: direct current (DC) via the biasing circuits to the gate and drain of the transistor, and input RF power. The RF input power is amplified by transforming the DC power into RF power at the drain level. Practically, part of the DC energy is dissipated as heat, which reduces the PA's power efficiency. The definitions of power efficiency that are commonly used in practice are the drain efficiency and the power-added efficiency.

- *Drain Efficiency* ( $\eta_{\text{D trans.}}$ ): This is the ratio of the RF output power to the DC power at the drain level, which is specific to the field-effect transistors (FETs). This efficiency is called collector efficiency in bipolar junction transistors (BJTs). Drain efficiency is given by

$$\eta_{\text{D trans.}} = \frac{P_{\text{RF Drain}}}{P_{\text{dc Drain}}} \quad (1.34)$$

where  $P_{\text{dc Drain}}$  and  $P_{\text{RF Drain}}$  are the DC power and the RF power at the drain level of the transistor, respectively.

The DC power at the gate level of a transistor is usually very small compared with the DC power at the drain level. Hence, the DC power at the drain level of the transistor,  $P_{\text{dc Drain}}$ , can be approximated as the total DC power that entered the PA,  $P_{\text{dc}}$ .

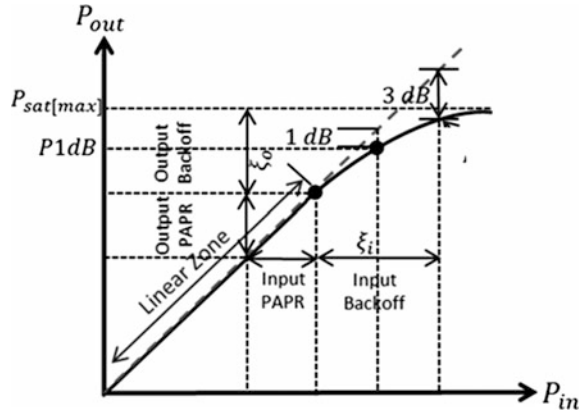
- *Power-Added Efficiency*,  $\eta_{\text{PAE}}$ : It demonstrates the ability of the PA to transform DC power to RF power. PAE can be obtained as the ratio of the added power, which is the difference between the output RF power,  $P_{\text{out}}$ , and the input RF power,  $P_{\text{in}}$ , to the DC power,  $P_{\text{dc}}$ . PAE is given by

$$\eta_{\text{PAE}} = \frac{P_{\text{out}} - P_{\text{in}}}{P_{\text{dc}}} \quad (1.35)$$

### 1.3.1.9 $P_{1\text{dB}}$

The 1 dB compression point ( $P_{1\text{dB}}$ ) is a measure of amplitude linearity. The gain of an amplifier goes down when its output reaches saturation. The  $P_{1\text{dB}}$  point is the input power that causes the gain to decrease 1 dB from the normal expected linear

**Fig. 1.6** Typical  $P_{in} - P_{out}$  characteristic of a PA



gain plot. It is the point where the amplifier goes into compression and becomes nonlinear. Similarly, the saturation power,  $P_{sat[\text{dB}]}$ , corresponds to the maximum power that the PA can deliver and often corresponds to 3–5 dB gain compression from the small-signal gain. Operation above this point should not occur to avoid signal clipping and strong distortions. Figure 1.6 illustrates the  $P_{1\text{dB}}$ , maximum saturation and 3 dB saturation points for a typical PA.

### 1.3.1.10 Intermodulation Distortion

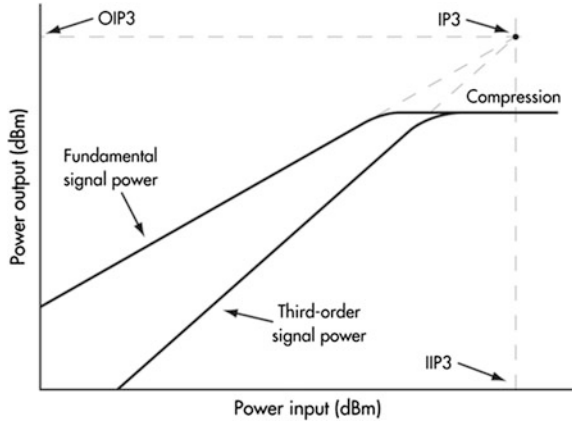
PA nonlinearity gives rise to intermodulation products that are the undesired frequency components that affect the performance of transmitters. In transmitter design, an important consideration is to meet the spectral mask requirements set by telecommunication authorities. In the presence of strong nonlinear effects, the transmitted signal fails to meet the requirement because of spectral regrowth and causes adjacent channel interference. The third-order distortions, in particular, demand greater consideration because they fall in the band of interest, i.e., the intermodulation distortions caused by the third-order nonlinearity lie close to the fundamental frequency or channel and, hence, distort the signal of interest in addition to causing out-of-band distortion. A measure of the intermodulation distortions can be provided by employing the Two-Tone Test.

### 1.3.1.11 Third-Order Intercept Point

Similar to  $P_{sat}$  and  $P_{1\text{dB}}$ , there are other device parameters that specify the nonlinearity of the DUT. These include the intercept points. In general, the  $n$ th-order intercept point,  $IIP_n$ , is the intersection between the extended linear gain,  $G$ , of the PA and the linearly extended gain of the  $n$ th-order intermodulation distortions. This can be seen in Fig. 1.7. Since third-order nonlinearity requires more consideration,



**Fig. 1.7** Third-order intercept point (IP3)



the third-order intercept point becomes more important than other order intercept points. An important design criterion is to keep the  $IIP_3$  higher so as to yield better linearity. Mathematically, in logarithmic scale,

$$IIP_n = \frac{1}{n-1} (nP_{in} - P_{IMD_n}) \tag{1.36a}$$

where  $P_{in}$  is the input power per carrier to the device, and  $P_{IMD_n}$  is the power of the intermodulation distortion of order  $n$ . In the case of third-order distortion, (1.36a, 1.36b) becomes, in dB:

$$IIP_3 = \frac{1}{2} (3P_{in} - P_{IMD_3}) \tag{1.36b}$$

It can be seen in Eq. (1.36b) that a lower intermodulation distortion means a higher intercept point and hence better linearity.

For Eq. (1.37a, 1.37b), one can deduce the difference in dB between the carrier level and third-order intermodulation distortion, as follows:

$$C/IMD_3 = P_{out} - P_{IMD_3} = 2(IP_3 - P_{in}) \tag{1.37a}$$

with

$$OIP_3 = G + IIP_3 \quad \text{and} \quad P_{out} = G + P_{in} \tag{1.37b}$$

$P_{out}$  is the output power per carrier.

### 1.3.1.12 PAPR

Peak-to-average power ratio (PAPR) is the ratio between the peak power  $P_{\text{peak}}$  (related to peak amplitude) and the average power  $P_{\text{avg}}$  (related to mean amplitude) of a modulated signal,  $x(t)$ . It is also called crest factor and is given by

$$\text{PAR(dB)} = 10\log\left(\frac{\max(|x(t)|^2)}{\text{mean}(|x(t)|^2)}\right) = 10\log\left(\frac{P_{\text{peak}}}{P_{\text{avg}}}\right) \quad (1.38)$$

### 1.3.1.13 Power Back-off

An amplifier appears linear for a sufficiently small perturbation from its bias conditions. Power back-off is defined as the ratio between the PA's saturation power to the RF signal's mean power. There are two types of power back-off: input power back-off and output power back-off. The back-off at the input of the PA,  $\xi_i$ , is obtained by

$$\xi_i = P_{i,\text{sat}} - P_{i,\text{mean}}(\text{dB}) \quad (1.39)$$

where  $P_{i,\text{sat}}$  and  $P_{i,\text{mean}}$  are the saturation power and the mean signal power at the input of the PA, respectively.

Similarly, the back-off at the output of the PA,  $\xi_o$ , is given by

$$\xi_o = P_{o,\text{sat}} - P_{o,\text{mean}} \quad (1.40)$$

where  $P_{o,\text{sat}}$  and  $P_{o,\text{mean}}$  are the saturation power and the mean signal power at the output of the PA, respectively. The input power back-off and output power back-off are illustrated in Fig. 1.6.

### 1.3.1.14 ACPR

Adjacent channel power ratio (ACPR) is a critical figure of merit to evaluate the out-of-band intermodulation distortion performance of RF PAs. It is a measure of spectral regrowth that appears in the signal sidebands. ACPR is desired to be as low as possible. A high ACPR indicates that significant spectral spreading has occurred because of the nonlinearity of the PA. As illustrated in Fig. 1.8, ACPR is defined as the ratio of the output power in the adjacent channel to a smaller BW around the center of the carrier and is expressed as

$$\text{ACPR(dBc)} = 10\log\left(\frac{P_{\text{adj}}}{P_{\text{ref}}}\right) \quad (1.41a)$$

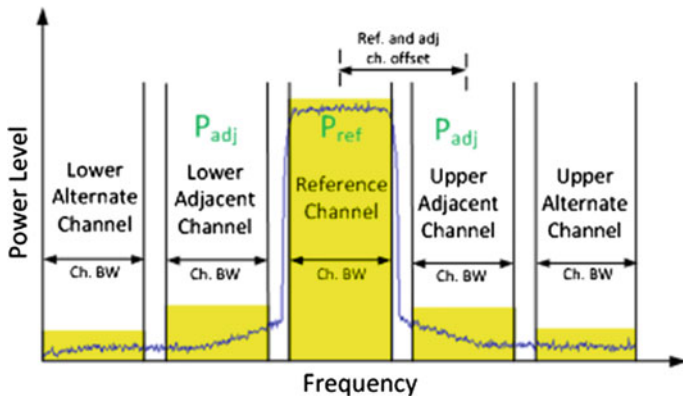


Fig. 1.8 Adjacent channel power ratio (ACPR)

and

$$ALCPR(dBc) = 10\log\left(\frac{P_{alt}}{P_{ref}}\right) \tag{1.41b}$$

### 1.3.1.15 EVM

The error vector magnitude, or EVM, is a measure used to quantify the in-band distortion performance of a PA. A signal amplified by an ideal PA would have all constellation points precisely at the ideal locations. The discrepancy between actual and ideal symbol vectors is quantified through the error vector as shown in Fig. 1.9 Noise, distortion, spurious signals, and phase noise all degrade the EVM, and therefore the EVM provides a comprehensive measure of the quality of the PA for its use in digital communication systems.

The EVM is the ratio of the power of the error vector of the measured constellation to the power of the reference vector related to the ideal constellation. The EVM can be defined in dB or percentage (%) as

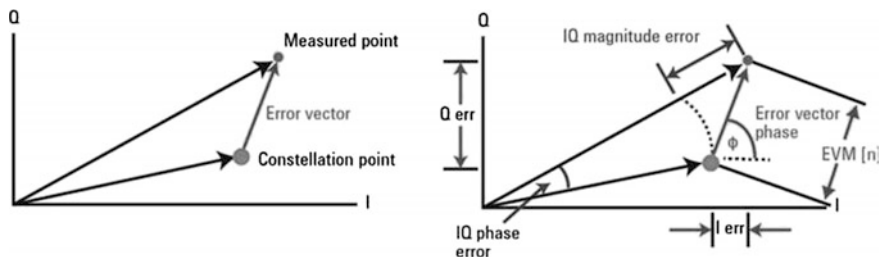


Fig. 1.9 Error vector magnitude representation

$$\begin{aligned} \text{EVM(dB)} &= 10\log_{10}\left(\frac{P_{\text{error}}}{P_{\text{ideal}}}\right) \\ &= 10\log_{10}\left(\text{mean}\left(\frac{(I_{\text{actual}} - I_{\text{ideal}})^2 + (Q_{\text{actual}} - Q_{\text{ideal}})^2}{I_{\text{ideal}}^2 + Q_{\text{ideal}}^2}\right)\right) \end{aligned} \quad (1.42)$$

$$\text{EVM}(\%) = \sqrt{\frac{P_{\text{error}}}{P_{\text{ideal}}}} \times 100 \quad (1.43)$$

where  $P_{\text{error}}$  and  $P_{\text{ideal}}$  are the root mean square (RMS) powers of the error vector and the outermost (highest power) point in the reference signal constellation, respectively. Furthermore,  $I_{\text{ideal}}$  and  $Q_{\text{ideal}}$  are the ideal in-phase and quadrature signals, and  $I_{\text{actual}}$  and  $Q_{\text{actual}}$  are the transmitted in-phase and quadrature signals. EVM can also be represented as

$$\text{EVM} = \sqrt{\frac{\frac{1}{N} \sum_{n=1}^N |S_{\text{ideal},n} - S_{\text{actual},n}|^2}{\frac{1}{N} \sum_{n=1}^N |S_{\text{ideal},n}|^2}} \quad (1.44)$$

where  $S_{\text{ideal}}$  and  $S_{\text{actual}}$  are the ideal and actual/measured symbols and  $N$  is the number of unique symbols in the constellation.

### 1.3.2 PA Classes of Operations (A, B, AB, and C)

The classes of operations of PAs form the foundation of advanced power amplification architectures, which will be presented in the next section. Therefore, most significant aspects related to this topic are outlined herein. The analysis assumes an FET. However, in principle, it is applicable to any other type of transistor with appropriate correspondence.

Figure 1.10 defines the parameters of the output current waveform to be used for the analysis. The conduction angle is denoted by  $\alpha$ , the quiescent current by  $I_q$ , the output drain current by  $i_d$  and the amplitude of the maximal current by  $I_{\text{max}}$ .

In theory, the general expression of the output drain current illustrated in Fig. 1.10 is given by

$$i_d(\theta) = \begin{cases} \frac{I_{\text{max}}}{1 - \cos(\alpha/2)} \cdot (\cos \theta - \cos(\alpha/2)), & -\alpha/2 < \theta < \alpha/2 \\ 0, & -\pi < \theta \leq -\alpha/2; \alpha/2 \leq \theta \leq \pi \end{cases} \quad (1.45)$$

Where  $\theta$  is the angular frequency.

Assuming a periodic wave shaping, the amplitude of the DC current  $I_{\text{dc}}$ , of the fundamental component  $I_1$ , and the harmonics  $I_n$  can be expressed based on Fourier decomposition as

**Fig. 1.10** Definition of the conduction angle of a PA

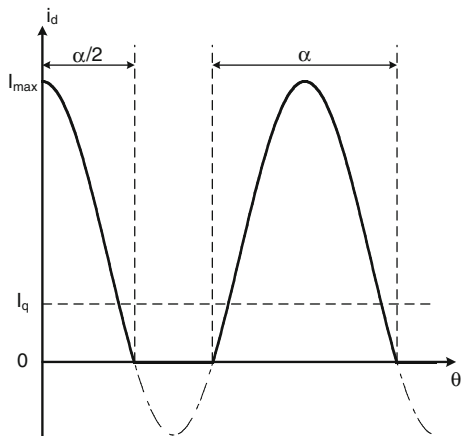
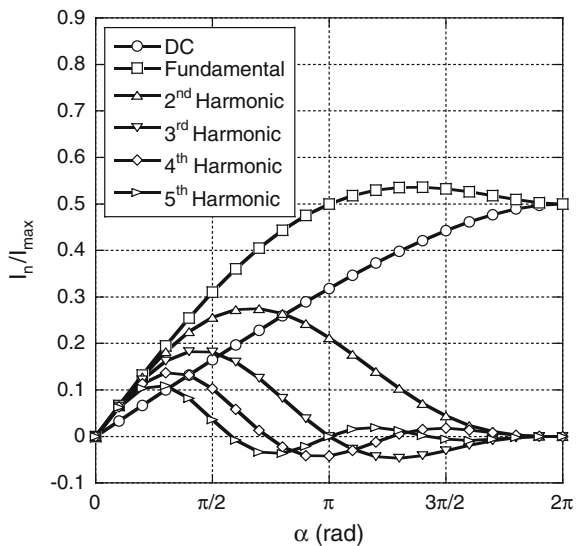


**Fig. 1.11** Frequency components of the drain current versus conduction angle



$$I_{dc} = \frac{I_{max}}{2\pi} \cdot \frac{2 \sin(\alpha/2) - \alpha \cos(\alpha/2)}{1 - \cos(\alpha/2)} \quad (1.46)$$

$$I_1 = \frac{I_{max}}{2\pi} \cdot \frac{\alpha - \sin \alpha}{1 - \cos(\alpha/2)} \quad (1.47)$$

$$I_n = \frac{I_{max}}{\pi(1 - \cos(\alpha/2))} \cdot \left[ \frac{\sin((n-1) \cdot \alpha/2)}{n(n-1)} - \frac{\sin((n+1) \cdot \alpha/2)}{n(n+1)} \right] \quad (1.48)$$

Figure 1.11 illustrates the frequency components of the drain current as a function of the conduction angle  $\alpha$ , which were calculated using (1.46)–(1.48). It is noted that the reduction of  $\alpha$  leads to the creation of harmonic components in the output signal. The amplitude of these harmonics increases with the reduction of  $\alpha$ , which degrades the linearity of the PA.

For a given  $\alpha$ , the maximal drain efficiency,  $\eta_{\max}$ , has been demonstrated to be

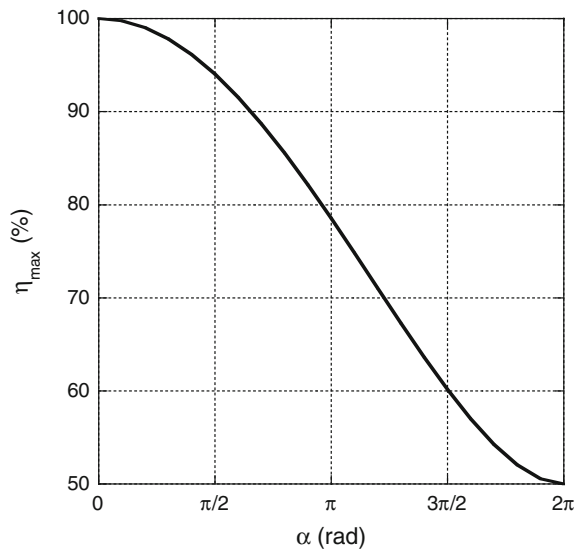
$$\eta_{\max} = \frac{\alpha - \sin \alpha}{4 \sin(\alpha/2) - 2\alpha \cos(\alpha/2)} \quad (1.49)$$

Figure 1.12 shows that the maximal drain efficiency,  $\eta_{\max}$ , increases with the reduction of  $\alpha$ . This trend is opposite to the one observed in Fig. 1.11 which infers that the linearity worsens when  $\alpha$  decreases. These two opposite tendencies show that efficiency and linearity are two antagonists that cannot be achieved simultaneously.

Starting from the previously presented theory, four classes of operations have been established on the basis of the conduction angle:

- **Class A** ( $\alpha = 2\pi$ ,  $I_q = 0.5I_{\max}$ ) is the most linear mode of operation. With a class A bias, a sine wave at the input results in a linearly amplified version at the output. However, there is a DC current constantly flowing through the transistor, even if there is no input signal, which limits the efficiency. Based on (1.49), the maximal drain efficiency of a class A PA is 50 %.
- **Class B** ( $\alpha = \pi$ ,  $I_q = 0$ ) allows for a significant efficiency increase given that the DC current consumption is 0 when no RF signal is driving the PA. With a class B operation, the drain efficiency is improved to a theoretical maximum of

**Fig. 1.12** Maximal drain efficiency versus conduction angle



78.5 % [the exact value is  $\pi/4$  as inferred from (1.49)]. However, with a class B bias, only half of the input waveform is amplified and the output waveform is distorted in a nonlinear way.

- **Class AB** ( $\pi < \alpha < 2\pi$ ,  $0 < I_q < 0.5I_{\max}$ ) is biased somewhere between class A and class B and represents a good trade-off between linearity and power efficiency.
- **Class C** ( $0 < \alpha < \pi$ ,  $I_q = 0$ ) is biased to be turned *off* during more than half of the sine wave period. This gives rise to larger distortions than the class B PA, but also to higher power efficiency (theoretically up to 100 %). The gain of the amplifier is, however, lowered compared to the other classes of operations. Class C PAs are mainly used in advanced PA architectures (e.g., Doherty PA) and in power amplification of constant envelope radios.

### 1.3.3 Current and Voltage Waveforms

In large-signal mode, the current and voltage periodic waveforms at the output terminal of an FET can be approximated by a Fourier series and expressed as follows:

$$V(t) = V_{dc} - \sum_{n=1}^{\infty} (V_{nr} \cos n\omega_0 t - V_{ni} \sin n\omega_0 t) \quad (1.50)$$

$$I(t) = I_{dc} + \sum_{n=1}^{\infty} (I_{nr} \cos n\omega_0 t - I_{ni} \sin n\omega_0 t) \quad (1.51)$$

where  $V_{dc}$  and  $I_{dc}$  are the DC voltage and current at the drain of the FET-based transistor, and  $\omega_0$  is the angular frequency related to the period of the waveform  $V(t)$  and  $I(t)$ .

The load impedance seen by the transistor at the  $n$ th harmonic of  $\omega_0$  is directly related to the coefficients of a Fourier series, as follows:

$$Z_n = \frac{V_{nr}}{I_{nr}} + j \frac{V_{ni}}{I_{ni}} \quad (1.52)$$

It is clear from the above expressions that engineering the voltage and current waveforms to design specific classes of operations comes down to accurate synthesis of appropriate harmonic impedances to the transistor output port.

Figure 1.13 shows the currents and voltage waveform for two classes of operations, namely, class A, where the voltage and currents are both sinusoidal and correspond to perfect impedance matching at the fundamental frequency and shortening all the harmonics; and class F, where the current waveform is a half-sine wave and the voltage waveform is a square wave corresponding to the class B mode of operation, with perfect impedance matching at the fundamental, and short-circuiting the even harmonic and open-circuiting the odd harmonics, as is explained in the next section.

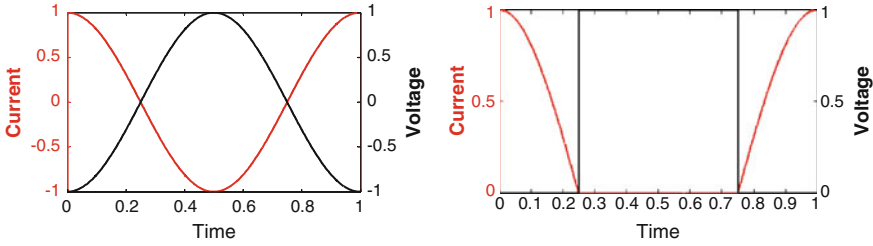


**Fig. 1.13** Power amplifier modes of operation: class A (*left*) and class F (*right*)

Using high-frequency waveform measurement instruments, such as high-speed scope, the voltage,  $V(t)$ , and current,  $I(t)$ , waveforms are not directly measured, but extracted from the normalized traveling waves,  $a(t)$  and  $b(t)$ , as shown below:

$$V(t) = \sqrt{Z_0}[a(t) + b(t)] \tag{1.53}$$

$$I(t) = \frac{[a(t) - b(t)]}{\sqrt{Z_0}} \tag{1.54}$$

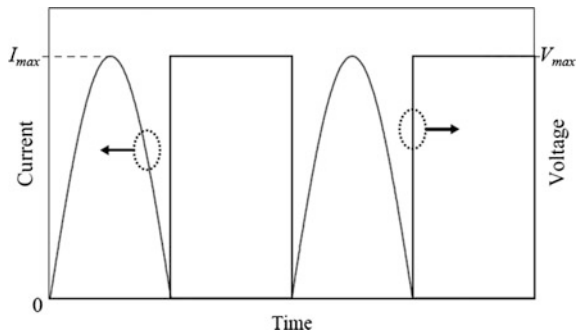
### 1.3.4 Harmonic Impedance-Controlled Amplifiers

In the reduced conduction angle classes of operations, engineering the drain current waveform results in drastic efficiency improvements over class A. By applying the same technique to the drain voltage, class F and inverse F ( $F^{-1}$ ) offer further efficiency enhancement without compromising the output power.

#### 1.3.4.1 Class F PAs

Figure 1.14 illustrates the ideal class-F waveforms. Biased in class B, class F benefits from the efficiency improvement of a half-wave rectified sine wave current.

**Fig. 1.14** The ideal class-F waveforms





Computing the maximum class-F efficiency requires a Fourier analysis of the drain waveforms, because the DC and fundamental components are not apparent from the time domain.

For the half-wave rectified sine wave current in Fig. 1.14, the Fourier series is given by

$$I(t) = I_{\max} \left[ \frac{1}{\pi} + \frac{1}{2} \sin(\omega t) - \frac{2}{\pi} \left( \frac{\cos(2\omega t)}{1 \times 3} + \frac{\cos(4\omega t)}{3 \times 5} + \frac{\cos(6\omega t)}{5 \times 7} + \dots \right) \right] \quad (1.55)$$

Similarly, the Fourier series of the square-wave voltage is expressed as

$$V(t) = V_{\max} \left[ \frac{1}{2} + \frac{2}{\pi} \left( \frac{\sin(\omega t - \pi)}{1} + \frac{\sin[3(\omega t - \pi)]}{3} + \frac{\sin[5(\omega t - \pi)]}{5} + \dots \right) \right] \quad (1.56)$$

Taking only the DC and fundamental components from (1.55) and (1.56), the maximum class-F efficiency is determined as

$$\eta_{\max, \text{Class F}} = \frac{1}{2} \frac{I_{\max} \frac{2V_{\max}}{\pi}}{\frac{I_{\max} V_{\max}}{\pi}} = 100\% \quad (1.57)$$

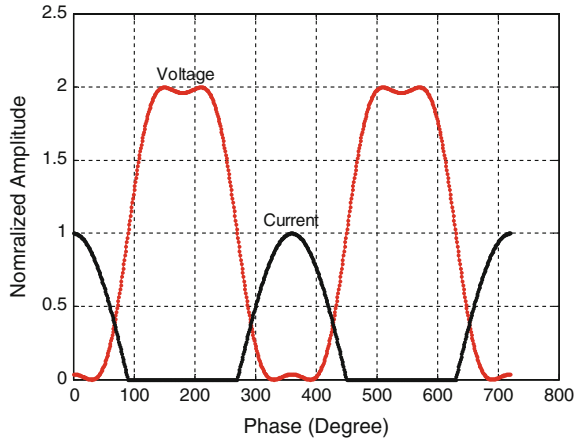
From the above analysis, class F is preferred to class A from an efficiency perspective since it acts as a perfect DC-to-RF converter by engineering the waveforms to eliminate any overlap between the instantaneous voltage and current waveforms. As a result, in practice, the power dissipation within the device is drastically minimized in class F mode of operation. However, the class F waveforms contain harmonic components that require advanced technique to synthesize and control the harmonics matching networks. In principle, class F waveforms shown in Fig. 1.14 are obtained by terminating the odd harmonics to open circuits and the even harmonics to short circuits.

The square and half-wave rectified sine wave expressions given by (1.55) and (1.56) is valid when infinite harmonics are taken into account. But generally in practice, the control of up to the third harmonic is customary, as the benefit of further harmonic control typically produces negligible efficiency improvements. Considering first three harmonics with purely resistive condition, the generalized drain voltage is expressed as function of voltage gain function ( $\delta$ ), second harmonic coefficient ( $k_2$ ) and third harmonic voltage coefficient ( $k_3$ ) as

$$V_{\text{ds}}(\omega t) = V_{\text{dd}} - \delta[\cos(\omega t) - k_2 \cos(2\omega t) - k_3 \cos(3\omega t)] \quad (1.58)$$

Considering the second harmonic impedance to be short, i.e.,  $k_2 = 0$ , Eq. (1.58) is exploited to maximize the voltage gain function ( $\delta$ ), leading to formation of the rectified half-sine wave for  $\delta = 2/\sqrt{3}$  and  $k_3 = -1/6$ . Thus, assuming a knee

**Fig. 1.15** Third harmonic manipulation for achieving close-to-ideal class-F operation



voltage of zero the normalized square voltage waveform can be computed is given by Rezaei Nazifi et al. [3]

$$V_{ds}(wt) = 1 - \frac{2}{\sqrt{3}}\cos(wt) + \frac{1}{3\sqrt{3}}\cos(3wt) \tag{1.59}$$

The above equation represents a voltage waveform that uniquely delivers maximum power with 90.7 % efficiency. Imposing this exact waveform at the current generator plane of the device requires precise tuning to compensate for the device parasitic at RF. The waveforms resulting from class F operating via manipulation of a third harmonic component is represented in Fig. 1.15

**1.3.4.2 Inverse Class-F PAs**

Inverse class-F or current-mode class-F PA operation is obtained by terminating the odd harmonics to short circuits and the even harmonics to open circuits as shown in

**Fig. 1.16** The ideal class-F<sup>-1</sup> waveforms

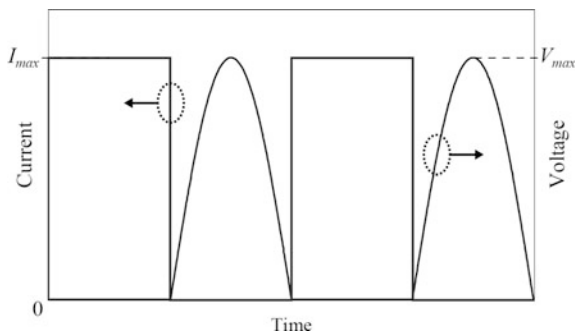


**Fig. 1.17** Second harmonic manipulation for achieving close-to-ideal class-F<sup>-1</sup> operation

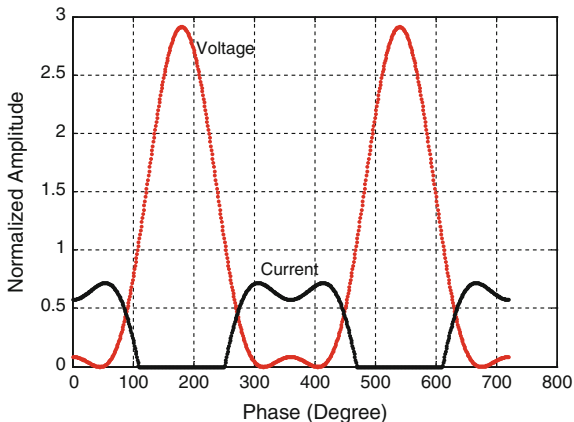


Fig. 1.16 As in class F, the power dissipation of inverse class F is zero, and therefore, this class is also capable of achieving 100 % efficiency in theory.

The inverse class-F amplifier considers third harmonic impedance to be short which shapes the voltage waveform to rectified half-sine. Similar to class-F, assuming the third harmonic impedance to be short under class F<sup>-1</sup> condition, i.e.,  $k_3 = 0$ , Eq. (1.58) is exploited to maximize the voltage gain function ( $\delta$ ), leading to formation of the rectified half-sine wave for  $\delta = \sqrt{2}$  and  $k_2 = -\sqrt{2}/4$ . Thus, assuming a knee voltage of zero the normalized half-wave rectified sine wave that gives maximum efficiency is given by

$$V_{ds}(wt) = 1 - \sqrt{2} \cos(wt) + \frac{1}{2} \cos(2wt) \tag{1.60}$$

When tuning the second harmonic impedance, the intrinsic current waveform is not only influenced by the conduction angle, but also by the infinite second harmonic impedance. As illustrated in Fig. 1.17, the effect of second harmonic manipulation is evident from the rectified half-sinusoidal voltage [obtained from (1.60)] and quasi-square-wave current waveforms.

### 1.3.5 Continuous-Mode PAs

The continuous-mode PAs utilize waveform engineering that helps to define the drain voltage and current equations for an operational mode of transistor. The movement of fundamental impedance starting from optimum point and the corresponding movement of harmonic impedances on the edge of the Smith chart help to theoretically maintain the same efficiency and output power over broadband frequency ranges. The process of waveform engineering deals with shaping the waveforms to rectify half-sinusoidal and square waveforms in order to minimize the

DC power consumption of PAs. Each family of waveforms leads to a different set of fundamental and harmonic loads, thereby providing constant output power and efficiency for broadband frequencies.

### 1.3.5.1 Class J PA

The starting point of class J mode is class B. In class J mode, the current is maintained at constant half-rectified sine wave, and the introduction of second reactive components give rise to a new family of rectified half-sine voltage waveforms as shown in Fig. 1.18a. The normalized drain voltage ( $V_{B/J}$ ) is given by (1.61) and expands to (1.62) as

$$V_{B/J} = (1 - \cos \theta)(1 - \alpha \sin \theta) \quad (1.61)$$

$$V_{B/J} = \left(1 - \cos \theta - \alpha \sin \theta + \frac{\alpha}{2} \sin 2\theta\right) \quad (1.62)$$

where  $-1 \leq \alpha \leq 1$ .

The normalized drain current can be expressed as a half-rectified sine wave and expressed in (1.63) using a Fourier series expansion.

$$i_{B/J}(\theta) = \frac{1}{\pi} + \frac{1}{2} \cos \theta + \frac{2}{3\pi} \cos 2\theta - \frac{2}{15\pi} \cos 4\theta + \frac{2}{35\pi} \cos 6\theta + \dots \quad (1.63)$$

For  $\alpha = 0$ , the conventional class-B sinusoidal waveform is obtained. Sweeping  $\alpha$  between  $-1$  and  $1$  results in a new family of voltage waveforms that help extend the impedances to a multiple set of solutions. Using the voltage and current

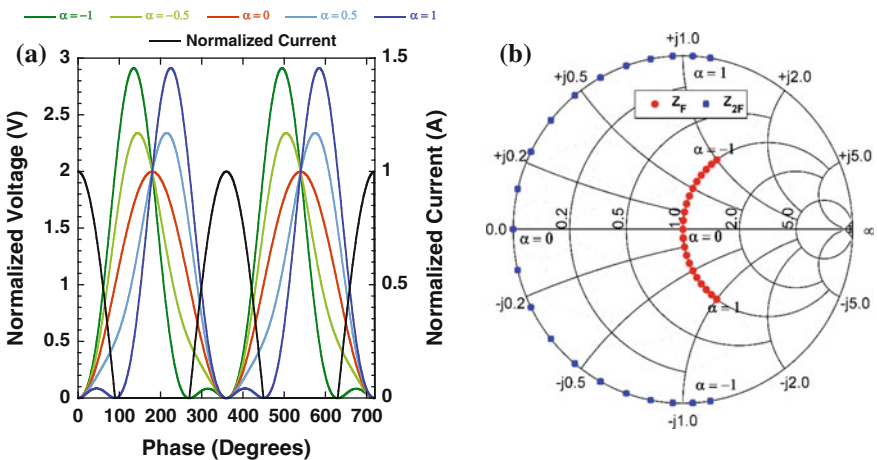


Fig. 1.18 Class J PA operation. **a** Voltage and current waveforms. **b** Design space

equations given in (1.62) and (1.63), the fundamental impedance ( $Z_F$ ) and the second harmonic impedance ( $Z_{2F}$ ) can be calculated as function of the optimal device impedance,  $R_{opt}$ , given by (1.64).

$$R_{opt} = \frac{(V_{dc} - V_k)}{I_{max}/2} \tag{1.64}$$

$$Z_F = R_{opt} - j\alpha R_{opt} \tag{1.65}$$

$$Z_{2F} = j\frac{3\pi\alpha}{8}R_{opt} \tag{1.66}$$

where  $V_k$  is the device knee voltage.

As shown in Fig. 1.18b, the reactive movement of  $Z_F$  accompanied by variation in  $Z_{2F}$  helps maintain the performance over broadband frequencies. In addition, the fundamental and second harmonic terminations are related with an inverse relation, wherein any positive variation in  $\alpha$  is accompanied by a negative variation in fundamental reactance. The variation of both fundamental and second harmonic impedances provides design space, wherein the theoretical drain efficiency of 78.5 % and the output power are kept constant for any variation of  $\alpha$ .

### 1.3.5.2 Continuous Class-F PA

The starting point of continuous class-F mode is the conventional class F [4]. The device is biased at pinch-off and operated in class B mode, which leads to a drain current waveform having half-sinusoidal shape modeled by Eq. (1.63). The quasi-square voltage waveform expression of class F is multiplied by a new term containing an additional degree of freedom ( $\gamma$ ) as shown by (1.67)–(1.68). The

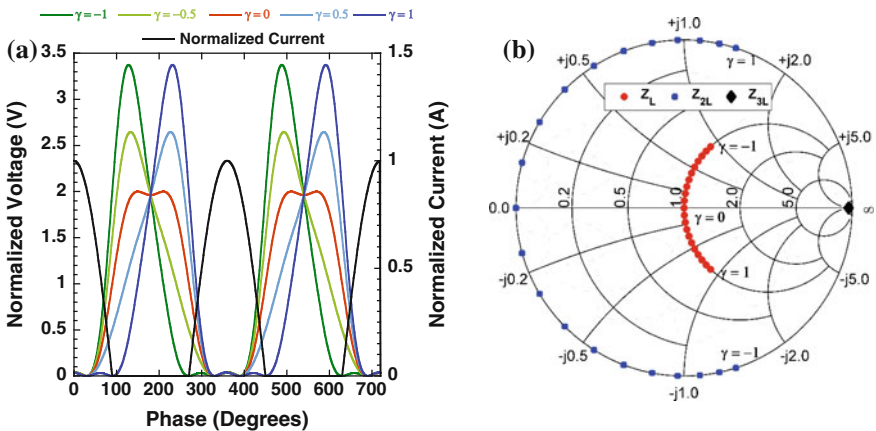


Fig. 1.19 Continuous class-F PA. a Voltage and current waveforms. b Design space

resulting waveforms for different values of  $\gamma$  are shown in Fig. 1.19a. The drain current is maintained rectified half-sinusoidal, as in the case of class B.

$$V_F = \left( 1 - \frac{2}{\sqrt{3}} \cos \theta + \frac{1}{3\sqrt{3}} \cos 3\theta \right) (1 - \gamma \sin \theta) \quad (1.67)$$

$$V_F = \left( 1 - \frac{2}{\sqrt{3}} \cos \theta + \frac{1}{3\sqrt{3}} \cos 3\theta - \gamma \sin \theta + \gamma \frac{7}{6\sqrt{3}} \sin 2\theta - \gamma \frac{1}{6\sqrt{3}} \sin 4\theta \right) \quad (1.68)$$

For  $\gamma = 0$ , the conventional class-F square waveform is obtained. The  $\gamma$  is swept between  $-1$  and  $1$ , resulting in a family of voltage waveforms that helps in the extension of a single set of impedances to multiple solutions at fundamental and harmonic frequencies. Using the voltage and current equations given in (1.63) and (1.68), the fundamental ( $Z_F$ ), second harmonic ( $Z_{2F}$ ) and third harmonic ( $Z_{3F}$ ) impedances can be calculated as functions of  $R_{\text{opt}}$ , as

$$Z_F = \frac{2}{\sqrt{3}} R_{\text{opt}} - j\gamma R_{\text{opt}} \quad (1.69)$$

$$Z_{2F} = j \frac{7\sqrt{3}\gamma}{24} R_{\text{opt}} \quad (1.70)$$

$$Z_{3F} = \infty \quad (1.71)$$

Since current expansion of the half-sinusoidal waveform does not have a third harmonic current component, the third harmonic impedance is forced to be at open-circuit condition. The reactive movement of a second harmonic component is accompanied by variation in  $Z_F$ , which helps to maintain the same performance over broadband frequencies. Again, the fundamental and second harmonic impedances are related to an inverse relationship, whereby varying  $\gamma$  positively, the fundamental reactance moves with a negative sign and the second harmonic varies with a positive sign as seen in Fig. 1.19b.

The combination of square voltage and rectified half-sinusoidal waveform helps in achieving a higher theoretical efficiency of 90.6 % and a constant output power for any variation in  $\gamma$  that transforms to a wide range of frequencies allowing the design of class F broadband PAs.

### 1.3.5.3 Continuous-Inverse Class-F PA

The continuous-inverse class F is realized from the starting point of conventional inverse-class FPA. As depicted in Fig. 1.20a, the drain voltage waveform includes only even harmonic components and is considered to be a rectified half-sinusoidal. A mathematical expression for the drain voltage is given in (1.72). The square

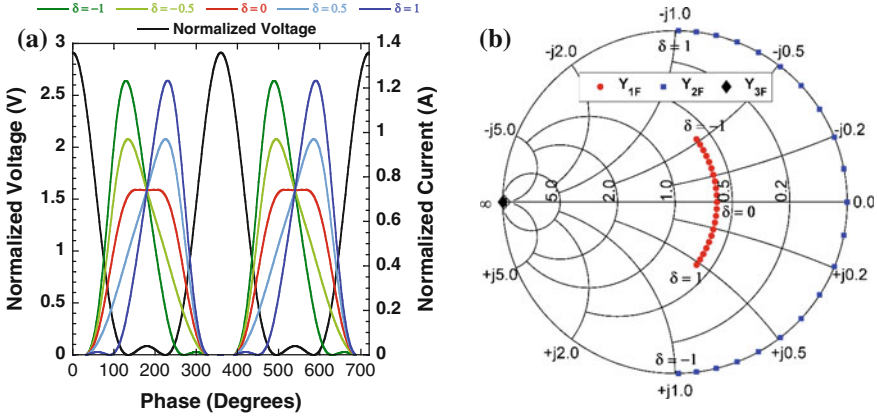


**Fig. 1.20** Continuous-inverse class-F PA. **a** Voltage and current waveforms. **b** Design space

current waveform is multiplied by an operator  $(1 - \delta \sin \theta)$  where  $-1 \leq \delta \leq 1$  and is given by (1.73) and (1.74). The shaping square current and rectified half-sinusoidal voltage waveform helps in extracting design space, which keeps the theoretical drain efficiency and output power constant.

$$V_{F^{-1}} = \left( 1 + \frac{2}{\sqrt{2}} \cos \theta + \frac{1}{2} \cos 2\theta \right) \quad (1.72)$$

$$i_{F^{-1}} = (0.37 - 0.43 \cos \theta + 0.06 \cos 3\theta)(1 - \delta \sin \theta) \quad (1.73)$$

$$i_{F^{-1}} = 0.37 - 0.43 \cos \theta + 0.06 \cos 3\theta - 0.37\delta \sin \theta + 0.185\delta \sin 2\theta - 0.03\delta \sin 4\theta \quad (1.74)$$

For  $\delta = 0$ , the conventional class- $F^{-1}$  operation is obtained. Using the voltage and current equations given in (1.72)–(1.74), the fundamental ( $Y_{F^{-1}}$ ), second harmonic ( $Y_{2F^{-1}}$ ) and third harmonic ( $Y_{3F^{-1}}$ ) admittances can be calculated as a function of  $G_{\text{opt}} (=1/R_{\text{opt}})$ , as

$$Y_{F^{-1}} = \sqrt{2}G_{\text{opt}}0.43 - j\delta\sqrt{2}G_{\text{opt}}0.37 \quad (1.75)$$

$$Y_{2F^{-1}} = j0.98\delta G_{\text{opt}} \quad (1.76)$$

$$Y_{3F^{-1}} = \infty \quad (1.77)$$

Since the voltage waveform has no third harmonic components, the third harmonic impedance is fixed at short circuit or admittance at open circuit condition. As depicted in Fig. 1.20b, when  $\delta$  is varied the fundamental admittance varies on a constant conductance circle, while the second harmonic admittance varies on the edge of the Smith chart from a short circuit condition.

In continuous class-F<sup>-1</sup> condition, fundamental and second harmonic admittances exhibit an inverse relation wherein every positive variation in fundamental susceptance is accompanied by a negative movement of the second harmonic susceptance.

## References

1. G. Gonzalez, *Microwave Transistor Amplifiers: Analysis and Design*, 2nd edn. (Prentice Hall, Upper Saddle River, 1996)
2. A.A.M. Saleh, Frequency-independent and frequency-dependent nonlinear models of TWT amplifiers. *IEEE Trans. Commun.* **29**(11), 1715–1720 (1981)
3. S. Rezaei Nazifi, L. Belostotski, F.M. Ghannouchi, P. Aflaki, Integrated design of a class-J power amplifier. *IEEE Trans. Microw. Theory Tech.* **61**(4), 1639–1648 (2013)
4. V. Carrubba, A.L. Clarke, M. Akmal, J. Lees, J. Benedikt, P.J. Tasker, S.C. Cripps, The continuous class-F mode power amplifier, in *Proceedings of the 5th European Microwave Integrated Circuits Conference*, pp. 432–435, Sept 2010



# Chapter 2

## Dual-Branch RF Amplifier Design and Architectures

### 2.1 Introduction

The previous chapter presents the conceptual understanding of power amplifier (PA) design as well as various design considerations and parameters. In the previously presented single-branch amplifiers, efficiency is maximal only at peak power drive, and drops rapidly as soon as the instantaneous input power is decreased. Accordingly, all single-branch PAs, regardless of their classes of operation, will fail to maintain satisfactory efficiency performance when driven with envelope varying wireless communication signals, owing to the high peak-to-average power ratio (PAPR) values of these signals. This stimulated the need for more appropriate alternatives. With the demand for highly efficient communication systems, the need for efficient PAs has increased considerably.

In this chapter, we provide a detailed analysis of the most common dual-branch-based radio frequency (RF) amplifiers with the aim of increasing the output power, power efficiency or the linearity of such amplifiers. These include balanced amplifiers, push–pull amplifiers, Doherty amplifiers, linear amplification with nonlinear components (LINC) amplifiers, and pulsed-load-modulated (PLM) amplifiers. The motivation of using two branches in such amplifiers is to have a combination of two single-ended amplifiers (belonging to the same class or different classes) working in parallel, resulting in higher efficiency and output power or linearity. Different design metrics will be used to evaluate the performance of the various dual-branch topologies, which will indicate significant improvement over their single-branch counterparts in terms of frequency response flatness, insertion loss, output power, power efficiency and linearity. An important step in the design of dual-branch amplifiers is the design of the input splitting couplers/signal separators and output combiners used to split the input signal and connect the output of the individual PAs to form a single output. A lossy or less efficient coupler or combiner will result in a reduced efficiency of the overall system.

## 2.2 Balanced Amplifiers

The motivation for two-branch balanced amplifiers (BAs) is to increase the 3 dB output power while exhibiting flatter frequency response and better return loss. In addition to increasing the output power, BA topology results in 3 dB higher  $OIP_3$ , in comparison to the  $OIP_3$  of the branch amplifier. A typical two-branch BA topology is shown in Fig. 2.1. It consists of a 3 dB quadrature hybrid coupler shown in Fig. 2.2 used to split the input signal into two components with a 90° phase difference between them. The signals are then fed to two paired amplifiers and then combined together by another 3 dB quadrature hybrid coupler at the output of the PAs. Ideally, this results in the same gain and twice the output power as the input signal.

The  $S$  matrix of a 4-port hybrid coupler is:

$$S_{90}^Q = \frac{1}{\sqrt{2}} \begin{bmatrix} 0 & 0 & -j & 1 \\ 0 & 0 & 1 & -j \\ -j & 1 & 0 & 0 \\ 1 & -j & 0 & 0 \end{bmatrix}$$

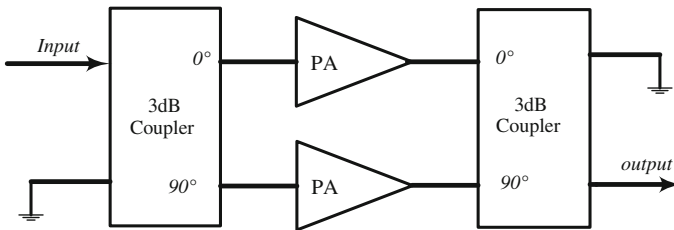
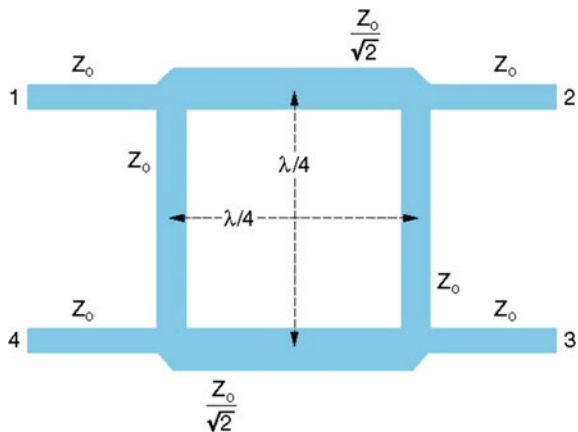


Fig. 2.1 Block diagram of a typical balanced amplifier

Fig. 2.2 Branch line hybrid coupler



The  $S$  parameters of the BA can be deduced from those of the PA using the following expressions:

$$S_{11}^{\text{BA}} = -\frac{1}{2}(S_{11}^{\text{A}} - S_{11}^{\text{B}}) \quad (2.1a)$$

$$S_{22}^{\text{BA}} = -\frac{1}{2}(S_{22}^{\text{A}} - S_{22}^{\text{B}}) \quad (2.1b)$$

$$S_{21}^{\text{BA}} = -\frac{j}{2}(S_{21}^{\text{A}} + S_{21}^{\text{B}}) \quad (2.1c)$$

$$S_{12}^{\text{BA}} = -\frac{j}{2}(S_{12}^{\text{A}} + S_{12}^{\text{B}}) \quad (2.1d)$$

It is obvious from the above equations that if amplifier A is identical to amplifier B, and the hybrid couplers are ideal, the resulting  $S$  parameters will be:

$$S_{11}^{\text{BA}} = S_{22}^{\text{BA}} = 0 \quad (2.2a)$$

$$S_{21}^{\text{BA}} = -jS_{21}^{\text{A}} \quad (2.2b)$$

$$S_{12}^{\text{BA}} = -jS_{12}^{\text{A}} \quad (2.2c)$$

From the above equations, it can be obviously concluded that the balanced amplifier will have perfect return loss, the same power gain as that of the branch amplifier and twice the output power.  $P_{1\text{dB}}$ ,  $P_{\text{sat}}$ , and  $\text{OIP}_3$  of the balanced amplifier are twice those of the branch amplifier.

The concept of balanced amplifier can be generalized to  $N$  balanced amplifiers, and the input and output couplers have to be designed such that they can equally split the input signal in  $N$  portions with incremental phase increase of  $\pi/N$  between the branches. The input signal to the amplifier of  $i$ th branch should be equal to

$$V_{\text{in}}^i = \frac{V_{\text{in}}}{\sqrt{N}} e^{j\frac{(i-1)\pi}{N}} \quad \text{with } i = 1, 2, \dots, N \quad (2.3a)$$

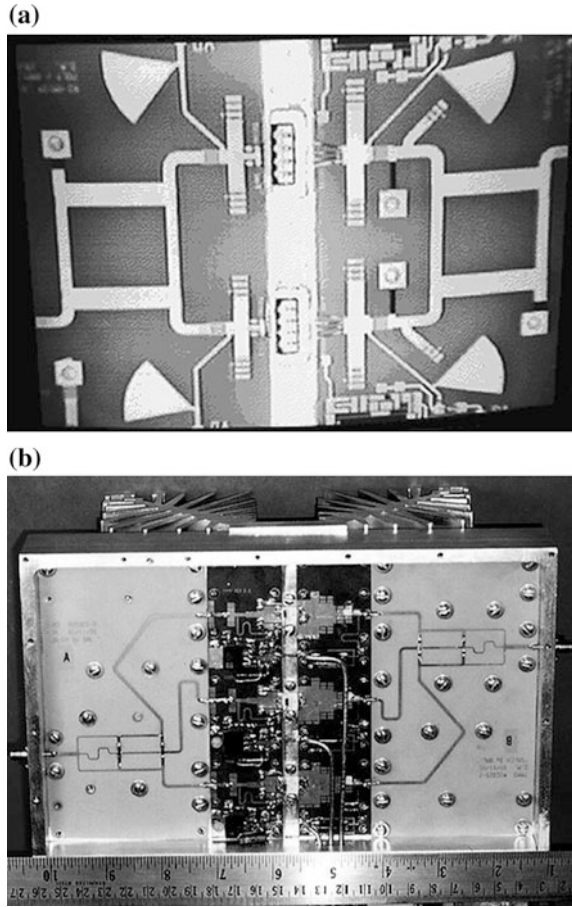
and the output signal power to the amplifier of  $i$ th branch should be

$$V_{\text{out}}^i = \frac{S_{21}^i V_{\text{in}}}{\sqrt{N}} e^{j\frac{(i-1)\pi}{N}} \quad (2.3b)$$

In such a case, the  $S$  parameters of the identical  $N$ -branch balanced amplifier can be written as

$$S_{11}^{\text{BA-N}} = S_{22}^{\text{BA-N}} = 0 \quad (2.5a)$$

**Fig. 2.3** Examples of balanced amplifiers: **a** two-branch balanced amplifier and **b** three-branch balanced amplifier



$$S_{21}^{BA-N} = -e^{j\frac{\pi}{N}} S_{21} \tag{2.5b}$$

$$S_{12}^{BA-N} = -e^{j\frac{\pi}{N}} S_{12} \tag{2.5c}$$

Design examples of two- and three-branch balanced amplifiers are shown in Fig. 2.3.

### 2.3 Push–Pull Amplifiers

Similar to the balanced amplifier topology, the push–pull amplifiers use two class-B amplifiers connected using two H-type (180°) hybrid couplers as shown in Fig. 2.4. The rat-race coupler is the H-coupler and is illustrated in Fig. 2.5. The topology

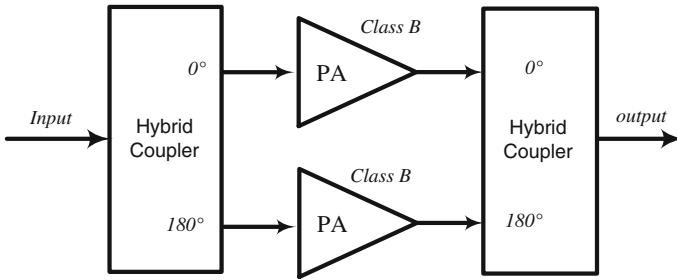
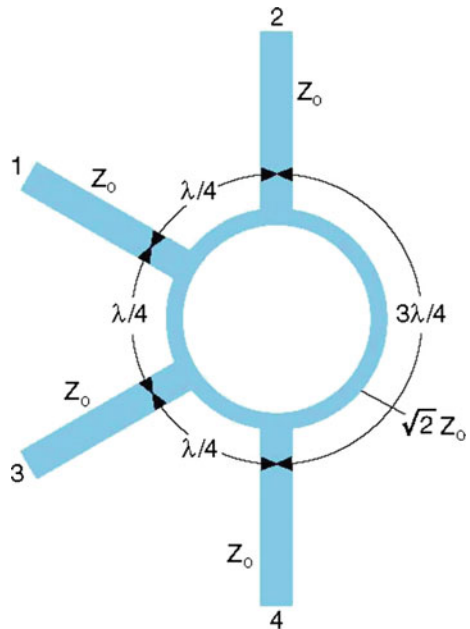


**Fig. 2.4** Block diagram of the push-pull amplifier

**Fig. 2.5** A rat-race H-coupler



doubles the output power of the branch amplifier while rejecting even order intermodulation distortions, leading to high linearity (despite the use of class-B amplifiers) and reasonable frequency response.

The  $S$ -parameter of the rat-race hybrid coupler is

$$S_{180}^H = \frac{-j}{\sqrt{2}} \begin{bmatrix} 0 & 1 & 1 & 0 \\ 1 & 0 & 1 & 0 \\ 0 & 1 & 0 & -1 \\ 1 & 0 & -1 & 0 \end{bmatrix} \quad (2.6)$$

### 2.3.1 Push–Pull Amplifier with Bipolar Transistors

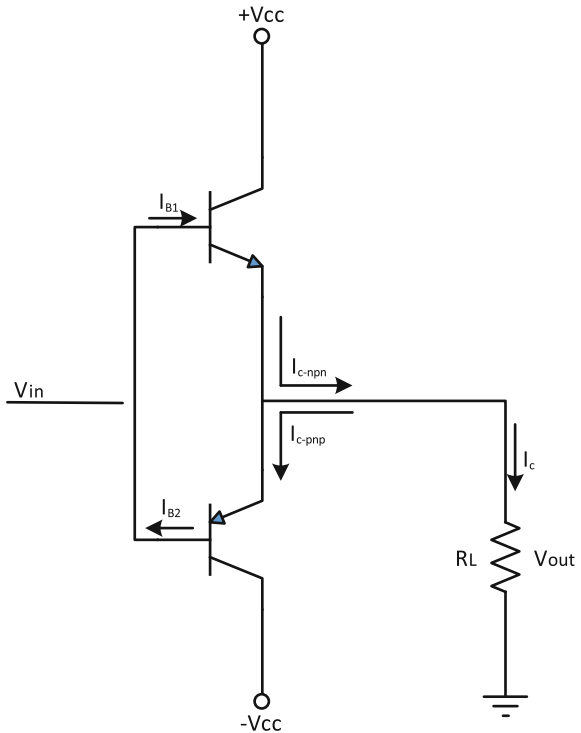
The basic circuit diagram of a balanced amplifier using NPN and PNP bipolar transistors is shown in Fig. 2.6. Here, the NPN and PNP transistors are working in push–pull configuration. Both NPN and PNP transistors are biased in class B but operate in the alternative half cycle of an input sinusoid. Thus, the current drawn from the direct current (DC) power supply by the NPN and PNP transistors are rectified alternative half-sine wave. Based on Eq. (1.55), the currents due to the two transistors are given by

$$I_{c-npn}(t) = I_{\max} \left[ \frac{1}{\pi} + \frac{1}{2} \sin(\omega t) - \frac{2}{\pi} \left( \frac{\cos(2\omega t)}{1 \times 3} + \frac{\cos(4\omega t)}{3 \times 5} + \frac{\cos(6\omega t)}{5 \times 7} + \dots \right) \right] \quad (2.7a)$$

$$I_{c-pnp}(t) = -I_{\max} \left[ \frac{1}{\pi} + \frac{1}{2} \sin(\omega t - \pi) - \frac{2}{\pi} \left( \frac{\cos(2\omega t - \pi)}{1 \times 3} + \frac{\cos(4\omega t - \pi)}{3 \times 5} + \frac{\cos(6\omega t - \pi)}{5 \times 7} + \dots \right) \right] \quad (2.7b)$$

The addition of the above two current waveforms leads to a pure current sine wave across the output resistance and cancels all even order harmonics. Therefore, in principle, a push–pull amplifier is a linear amplifier. One example of a microwave

**Fig. 2.6** Circuit-level implementation of an NPN and PNP push–pull amplifier



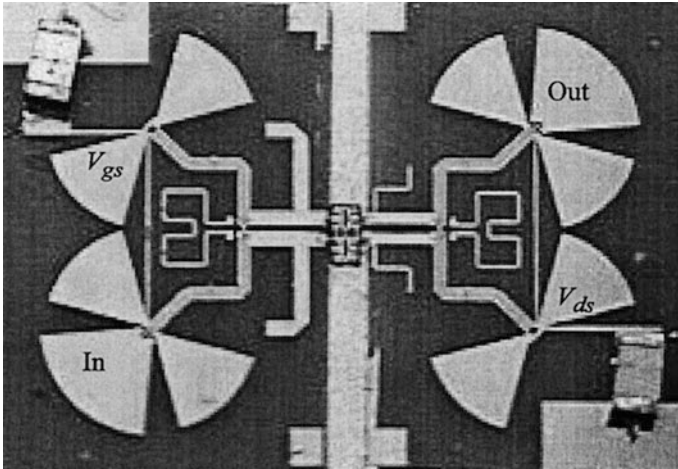


**Fig. 2.7** Photograph of a fabricated push–pull microwave power amplifier

power amplifier implementation using the push–pull amplifier configuration is shown in Fig. 2.7.

### 2.3.2 Push–Pull Amplifier with Baluns

Another topology of push–pull amplifiers requires a three-port balun (balanced–unbalanced) transformation instead of hybrid couplers for splitting and combining of the signals at the input and output of the amplifiers. The purpose of the balun is to transform the unbalanced input signal to balanced signals before being fed to the PAs. Baluns can be implemented as transformers or transmission lines. A transformer-type balun-based push–pull configuration is shown in Fig. 2.8.

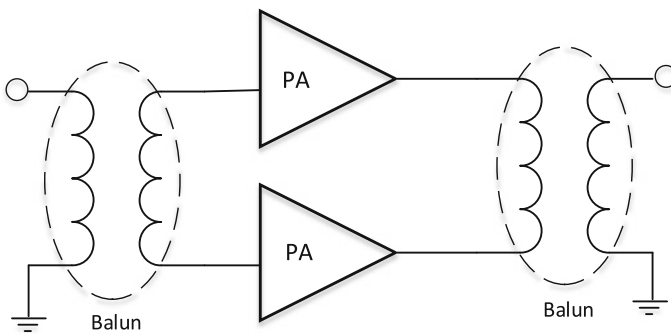


**Fig. 2.8** Transformer-type balun-based implementation of a push–pull amplifier

## 2.4 Doherty Amplifiers

### 2.4.1 Doherty Amplifier Architecture

The circuit diagram of a Doherty PA is presented in Fig. 2.9. It encompasses two parallel amplifiers, namely, the carrier amplifier (operating in class AB) and the peaking amplifier (operating in class C), an input analog splitter, and a nonisolated output power combiner that consists of two transmission lines, with an electrical length of  $90^\circ$ . In Fig. 2.9, the transmission line connected to the output load,  $Z_0$ , is commonly denominated as an impedance transformer, whereas that having a characteristic impedance of  $Z_0$  is designated as an impedance inverter. Typically, the carrier and peaking amplifiers have identical device sizes and matching networks and are evenly driven. The gate bias of the peaking PA is chosen to control its turn-on region. This defines the Doherty design parameter  $\alpha$  ( $0 \leq \alpha \leq 1$ ), which expresses the relative contribution, at full drive, of the carrier amplifier to the total output power of the Doherty PA.

Figure 2.10 shows the equivalent circuit diagram and the ideal output current profile model that are commonly considered for studying the operation of Doherty PAs. The operation of the circuit can be analyzed in two modes: at low-power mode, where only the carrier amplifier is active, and at high power mode, where

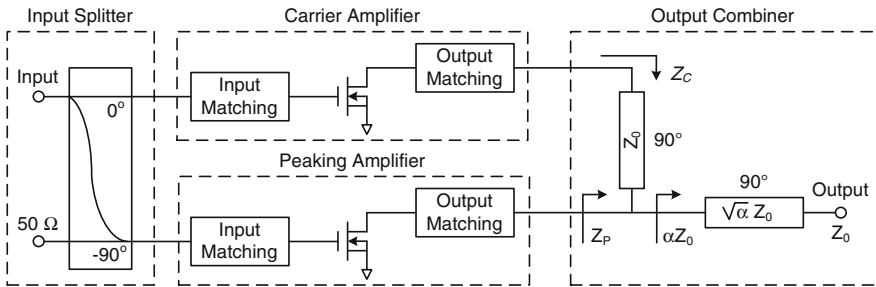


Fig. 2.9 Block diagram of the standard Doherty PA

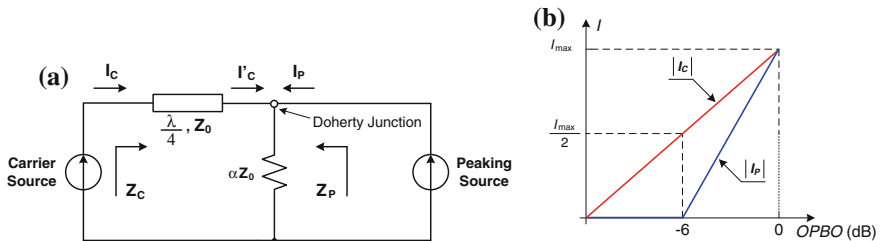
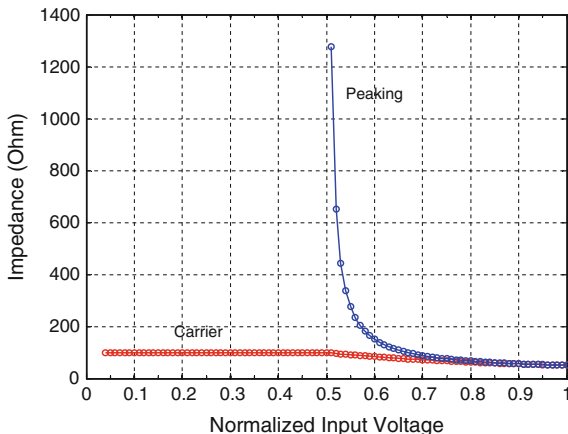


Fig. 2.10 **a** Equivalent operational circuit of the Doherty PA; **b** Ideal output current profile



**Fig. 2.11** Impedance seen by the Doherty amplifier



both carrier and peaking amplifiers are contributing to the output power of the Doherty PA.

At low input power levels, the peaking amplifier is turned *off*, and its branch ideally presents an open circuit. As inferred from Fig. 2.11, because of the action of the impedance inverter, the carrier amplifier will be operating into a load,  $Z_C$ , given by

$$Z_C = \frac{(Z_0)^2}{\alpha Z_0} = \frac{Z_0}{\alpha} \quad (2.7)$$

where  $Z_0$  is the output load of the Doherty PA, which is usually equal to  $50 \Omega$ .

The load impedance of the carrier amplifier remains unchanged as long as the peaking amplifier is still turned *off*. This causes the premature saturation of the carrier amplifier at  $20\log_{10}(\alpha)$  dB back-off from the Doherty PA-peak power level, which leads to an efficiency maximum at this power level.

As soon as the input power goes beyond the conduction threshold of the peaking amplifier, the latter starts contributing to the total output power of the Doherty PA. This creates an active load modulation mechanism; and, as illustrated in Fig. 2.11 (for  $\alpha = 0.5$  and  $Z_0 = 50 \Omega$ ), the load impedance of the carrier amplifier decreases gradually from its value given by (2.7) to  $Z_0$ , and that of the peaking amplifier,  $Z_P$ , drops rapidly from a very large value (theoretically infinite,  $\infty$ ) to  $Z_0$ . In this case, an efficiency maximum occurs at peak power drive.

#### 2.4.2 Efficiency Calculation and Optimization of Doherty Amplifier

The theoretical efficiency of a Doherty PA, the carrier and peaking amplifiers of which are operating in class B, is given by Ebrahimi et al. [1]

$$\eta(\text{OPBO}, \alpha) = \begin{cases} \frac{\pi}{4} \cdot \frac{1}{\alpha} \cdot 10^{\frac{\text{OPBO}}{20}}, & \text{OPBO} \leq 20\log_{10}(\alpha) \\ \frac{\pi}{4} \cdot \left( \frac{10^{\frac{\text{OPBO}}{10}}}{(1+\alpha) \cdot 10^{\frac{\text{OPBO}}{20}} - \alpha} \right), & 20\log_{10}(\alpha) \leq \text{OPBO} \leq 0 \end{cases}, \quad (2.8)$$

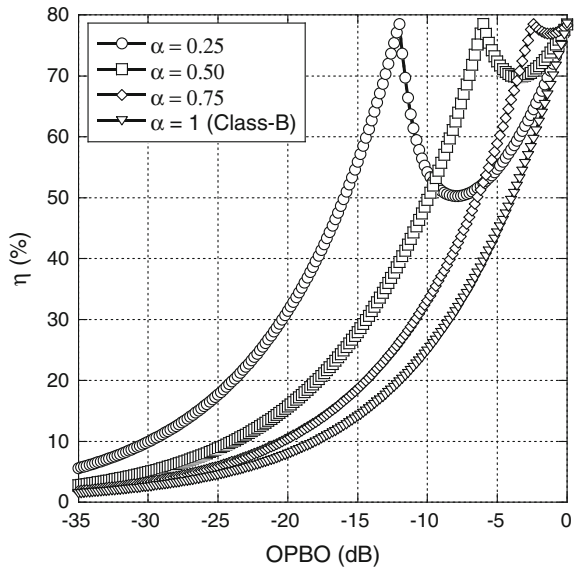
where output power back-off (OPBO) refers to the back-off of the actual output power of the Doherty PA from its saturation power.

Figure 2.12 depicts the simulated efficiency as a function of OPBO for various values of  $\alpha$ . It is clear that the active load modulation mechanism allows the maintenance of a relatively high efficiency over the power range  $P_{\text{sat,dB}} - 20\log_{10}(\alpha)$  to  $P_{\text{sat,dB}}$ , where  $P_{\text{sat,dB}}$  is the output saturation power, expressed in dB, of the Doherty PA. Furthermore, it can be seen that the choice of  $\alpha$  shapes the efficiency curve of the Doherty PA. A typical choice for the Doherty design parameter is  $\alpha = 0.5$ , which, by definition, means that the carrier and peaking amplifiers should contribute equally to the peak output power. Symmetrical Doherty PA commonly denotes this specific type.

In practice, the design of Doherty PAs for optimal performance should consider the operating conditions at high- and low-power regions.

At peak power condition, the carrier and peaking amplifiers are ideally operating into  $50 \Omega$ . The design of the single-ended carrier and peaking amplifiers consists of determining the appropriate source and load impedances and designing the input and output matching networks that are required to achieve the targeted performance in terms of power efficiency or output power. The design procedure is well established and a load-pull-based approach is often adopted.

**Fig. 2.12** Theoretical efficiency of the Doherty PA



**Fig. 2.13** Doherty PA design optimization in the peaking branch

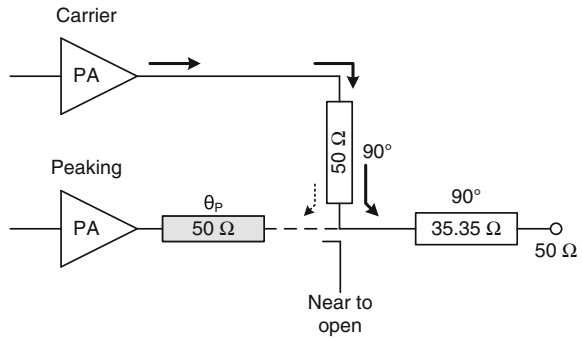
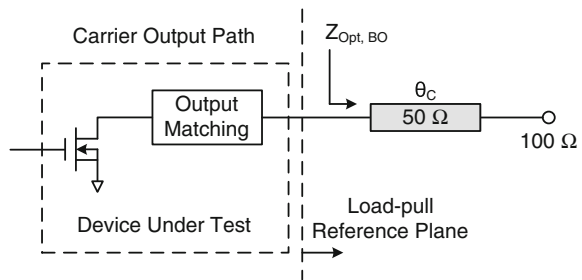


**Fig. 2.14** Doherty PA design optimization in the carrier branch



At the low-power region, the design considerations of the carrier and peaking amplifiers are different. First, the peaking branch should present an open circuit to prevent the leak of output power from the carrier amplifier into the peaking path when the peaking amplifier is still turned *off*. As depicted in Fig. 2.13, this problem can be surmounted by inserting an offset line ( $\theta_p$ ) following the peaking amplifier to ensure the quasi-open-circuit condition.

Second, the performance of the carrier amplifier at back-off (i.e., when the peaking amplifier is still inactive) should be optimized as it will dominate the overall performance of the Doherty PA when driven with modulated signals with high PAPRs. As illustrated in Fig. 2.14, this can be achieved by means of a series offset line ( $\theta_c$ ) that converts the 100  $\Omega$  seen by the carrier amplifier at back-off to an optimal matching point,  $Z_{Opt,BO}$ , that gives the best possible performance around the turn-on point of the peaking device. Detailed explanations related to design optimization of dual-branch Doherty PAs are discussed in [2].

### 2.5 Pulsed-Load-Modulated Amplifier

The pulsed-load-modulated (PLM) PA was first introduced in 2010 [3]. This technique benefits from the delta-sigma envelope modulation at the gate supply of the power amplifier to dynamically modulate the load at the output of the PA to improve

the power efficiency performance. Delta-sigma modulation (DSM) technique is explained in Sect. 2.7. Unlike Doherty PA, in the PLM PA, the dynamic load variation is dependent on the duty cycle of the DSM signal and it will be shown that the and the average efficiency of the ideal PLM amplifier stays at its maximum value for up to 6 dB back-off from the peak output power [4]. This section will survey the concept of the dynamic load modulation in PLM power amplifiers and its effect on their power efficiency performance.

### 2.5.1 Load Modulation in Switched Resonators

Digital load modulation of the PLM amplifier is based on dynamic load variations in switched resonator circuit. Figure 2.15 shows a typical switched resonator circuit with a series LC tank. A switched resonator consists of a switched controlled RF source, a high Q resonator [or band-pass filter (BPF)] tuned at the frequency of the RF input signal, terminated with a load.

The energy stored in the resonator is controlled by the switching action speed so that variable and duty-cycle dependent impedance behavior can be obtained at the input of the resonator. If the switching action happens with a switching period ( $T$ ) shorter than the time constant of the resonator and with a switching frequency less than the RF signal frequency ( $f_c$ ), the on-state voltage at the output of the resonator,  $V_{out}$  can be approximated by the product of the duty cycle,  $D$ , and the voltage at the input of the switched amplifier,  $V_A$  is as follows:

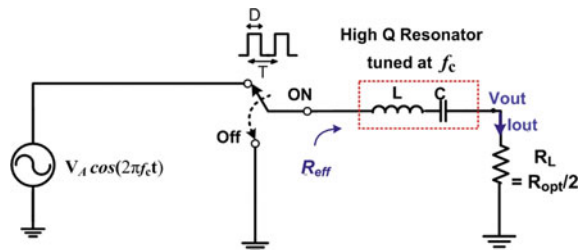
$$V_{out} = DV_A \quad (2.9)$$

The current at the output of the resonator,  $I_{out}$  is about the same as the one at its input and it can be approximated by the following equations:

$$I_{out} = \frac{V_{out}}{(R_{opt}/2)} = \frac{2DV_{max}}{(V_{max}/I_{max})} = 2DI_{max} \quad (2.10)$$

where  $R_{opt} = \frac{V_{max}}{I_{max}}$  is the optimum matching impedance of the class-B amplifier. In this equation,  $V_{max}$  and  $I_{max}$  are the maximum voltage and current of the class-B amplifier.

**Fig. 2.15** Block diagram of a switched resonator circuit with a series LC tank



Hereafter, we consider the switched amplifier is fully driven such that  $V_A = V_{\max}$ .

During the *off* state of the switched amplifier, the *off* state voltage is practically zero. Therefore, the effective resistance,  $R_{\text{eff}}$ , at the output of the switched amplifier can be approximated by the following:

$$R_{\text{eff}} = \begin{cases} \frac{V_A}{I_{\text{out}}} = \frac{(V_{\text{out}}/D)}{I_{\text{out}}} = \frac{1}{D} \cdot R_L = \frac{1}{D} \cdot R_{\text{opt}}/2 & 0 \leq t < D \cdot T \\ 0 & D \cdot T \leq t < T \end{cases} \quad (2.11)$$

From Eq. (2.11), one can conclude the effective output resistance of the switched amplifier increases from  $R_{\text{opt}}/2$  to infinity when the duty cycle varies from 100 to 0 %.

The output power at the load can be calculated as:

$$P_{\text{out}} = \frac{1}{2} I_{\text{out}} V_{\text{out}} = \frac{1}{2} \left( \frac{DV_A}{R_{\text{out}}/2} \right) (DV_A) = V_{\text{max}}^2 \frac{D^2}{R_{\text{opt}}} = D^2 V_{\text{max}} I_{\text{max}} \quad (2.12)$$

From these equations, it can be seen that in a switched resonator circuit, the load impedance at the input of the resonator and the output power can be controlled by the duty cycles of the switching pulses. This dynamic load variation is very beneficial in designing high efficiency PAs since the optimal efficiency in the amplifier can be achieved when the load impedance is inversely proportional to the square root of the output power.

### 2.5.2 PAs with Pulsed-Load Modulation

Figure 2.16 shows a simple block diagram of a PLM power amplifier. As can be seen in this figure, in the PLM amplifier structure, the main and auxiliary amplifiers are connected together by a  $90^\circ$  transmission line and they are switched at the same time by the modulated envelope of the signal between the class B (the *on* state) and pinch-off (the *off* state). Using digital signal processing techniques such as pulsed width modulation (PWM) or DSM, the time envelope varying signals can be converted to constant envelope signals. The constant envelope modulated signal is then transmitted to the gate biases of the main and auxiliary amplifiers. The phase of the signal is up-converted to the carrier frequency and is then fed to the input of the amplifier. In order to remove the quantization noise caused by the envelope modulator from the output signal, a band-pass filter (BPF) with a high quality factor is placed at the output of the power amplifier.

The efficiency enhancement method in the PLM PA is derived from the mechanism of the load modulation in series with LC switched resonators. If the switching action at the gates of the main and auxiliary amplifiers occurs faster than the bandwidth of the output filter, the effective input impedance of the filter ( $R_{\text{eff}}$ )

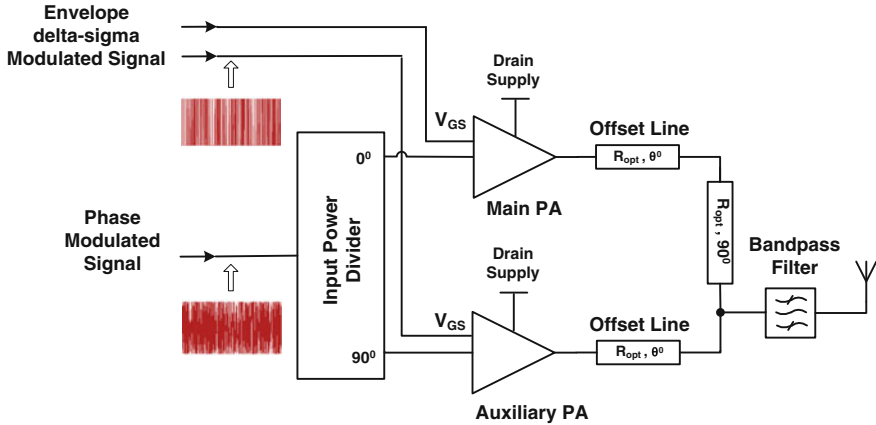


Fig. 2.16 A simple block diagram of the PLM power amplifier

varies inversely with the duty cycle of the gate bias pulses. Consequently, it can be shown that the output power is proportional to the square of the duty cycle of the switching pulses during the *on* state, and the optimal efficiency performance can be achieved.

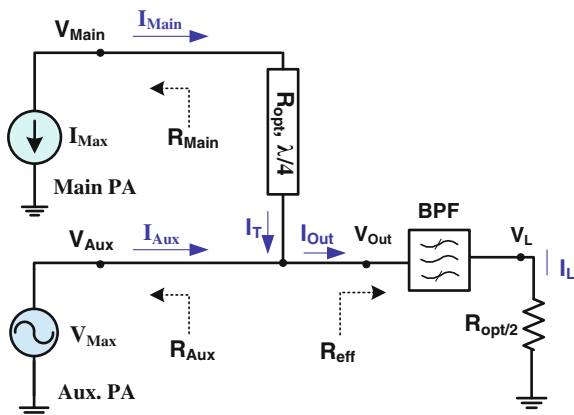
When the gate pulses are *off*, both transistors are turned *off* simultaneously. The  $\lambda/4$  transmission line is used at the output of the main amplifier to transfer the main PA high-output impedance to a virtual ground at the input of the BPF. Therefore, as in series LC switched resonators, there is a short circuit at the input of the filter and  $R_{\text{eff}}$  equals zero. During the high level of the gate pulses (*on* state), the auxiliary amplifier is forced to operate in the saturation mode due to the load modulation occurring at its output. Therefore, the auxiliary amplifier can be modeled as a voltage source during the *on* state such as in switched resonators.

In the design of the PLM PA, the main branch has slightly higher voltage than the auxiliary PA branch. Hence, for the low input power levels (when the gate pulse duty cycles are less than 50 %), the main amplifier provides most of the current to the output load. However, at high input power levels (when the duty cycle of the gate pulses are higher than 50 %), both main and auxiliary amplifiers conduct current to the load. Figure 2.17 depicts a simple model of the PA at the *on*-state level of the gate pulses.

The performance of the amplifier can be analyzed and tested using variable duty cycle pulses as gate biases for both main and auxiliary PAs.

*Back-off mode of operation (OPBO > 6 dB)* For pulses with duty cycles less than 50 %, the OPBO level is more than 6 dB. In this region, the main amplifier provides most of the current to the output load terminal. At OPBO levels greater than 6 dB or for duty cycles less than 50 %, according to (2.10) the output current at the combination point can be expressed as follows

**Fig. 2.17** Equivalent circuit of the PLM amplifier at high-level gate pulses



$$I_T = I_{out} = 2DI_{max} \quad (2.13)$$

Hence the output current and voltage of the main amplifier are

$$I_{Main} = jI_{max} \quad (2.14)$$

$$V_{Main} = jR_{opt}I_T = jR_{opt}(2DI_{max}) = 2jDV_{max} \quad (2.15)$$

and the load impedance seen by the main amplifier is given by

$$R_{Main} = \frac{V_{Main}}{I_{Main}} = 2DR_{opt} \quad (2.16)$$

Since the auxiliary amplifier is modeled as voltage source having amplitude of  $V_{max}$  and according to (2.11), it is loaded with relatively high impedance; therefore almost no current is generated from it. The current and voltage at the output of the auxiliary amplifier are  $I_{Aux} = 0$  and  $V_{Aux} = V_{max}$ .

Consequently, using (2.12) and assuming class B mode of operation for the main amplifier, the drain efficiency of the PLM amplifier can be calculated as follows:

$$\begin{aligned} \eta_{PA} &= \frac{P_{out}}{P_{DC}} = \frac{D^2 I_{max} V_{max}}{I_{DC-Main} V_{DC-Main}} = \frac{D^2 I_{max} V_{max}}{(I_{max}/\pi)(2DV_{max})} = \frac{D^2 I_{max} V_{max}}{(\frac{2}{\pi} DI_{max})(V_{max})} \quad (2.17) \\ &= \frac{\pi D}{2}, \quad 0 < D < 50\%. \end{aligned}$$

**Back-off mode of operation ( $0 \text{ dB} < \text{OPBO} < 6 \text{ dB}$ )** As the duty cycle of the gate pulses increases from 50 to 100 %, entering the 6 dB OPBO region, the main

amplifier provides  $I_{\max}$  to the output load, and the auxiliary amplifier starts providing the remaining current to the load as its output impedance reduces because of the load modulation behavior of the PLM power amplifier. At the full power level, both amplifiers contribute equally in delivering the maximum combined current of  $2I_{\max}$  to the load,  $R_{\text{opt}}/2$ . At less than 6 dB OPBO, considering (2.10), the currents in the main and auxiliary are as follows:

$$I_T = I_{\max}, \quad I_{\text{Aux}} = I_{\text{out}} - I_T = (2D - 1)I_{\max} \quad (2.18)$$

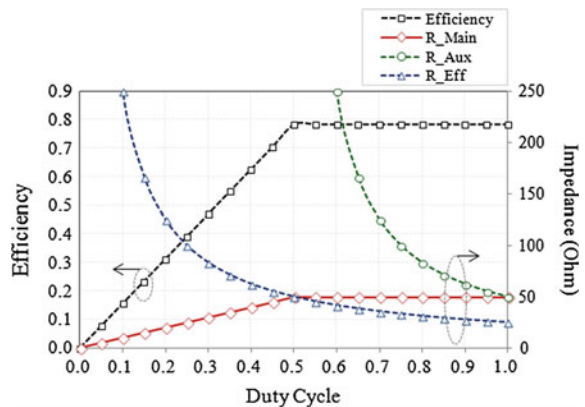
$$I_{\text{Main}} = jI_{\max}, \quad V_{\text{Main}} = jR_{\text{opt}}I_T = jV_{\max}. \quad (2.19)$$

Using (2.12), the drain efficiency of the PLM amplifier in the 6 dB OPBO region can be calculated as

$$\begin{aligned} \eta_{PA} &= \frac{D^2 I_{\max} V_{\max}}{I_{DC-\text{Main}} V_{DC-\text{Main}} + I_{DC-\text{Aux.}} V_{DC-\text{Aux.}}} \\ &= \frac{D^2 I_{\max} V_{\max}}{\left(\frac{1}{\pi}\right) [I_{\max} + (2D - 1)I_{\max}] 2DV_{\max}} = \frac{\pi}{4}, \quad 50 \leq D \leq 100\% \end{aligned} \quad (2.20)$$

Since both amplifiers stay in saturation at 6 dB OPBO region, the efficiency of the PLM PA stays at the optimum value (around 78 % for ideal class-B amplifiers). Figure 2.18 shows the ideal drain efficiency of the PA along with the load impedances seen at the output of the main and auxiliary amplifiers  $R_{\text{Main}}$  and  $R_{\text{Aux}}$  for different duty cycle values. In this analysis, the optimum load impedance of the main and auxiliary amplifiers  $R_{\text{opt}}$  is supposed to be  $50 \Omega$ . It can be seen in this figure that the load impedance  $R_{\text{eff}}$  varies inversely with the duty cycle values.

**Fig. 2.18** Theoretical drain efficiency of the PA and the load impedances seen at the output of the main and auxiliary amplifiers ( $R_{\text{Main}}$  and  $R_{\text{Aux}}$ ) for variable duty cycles





## 2.6 Linc Amplifiers

### 2.6.1 LINC Amplifier Architecture

The LINC amplifier is a two-branch amplifier, illustrated in Fig. 2.19.

The principle of operation of the LINC amplifier is based on converting the varying-envelope input signal,  $S_{in}(t)$ , into two constant envelop- and phase-modulated signals  $S_1(t)$  and  $S_2(t)$ , which can be obtained using the following expression:

$$S_{in}(t) = r(t) \cdot e^{j\phi(t)} = S_1(t) + S_2(t) \quad (2.21)$$

where  $r(t)$  is the envelop of the input baseband signal and  $\phi(t)$  is its phase.

By writing the envelop of the signal as

$$r(t) = r_{\max} \cdot \cos(\theta(t)) \quad (2.22)$$

With  $r_{\max} = \max(|s_{in}(t)|) = \max(r(t))$  and  $\theta(t) = [\cos(r(t)/r_{\max})]^{-1}$ .

One can deduce using the two equations above that the phase-modulated signals after signal decomposition are

$$\begin{cases} S_1(t) = \frac{r_{\max}}{2} \cdot e^{j(\phi(t) + \theta(t))} \\ S_2(t) = \frac{r_{\max}}{2} \cdot e^{j(\phi(t) - \theta(t))} \end{cases} \quad (2.23)$$

The resultant signal,  $S_{out}(t)$ , at the output of the amplifier, having voltage gain,  $G$ , is a linearly amplified version of the input signal  $S_{in}(t)$ :

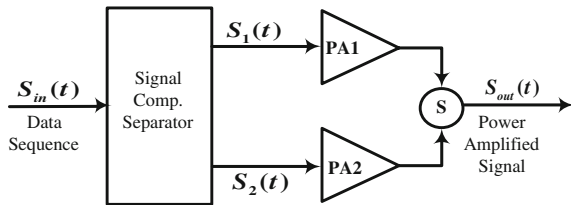
$$S_{out}(t) = G \cdot S_{in}(t) \quad (2.24)$$

Another way to compute  $S_1(t)$  and  $S_2(t)$  using geometrical reasoning is illustrated in Fig. 2.20:

$$\begin{cases} S_1(t) = \frac{1}{2}S(t)[1 + j \cdot e(t)] \\ S_2(t) = \frac{1}{2}S(t)[1 - j \cdot e(t)] \end{cases} \quad (2.25)$$

where  $e(t) = \sqrt{\frac{r_{\max}^2}{r^2(t)} - 1}$

**Fig. 2.19** LINC amplifier block diagram



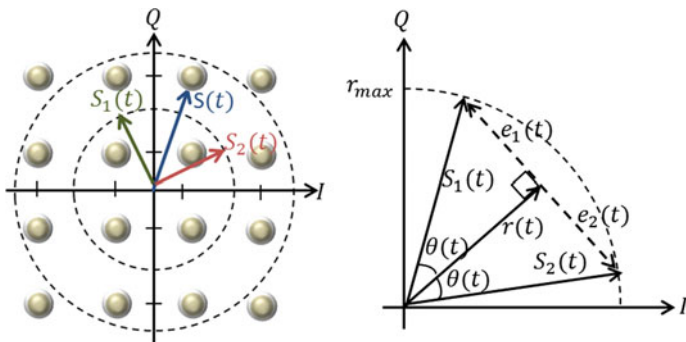


Fig. 2.20 LINC vector decomposition

Considering that  $S_1(t)$  and  $S_2(t)$  have constant envelopes, they can be efficiently amplified by means of power-efficient or saturated or switching-mode PAs. The two amplified signals are then combined to retrieve a linearly amplified replica of the original amplitude-modulated input signal. Therefore, the RF PAs can be operated at saturation, to achieve maximum power efficiency. The structure of a LINC amplification system is shown in Fig. 2.21. A vector representation of the separated baseband components is also given in Fig. 2.20. There are three main components in the LINC transmitter, which are the signal separator, the nonlinear amplifiers, and the signal combiner [5]. A brief discussion of each block is covered as follows.

A successful implementation of a LINC transmitter is highly dependent on the precision and control of signal separation, because the LINC architecture is sensitive to amplitude and phase balance [5].

The PAs should be designed for the highest possible efficiency at saturation, based on the selection of the biasing and impedance matching circuits. For this reason, class-F and inverse class-F PA designs that have high power efficiencies can be used. The bandwidth response of the PA needs to be carefully selected, as the LINC-separated signals have larger bandwidth than the original envelope modulated signal, because of added phase modulation. Additionally, the power-amplification

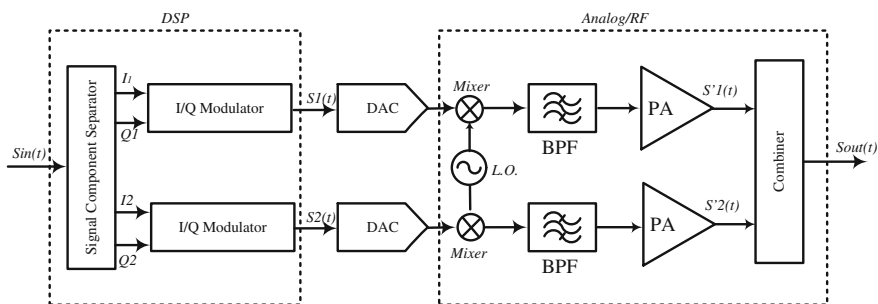


Fig. 2.21 LINC transmitter structure

block should be made of two identical or quasi-identical amplifiers in order to preserve amplitude and phase balance between two branches [5].

The use of two highly efficient PAs operated with constant envelope signals in the LINC system does not guarantee that the overall efficiency of the LINC transmitter will be high, but the available power at the output of the combiner will determine the transmitter's overall efficiency. The average efficiency of the LINC system depends also on the power distribution function (PDF) of signal and the type of combiner used. Hence, the combining structure is a key factor in the overall power efficiency as well as the linearity of the LINC transmitter.

Two possible combining structures can be used: (i) the matched and isolated combiner, and (ii) the nonmatched and nonisolated combiners that are also referred in the literature as outphasing or Chireix combiners [5]. The overall system efficiency of the LINC amplifier,  $\eta_{\text{LINC}}$ , is given by

$$\eta_{\text{LINC}} = \eta_{\text{PA}}^{\text{Peak}} \cdot \eta_c \quad (2.26)$$

where  $\eta_{\text{PA}}^{\text{Peak}}$  is the peak amplifier efficiency, and  $\eta_c$  is the system-combining efficiency.

### 2.6.2 Case of Matched and Isolated Combiner

In the case of a matched and isolated combiner shown in Fig. 2.22, the system instantaneous combining efficiency can be calculated as follows:

$$\eta_c(t) = \frac{P_{\text{out}}}{P_1 + P_2} = \frac{1}{2} \frac{|S_{\text{out}}|^2}{G^2 (|s_1|^2 + |s_2|^2)} = \frac{|s_{\text{in}}|^2}{r_{\text{max}}^2} = \cos^2(\theta(t)) \quad (2.27)$$

The system-combining efficiency reaches its maximum (unity) at peak power and drops fast as the signal drive level decreases. This equation concludes that despite the branch amplifier has very high efficiency, the LINC amplifier efficiency drops rapidly at low-level signals as low as  $\eta_{\text{PA}}^{\text{Peak}}/10$ , at power back-off operation of 10 dB.

**Fig. 2.22** The Wilkinson combiner

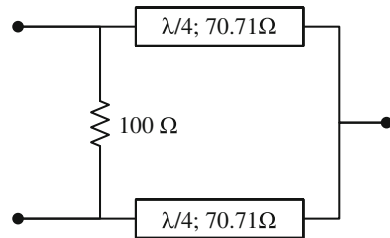


Figure 2.23 shows the comparative efficiency performance of the LINC system using isolated (Wilkinson) combiner against class-B amplifier:

The average efficiency of the LINC amplifier depends on the signal’s PDF. If the latter is known analytically, one can compute the average LINC efficiency by:

$$\eta_{Avg} = \eta_{PA}^{Peak} \int_0^{\pi/2} p(\theta) \cos^2(\theta) d\theta \tag{2.28}$$

where  $\eta_{PA}^{Peak}$  is the peak efficiency of each RF amplifier branch, and  $p(\theta)$  is the PDF of signal at  $\theta(t)$ .

Figure 2.24 illustrates how the average combining efficiency depends on the signal statistics. It is clear that the average combining efficiency for the orthogonal frequency division multiplexing (OFDM) signal will be about 65 % and that of CDMA signal will be about 50 %.

As for the linearity, the LINC system with hybrid combiner is assumed to occur with high linearity if the two branches are perfectly balanced and the combiner does not introduce any imbalance in phase or amplitude between two branches.

**Fig. 2.23** Efficiency of the LINC system using the Wilkinson combiner and class-B amplifier

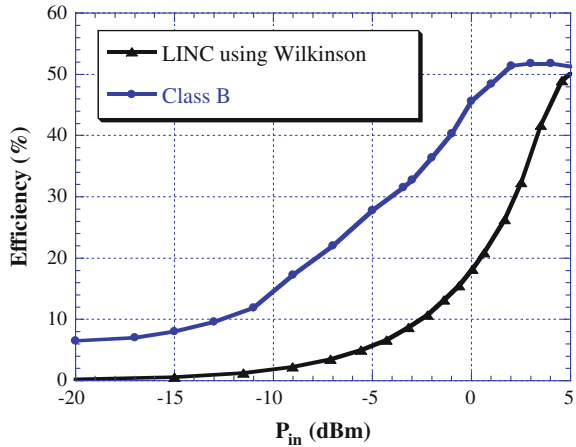
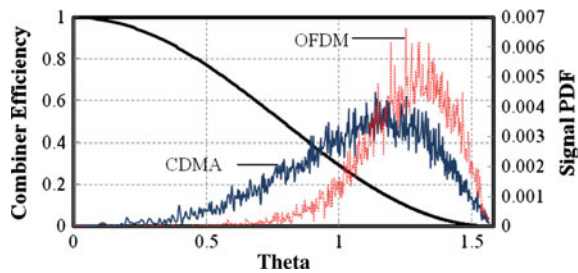


**Fig. 2.24** Average efficiency of the LINC amplifier for CDMA and OFDM signals

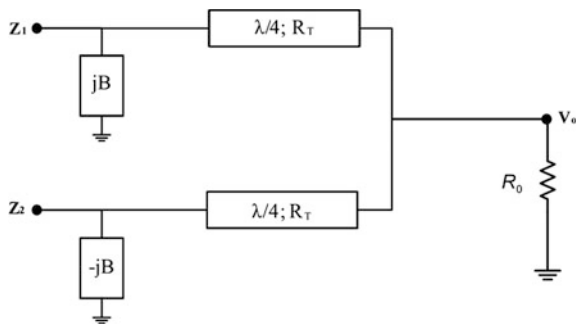


### 2.6.3 Case of Nonmatched Combiners (Chireix Combiners)

This second class of combining structures groups the unmatched lossless outphasing combiners. This class includes the lossless Wilkinson-type combiner, i.e., without the isolation resistor, and a combiner that typically includes two quarter-wavelength transmission lines, a tee junction, and shunt reactance of opposite values at the input of each transmission line, which is typically called the Chireix-outphasing combiner. Figure 2.25 shows the Chireix-outphasing combiner structure with  $Z_c$  representing the characteristic impedance of the quarter-wavelength transmission line, and  $B$  is the magnitude of the susceptance of the shunt elements in the combiner, which are named stubs. This susceptance is added to improve efficiency by canceling the imaginary part of load presented to the RF amplifier at a certain power back-off.  $Z_o$  is the impedance of the output load, and  $V_o$  is the output voltage. Branch 1 of this combiner amplifies the  $+\theta(t)$  phase signal and has a shunt element with  $+B$  susceptance. Branch 2 of the combiner amplifies the  $-\theta(t)$  phase signal and has a shunt element with  $-B$  susceptance.

The Chireix combiner or lossless combiner can be presented as a very good solution to the problem of degradation of efficiency observed when the matched combiner is used. The Chireix combiner as described above does not have an isolated port load to dissipate any energy. Consequently, the nonisolating combiner presents time-varying impedances to the output of the RF amplifier of each branch as the phase difference between the branches increases, thus improving the LINC average efficiency significantly. To describe the behavior of load impedance variation, Raab [6] gives the expression for time-varying impedance/admittance and its impact on the efficiency of several kinds of power amplifiers. In [7], Stengel found similar results on the combiner efficiency and optimization using a different approach and ideal voltage sources. Assuming that the RF amplifiers exhibit ideal voltage source behavior, the DC-power consumption will scale according to the load impedance, i.e., the efficiency remains high regardless of the phase difference between branches. For an ideal voltage source, its output voltage is not affected by its output current. The voltage magnitude remains fixed, and the voltage phase is only modulated by the phase of the control signal. Thus, the constant envelope

Fig. 2.25 The Chireix-outphasing combiner



signal principle at each branch is kept, and the internal impedance of RF amplifier of each branch is considered equal to zero. Using the topology of the Chireix combiner depicted in Fig. 2.25, where the shunt susceptance  $B$  is introduced to improve the LINC system average efficiency, the resulting formula of the impedance variation found in [7] is modified to introduce the  $R_o$  impact, as follows:

$$Z_{1,2} = \left[ \left( \frac{2R_o}{R_T^2} \right) (\cos^2(\theta(t)) \pm j(B' + \sin(2\theta(t)))) \right]^{-1} \quad (2.29)$$

with  $B' = \frac{BR_T^2}{2R_o}$

Figure 2.26 shows how the instantaneous efficiency changes as a function of the power back-off for given values of  $B'$ , directly related to the value of shunt susceptance,  $B$ , assuming that  $R_o$  and  $R_T$  are fixed by the design of the power combiner.

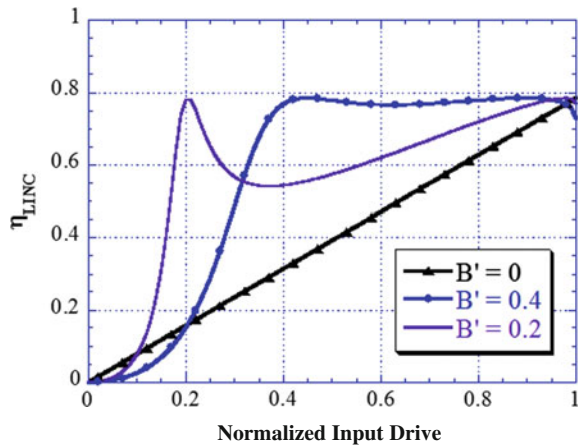
In the Chireix combiner, the parallel admittance  $B$  is introduced to improve the LINC average efficiency. In this case, the average efficiency can be expressed as

$$\eta_{\text{Avg}}^{\text{Chireix}} = \eta_{\text{PA}}^{\text{Peak}} \int_0^{\pi/2} p(\theta) \eta_c^{\text{Chireix}}(\theta) d\theta \quad (2.30)$$

where  $\eta_c^{\text{Chireix}}(\theta)$  is the instantaneous combiner efficiency that can be obtained, as follows [6]:

$$\eta_c^{\text{Chireix}}(\theta) = \frac{\text{real}(Z_{1,2})}{\text{mag}(Z_{1,2})} \quad (2.31)$$

**Fig. 2.26** Efficiency of the LINC amplifier



The parallel admittance  $B$  allows the designer to maximize the instantaneous efficiency of combiner  $\eta_{\text{Comb}}$ . By choosing the value of  $B$  when the imaginary part of  $Z_{1,2}$  is equal to zero, the instantaneous efficiency  $\eta_{\text{Comb}}$  is maximized for a certain value  $\theta_m$  of  $\theta$ . To optimize the average efficiency of the Chireix combiner, the designer needs to define the type of modulation used in the LINC system and use the PDF of the signal to obtain the optimum value  $\theta_m$  of  $\theta$ , which gives the maximum of the expression (2.31). If this is done, then the value of admittance  $B$  can be fixed. Indeed, the Chireix system presents an important improvement in efficiency compared to the LINC using the hybrid combiner. As noted above, this improvement in efficiency is obtained at the cost of degradation of linearity.

## 2.7 Delta-Sigma-Based Transmitters

A power amplifier (PA) operation in Class AB or in Class B outputs its maximum efficiency while it is driven by its maximum allowable input. For high throughput modulation signals, for example quadrature amplitude modulations (QAMs) such as 16-QAM and 64-QAM modulated, the envelope is varying and the peak power of the signal occurs at very short periods. Hence, the PA could not be driven to more than its saturation power, it should be driven at the back-off from its peak input power. This power difference is a property of the signal is defined as the peak to average ratio PAPR.

### 2.7.1 Delta-Sigma Modulation

A delta-sigma modulator as illustrated in Fig. 2.27c is able to shape the envelope varying signal, illustrated in Fig. 2.27a into a constant envelope pulse train signal illustrated in Fig. 2.27b, in such way the information in coded in the phase and the amplitude of the input signal will be converted to the pulse's width and pulse's separation information at the output of the sigma delta modulator (DSM). In this case, The PA fed by a DSM signal could work at its maximum efficiency without need to any power back-off. A high efficiency switching-mode PA (SMPA) placed at the output of the DSM could be used without causing a distortion to the delta-sigma modulated signal providing that an RF BPF is placed at the output of the PA. The DSM is based on oversampling and quantizing a baseband time-varying envelope signal and encode it to a bi-level constant envelope signal. A feedback signal in the DSM contains the quantized signal is subtracted from the input signal. A block diagram shows the building blocks of the DSM. At first, as illustrated in Fig. 2.27c, the input signal is subtracted from the feedback quantized signal to extract the quantization noise. Then, this quantization noise is filtered out and pushed away from the signal channel using filter with bandwidth equal to the input signal bandwidth [7] (Fig. 2.27).

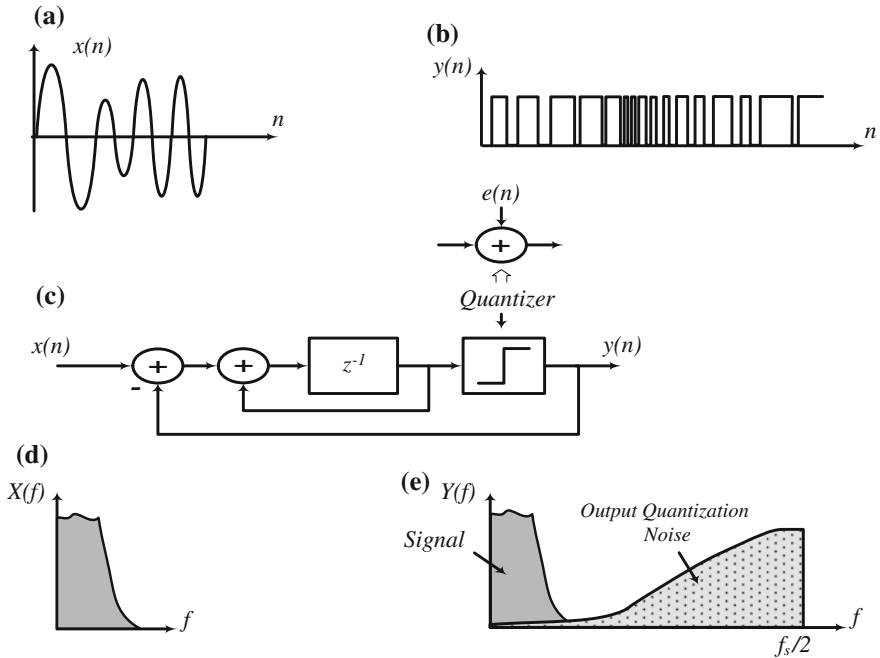


Fig. 2.27 First order delta-sigma modulator

The low-pass transfer function of the first-order DSM given in Eq. (2.1a) shows that the signal and quantization noise pass through different transfer functions; the signal transfer function STF and the noise transfer function NTF

$$Y(z) = z^{-1}X(z) + (1 - z^{-1})E(z) \quad (2.32)$$

With  $\text{STF} = z^{-1}$  and  $\text{NTF} = (1 - z^{-1})$ .

The two important parameters for a DSM which reduce and shape the quantization noise are the order of the modulator and the over sampling rate defined by

$$\text{OSR} = \frac{f_s}{\text{BW}}, \quad (2.33)$$

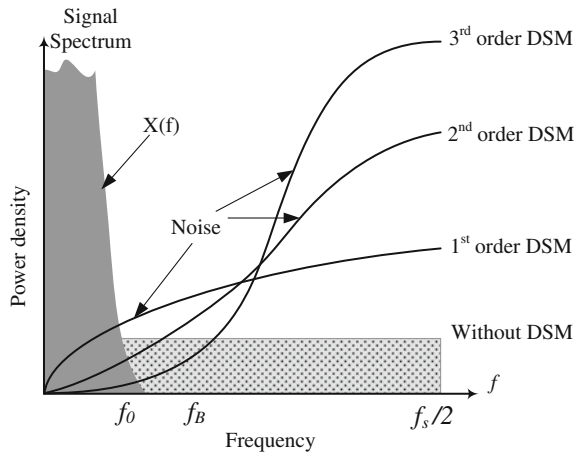
where  $f_s$  is the sampling frequency and BW is the bandwidth of the input signal.

In DSM the quantization and noise is distributed over  $-f_s/2$  to  $+f_s/2$ ; by increasing the OSR, the the quantization noise is spread further and its level is lowered. By increasing the order of the modulator, the quantization noise shaping results in better noise rejection as shown in Fig. 2.28.

Modulators with higher order such as the third-order perform a higher order difference operation of the error produced by the quantizer and thus stronger attenuation at low frequencies for the quantization noise signal. The baseband



**Fig. 2.28** Noise transfer function for different DSM orders



quantization error power for the third-order system is clearly smaller than for the first-order modulator as shown in Fig. 2.28. The increase of the order of the DSM improves the noise shaping but it is limited by some stability issues during actual implementation.

A block diagram of a second-order DSM is illustrated in Fig. 2.29

The transfer function of the second-order modulator is as follows:

$$Y(z) = z^{-1}X(z) + (1 - z^{-1})^2 E(z) \tag{2.34}$$

The general block diagram of practical DSM modulator can be illustrated by Fig. 2.30.

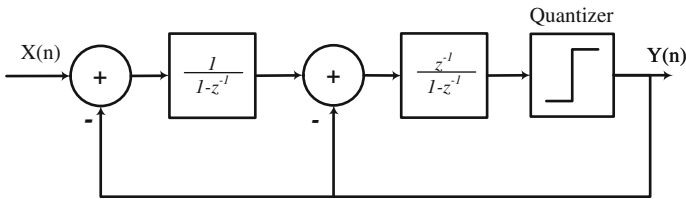
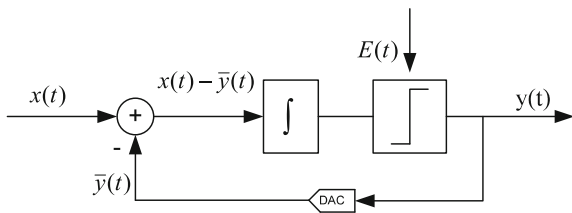


**Fig. 2.29** Second order delta-sigma modulator

**Fig. 2.30** Generic functional block diagram of delta-sigma modulator



### 2.7.2 DSM-Based Transmitter

There are three types of the DSMs classified according to the transfer function of the filter type: low-pass (LPDSM), band-pass (BPDSM) and high-pass (HPDSM).

Besides the low-pass LPDSM, two other delta-sigma topologies, BPDSM and HPDSM are used for delta-sigma-based transmitters. Unlike the LPDSM, the signal at the input of the BPDSM and the HPDSM should not be a baseband signal, but rather a signal at the IF or RF frequency, where low frequency noise does not degrade the signal quality.

The BPDSM and the HPDSM transfer functions are easily found by replacing  $z^{-1}$  in the LPDSM's transfer function depicted by (1) with  $-z^{-2}$  and  $-z^{-1}$ , respectively.

The output of the DSMs for the LPDSM, BPDSM and HPDSM configurations are located at frequencies of zero,  $f_s/4$  and  $f_s/2$ ,

Considering the modulator output frequency, different architectures can be used for the DSM transmitter: direct-conversion architecture for LPDSM and low-IF architecture for BPDSM and HPDSM [8].

Delta-sigma-based transmitter offers, in principle, some advantages such as linearity and PA efficiency, it suffers from few drawbacks. A major drawback is the need for a high clock speed to oversample the data to achieve good signal quality by distributing the same amount of the quantization noise over larger frequency band and consequently achieve smaller in-band noise. To overcome this limitation, parallel processing is often adopted, where parallel DSM branches work simultaneously at a lower speed to provide the same performance as the original DSM.

Figure 2.31 illustrates a typical delta-sigma-based transmitter that includes the DM modulator, a frequency up-converter, a saturated or switching-mode amplifier and RF BPF.

The main parameters of the DSM modulator are the coding efficiency of the baseband encoder (DS modulator),  $C_{\text{eff}}$  and the signal to noise and distortion ratio (SNDR) illustrated in Fig. 2.32 and defined by the following equations:

$$C_{\text{eff}} = \frac{\text{Mean Power (inband signal)}}{\text{Mean Power (total signal)}} \quad (2.35)$$

$$\text{SNDR} = 10\log\left(\frac{\text{signal Power}}{\text{In - band Noise and Distortion power}}\right) \quad (2.36)$$

### 2.7.3 Efficiency Calculation of DSM Transmitter

The overall power efficiency of the DSM transmitter is product of the DSM modulator coding efficiency and the power amplifier modulated peak efficiency corrected by a factor related of the duty cycle statistics of the bit stream encoded signal.

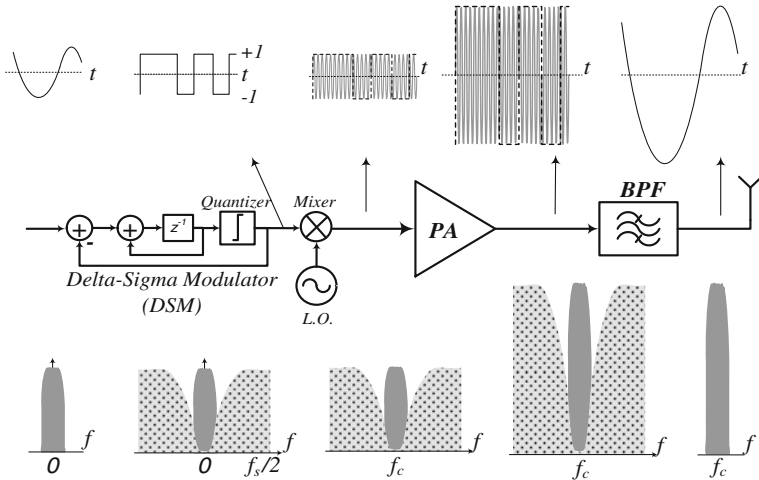


Fig. 2.31 Block diagram of DSM-based transmitter

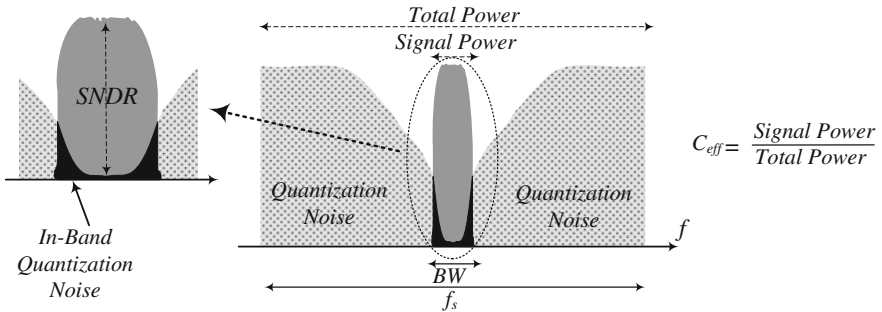


Fig. 2.32 SNDR and coding efficiency definition

The power amplifier modulated peak efficiency over the signal bandwidth,  $\eta_{PA\_Peak}^{BW}$ , can be calculated as:

$$\eta_{PA\_Peak}^{BW} = \frac{\int_{f_c - BW/2}^{f_c + BW/2} PSD(f) \eta_{PA\_Peak}^{CW}(f) df}{\int_{f_c - BW/2}^{f_c + BW/2} PSD(f) df} \tag{2.37}$$

With  $f_c$  is the carrier frequency, PSD is power signal density of the signal at the output of the amplifier and BW is the bandwidth of the signal.

The bi-level signal at the output of the DS modulator, in most cases, does not have a 50 % duty cycle, which is a function of the signal bandwidth and its statistics. To compute the system average efficiency, the duty-cycle effect on the efficiency of the saturated or switching-mode PA has to be considered. Peak drain

efficiency, as a function of the duty cycle, can be defined for each PA class of operation as a parameter that accounts for the effect of the duty cycle on the average PA efficiency. Since different switching-mode PA classes respond differently to the variation of the duty cycle, duty-cycle effect on the efficiency calculation of DSM transmitters have to be taken into consideration when driven with different signals having different statistics. It has been demonstrated in [9] that class E amplifiers are the preeminent choice for efficient amplification purpose when driven with DSM signal.

The effect of the Duty cycle on the overall efficiency can be computed as follows:

$$\eta_{\text{Duty-cycle}} = \int_0^1 \text{PDF}_{\text{Duty-cycle}}(D) \eta_{\text{PA-Peak}}(D) dD \quad (2.38)$$

where  $D$  is the duty cycle,  $\text{PDF}_{\text{duty-cycle}}(D)$  is the probability density function of the duty cycle of the signal and  $\eta_{\text{PA-Peak}}(D)$  is the peak efficiency response of the switching-mode PA versus the duty cycle,

The overall average efficiency of the transmitter can be calculated as:

$$\eta_{\text{Average}} = C_{\text{eff}} \eta_{\text{PA-peak}}^{\text{BW}} \eta_{\text{Duty-cycle}} \quad (2.39)$$

It has been demonstrated in [9] that the effect in duty cycle on the LPDSM transmitter's efficiency is negligible and tends to unity.

For low-pass DSM transmitter using broadband PA, the average efficiency can be well approximated by the product of the coding efficiency and the peak efficiency of the PA as follows:

$$\eta_{\text{Average}} = C_{\text{eff}} \eta_{\text{PA-peak}} \quad (2.40)$$

### 2.7.4 Cartesian Delta-Sigma Transmitter

In this topology, the idea is to simply quantize both  $I$  and  $Q$  of the signal using two similar delta-sigma modulators. In that case, the  $I$  and  $Q$  information generate two quantized constant envelope signals and accordingly, the PA operates with the constant envelope signal to achieve the maximum efficiency. This architecture is very simple and easy to implement and is not sensitive to device linearity [1] (Fig. 2.33).

The output of the LPDSM is bi-level constant envelope signal which is directly up-converted by the  $IQ$  modulator. The output of the  $IQ$  modulator remains a constant envelope signal with four values of phases:  $\pi/4$ ,  $3\pi/4$ ,  $5\pi/4$  and  $7\pi/4$  while maintaining a constant envelope signal. The equation of the signals at the output of the  $IQ$  modulator is:

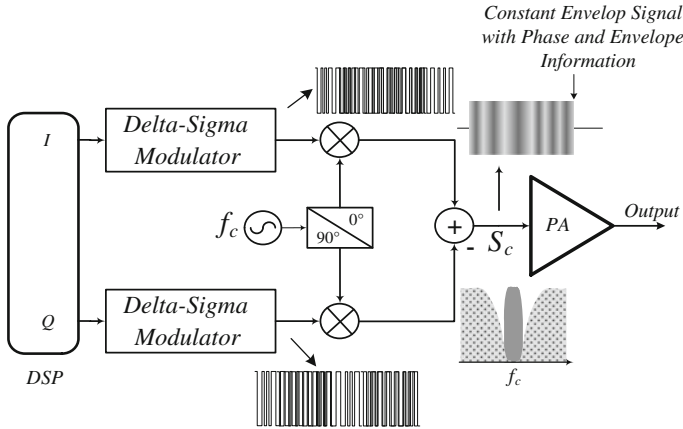


Fig. 2.33 Cartesian delta-sigma modulator

$$S_c = \sqrt{I^2 + Q^2} \cos\left(\omega_c t + \tan^{-1}\left(\frac{I}{Q}\right)\right) \quad (2.41)$$

$$|S_c| = \sqrt{I^2 + Q^2} = \sqrt{2} \quad (2.42)$$

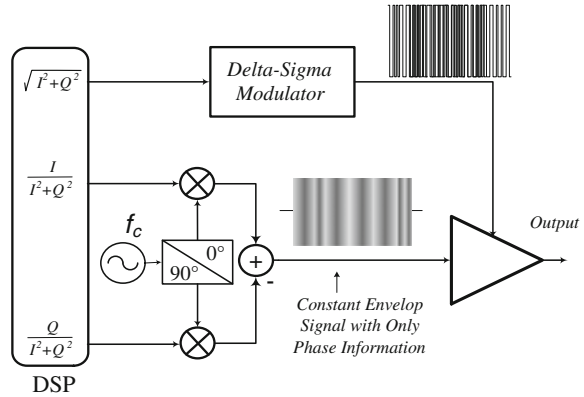
$$\angle S_c = \tan^{-1}\left(\frac{I}{Q}\right) = \frac{\pi}{4}, \frac{3\pi}{4}, \frac{5\pi}{4}, \frac{7\pi}{4} \quad (2.43)$$

### 2.7.5 Polar Delta-Sigma Transmitter

The polar DSM (PDSM) architecture is combined with the envelope elimination and reconstruction technique (EER) where the envelope of the signal is extracted from the signal and the constant envelope signal, which has only the phase information, is used to drive the SMPA. The envelope of the signal is restored back to the signal through the SMPA power supply. With a constant envelope input signal, the PA always operates at its saturation and accordingly, the efficiency of the PA and the transmitter is maximized [10] (Fig. 2.34).

The signal envelope in this technique is restored through modulation of the PA's power supply that works at its maximum efficiency. Consequently, a linear envelope modulation capability of the PA is necessary. In Cartesian DSM,  $I$  and  $Q$  components of the input signal are generated. Two DSM circuits are required to process the  $I$  and the  $Q$  components, then the two quantized  $I$  and  $Q$  are summed together. It was shown that increasing the number of the quantization levels improves the coding efficiency of the DSM circuit [10]. In addition of the level quantization, the phase is also quantized to different four phase values.

**Fig. 2.34** Polar delta-sigma modulator



## References

1. M.M. Ebrahimi, M. Helaoui, F.M. Ghannouchi, Time-interleaved delta-sigma modulator for wideband digital GHz transmitters design and SDR applications. *Prog. Electromagnet. Res. B* **34**, 263–281 (2011)
2. Darraji, R., Ghannouchi, F.M., Hammi, O., Generic load-pull-based design methodology for performance optimisation of doherty amplifiers. *Sci. Measure. Technol. IET*, **6**(3), 132, 138, May 2012
3. Shu-Hsien Liao; Yuanxun Ethan Wang, High efficiency WCDMA power amplifier with pulsed load modulation (PLM). *IEEE J Solid-State Circ* **45**(10), 2030, 2037, Oct 2010
4. M. Jouzdani, M.M. Ebrahimi, K. Rawat, M. Helaoui, F.M. Ghannouchi, Envelope tracked pulse gate modulated GaN HEMT power amplifier for wireless transmitters. *IEEE Transac. Circ. Syst. I* **62**(2), 571–579 (2015)
5. A. Birafane, M. El-Asmar, A.B. Kouki, M. Helaoui, F.M. Ghannouchi, Analyzing LINC systems. *IEEE Microw. Mag.* **11**(5), 59–71 (2010)
6. F.H. Raab, Efficiency of outphasing RF power-amplifier systems, *IEEE Transac. Commun.*, **COM-33**(10), 1094–1099, Oct. 1985
7. B. Stengel, W.R. Eisenstadt, LINC power amplifier combiner method efficiency optimization. *IEEE Trans. Veh. Technol.* **49**(1), 229–234 (2000)
8. M.M. Ebrahimi, M. Helaoui, F.M. Ghannouchi, Delta-sigmabased transmitters. *IEEE Microw. Mag.*, Jan/Feb 2013
9. F.M Ghannouchi, S. Hatami, P. Aflaki, M. Helaoui, R. Negra, Accurate power efficiency estimation of GHz wireless delta-sigma transmitters for different classes of switching mode power amplifiers. *IEEE TMTT* **58**(11), Nov 2010
10. M. Jouzdani, M.M. Ebrahimi, F.M. Ghannouchi, GaN polar transmitter design for base-station applications. *IEEE CCECE* (2014)
11. F.H. Raab, Efficiency of doherty RF power-amplifier systems. *IEEE Transac. Broadcast.* **BC-33**, 77–83, Sept 1987

# Chapter 3

## Multiband RF Transmitters

### 3.1 Introduction

This chapter will introduce the transmitter solutions for multiband applications both in architecture and circuit levels. For the sake of efficiency enhancement, different multiband transmitter architectures will be discussed, including multiband Doherty architecture, multiband envelope-tracking architecture, multiband outphasing architecture as well as multiband delta-sigma architecture. To fulfill the multiband transmitters, reconfigurable and concurrent multiband circuits will be also investigated, especially for the concurrent multiband matching method.

### 3.2 RF Transmitters

#### 3.2.1 *Conventional Single-Band Transmitter*

Super-heterodyne, low-intermediate frequency (IF), and direct conversion are the well-known transmitter schemes [1, 2]. Figure 3.1 presents a conventional transmitter architecture that consists of digital baseband processing unit and single-band passive and active RF components. The heterodyne transmitter architecture is widely used in wireless communication, since it divides the signal up-conversion into two steps so that the local oscillator (LO) frequency remains far from the power-amplifier (PA) output spectrum. As shown in Fig. 3.1, the baseband signals are up-converted and translated into a carrier frequency. The bandpass filter can filter out the image frequency produced by the mixer. The final stage of the transmitter is the PA, which amplifies the input signals and feeds them to the antenna. In

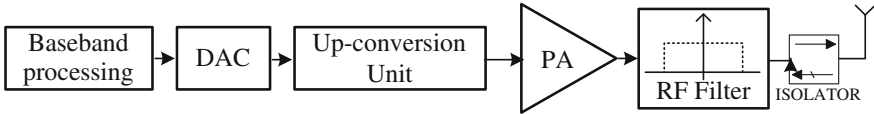


**Fig. 3.1** The basic architecture of the single-band transmitter. Reprinted with permission from the IEEE

radio-frequency (RF) transmitters, the PA is the highest power-consumption device in the chain, which dominates the overall efficiency of the whole transmitter.

For the sake of PA efficiency, the impedance-matching of the PA is only performed in a narrow bandwidth. According to the Bode-Fano criterion, the matching performance will deteriorate as the bandwidth is increased. To satisfy the fast expansion of wireless communication data rate, multiband, multimode transmitters and techniques are highly desirable for mobile-phone operators and users [3–5]. In the digital domain, multiband requirements are more flexible owing to the FPGA's reconfigurable and paralleled computation capability. Thus, the biggest challenge is presented to the RF parts in the transmitters, since the RF bandwidth is restricted by the physical limitation.

### 3.2.2 Multiband Transmitter

As shown in Fig. 3.2, there are several solutions for multiband transmitters [6]. The simplest method is to parallel RF channels of different frequencies together and then use a multiplexer to combine them as illustrated in Fig. 3.2a. However, the multiplexers are lossy passive modules that will cause significant power loss. The bulky size and packaging issues might be of high concern in multiple-branch architectures and need to be considered up front.

An alternative solution is to use multiband RF devices, such as concurrent multiband PAs and filters. Using multiband active and passive RF components could be an efficient approach to design a compact and efficient transmitter. In this architecture, one multiband component working at multiple operating frequencies replaces the bank of components each working in single operating frequency, and as a result, the power combination module loss can be reduced. Considering the position of the power combination module before or after the PA, the amount of power consumed in the multiple branches model in Fig. 3.2b is always higher than that in the multiband transmitter in Fig. 3.2c. This significantly increases the power loss in the system and degrades the transmitter's power efficiency. A typical isolator has about 0.3–0.5 dB insertion loss and an RF multiplexer (such as diplexer) could have about 1.5 dB insertion loss, which results in about 2 dB insertion loss at the output stage of the transmitter.



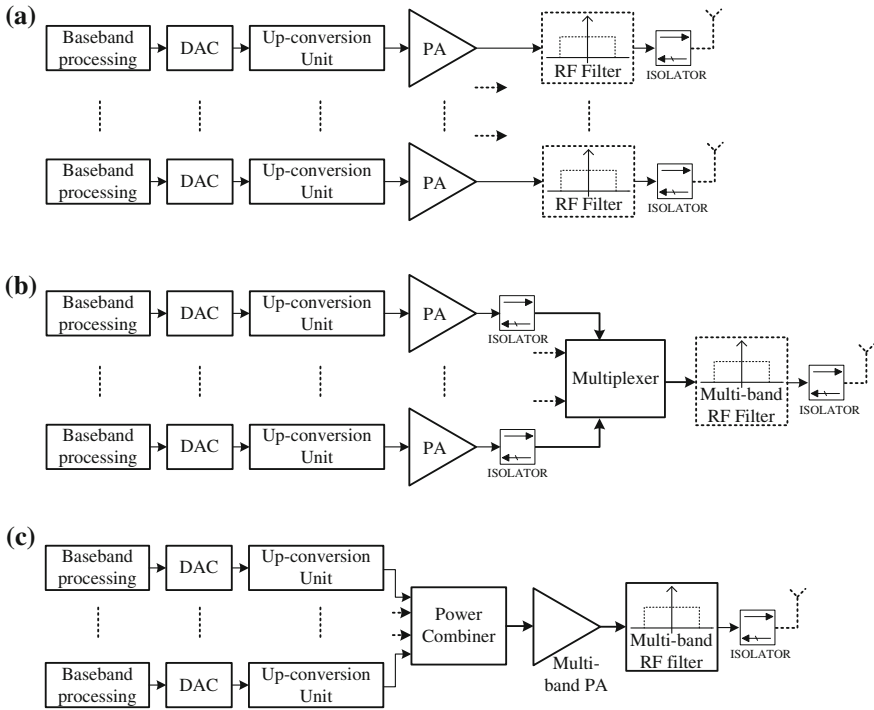


Fig. 3.2 Multiband transmitter architectures. Reprinted with permission from the IEEE

### 3.3 Multiband Transmitter Architectures

In order to realize energy-efficient and high-linear transmitters, especially for modulated signals with high peak-to-average power ratio (PAPR), several promising transmitter architectures are proposed in wireless communication systems, such as the Doherty, envelope-tracking, outphasing and delta-sigma architectures. To meet the requirements in multiband applications, similar transmitter architectures are also investigated and demonstrated in many literatures.

#### 3.3.1 Multiband Doherty Transmitter

With the rapid evolution of communication technologies, nonconstant envelope modulation schemes, such as high-order quadrature amplitude modulation (QAM) and orthogonal frequency-division multiplexing (OFDM), have been widely used for high capacity in wireless communications. A nonconstant envelope signal leads to a high PAPR, which significantly decreases the efficiency of the PA

in order to meet the linearity requirements of wireless communication standards. To enhance the PA efficiency in the power back-off region, the Doherty PA has been studied extensively and adopted in base stations. Recently, some new techniques to design a Doherty PA that supports concurrent dual-band operation have been proposed by using dual-band transformers [7, 8].

The circuit diagram of the proposed concurrent dual-band Doherty PA is shown in Fig. 3.3. It consists of a dual-band 3 dB branch-line coupler, two single-branch dual-band PAs, two dual-band offset lines and two dual-band quarter-wavelength ( $\lambda/4$ ) transmission lines. A simplified model of this Doherty PA, as shown in Fig. 3.4, is used to describe the operation mechanism. Similar to the conventional single-band Doherty PA, the concurrent dual-band Doherty PA contains a dual-band  $\lambda/4$  transformer, which has frequency-dependent characteristic impedances.

As shown in Fig. 3.4, the transistor outputs are modeled as current sources controlled by their input voltages; thus, the output voltages of the main amplifier and the load are calculated to be

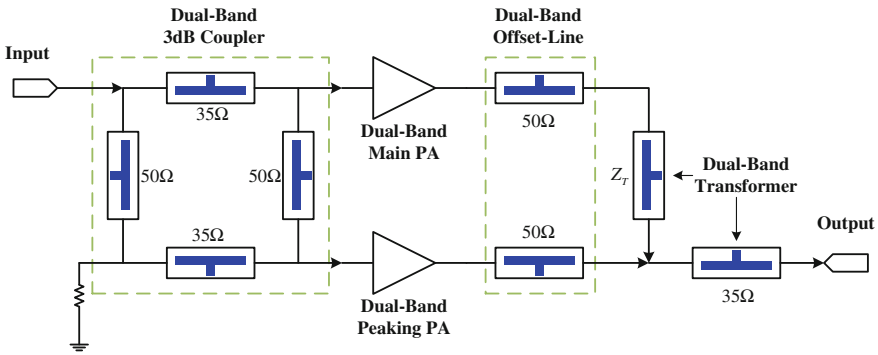


Fig. 3.3 Circuit diagram of the dual-band Doherty PA. Reprinted with permission from the IEEE

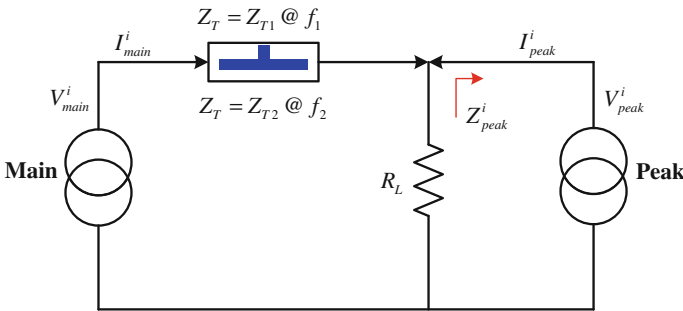


Fig. 3.4 Equivalent circuit model of the dual-band Doherty PA. Reprinted with permission from the IEEE

$$\begin{cases} V_{\text{main}}^i = \frac{Z_{T_i}^2}{R_L} I_{\text{main}}^i - jZ_{T_i} I_{\text{peak}}^i \\ V_L = -jZ_{T_i} I_{\text{main}}^i \end{cases} \quad i = 1, 2 \quad (3.1)$$

In the above equation, instances of  $Z_{T_i}$  are the characteristic impedances of the  $\lambda/4$  transformer. These characteristic impedances can be uniform or distinguished in the dual bands, in which superscripts 1 and 2 relate to the lower and upper bands, respectively.

To illustrate the power back-off range induced by different characteristic impedances, the value of  $I_{\text{main}}^i$  when the main amplifier reaches saturation is defined as

$$I_{\text{th}}^i = \frac{1}{\gamma^i} I_{\text{main\_max}}^i \quad (3.2)$$

where  $\gamma^i$  is a design parameter that determines the value of  $I_{\text{th}}^i$ , in relation to  $I_{\text{main\_max}}^i$ . Consequently, the current in the peaking amplifier can be written as

$$I_{\text{peak}}^i = \begin{cases} 0, & I_{\text{main}}^i < I_{\text{th}}^i \\ -j\gamma^i (I_{\text{main}}^i - I_{\text{th}}^i), & I_{\text{main}}^i \geq I_{\text{th}}^i \end{cases} \quad i = 1, 2 \quad (3.3)$$

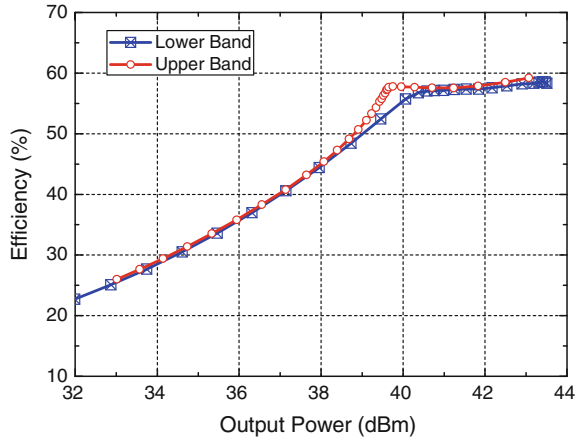
By substituting (3.2) and (3.3) into (3.1) and solving for the  $Z_{T_i}$  that makes  $V_{\text{main}}^i$  constant, we can obtain

$$Z_{T_i} = \gamma^i R_L \quad i = 1, 2 \quad (3.4)$$

It can be found that  $\gamma^i$  is distinct, if the characteristic impedances of the  $\lambda/4$  transformer are different in the two bands. From another point of view, the back-off power ranges of the Doherty PA in dual bands will be different by developing a frequency-dependent characteristic impedance transformer, which can provide us with more design freedom and eventually improve the average efficiency of different signal statistical distributions. As shown in Fig. 3.5, if the efficiencies of the dual-band Doherty PA are simulated, it can be seen that the dual-band Doherty PA architecture achieves double-peak efficiency profiles to improve the PA efficiency at the back-off region.

The demonstrated dual-band Doherty PA can be used in a dual-standard base station to improve the efficiency and reduce the bulk size. For China mobile band *F* (1.88–1.92 GHz) and band *A* (2.010–2.025 GHz) application, the dual-band Doherty design can outperform the broadband Doherty design with 5 % efficiency improvement. Certainly, the design method can be also extended to multiband scenario as demonstrated in [9].

**Fig. 3.5** Efficiency of the Doherty PA in the balanced power-range mode. Reprinted with permission from IEEE



### 3.3.2 Multiband Envelope-Tracking Transmitter

Envelope-tracking (ET) is a widely used architecture for boosting the efficiency of wireless transmitters, where the supply voltage of the PA is dynamically adjusted by an envelope amplifier in order to track the envelope of the drive RF signal. Thus, the PA is kept near saturation throughout most of the operation, improving the average efficiency of transmission. For multiband applications, the bandwidth of the envelope amplifier is a huge factor that should be considered—since the bandwidth of the envelope signal is around five times that of the drive signal [10, 11], it is almost impracticable as the different bands are widely spaced. For example, an envelope amplifier of bandwidth of 500 MHz is required for carrier aggregation (CA) long-term evolution (LTE) signal of 100 MHz, which is not feasible. Actually, the envelope of each transmitted band is much lower. An effective solution is to dynamically adjust the envelope amplifier according to the envelopes of the transmitted signals as shown in Fig. 3.6, as the envelope amplifier is independent of the frequency separation of the carriers.

In the Doherty PA architecture, the bandwidth of the PA is often limited because of the quarter-wavelength transformer. Fortunately, the conventional single-way class-AB PA is sufficient for multiband ET architecture, as the bandwidth limitation can be alleviated. Compared with the Doherty architecture, it is easier to enhance the bandwidth in ET architecture. On the other hand, the envelope amplifier in ET architecture has to deal with several different bands simultaneously, which will lead to heavy burden on the bandwidth of the envelope amplifier.

For baseband signals, the spectra of the signal envelope are much larger, and can be extended to five or more times the original complex baseband signal spectra. This is further increased when multiband systems are used, where the envelope is determined by the frequency separation of each band. To relax the envelope

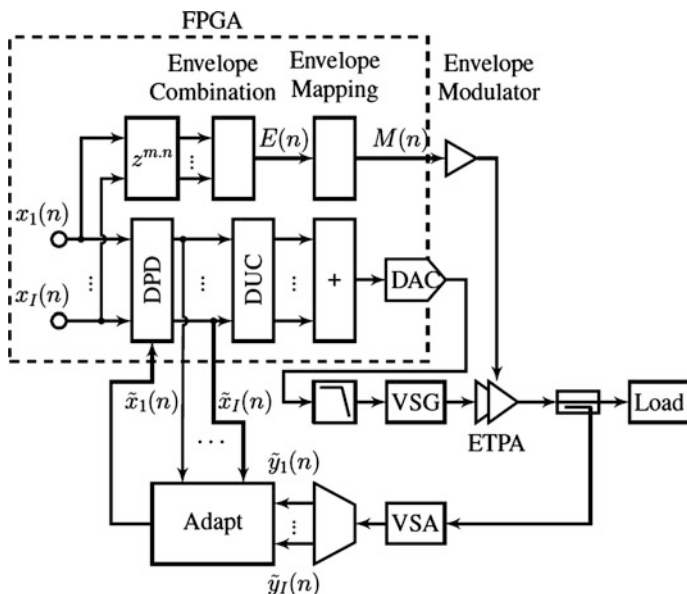


**Fig. 3.6** Block diagram for envelope and digital predistortion generation for multiband envelope-tracking PAs. Reprinted with permission from the IEEE

modulator requirements, suboptimal envelope-combination techniques are constructed based on the transmitted signals' individual envelopes.

The low pass equivalent of a multiband signal's full envelope can be described as

$$E_{\text{full}}(n) = |x_{\text{full}}(n)| \quad (3.5)$$

where

$$x_{\text{full}}(n) = \sum_{i=1}^I x_i(n) e^{j(\omega_i - \omega_1)}$$

The full envelope bandwidth is dependent on the maximum frequency separation. To alleviate this problem, suboptimal envelopes based on the individual envelopes can be used.

The summation of the instantaneous envelopes results in the peak envelope. This is described as

$$E_{\text{peak}}(n) = \sum_{i=1}^I |x_i(n)| \quad (3.6)$$

The average envelope may be used to comprise the signal. This is defined as

$$E_{\text{avg}}(n) = \sqrt{\sum_{i=1}^I |x_i(n)|} \quad (3.7)$$

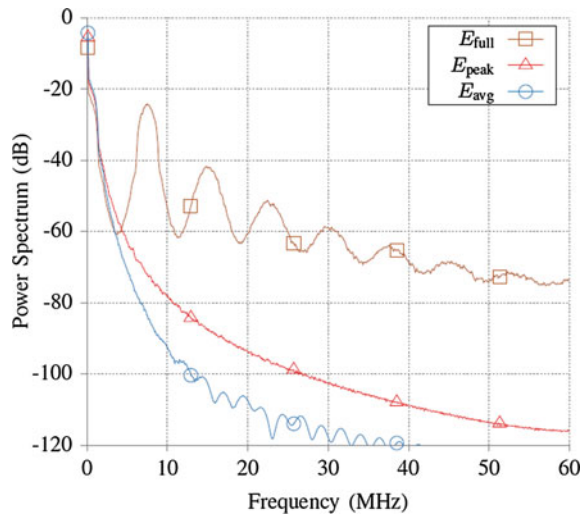
The spectra of different envelope-combination functions are shown in Fig. 3.7, using two LTE signals with bandwidths of 3 MHz, and having a frequency separation of 18 MHz. It is clear that the full envelope requires a significantly higher bandwidth to reproduce, and is controlled by the frequency separation. However, using the baseband envelopes to compute the peak envelope eliminates the high frequency component, while the average envelope results in lower output spectra at higher frequencies.

To map the envelope to the drain voltage, the instantaneous combined envelope is scaled between a normalized magnitude of 0 and 1. Taking into account that the PA will operate between the minimum voltage and the maximum voltage, a linear mapping function between the input envelope and the drain voltage may be constructed as

$$M_{\text{lin}}(n) = V_{\text{min}} + (V_{\text{max}} - V_{\text{min}}) \times E(n) \quad (3.8)$$

where the generation of the envelope is defined in above equation. The mapping function may be optimized such that the PA operates at a lower drain voltage up to a certain normalized input envelope value. The formulation of the relationship between the envelope and the drain voltage is

**Fig. 3.7** Mapping combined envelope to the drain voltage under various scenarios. Reprinted with permission from the IEEE



$$M_{\text{lin}, \alpha}(n) = \begin{cases} V_{\text{min}} & E(n) < \alpha \\ \frac{(V_{\text{max}} - V_{\text{min}})}{1 - \alpha} (E(n) - \alpha) + V_{\text{min}} & E(n) \geq \alpha \end{cases} \quad (3.9)$$

### 3.3.3 Multiband Outphasing Transmitter

The outphasing technique consists of decomposing the magnitude and the phase-modulated signal into two-phase modulated signals. Each of the signals can be amplified using highly nonlinear or switching-mode PA. The power combiner sums the signals at the output of the PAs to recover the amplitude modulation of the original signal. In the literature one can distinguish two major types of power combiners used with the outphasing technique: the isolated and the nonisolated combiners. The isolated combiners such as Wilkinson or hybrid combiners are matched at all input and output ports independently from the magnitude and phase of their input signals. Consequently, when input signals are out-of-phase, all the energy delivered to the isolated combiner is dissipated in the matching resistor as heat, and the mean efficiency degrades considerably [12]. The use of nonisolated power combiners, such as the Chireix combiner, avoids the power loss. However, owing to the nature of these nonisolated combiners, the loads presented by the combiner at its input ports vary as a function of magnitudes and phases of the input signals. Hence, a cross-load modulation occurs between input ports, which introduces a variation in the PA’s behavior, such as the gain, the output power and the DC consumption. The use of this type of combiners, despite its efficiency improvement, results in a severe degradation of the system linearity. Previously, several attempts were made to analyze the origins of the nonlinearity and propose a method to compensate for it.

The outphasing transmitter is also an efficient way for multiband applications. Figure 3.8 shows the concurrent multiband digital outphasing transmitter architecture with two-dimensional power coding [13]. The multiple quadrature baseband signals

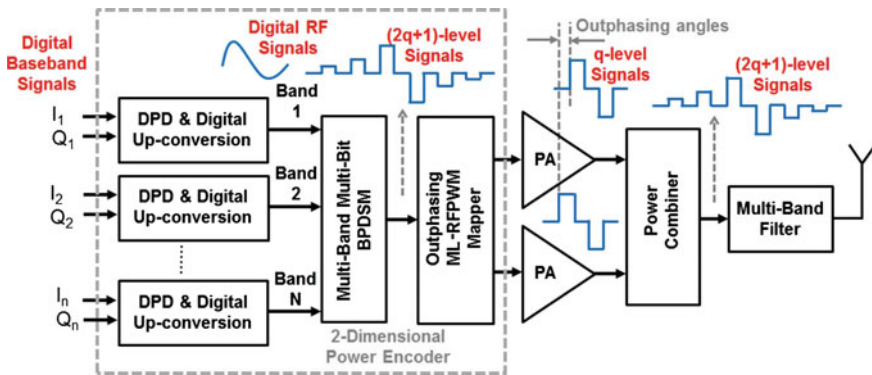


Fig. 3.8 Digital transmitter architecture with 2-D power coding. Reprinted with permission from the IEEE

are up-converted to each band (component carrier in carrier aggregation) in the digital domain. The multiband multibit bandpass delta-sigma modulation combines the high-resolution digital baseband inputs into a single-stream multilevel digital signal with high linearity. Because the implementation complexity of class-S digital PAs is increasingly difficult with a large number of output levels, the single-stream multilevel output signal is transformed into dual-stream multilevel pulse width modulation (PWM) signals that are outphased to each other. As a result, the PAs can produce only a small number of output levels. By keeping the outphasing angles small, nonisolated Chireix power combiners can be used with a very high efficiency in summing the output power of the two PAs. Therefore, both high efficiency and high linearity can be obtained with low sensitivity to mismatch.

The digital outphasing transmitter uses oversampling bandpass delta-sigma modulation, which reduces the digital RF signal resolution and also differentiates the digital outphasing transmitter from the conventional outphasing transmitters. Outphasing transmitter with discrete PWM improves the transmitter power efficiency by combining outphasing and PWM, but the outphasing requires very fine resolution. Furthermore, envelope PWM needs a sampling rate that is more than 100 times higher than the largest frequency difference among multiband carriers.

### 3.3.4 Multiband Delta-Sigma Transmitter

There is also another approach in using the concurrent multiband transmitter, which is based on delta-sigma modulator and switching-mode PAs [14, 15]. As shown in Fig. 3.9, this topology consists of delta-sigma modulators, digital up-conversion units, a combiner and power amplifiers. The delta-sigma modulators produce two-level output signals that are up-converted to RF using a digital multiplexer. The nature of the signal is digital and, therefore, a digital combiner can be used.

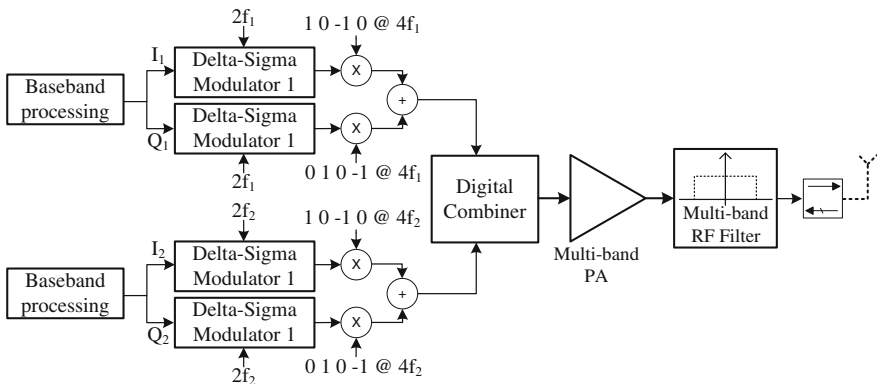


**Fig. 3.9** Multiband delta-sigma transmitter's architecture. Reprinted with permission from the IEEE



To improve the energy efficiency, switching-mode PAs could be used in this architecture. By optimizing their driver amplifier, the bandwidth of switching-mode PAs can be enhanced to more than one octave, since the input signals are time-domain pulses instead of continuous waves, and thus the impedance-matching in the frequency domain can be relaxed.

What makes this architecture applicable to carrier aggregation is the modification of the design of the noise transfer function in order to prevent the noise generated by the delta-sigma modulator from interfering with the signal within each frequency operation band. In theory, the delta-sigma-based transmitters using the switching model PA could improve the overall efficiency of the system. Moreover, the fact that delta-sigma modulators perform as digital modulator and up-converter units makes these topologies a potential candidate for future reconfigurable and cognitive radio systems. But most of the published works based on this concept continue to suffer from inefficiency mostly because of unnecessary, but at the same time unavoidable, amplification of out-of-band noise. In fact, because of the high level of noise, the overall efficiency of delta-sigma-based transmitters is still very low.

### **3.4 Multiband RF Transmitter Circuits**

Owing to the limitation of the Bode-Fano criterion and the parasitic effects of the transistors, many challenges have been presented to RF circuits, especially for the PA module. For handset terminal applications, the cell phone will be operated in a specific frequency band according to the wireless base station coverage. To meet the multiband and multimode demand, the transmitter circuits can transmit the signals selectively. In order to select the corresponding RF channel, tunable RF devices are integrated into the transmitter circuits, such as varactors and switches. For the base station, the transmitter has to deal with the different frequency bands at the same time, and thus a concurrent matching load network is required, which provides optimum load impedances for the target frequencies. In concurrent multiband transmitter circuits design, all the load impedances at the fundamental, harmonic and intermodulation frequencies should be carefully designed.

#### ***3.4.1 Reconfigurable Multiband Transmitter***

##### **3.4.1.1 Broadband PA with Tunable Output-Matching**

Since the output-matching network plays a significant role in determining the performance of PAs, a lot of design effort has been geared to its implementation with PA circuit topologies. In order to make the output-matching network reconfigurable for various operation frequencies, it is often made off-chip with tunable components. Not only can the power-added efficiency (PAE) of broadband PAs be

improved by tuning the components value in the output-matching network, but also broadband matching can be realized by using two output-matching routes.

It is very clear by now that a broadband PA and its tunable matching circuits are not readily available for implementing desirable multiband PAs because of the broadband matching trade-off and insertion loss of tunable devices. Thus, it is essential to explore an alternative design of broadband PA topology and matching circuit approach to achieve multiband power amplification with minimum adverse impact on circuit performance. As demonstrated in Fig. 3.10, a three-stage PA is designed with the incorporation of a novel emitter structure and layout [16], an input stage with a shunt-series feedback topology, a built-in predistortion function, a broadband and compensating matching at input and interstages, and an optimum power gain distribution among stages. This reconfigurable broadband PA achieves high gain, power, and efficiency without compromising the chip area. For the output-matching network, a novel reconfigurable circuit using p-i-n diodes to adjust inductor values in the inductance-capacitance (LC) tank without compromising power insertion loss and linearity is also proposed to select the frequency band of the multiband PA.

#### 3.4.1.2 Multiband RF Path Reconfigurable PA

Switches for the reconfigurable matching circuit can be avoided if multisection matching networks are used to make the PA broadband. However, the efficiency of

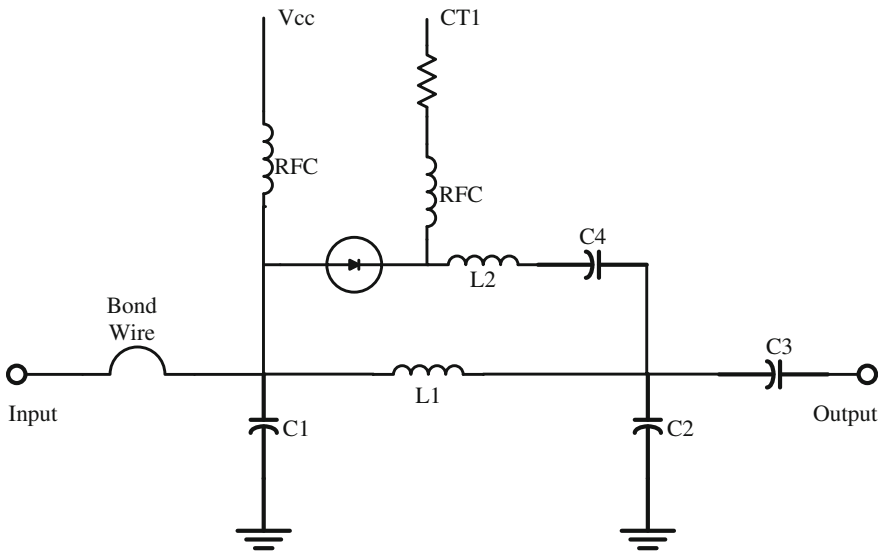


**Fig. 3.10** Schematic of reconfigurable output-matching circuit. Reprinted with permission from the IEEE

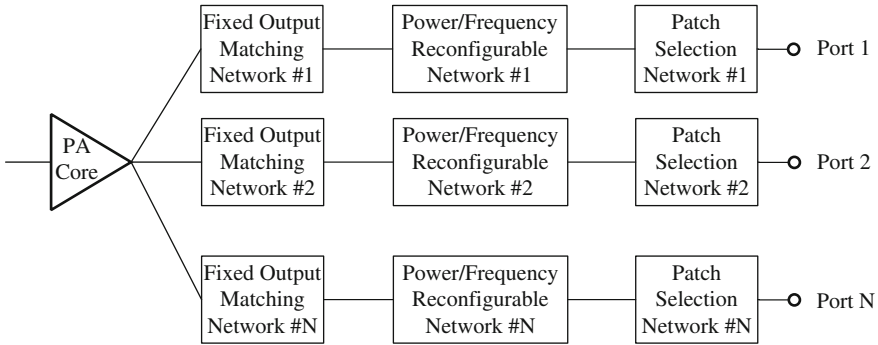


**Fig. 3.11** Multiband RF path reconfigurable PA. Reprinted with permission from the IEEE

the PA is degraded because of the suboptimal impedance trajectory across the operating frequency band in addition to the increased loss of the matching network. Moreover, the approach of using a single RF input and output port for broadband amplifier design will lead to further PAE degradation because of the requirement of post-PA distribution switches, whose loss further degrades the overall efficiency.

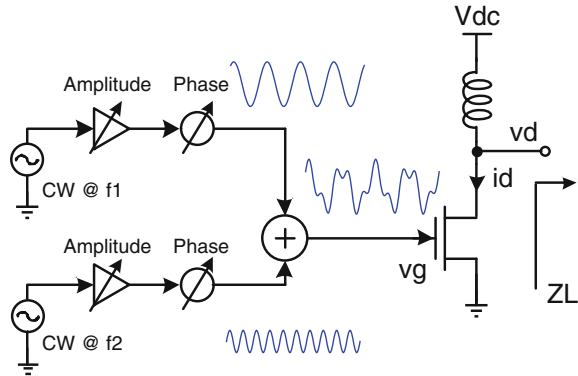
A new approach, as shown in Fig. 3.11, to multiband reconfigurable PA for practical handset applications was implemented [17], showing a small PAE degradation of 2–3 % compared with the single-band designs. The transmit (Tx) frequency bands were grouped into a low band (0.7–0.9 GHz) and a high band (1.4–2.5 GHz). The complication in covering too wide a frequency range is mitigated in this approach by limiting the band reconfigurability within either the low- or high-band group. The additional losses because of post-PA switches are also avoided by expanding the number of output ports in the PA design. Moreover, the RF path reconfigurable network reconfigures not only the frequency band, but also the linear output power according to the selected band. This allows the PA to operate at optimum power and efficiency in the system, by avoiding different power requirements owing to different post-PA duplexer losses.

### 3.4.2 Concurrent Multiband PA

#### 3.4.2.1 Concurrent Multiband Nonlinear Analysis

In conventional concurrent multiband PAs, the PA often suffers from performance degradation including total output power and overall efficiency, and its mechanism is not very clear. Given this situation, a more in-depth theoretical analysis has to be conducted [18]. As shown in Fig. 3.12, in the dual-band concurrent transmitter, both the amplitude and phase should be controlled for the two carriers. Accordingly, the two-carrier CW signal can be written as (3.10).

**Fig. 3.12** Concurrent CW analysis. Reprinted with permission from the IEEE



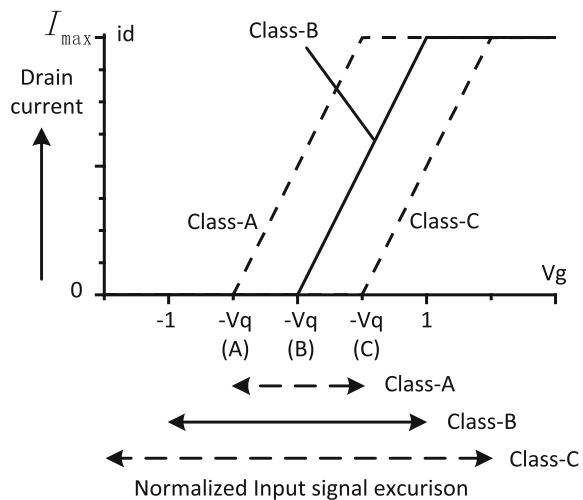
$$v_g(t) = V_{s1} \cos(\omega_1 t + \theta_1) + V_{s2} \cos(\omega_2 t + \theta_2) \tag{3.10}$$

On the other hand, the theoretical analysis of the PA is typically based on the ideal device to obtain general results. One frequently used model is the strong nonlinearity model, which is shown in Fig. 3.13. Obviously, the strong nonlinearity model is a simplified model of realistic devices; however, it has been proven to be quite suitable for modern field-effect transistor (FET) devices [14] and is, therefore, widely used.

The concurrent CW signal shown in (3.10) is worth studying first, and it can be simplified by defining the sum of the amplitudes of two carriers as  $V_s$  and the ratio of them as  $K_s$ , as shown in (3.11) and (3.12), respectively.

$$V_s = V_{s1} + V_{s2} \tag{3.11}$$

**Fig. 3.13** Strong nonlinearity model of device. Reprinted with permission from the IEEE



$$K_s = \frac{V_{s2}}{V_{s1}} \quad (3.12)$$

Given (3.11) and (3.12), the concurrent CW signal can be simplified to (3.13)

$$v_g(t) = V_s \cdot \text{NCCW}_{K_s, \omega_1, \omega_2, \Delta\theta}(t) \quad (3.13)$$

where NCCW is the normalized concurrent CW signal defined as (3.14)

$$\text{NCCW}(t) = \frac{1}{1 + K_s} \cos(\omega_1 t) + \frac{K_s}{1 + K_s} \cos(\omega_2 t + \Delta\theta) \leq 1 \quad (3.14)$$

Typically, we will treat the magnitude ratio  $K_s$  as a parameter, for a certain  $K_s$ ,  $V_s$  can be swept to observe the PA's response, and then go on with the next value of  $K_s$ . Now, go on to the frequency. The ratio of frequency of the two carriers is defined to be  $\omega_R$  in (3.15). We assume that R is a rational number; thus,  $\omega_R$  can be written in the standardized form as shown in (3.15).

$$\omega_R = \frac{\omega_2}{\omega_1} = \frac{p}{q}, p, q \in Z \quad \text{and} \quad (p, q) = 1 \quad (3.15)$$

Obviously, the time-domain waveform of the concurrent CW signal is dependent on  $K_s$ ,  $\omega_R$  and  $\Delta\theta$ . Several examples are given in Fig. 3.14.

When concurrent CW signal is applied to the device transconductance, if the device is desired to operate without clipping, then  $v_g(t)$  should be kept below  $(1 - V_q)$  at all times. Therefore, the maximum allowed stimulus level can be estimated. Applying the concurrent CW stimulus to normalized transconductance function, we can get the time-domain waveform of the drain current. For the stimulus shown in Fig. 3.14, the corresponding drain current waveforms are shown in Fig. 3.15 for class-B PA, and the spectrum components are illustrated in Fig. 3.16.

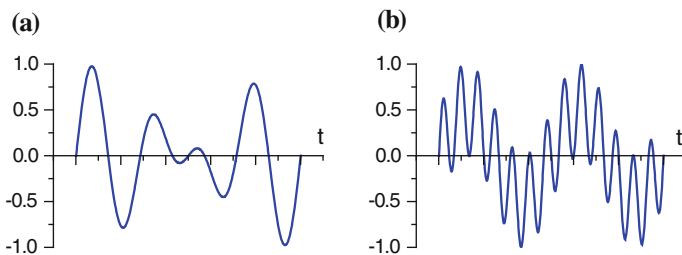


**Fig. 3.14** Concurrent CW signals with various parameters. **a**  $K_s = V_{s2}/V_{s1} = 1$ ,  $\omega_2/\omega_1 = 4/3$ , and  $\Delta\theta = 0$ , **b**  $K_s = V_{s2}/V_{s1} = 1$ ,  $\omega_2/\omega_1 = 13/2$ , and  $\Delta\theta = 0$ . Reprinted with permission from the IEEE

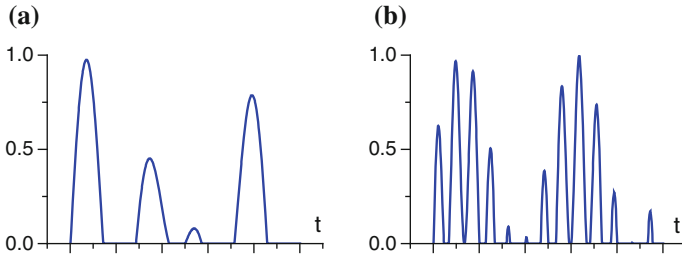


**Fig. 3.15** Normalized drain current waveforms for class B. **a**  $K_s = V_{s2}/V_{s1} = 1$ ,  $\omega_2/\omega_1 = 4/3$ , and  $\Delta\theta = 0$ , **b**  $K_s = V_{s2}/V_{s1} = 1$ ,  $\omega_2/\omega_1 = 13/2$ , and  $\Delta\theta = 0$ , Reprinted with permission from the IEEE

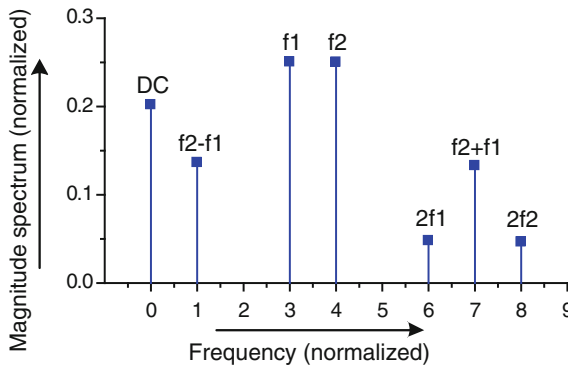


**Fig. 3.16** Spectrum of concurrent dual-band class-B drain current. ( $K_s = V_{s2}/V_{s1} = 1$ ,  $\omega_2/\omega_1 = 4/3$ , and  $\Delta\theta = 0$ . Reprinted with permission from the IEEE)

### 3.4.2.2 Intermodulation Tuning for Concurrent Multiband PAs

In addition to fundamental components and harmonics components, the drain current also contains intermodulation (IM) components, which directly leads to the concept of IM tuning. The basic idea of IM tuning is that the IM components in the drain current must be presented proper load impedances to reduce the drain voltage swing and consequently improve the PA's performance, which is similar to the harmonic tuning in the classical single-band PA. Obviously, the simplest way of IM tuning is simply shorting them out by exhibiting zero-load impedances to the drain at all IM frequencies. Leaving the IM impedances uncontrolled will result in an unpredictable performance in the concurrent mode. The drain voltages with and without proper IM tuning are shown in Fig. 3.17, indicating the impact of drain voltage swing by IM impedance.

A fact that is noteworthy here, in the conventional design of the dual-band PA, a concept of IM suppression is sometimes mentioned, which involves suppressing the IM components in the output signal, usually by exhibiting reactive impedance

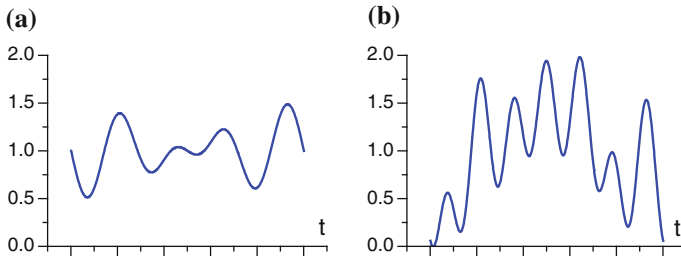


**Fig. 3.17** Drain voltage waveform with varied second-order IM impedance  $Z_{IM2}$  at  $\omega_2 - \omega_1$  and  $\omega_2 + \omega_1$ . **a** With perfect IM shorting, **b**  $Z_{IM2} = j3.5R_L$ . Reprinted with permission from the IEEE

presented to the drain at those IM frequencies. Though it also can be considered as a type of IM tuning, IM suppression is a completely different concept, with a different intention, different method and different effect. The comparison between the goal of IM shorting and conventional IM suppression is shown in Fig. 3.18.

Generally speaking, the analysis and design of the classical single-band PA are based on harmonic control, or harmonic tuning. Similarly, the introduction of IM tuning for concurrent dual-band PA will bring in a family of novel operation modes, which can be referred to as “concurrent mode PA” collectively. By simply eliminating IM components in drain voltages, we have concurrent reduced conduction angle modes, including concurrent class A, AB, B and C, in comparison with their single-band counterparts, in which harmonic voltages are simply shorted out. On the other hand, by utilizing the IM components to further tune the voltage waveforms, we can define concurrent class-F, E and J. The desired load impedance for concurrent reduced conduction angle modes are summarized in Fig. 3.19, showing perfect harmonic shorting and IM shorting.

For each  $(V_s, K_s)$ , the corresponding fundamental power of two carriers constitutes a vector  $(P_1, P_2)$ . For each given  $K_s$ , a power trajectory can be generated on

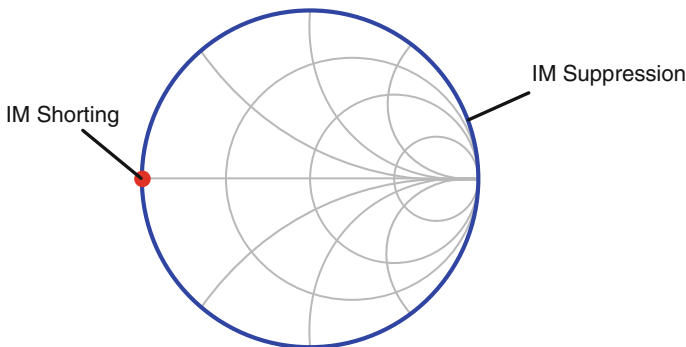


**Fig. 3.18** The comparison of IM shorting and conventional IM suppression. Reprinted with permission from the IEEE

**Fig. 3.19** Desired load impedance for concurrent reduced conduction angle modes, showing perfect shorting at all harmonic and IM frequencies. Reprinted with permission from the IEEE

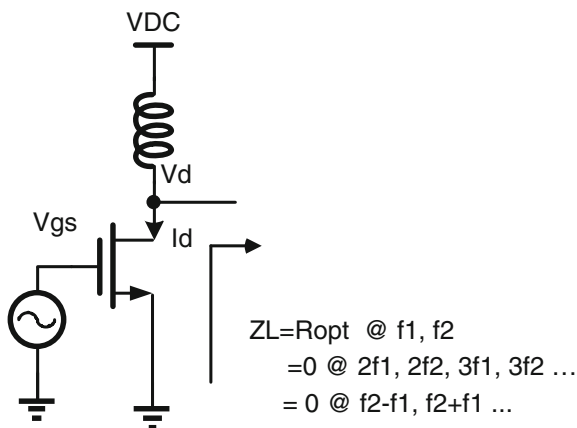
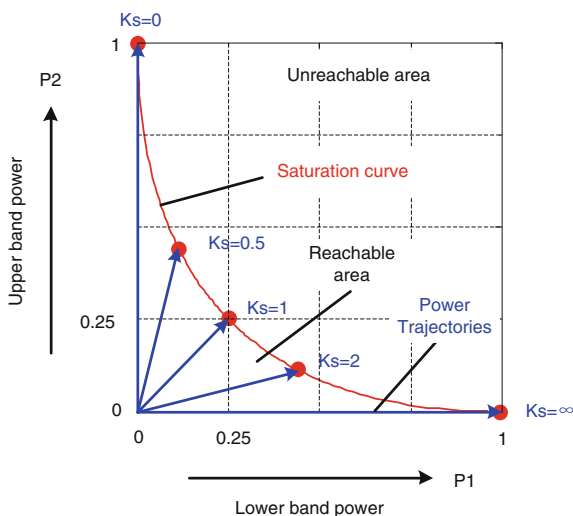


**Fig. 3.20** Normalized output capacity of concurrent class-B mode, showing power trajectories and the saturation curve. Reprinted with permission from the IEEE

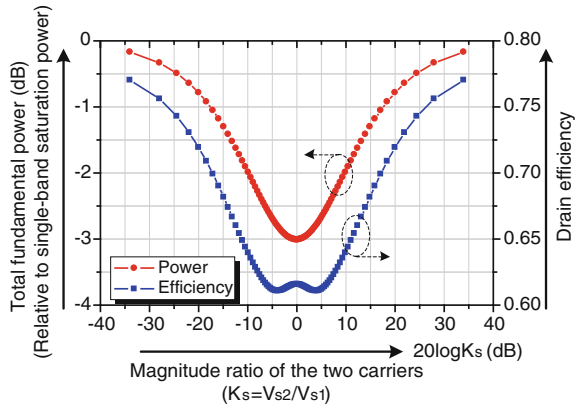


the  $P_1 - P_2$  plane by sweeping  $V_s$  from 0 to 1, as shown in Fig. 3.20. Connecting the end of all power trajectories in Fig. 3.20, we can get a curve that divides the whole plane into two separated areas: reachable area and unreachable area. Actually, the curve stands for saturation points for each  $K_s$  when  $V_s = 1$ , so it can be referred to as the saturation curve. The output power and drain efficiency along the saturation curve can be plotted as in Fig. 3.21. Actually, the PA often suffers from an evident performance degradation in concurrent mode. In equally driven concurrent mode (when  $K_s = 1$ ), the degradation is about 3 dB in output power capacity or 50 % in power utilization factor (PUF), and 16 % in drain efficiency.

Once the optimized source and load impedances are obtained, a pair of input- and output-matching networks can be designed to implement the desired impedances, at fundamental frequencies, harmonics frequencies, and IM frequencies.



**Fig. 3.21** Theoretical performance of concurrent class-B mode. Reprinted with permission from the IEEE



Compared with single-band PA, in which exist only one fundamental frequency and corresponding harmonics, we have to take two fundamental frequencies along with their corresponding harmonics, and also IM frequencies, into account, which is very difficult. So, generally speaking, compromises have to be made because of the difficulty in implementing matching networks. Fortunately, the significance of these impedances can be estimated in the procedure of load-pull, according to the relevance between the performance and each impedance. A designed circuit example is shown in Fig. 3.22, the key components in Fig. 3.22 is the IM trapping capacitors C1, C2 and C3, which can perform the desired IM shorting in lower second-order IM frequency 700 MHz, owing to their large capacity.

According to the design shown in Fig. 3.22, the load impedance of the fabricated PA has been measured and compared with the simulated value, as shown in Fig. 3.23. According to Fig. 3.23, the measured load impedance is in good consistency with the stimulated values. The concurrent performance has been acquired

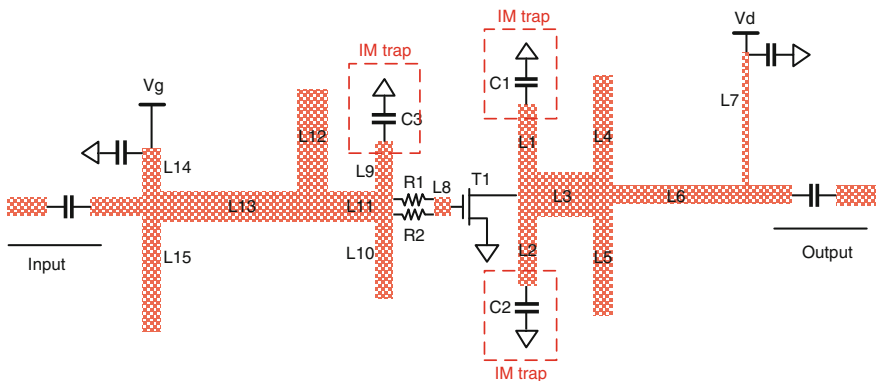


**Fig. 3.22** Designed 1.9/2.6 GHz concurrent class-AB dual-band PA with proposed IM matching. (Reprinted with permission from the IEEE)

**Fig. 3.23** Measured and simulated output impedance. The frequency is in MHz. Reprinted with permission from the IEEE

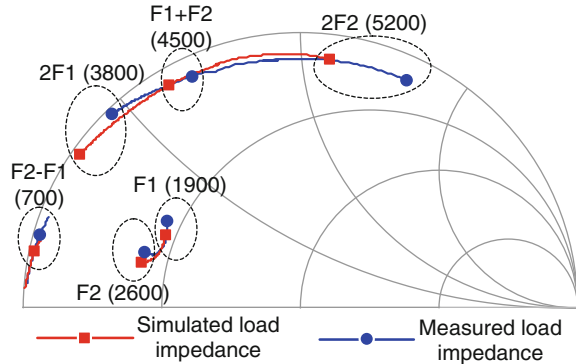
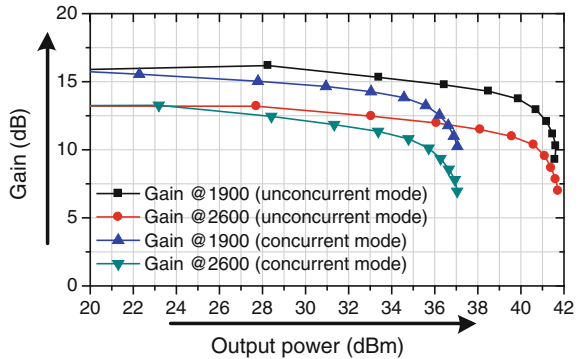


**Fig. 3.24** Gain of the two bands in nonconcurrent and concurrent modes. Reprinted with permission from the IEEE



as shown in Fig. 3.24. Compared with the conventional multiband PA design, the IM tuning improves the concurrent PA performance significantly. In broadband PA design, the video bandwidth of the output-matching network should be optimized to compress output power degradation and memory effects. The IM tuning technique is a similar concept in multiband PA design.

## References

1. B. Razavi, *RF Microelectronics*, 2nd edn. (Prentice Hall, New Jersey, 1998)
2. S. Cripps, *Advanced Techniques in RF Power Amplifier Design* (Artech House, 2002)
3. C. Baylis, M. Fellows, L. Cohen, R. Marks II, Solving the spectrum crisis. *IEEE Microwave Mag.* **15**(5), 94–107 (2015)
4. S. Boumaiza, H. Golestaneh, M. Abadi, Multispectrum signal transmitter. *IEEE Microwave Mag.* **15**(7), 14–24 (2014)
5. A. Tasic, W. Serdijn, J. Long, Adaptive multi-standard circuits and systems for wireless communications. *IEEE Circuits Syst. Mag.* **6**(1), 29–37 (2006)
6. S.A. Bassam, W. Chen, M. Helaloui, F. Ghannouchi, Transmitter architecture for CA: carrier aggregation in LTE-advanced systems. *IEEE Microwave Mag.* **14**(5), 78–86 (2013)

7. W. Chen, S.A. Bassam, X. Li, Y. Liu, M. Helaoui, K. Rawat, F.M. Ghannouchi, Z. Feng, Design and linearization of concurrent dual-band Doherty power amplifier with frequency-dependent power ranges. *IEEE Trans. Microw. Theory Tech.* **59**(10), 2537–2546 (2011)
8. K. Rawat, F. Ghannouchi, Design methodology for dual-band Doherty power amplifier with performance enhancement using dual-band offset lines. *IEEE Trans. Industr. Electron.* **59**(12), 4831–4842 (2012)
9. X. Nghiem, J. Guan, T. Hone, R. Negra, Design of concurrent multiband Doherty power amplifiers for wireless applications. *IEEE Trans. Microw. Theory Tech.* **61**(12), 4559–4568 (2013)
10. A. Kwan, M. Younes, F. Gahnouchi, S. Zhang, W. Chen, R. Darraji, M. Helaoui, O. Hammi, Concurrent multi-band envelope modulated power amplifier linearized using extended phase-aligned DPD. *IEEE Trans. Microw. Theory Tech.* **62**(12), 3298–3308 (2014)
11. J. Moon, J. Son, J. Lee, B. Kim, A multimode/multiband envelope tracking transmitter with broadband saturated amplifier. *IEEE Trans. Microw. Theory Tech.* **59**(12), 3463–3473 (2011)
12. A. Birafane, M. EI-Asmar, A. Kouki, M. Helaoui, F. Ghannouchi, Analyzing LINC systems. *IEEE Microwave Mag.* **11**(5) 59–71 (2010)
13. S. Chung, R. Ma, S. Shinjo, H. Nkamizo, K. Parsons, K. Teo, Concurrent multiband digital outphasing transmitter architecture using multidimensional power coding. *IEEE Trans. Microw. Theory Tech.* **63**(2), 598–613 (2015)
14. M. Helaoui, S. Hatami, R. Negra, F. Ghannouchi, A novel architecture of delta-sigma modulator enabling all-digital multiband multistandard RF transmitter design. *IEEE Trans. Circuits Syst. II Express Briefs* **55**(11), 1129–1133 (2008)
15. H. Wang, C. Peng, Y. Chang, R. Huang, C. Chang, X. Shih et al., A highly-efficient multi-band multi-mode all-digital quadrature transmitter. *IEEE Trans. Circuits Syst. I* **61**(5), 1321–1330 (2014)
16. H.T. Zhang, H. Gao, G.P. Li, Broad-band power amplifier with a novel tunable output matching network. *IEEE Trans. Microw. Theory Tech.* **53**(11), 3606–3614 (2005)
17. U. Kim, S. Kang, J. Woo, Y. Kwon, J. Kim, A multiband reconfigurable power amplifier for umts handset applications. *IEEE Trans. Microw. Theory Tech.* **60**(8), 2532–2542 (2012)
18. X. Chen, W. Chen, F. Ghannouchi et al., Enhanced analysis and design method of concurrent dual-band power amplifiers with intermodulation impedance tuning. *IEEE Trans. Microw. Theory Tech.* **61**(12), 4544–4558 (2013)

# Chapter 4

## Multiband RF Passive Circuits

### 4.1 Introduction

This chapter is dedicated to the design of various passive circuits for the dual-band operation. The chapter starts with the fundamentals of radiofrequency (RF) passive-circuit design and an introduction to the basic dual-band elements used for various RF passive-circuit designs. These basic elements are then used for the development of various RF passive circuits intended for applications such as power dividers, filters, and hybrid couplers. The multiband design is finally extended to multiband RF filter design.

### 4.2 Fundamentals of Network Theory

At RF, the physical dimensions of the circuit are small compared with the wavelength of the operation. Therefore, such circuits can be described using lumped components. These lumped components can be active or passive; hence, the network response can be obtained in terms of various network parameters relating to currents and voltages at different terminals. These network parameters can be impedance/admittance ( $Z/Y$ ) parameters, transmission-line parameters (ABCD),  $s$ -parameters, etc. In fact, the distributed element, such as a transmission line, can be initially analyzed using field analysis and Maxwell's equation such that these components can also be described in terms of quantities related to the network parameters. For example, a simple transmission line can be characterized by its characteristic impedance and electrical length and can be described by unique network parameters such as ABCD. Therefore, for an RF engineer, it is not necessary to solve each component using field analysis and Maxwell's equations. Network analyses can be used to analyze or design several commonly used passive circuits based on transmission lines.

### 4.2.1 Introduction to Some Important Network Parameters Designs

The network parameters describe the relationship between voltages and currents at various points in the RF network. These points or terminals are defined as ports, and the network parameters are expressed in terms of a matrix describing the particular relationship among voltages or currents. Figure 4.1 illustrates an arbitrary M-port RF network, where voltages and currents are described at each port.

The impedance matrix relates voltage at a given port to the currents at each port as

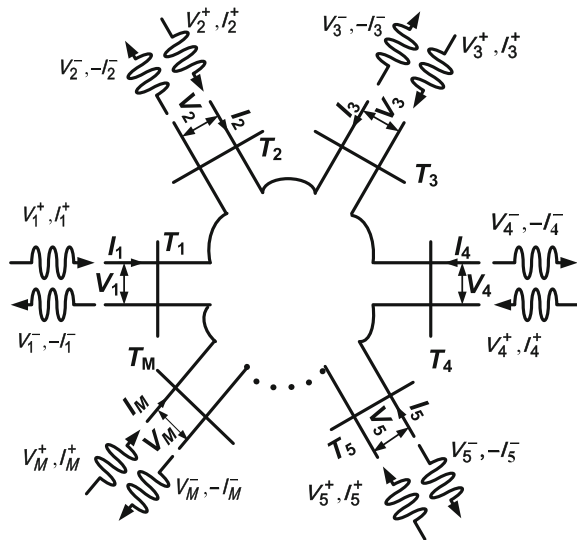
$$\begin{bmatrix} V_1 \\ V_2 \\ \vdots \\ \vdots \\ V_M \end{bmatrix} = \begin{bmatrix} Z_{11} & Z_{12} & \cdots & Z_{1M} \\ Z_{21} & Z_{22} & \cdots & Z_{2M} \\ \vdots & \vdots & \cdots & \vdots \\ \vdots & \vdots & \cdots & \vdots \\ Z_{M1} & Z_{M2} & \cdots & Z_{MM} \end{bmatrix} \begin{bmatrix} I_1 \\ I_2 \\ \vdots \\ \vdots \\ I_M \end{bmatrix}, \quad (4.1)$$

where the above expression can be rewritten as  $[\mathbf{V}] = [\mathbf{Z}][\mathbf{I}]$ , and where  $[\mathbf{Z}]$  is defined as the impedance matrix and each of its elements relates voltages and currents at ports as

$$Z_{m,n} = \left. \frac{V_m}{I_n} \right|_{I_k=0, \text{ for } k \neq n}, \quad (4.2)$$

where  $Z_{m,n}$  is obtained by measuring the open-circuit voltage at port  $m$  when an input current  $I_n$  is applied at port  $n$ , whereas all other ports are kept as open circuits.

**Fig. 4.1** An arbitrary M-port microwave network



Therefore, when  $m = n$ , the expression (3.2) gives input impedance, and when  $m \neq n$ , the same expression gives transfer impedance.

Similarly, one can define admittance matrix  $[\mathbf{Y}]$  such that  $[\mathbf{I}] = [\mathbf{Y}][\mathbf{V}]$ , which can be elaborated as

$$\begin{bmatrix} I_1 \\ I_2 \\ \vdots \\ \vdots \\ I_M \end{bmatrix} = \begin{bmatrix} Y_{11} & Y_{12} & \cdots & Y_{1M} \\ Y_{21} & Y_{22} & \cdots & Y_{2M} \\ \vdots & & \cdots & \\ \vdots & & \cdots & \\ Y_{M1} & Y_{M2} & \cdots & Y_{MM} \end{bmatrix} \begin{bmatrix} V_1 \\ V_2 \\ \vdots \\ \vdots \\ V_M \end{bmatrix}, \quad (4.3)$$

where each matrix element relates voltages and currents at ports as

$$Y_{m,n} = \left. \frac{I_m}{V_n} \right|_{V_k=0, \text{ for } k \neq n}, \quad (4.4)$$

where  $Y_{m,n}$  is obtained by measuring the short-circuit current  $I_m$  at port  $m$  when an input voltage  $V_n$  is applied at port  $n$ , whereas all other ports are kept as short circuits. Therefore, when,  $m = n$ , the expression (4.4) gives the input admittance, and when  $m \neq n$ , the same expression gives the transfer admittance.

The most commonly used network parameter in the field of RF engineering is the scattering parameter, which relates incident and reflected voltage waves at any port. This is quite different from the admittance and impedance parameters, which relate total voltages and currents at different ports. The scattering matrix  $[\mathbf{S}]$  describes the relationship of the incident and reflected voltages at each port of the network as  $[\mathbf{V}^-] = [\mathbf{S}][\mathbf{V}^+]$ , which can be given by

$$\begin{bmatrix} V_1^- \\ V_2^- \\ \vdots \\ \vdots \\ V_M^- \end{bmatrix} = \begin{bmatrix} S_{11} & S_{12} & \cdots & S_{1M} \\ S_{21} & S_{22} & \cdots & S_{2M} \\ \vdots & & \cdots & \\ \vdots & & \cdots & \\ S_{M1} & S_{M2} & \cdots & S_{MM} \end{bmatrix} \begin{bmatrix} V_1^+ \\ V_2^+ \\ \vdots \\ \vdots \\ V_M^+ \end{bmatrix}, \quad (4.5)$$

where each matrix element relates the incident and reflected voltages at ports as

$$S_{m,n} = \left. \frac{V_m^-}{V_n^+} \right|_{V_k^+=0, \text{ for } k \neq n}. \quad (4.6)$$

The element  $S_{m,n}$  is the ratio of the reflected voltage wave amplitude  $V_m^-$  and the incident voltage  $V_n^+$  driving the port  $n$ , while keeping all other ports matched. Therefore, when,  $m = n$ , the expression gives the input reflection coefficient, and when  $m \neq n$ , the same expression gives the transmission coefficient.

The network parameters discussed above can be defined in a general sense for  $m$ -arbitrary ports. However, many complicated networks with  $m$ -ports can be described as combinations of several basic 2-port networks. Such combinations can be in terms of cascaded 2-port networks, and in view of this fact, 2-port transmission-line parameters described in terms of the ABCD matrix are given by

$$\begin{bmatrix} V_1 \\ I_1 \end{bmatrix} = \begin{bmatrix} A & B \\ C & D \end{bmatrix} \begin{bmatrix} V_2 \\ I_2 \end{bmatrix}. \tag{4.7}$$

In the case of other 2-port networks, with the ABCD matrix defined as

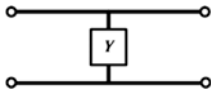
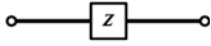
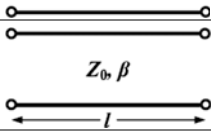
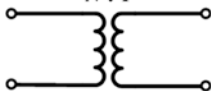
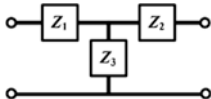
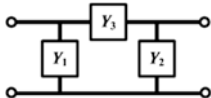
$$\begin{bmatrix} V_2 \\ I_2 \end{bmatrix} = \begin{bmatrix} A' & B' \\ C' & D' \end{bmatrix} \begin{bmatrix} V_3 \\ I_3 \end{bmatrix}, \tag{4.8}$$

if the two 2-port networks with ABCD parameters described by (4.7) and (4.8) are cascaded, then the overall cascaded network has the ABCD matrix defined as

$$\begin{bmatrix} V_1 \\ I_1 \end{bmatrix} = \begin{bmatrix} A & B \\ C & D \end{bmatrix} \begin{bmatrix} A' & B' \\ C' & D' \end{bmatrix} \begin{bmatrix} V_3 \\ I_3 \end{bmatrix}. \tag{4.9}$$

Table 4.1 shows the ABCD parameters of some common 2-port network, which can be useful in describing more complicated RF networks.

**Table 4.1** The ABCD matrix of some common circuits [1]

Circuit	ABCD parameters	
	$A = 1$	$B = 0$
	$C = Y$	$D = 1$
	$A = 1$	$B = Z$
	$C = 0$	$D = 1$
	$A = \cos \beta l$	$B = jZ_0 \sin \beta l$
	$C = jY_0 \sin \beta l$	$D = \cos \beta l$
	$A = N$	$B = 0$
	$C = 0$	$D = 1/N$
	$A = 1 + \frac{Z_1}{Z_3}$	$B = Z_1 + Z_2 + \frac{Z_1 Z_2}{Z_3}$
	$C = \frac{1}{Z_3}$	$D = 1 + \frac{Z_2}{Z_3}$
	$A = 1 + \frac{Y_2}{Y_3}$	$B = \frac{1}{Y_3}$
	$C = Y_1 + Y_2 + \frac{Y_1 Y_2}{Y_3}$	$D = 1 + \frac{Y_1}{Y_3}$

### 4.2.2 Properties of RF Networks in Terms of Network Parameters

A reciprocal network is a network where the response does not change if the excitation and measurement ports are interchanged.

If a linear passive component contains no active device or nonreciprocal media, then it is reciprocal. In such case its admittance and impedance matrices are symmetric [1]. Thus, the Z- and Y-parameters for a reciprocal network should follow the following conditions:

$$Z_{mn} = Z_{nm} \quad (4.10)$$

$$Y_{mn} = Y_{nm} \quad (4.11)$$

For a lossless passive network, all the elements of the [Z] and [Y] matrices are purely imaginary.

For any 2-port network described by the ABCD matrix, the properties discussed above can also be expressed in terms of ABCD parameters. For example, the ABCD matrix representing symmetric network should have

$$A = D \quad (4.12)$$

such that  $Z_{mm} = Z_{nn}$  is satisfied. Similarly, for the reciprocity condition of (4.10) to be satisfied, the ABCD matrix representing the reciprocal network should follow:

$$AD - BC = 1. \quad (4.13)$$

For a lossless 2-port network, the diagonal elements  $A$  and  $D$  are real, whereas the off-diagonal elements  $B$  and  $C$  are imaginary.

In terms of s-parameters, the reciprocal network is also symmetric, and one can define the condition as

$$[S] = [S]^T, \quad (4.14)$$

where  $[S]^T$  is the transpose of the [S] matrix and, hence, (4.14) implies

$$S_{mn} = S_{nm}. \quad (4.15)$$

Similarly, for a lossless network, the [S] parameters matrix should be a unitary matrix and hence should satisfy the following two conditions simultaneously [1]:

$$\sum_{k=1}^M S_{km} S_{km}^* = 1; \quad \text{if } m = n. \quad (4.16)$$



$$\sum_{k=1}^M S_{km} S_{kn}^* = 0; \quad \text{if } m \neq n. \quad (4.17)$$

Equations (4.16) and (4.17) state that the dot product of any column with the conjugate of the same column gives unity, whereas the dot product of any column with the conjugate of a different column results in zero value. In case of a symmetric network, the same statement is applicable to the rows also.

### 4.2.3 Image Parameters and Design of RF Networks Using ABCD Matrix

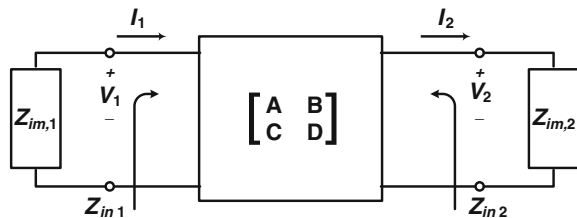
Image parameters are used for simple filter designs, where only passband and stopband characteristics are of prime importance. However, as the applications evolve, the required response of a filter becomes challenging, and specifications in terms of arbitrary frequencies are also required. This has led to the popularity of the design based on insertion loss, which is the most common method of filter design [1–3]. Nevertheless, image-parameter-based designs are still used in imitating transmission-line response in certain specified frequency ranges [1, 4]. Generally, this method utilizes cascaded 2-port networks, and therefore, they are represented in terms of the ABCD parameters.

Image impedance is one of the important parameters in image-parameter-based design. Figure 4.2 shows a 2-port network used to define image impedance. In Fig. 4.2, the image impedance  $Z_{im,1}$  is the input impedance  $Z_{in,1}$  at port 1 when an impedance of  $Z_{im,2}$  terminates port 2. The image impedance  $Z_{im,2}$  is an input impedance  $Z_{in,2}$  at port 2 when port 1 is terminated with  $Z_{im,1}$ .

Thus, image impedances are the terminating impedances presented at both the ports, which results in a matched condition at these ports. The expressions for the image impedances of a reciprocal, lossless 2-port network can be obtained in terms of the ABCD parameters as [1, 5]:

$$Z_{im,1} = \sqrt{\frac{AB}{CD}}. \quad (4.18)$$

**Fig. 4.2** A 2-port network defining image impedance



$$Z_{\text{im},2} = \sqrt{\frac{DB}{CA}}. \quad (4.19)$$

For a symmetric network,  $A = D$ , which further simplifies (4.18) and (4.19) as

$$Z_{\text{im},1} = Z_{\text{im},2} = \sqrt{\frac{B}{C}}. \quad (4.20)$$

Similarly, the voltage transfer function of a 2-port network when terminated in its image impedances can be expressed in terms of the ABCD parameters as

$$\frac{V_2}{V_1} = \sqrt{\frac{D}{A}}(\sqrt{AD} - \sqrt{BC}), \quad (4.21)$$

where one can define a propagation factor for the network as

$$e^{-\gamma} = \sqrt{AD} - \sqrt{BC}. \quad (4.22)$$

The expression in (4.22) will be further simplified to

$$\cosh \gamma = \sqrt{AD}. \quad (4.23)$$

#### 4.2.4 *Transmission-Line Equivalence with Image Parameters*

In a generic sense, a 2-port symmetric, lossless and reciprocal network can emulate a transmission line with effective characteristic impedance defined as image impedance given by (4.20) and with effective electrical length directly related to propagation factor as defined by (4.23) [5]. Thus, a symmetric 2-port network can emulate a transmission line response that has design parameters such as characteristic impedance and electrical length, calculated from its ABCD parameters. This equivalence is shown in Fig. 4.3, where the effective characteristic impedance and the electrical length are given by

$$Z_T = \sqrt{\frac{B}{C}} \quad (4.24)$$

$$\cos \theta_T = \frac{A+D}{2} \quad (4.25)$$

The most common example of 2-port networks that are used for imitating transmission-line behavior is a stub-loaded transmission line as shown in Fig. 4.4.

**Fig. 4.3** Equivalence of a 2-port network and a transmission line: **a** a 2-port symmetric and reciprocal network and **b** equivalent transmission line with design parameters

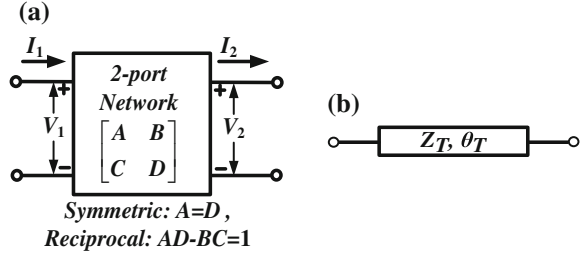
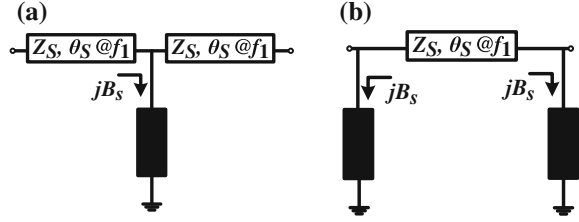


**Fig. 4.4** A 2-port network used for imitating a transmission line: **a** T-type and **b** pi-type



The structure in Fig. 4.4a is a center-tapped stub-loaded line (T-type network) [5], whereas Fig. 4.4b shows a transmission line loaded with stubs at the edges (pi-type network) [6].

The purpose of using a stub-loaded transmission line for imitating a transmission line response is to obtain a desired frequency-selective behavior. Such a structure can emulate specific transmission-line properties—for example, a quarter-wave response—at the desired frequencies of operation. Thus, the image-parameter-based design is well known in the realization of multiband quarter-wave transmission-line design [5].

The ABCD matrix of a center-tapped stub-loaded line (T-type structure as shown in Fig. 4.4a) is given by [5, 7]:

$$\begin{bmatrix} A & B \\ C & D \end{bmatrix} = \begin{bmatrix} \cos 2\theta_{S,T} - \frac{1}{2}B_{S,T}Z_{S,T} \sin 2\theta_{S,T} & jZ_S (\sin 2\theta_{S,T} - B_{S,T}Z_{S,T} \sin^2 \theta_{S,T}) \\ j\frac{1}{Z_{S,T}} (\sin 2\theta_{S,T} + B_{S,T}Z_{S,T} \cos^2 \theta_{S,T}) & \cos 2\theta_{S,T} - \frac{1}{2}B_{S,T}Z_{S,T} \sin 2\theta_{S,T} \end{bmatrix}, \quad (4.26)$$

where  $Z_{S,T}$  is the characteristic impedance of a series line of electrical length,  $\theta_{S,T}$ , loaded by a susceptance of  $B_{S,T}$ , as shown in Fig. 4.4a.

Recalling (4.24) and (4.25), the effective electrical length ( $\theta_T$ ) and the characteristic impedance ( $Z_T$ ) of an equivalent loaded transmission line can be obtained by using ABCD parameters of (4.26) as

$$\cos(\theta_T) = \frac{A+D}{2} = \cos 2\theta_{S,T} - \frac{1}{2}B_{S,T}Z_{S,T} \sin 2\theta_{S,T}. \quad (4.27)$$

$$Z_T = \sqrt{\frac{B}{C}} = Z_{S,T} \sqrt{\frac{\sin 2\theta_{S,T} - B_{S,T} Z_{S,T} \sin^2 \theta_{S,T}}{\sin 2\theta_{S,T} + B_{S,T} Z_{S,T} \cos^2 \theta_{S,T}}}. \quad (4.28)$$

In order to emulate quarter-wave-transformer characteristics, the effective electrical length,  $\theta_T$ , should be set to  $90^\circ$  in (4.27), resulting in the following condition:

$$B_{S,T} = \frac{2}{Z_{S,T} \tan 2\theta_{S,T}}. \quad (4.29)$$

Using (4.29) in (4.28) results in another relation, as follows:

$$Z_T = Z_{S,T} \tan \theta_{S,T}. \quad (4.30)$$

Thus, (4.29) and (4.30) together guarantee the condition for the T-type structure of Fig. 4.4a to behave as a transmission line of  $90^\circ$  electrical length.

Similarly, the ABCD matrix of a transmission line with edge-loading (pi-type structure, as shown in Fig. 4.4b) is given by [5–8]

$$\begin{bmatrix} A & B \\ C & D \end{bmatrix} = \begin{bmatrix} \cos \theta_{S,PI} - B_{S,PI} Z_{S,PI} \sin \theta_{S,PI} & jZ_{S,PI} \sin \theta_{S,PI} \\ j \frac{\sin \theta_{S,PI}}{Z_{S,PI}} \left( 1 - Z_{S,PI}^2 B_{S,PI}^2 + 2B_{S,PI} Z_{S,PI} \cot \theta_{S,PI} \right) & \cos \theta_{S,PI} - B_{S,PI} Z_{S,PI} \sin \theta_{S,PI} \end{bmatrix}. \quad (4.31)$$

The overall effective electrical length ( $\theta_T$ ) and the characteristic impedance ( $Z_T$ ) of the pi-type structure depicted in Fig. 4.4b can be obtained by using the ABCD matrix of (4.31) as

$$\cos(\theta_T) = \frac{A + D}{2} = \cos \theta_{S,PI} - B_{S,PI} Z_{S,PI} \sin \theta_{S,PI}, \quad (4.32)$$

$$Z_T = \sqrt{\frac{B}{C}} = Z_{S,PI} = \sqrt{\frac{1}{1 - Z_{S,PI}^2 B_{S,PI}^2 + 2Z_{S,PI} B_{S,PI} \cot \theta_{S,PI}}}. \quad (4.33)$$

where  $Z_{S,PI}$  is the characteristic impedance of a series line of electrical length,  $\theta_{S,PI}$ , loaded by a susceptance of  $B_{S,PI}$ , as shown in Fig. 4.4b. For a 90-degree transformer (i.e.,  $\theta_T = 90^\circ$ ), one can obtain  $B_{S,PI}$  by using (4.32), as

$$B_{S,PI} = \frac{1}{Z_{S,PI} \tan \theta_{S,PI}}. \quad (4.34)$$

Using (4.34) in (4.33) gives another condition:

$$Z_T = Z_{S,PI} = Z_{S,PI} \sin \theta_{S,PI}. \quad (4.35)$$

For the pi-type structure in Fig. 4.4b, Eqs. (4.34) and (4.35) simultaneously guarantee the overall 90-degree electrical length and effective characteristic impedance of  $Z_T$ .

### 4.3 Multiband RF Transformers

RF transformers are often used for impedance transformation at RF frequencies. This can simply be realized by using transmission line of quarter-wavelength or stepped impedance transformers [5]. The latter is obtained by cascading transmission lines of different impedances [5, 9].

#### 4.3.1 Stub-Loaded (T-Shape and Pi-Shape) Transformers

In Sect. 4.1, it has been shown that a 2-port symmetric, lossless and reciprocal network can emulate a transmission line. A transmission line of a certain characteristic impedance with an electrical length of  $90^\circ$  acts as a quarter-wave transformer that can provide impedance transformation at the frequency where the effective electrical length is  $90^\circ$ . If the effective length of 2-port networks as shown in Fig. 4.4 is  $90^\circ$  at multiple frequencies, then the network emulates the behavior of a multiband RF transformer. This section describes dual-band RF transformers based on 2-port networks as shown in Fig. 4.4.

The electrical lengths  $\theta_{S,T}$  in (4.30) and  $\theta_{S,PI}$  in (4.35) vary with frequency, and for these equations to satisfy simultaneously at two distinct frequencies, the expression in (4.36) should hold true [5, 10].

$$\theta_{S,T} = \theta_{S,PI} = \frac{p\pi}{n \mp 1}, \quad (4.36)$$

where  $n$  is the frequency ratio  $f_2/f_1$  with  $f_1$  being the lower frequency and  $p$  is 1 for the principal argument of the sine and tangent functions of (4.30) and (4.35), corresponding to the smallest physical length of the unloaded line in Fig. 4.4a, b.

The negative and positive signs in (4.36) correspond to electrical lengths  $90^\circ$  and  $270^\circ$ , respectively. It is worth mentioning that any odd multiple of the electrical length of  $90^\circ$  provides the same performance as a quarter-wave transformer. Therefore, for the dual-band case, there exist two solutions for (4.36) that provide the requisite dual-band quarter-wave transformers at two distinct frequencies [5, 10]. The first solution is achieved with an electrical length of  $90^\circ$ , corresponding

to the negative sign in (4.36), for both the frequencies, whereas the other solution is obtained with electrical lengths of  $90^\circ$  in the first frequency and  $270^\circ$  in the second frequency, which corresponds to the positive sign in (4.36). For smaller frequency ratios, the first case gives larger physical dimensions compared with the second case [5, 10].

The design approach includes varying  $n$  in (4.36) for obtaining different values of electrical length  $\theta_{S,T}$  or  $\theta_{S,PI}$ . These values of electrical lengths of series lines in T-type and pi-type structures are used in (4.30) and (4.35), respectively, to obtain the design curves shown in Figs. 4.5 and 4.6 for  $Z_T = 50 \Omega$ .

For a given value of  $n$  and  $p$  (corresponding to the value of  $\theta_{S,T}$  or  $\theta_{S,PI}$ ), the realizable values of characteristic impedances  $Z_{S,T}$  or  $Z_{S,PI}$  can be obtained from Figs. 4.5 and 4.6, respectively, for a required value of effective characteristic impedance  $Z_T$  (of the emulated quarter-wave transformer). The upper limit for the values of  $Z_{S,T}$  or  $Z_{S,PI}$  depends on the minimum width of the line that can be fabricated precisely with the fabrication facility. Therefore, the minimum possible width of the transmission line puts a constraint over the maximum value of  $Z_{S,T}$  or  $Z_{S,PI}$ .

Upon determining the values of  $Z_{S,T}$  or  $Z_{S,PI}$  for particular values of  $\theta_{S,T}$  or  $\theta_{S,PI}$ ,  $n$  and  $Z_T$ , the corresponding values for the other values of  $Z_T$  for a given value of  $n$  can easily be predicted by the linear relation given by (4.30) and (4.35) as described in [10]. For example, once the values for  $Z_{S,T}$  or  $Z_{S,PI}$  and the associated  $\theta_{S,T}$  or  $\theta_{S,PI}$  are obtained from the design curves of Figs. 4.5 and 4.6, respectively, their values are used for calculating the corresponding values of stubs. This will guarantee simultaneous solution of (4.29) and (4.30) for the structure shown in Fig. 4.4a and similarly simultaneous solution of (4.34) and (4.35) for the structure in Fig. 4.4b.

Fig. 4.5 Design curve for a T-type structure

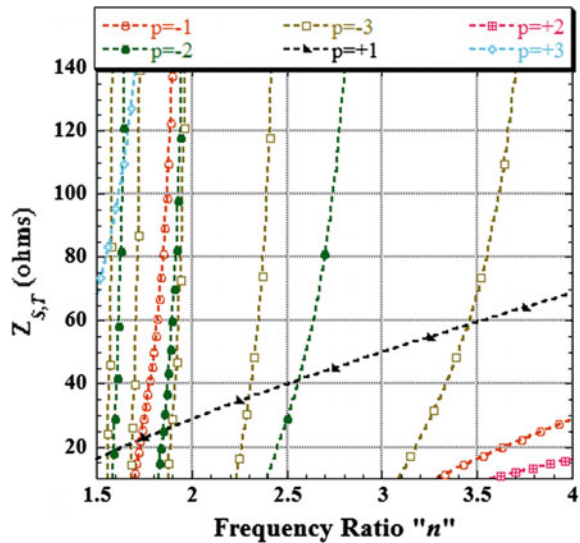
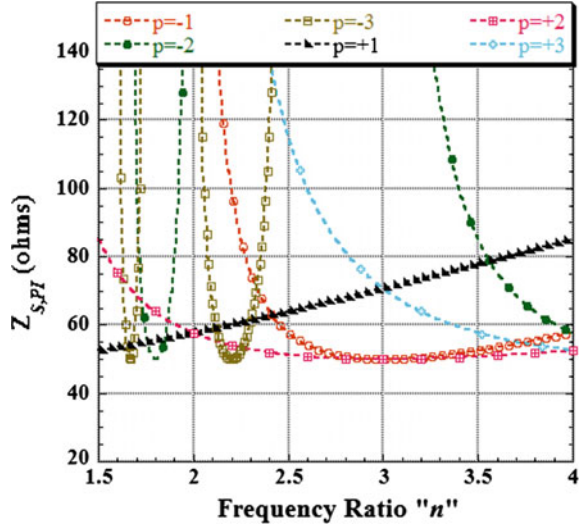


**Fig. 4.6** Design curve for a pi-type structure



At the two frequencies, the values of stub  $B_{S,T}$  for the center-tapped loaded structure is calculated using (4.29), whereas, for the edge-loaded structure, (4.34) is used to calculate the corresponding values of  $B_{S,PI}$  for the two frequencies.

If the  $B_{S,T}$  in (4.29) is realized by an open- or short-circuit transmission line of characteristic impedance  $Z_{P,T}$  and electrical length  $\theta_{P,T}$  [7] as shown in Fig. 4.4a, the following condition can be obtained for the design parameters of the loading stub:

$$Z_{P,T} = \begin{cases} \frac{Z_T Z_{S,T}^2}{Z_{S,T}^2 - Z_T^2} \tan \theta_{P,T} & \text{for stub realized with open-circuit transmission line} \\ \frac{Z_T Z_{S,T}^2}{Z_T^2 - Z_{S,T}^2} \frac{1}{\tan \theta_{P,T}} & \text{for stub realized with short-circuit transmission line} \end{cases} \quad (4.37)$$

Similarly, if the  $B_{S,PI}$  in (4.34) is realized by an open- or short-circuit transmission line of characteristic impedance  $Z_{P,PI}$  and electrical length  $\theta_{P,PI}$  as shown in Fig. 4.4b [7], the following condition can be obtained for the design parameters of the loading stub:

$$Z_{P,T} = \begin{cases} \frac{Z_T Z_{S,PI}}{\sqrt{Z_{S,PI}^2 - Z_T^2}} \tan \theta_{P,PI} & \text{for stub realized with open-circuit transmission line} \\ \frac{-Z_T Z_{S,PI}}{\sqrt{Z_{S,PI}^2 - Z_T^2}} \frac{1}{\tan \theta_{P,PI}} & \text{for stub realized with short-circuit transmission line} \end{cases} \quad (4.38)$$

In addition, to ensure the dual-band operation for the arbitrary ratio,  $n$ , the condition given by (4.37) and (4.38) should also be repeated for the second frequency  $f_2$ ; hence, the electrical length of the open stub is given by

$$\theta_{P,T} = \theta_{P,PI} = \frac{q\pi}{n \mp 1}, \tag{4.39}$$

where  $q$  is the integer with value 1 for the principal argument of the tangent function in (4.37) and (4.38) and  $n$  is the frequency ratio.

A graph similar to Figs. 4.5 and 4.6 can be obtained for obtaining stub parameters. From these graphs, the values of  $Z_{P,T}$  or  $Z_{P,PI}$  and  $\theta_{P,T}$  or  $\theta_{P,PI}$  can be calculated. The maximum values of  $Z_{P,T}$  or  $Z_{P,PI}$  are selected depending on the technology used for fabrication.

Once the design parameters for a particular  $n$  and  $Z_T$  are known, the values of the corresponding  $Z_{P,T}$  or  $Z_{P,PI}$  for any other values of  $Z_T$  for the same  $n$  can also be determined using the expressions (4.37) and (4.38) [5, 7, 10].

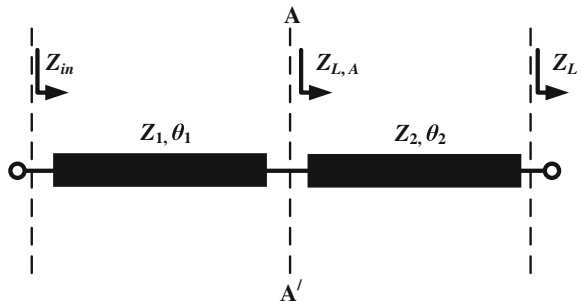
### 4.3.2 Multisection Non-quarter-Wave Impedance Transformer

The topology for the two-section stepped impedance transformer is shown in Fig. 4.7, where the two transmission lines of characteristic impedances  $Z_1$  and  $Z_2$  and the corresponding electrical lengths  $\theta_1$  and  $\theta_2$  are cascaded. The transformer is used to transform the load impedance  $Z_L$  to  $Z_{in}$  at two frequencies of operation. This structure is used for dual-band impedance transformation and is also known as the Monzon transformer [9].

As shown in Fig. 4.7, if  $Z_{L,A}$  is the intermediate load seen by the transmission line at reference AA', then the input impedance,  $Z_{in}$ , is given by

$$Z_{in} = Z_1 \frac{Z_{L,A} + jZ_1 \tan \theta_1}{Z_1 + jZ_{L,A} \tan \theta_1}, \tag{4.40}$$

Fig. 4.7 Topology of a Monzon transformer





where the load  $Z_{L,A}$  can be expressed in terms of the load  $Z_L$  and the transmission-line parameters  $Z_2$  and  $\theta_2$  as

$$Z_{L,A} = Z_2 \frac{Z_L + jZ_2 \tan \theta_2}{Z_2 + jZ_L \tan \theta_2}, \quad (4.41)$$

Rearranging (4.40), one can obtain the additional expression of  $Z_{L,A}$  as

$$Z_{L,A} = Z_1 \frac{Z_{in} + jZ_1 \tan \theta_1}{Z_1 + jZ_{in} \tan \theta_1}, \quad (4.42)$$

Equating the corresponding right-hand-side terms of Eqs. (4.41) and (4.42) and separating the real and imaginary part results into [9]:

$$\tan \theta_1 \tan \theta_2 = \zeta = \frac{Z_1 Z_2 (R_L - Z_{in})}{Z_1^2 R_L - Z_2^2 Z_{in}}, \quad (4.43)$$

$$\frac{\tan \theta_1}{\tan \theta_2} = \sigma = \frac{Z_1 (Z_2^2 - R_L Z_{in})}{Z_2 (R_L Z_{in} - Z_1^2)}, \quad (4.44)$$

where  $\zeta$  and  $\sigma$  are constants with respect to the frequency and depends on the given load, the required input impedances, and the design parameters  $Z_1$  and  $Z_2$ . The design parameters  $Z_1$  and  $Z_2$  are the characteristic impedances of the two cascaded transmission lines shown in Fig. 4.7.

From (4.43) and (4.44), the following identities can be written as:

$$\tan^2(\theta_1) = \zeta \sigma. \quad (4.45)$$

$$\tan^2(\theta_2) = \frac{\zeta}{\sigma}. \quad (4.46)$$

The identities described by Eqs. (4.45) and (4.46) express the conditions over the electrical lengths of the two transmission lines in Fig. 4.7 such that the cascaded structure of these transmission lines will act as an impedance transformer. In order to act as a dual-band impedance transformer, Eqs. (4.45) and (4.46) should individually apply to both frequencies of operations  $f_1$  and  $f_2$ . Thus, the dual-band operation conditions expressed in (4.45) can be rewritten as

$$\tan^2(\theta_1) = \zeta \sigma. \quad (4.47a)$$

$$\tan^2(n\theta_1) = \zeta \sigma. \quad (4.47b)$$

Similarly, the condition expressed in (4.46) can be rewritten as

$$\tan^2(\theta_2) = \frac{\xi}{\sigma}, \quad (4.48a)$$

$$\tan^2(n\theta_2) = \frac{\xi}{\sigma}, \quad (4.48b)$$

where the electrical lengths  $\theta_1$  and  $\theta_2$  of the two transmission lines in Fig. 4.7 are defined at the first frequency  $f_1$  and  $n$  is the frequency ratio defined as  $f_2/f_1$ .

For the dual-band operation, (4.47a) and (4.47b) should be equal. Similarly, (4.48a) and (4.48b) should be equal in order to ensure dual-band operation. Thus, for dual-band operation, the following conditions must be imposed over the electrical lengths of the two transmission lines in Fig. 4.7.

$$\theta_1 = \frac{q\pi}{n \mp 1}. \quad (4.49a)$$

$$\theta_2 = \frac{q\pi}{n \mp 1}. \quad (4.49b)$$

For the shortest length of the transmission line in Fig. 4.7, one can choose  $p = q = 1$  and the positive sign in the denominator, which results in

$$\theta_1 = \theta_2 = \frac{\pi}{n + 1}. \quad (4.50)$$

Using (4.50) in (4.44), one can infer  $\sigma = 1$ . Accordingly, rearranging (4.44) using  $\sigma = 1$  gives the antimetry condition [9] as

$$Z_{in}R_L = Z_1Z_2. \quad (4.51)$$

The above condition of (4.51) is further used in (4.43) to give

$$Z_1^2R_L - Z_2^2Z_0 = \frac{Z_0R_L(R_L - Z_0)}{\xi}. \quad (4.52)$$

Using (4.51) and (4.52), a fourth-order equation can be obtained in terms of  $Z_1$ , which results in the following solutions for the characteristic impedances of the transmission lines in Fig. 4.7.

$$Z_1 = R_L \sqrt{\frac{p}{2\xi}(1-p) + \sqrt{\left[\frac{p}{2\xi}(1-p)\right]^2 + p^3}}, \quad (4.53)$$

and

$$Z_2 = \frac{R_L^2}{Z_1}, \tag{4.54}$$

where  $p$  is the impedance transformation ratio of the input impedance,  $Z_{in}$ , to the load impedance,  $Z_L$ , for the impedance transformer, as shown in Fig. 4.7. The constant,  $\xi$ , is defined as [9, 11]

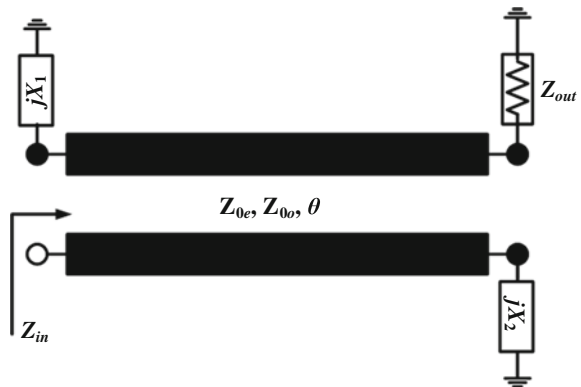
$$\xi = \tan^2\left(\frac{\pi f_1}{f_1 + f_2}\right). \tag{4.55}$$

The electrical lengths of the two transmission lines in Fig. 4.7 can be calculated using (4.50), where the physical lengths are calculated by considering these electrical lengths at the first frequency of operation  $f_1$ .

### 4.3.3 Coupled-Line-Based Impedance Transformer

A 4-port coupled-line section can be used as a 2-port quarter-wave transformer by presenting proper terminations at the two ports. Figure 4.8 shows such a configuration, where two ports are terminated by the load  $Z_T$ . For any coupled-line design, the even- and odd-mode characteristic impedances along with the electrical length represent the electrical design parameters [1]. The physical design parameters such as the physical length, the width of the coupled lines, and the spacing between them can easily be expressed in terms of the electrical design parameters. Assuming the transverse electromagnetic TEM mode of operation, the even-mode and odd-mode characteristic impedances,  $Z_{0,e}$  and  $Z_{0,o}$ , respectively, are related with the voltage coupling coefficient  $C$  as [1]

**Fig. 4.8** Topology of a coupled-line-based impedance transformer



$$\frac{Z_{0,o}}{Z_{0,e}} = \frac{1 - C}{1 + C} = \frac{1 - 10^{-X/20}}{1 + 10^{-X/20}}, \quad (4.56)$$

where  $X$  is the coupling factor, which is related to the coupling coefficient as

$$X = -20 \log C. \quad (4.57)$$

Similarly, the even-mode and odd-mode characteristic impedances are related to the matched load  $Z_0$  as

$$Z_0 = \sqrt{Z_{0,o}Z_{0,e}}. \quad (4.58)$$

If the coupling coefficient and the matched load are known, Eqs. (4.56) and (4.58) can be simultaneously solved to obtain the design parameters  $Z_{0,e}$  and  $Z_{0,o}$ , which can directly be used to obtain the physical design parameters in terms of the width of the coupled lines and the spacing between them [5].

The coupled-line transformer in Fig. 4.8 is a 2-port network obtained by terminating two ports of a 4-port coupled-line section with reactances  $jX_1$  and  $jX_2$ .

The overall design parameters for such coupled-line-based impedance transformers are the loading reactances  $jX_1$  and  $jX_2$  and the coupled-line design parameters  $Z_{0e}$ ,  $Z_{0o}$ , and  $\theta$ . These five parameters, if chosen properly, can transform a wide range of complex impedances  $Z_{out}$  into  $Z_{in}$ , where  $Z_{in}$  can also be complex, and thus can also be readily used in direct matching applications.

The structure in Fig. 4.8 can be analyzed using  $Z$  and ABCD parameters as described in [12, 13]. For a reasonable choice of the design parameters  $Z_{0e}$ ,  $Z_{0o}$ , and  $\theta$ , other two parameters can be obtained from the following expressions:

$$X_1 = \frac{C_1 + C_3 \pm \sqrt{2C_2}}{C_4}, \quad (4.59a)$$

$$X_2 = \frac{C_5 + C_6 \pm \sqrt{2C_2}}{C_7}, \quad (4.59b)$$

where  $C_1$ – $C_7$  are intermediate variables depending on  $Z_{0e}$ ,  $Z_{0o}$ ,  $\theta$ ,  $Z_L$ , and  $Z_{in}$ , as described in [12]. It is worth mentioning that the initial values of  $Z_{0e}$ ,  $Z_{0o}$ , and  $\theta$  chosen to calculate  $X_1$  and  $X_2$  must satisfy  $C_2 \geq 0$ . It is evident from (4.59a) and (4.59b) that there exist two solutions for each  $X_1$  and  $X_2$ .

In order to extend this transformer into dual-band operation, the values of  $X_1$  and  $X_2$  are calculated using two frequencies  $f_1$  and  $f_2$  by using electrical lengths  $\theta$  at  $f_1$ . The other design parameters  $Z_{0e}$  and  $Z_{0o}$  remain the same for both frequencies. Therefore, initially, the procedure for the design is similar to that for the single-band design, where,  $Z_{0e}$ ,  $Z_{0o}$ , and  $\theta$  are chosen to satisfy  $C_2 \geq 0$ . The value of  $\theta$  is considered at  $f_1$  to calculate the physical length of the coupled line. These values of the design parameters will be used to calculate reactances  $X_1(f_1)$  and  $X_2(f_1)$  at the

first frequency of operation  $f_1$ . Later,  $X_1(f_2)$  and  $X_2(f_2)$  are calculated using  $Z_{0e}$ ,  $Z_{0o}$ , and  $n\theta$ , where  $n$  is frequency ratio  $f_2/f_1$  [12, 13]. In order to physically realize the reactances  $X_1$  and  $X_2$  at  $f_1$  and  $f_2$ , a dual-band/dual-susceptance stub with open and short transmission lines can be used as described in Sect. 4.2.1 and using Eqs. (4.37)–(4.39). An alternative approach for dual-band/dual-susceptance using multisection stubs is also described in Sect. 4.3.3.

## 4.4 Multiband Power Divider and Hybrid Design

The most common RF passive circuits are power dividers and hybrid couplers. This section describes the utilization of dual-band elements discussed in previous sections for the design of power dividers and hybrid couplers.

### 4.4.1 Multiband Wilkinson Power Divider

A conventional Wilkinson power divider requires an impedance transformer that can transform 50–100  $\Omega$ . This impedance transformer can be realized using a transmission line of 90-degree electrical length and a characteristic impedance of 70.7  $\Omega$ . Therefore, in order to obtain dual-band operation, each branch of a conventional Wilkinson power divider can be replaced by a stub-loaded transmission line, i.e., pi-type or T-type (as described in Sect. 4.2.1) with an effective electrical length of 90° and a characteristic impedance of 70.7  $\Omega$  [14]. In principle, for a Wilkinson power divider, the main requirement is the impedance transformation [15], which can be achieved through the use of either quarter-wave transformers or non-quarter-wave transformers, such as Chebyshev or Monzon multisection transformers [9, 16, 17] as described in Sect. 4.2.2. However, the Monzon transformer, as described in Sect. 4.2.2, is simpler to design and is, therefore, the most commonly used topology for dual-band application [18–20].

Figure 4.9 shows the circuit topology and the photograph of a dual-band power divider based on the Monzon transformer.

This power divider operates at 880 and 1960 MHz and hence can be used for Global System for Mobile Communications (GSM) and Wideband Code Division Multiple Access (WCDMA) applications, respectively.

Using (4.50) and (4.53)–(4.55), one can design the dual-band Monzon transformer, as shown in Fig. 4.9a, to match  $Z_L = 50 \Omega$  impedance to  $Z_{in} = 100 \Omega$  impedance in each branch of a Wilkinson power divider. Table 4.2 shows the electrical and physical design parameters of the dual-band Monzon transformer, replacing each branch of a conventional power divider as shown in Fig. 4.9 and realized in microstrip technology using a substrate RT5870 with a height of 20 mil, dielectric constant of 2.33, and loss tangent of 0.0012.

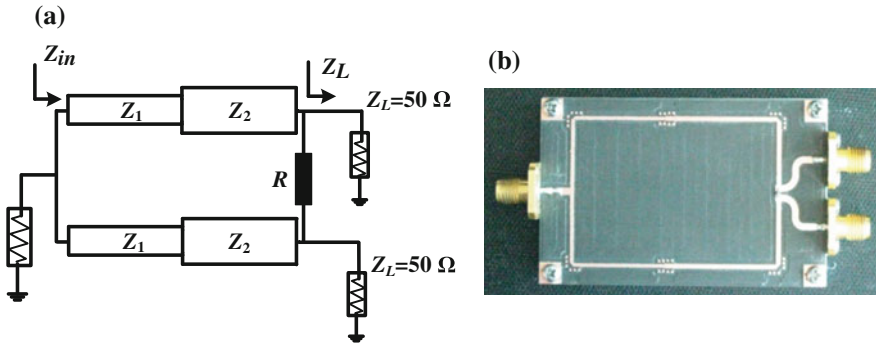


**Fig. 4.9** Design example of a dual-band power divider using a dual-band Monzon transformer: **a** schematic and **b** photograph. Reprinted with permission from the IEEE

**Table 4.2** Electrical and physical design parameters for the 70.7 Ω branch of a dual-band Wilkinson power divider using the dual-band Monzon transformer [11]

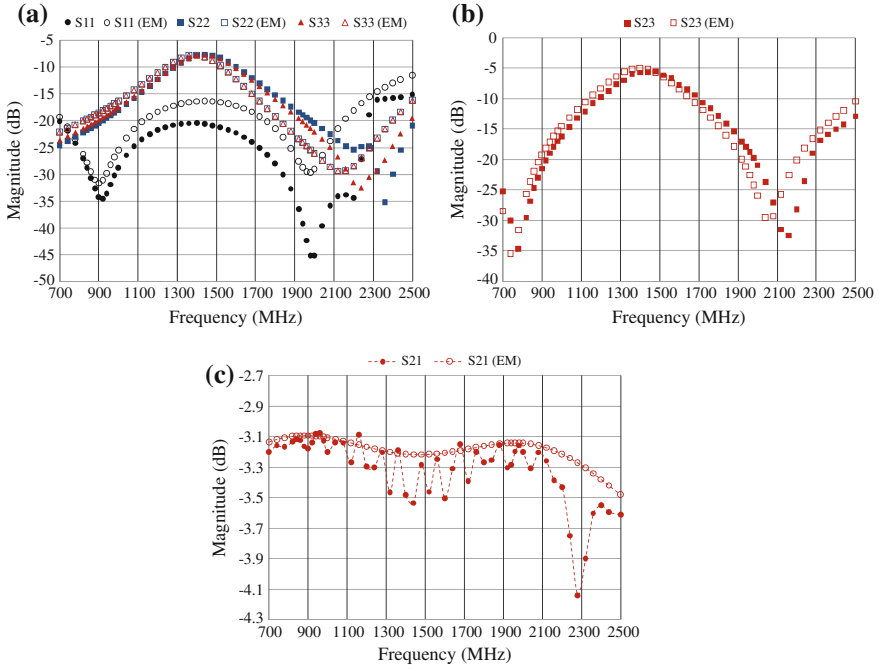
Electrical design parameter	Electrical design parameters values	Physical design parameters	Physical design parameter values (mm)	
			Calculated	Optimized
$Z_1$ (Ω)	77.5	$w_1$	0.7	0.7
$Z_2$ (Ω)	64.5	$w_2$	0.98	0.98
$\eta_1$ @ $f_1$ (°)	55.7	$l_1$	39.5	39.6
$\eta_2$ @ $f_2$ (°)	124.2	$l_2$	39.5	39.6

Figure 4.10 shows some important measured and simulated results of a dual-band power divider based on the Monzon transformer.

Figure 4.10a, b shows that the return losses and the isolation are greater than 15 dB at all the ports over the bands. Figure 4.10c shows that the insertion loss is less than 3.3 dB over the band of ±110 MHz around the two selected frequencies of 850 and 1960 MHz.

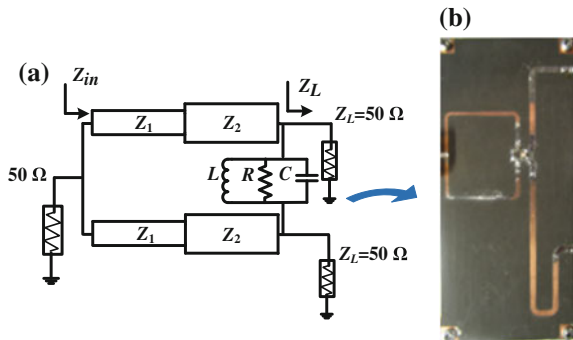
The circuit in Fig. 4.9 utilizes a resistance of  $R = 100 \Omega$ , for isolation similar to a conventional Wilkinson power divider. However, for dual-band application, the even- and odd-mode analysis of this circuit topology as described in [21] leads to the utilization of an LC tank circuit in the shunt of this resistor as shown in Fig. 4.11. This LC circuit is designed to resonate at the center of the two frequencies of operation. Figure 4.11 also shows a photograph of a dual-band Wilkinson power divider using an LC tank circuit along with an isolation resistor. Figure 4.12 shows some important results of the Monzon-transformer-based Wilkinson power divider as shown in Fig. 4.11.

One can see from Fig. 4.12 that the return loss is better than 20 dB over the band of interest at each frequency of operation. Similarly, the isolation is better than 20 dB in both the bands as shown in Fig. 4.12b. The magnitude and phase differences are within 0.5 dB and 10°, respectively.



**Fig. 4.10** Simulated and measured results of a dual-band power divider based on the Monzon transformer [11]: **a** reflection coefficients, **b** isolation and **c** transmission coefficient. Reprinted with permission from the IEEE

**Fig. 4.11** A Monzon-transformer-based dual-band power divider design with improved isolation: **a** schematic and **b** photograph. Reprinted with permission from the IEEE



### 4.4.2 Multiband Hybrid Couplers

The RF hybrid coupler can be a branch-line hybrid coupler (quadrature type) or a rat-race coupler (180-degree type). In order to extend the inherent single-band operation of these hybrid couplers into dual-band, one direct approach involves

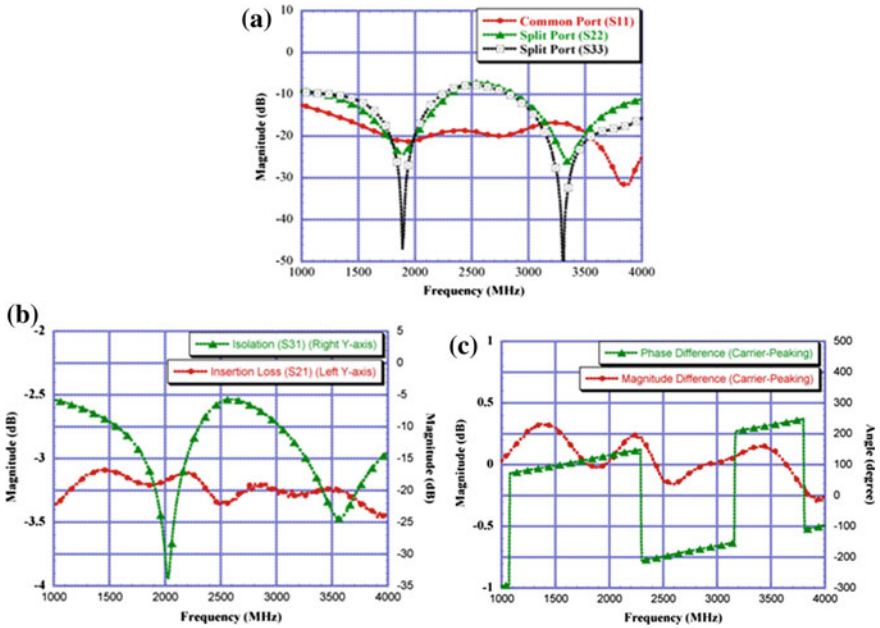


**Fig. 4.12** Results from a dual-band power divider with improved isolation: **a** reflection coefficients at different ports, **b** isolation between the ports and insertion loss in the path and **c** magnitude and phase difference between two paths [5]. Reprinted with permission from the IEEE

replacing each quarter-wave line by a dual-band stub-loaded structure, as discussed in Sect. 4.2.1.

Figure 4.13 shows the dual-band branch-line hybrid coupler topology and a photograph of a fabricated circuit. This circuit prototype is fabricated using RO5870 substrate with a dielectric constant of 2.33 and operates at the two frequencies of 850 and 2140 MHz.

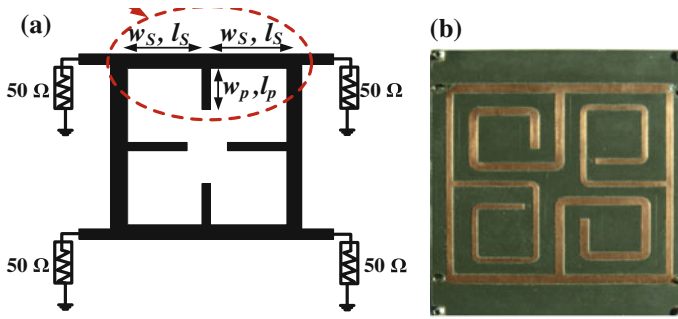
As shown in Fig. 4.13, each branch of characteristic impedances 35.35 and 50  $\Omega$  of the conventional branch-line hybrid coupler is replaced with the corresponding dual-band quarter-wave transformer realized by a T-type dual-band transformer.

Table 4.3 describes the physical design parameters of the dual-band branch-line coupler shown in Fig. 4.13b.

Figure 4.14 shows the measured and simulated results of the 850/2140 MHz dual-band branch-line coupler. The simulated result is represented as EM in parentheses representing electromagnetic simulation results obtained from momentum simulations in the advanced design system (ADS).

From Fig. 4.14, one can observe that the insertion loss was less than 3.8 dB over the band of 60 MHz, centered on the two selected frequencies of 850 and 2140 MHz. The return losses were greater than 15 dB at all ports over the bands. The isolation achieved between the two output ports was better than 15 dB over the bands. An alternative design methodology uses pi-type dual-band transformers to





**Fig. 4.13** A dual-band branch-line hybrid coupler designed using T-type transformers. Reprinted with permission from the John Wiley & Sons, Inc

**Table 4.3** Design parameters for an 850/2140 MHz dual-band branch-line coupler [10]

Branch impedance ( $\Omega$ )	Design parameters (mm)	Calculated	Optimized
35.35	Width of unloaded line ( $w_s$ )	3.25	3.3
	Length of unloaded line ( $l_s$ )	38.89	34.47
	Width of open stub ( $w_p$ )	2.73	2.74
	Length of open stub ( $l_p$ )	105.24	97.38
50	Width of unloaded line ( $w_s$ )	2.04	2.04
	Length of unloaded line ( $l_s$ )	35.42	34.34
	Width of open stub ( $w_p$ )	1.69	1.67
	Length of open stub ( $l_p$ )	106.94	99.05

replace each branch of the branch-line hybrid coupler. Figure 4.15 shows the topology and fabricated prototype of dual-band branch-line hybrid coupler designed using a pi-type dual-band transformer as described in Sect. 4.2.1.

The prototype is fabricated by means of microstrip technology using a substrate RT5870 with a height of 20 mil, dielectric constant of 2.33, and loss tangent of 0.0012. The two frequencies for this dual-band prototype are 1960 and 3500 MHz [5, 22]. Table 4.4 shows the electrical and physical design parameters for the 35.35 and 50  $\Omega$  branches of the dual-band branch-line coupler realized using an edge-loaded transmission line realized in microstrip technology.

Figure 4.16 shows the results of a dual-band branch-line hybrid designed to operate at 1960 and 3500 MHz.

From Fig. 4.16a, one can see that the return loss of 20 dB is achieved over the band of 80 MHz. This hybrid has an insertion loss of 3.41 dB and an isolation of 20 dB between the ports over the band of 80 MHz.

A similar approach has also been opted for the design of the rat-race coupler, where each quarter-wave-length branch is replaced by a dual-band T-type transformer as described in Sect. 4.2.1. Figure 4.17 shows the topology and fabricated prototype of the rat-race coupler using a center-tapped stub-loaded transmission line [10].

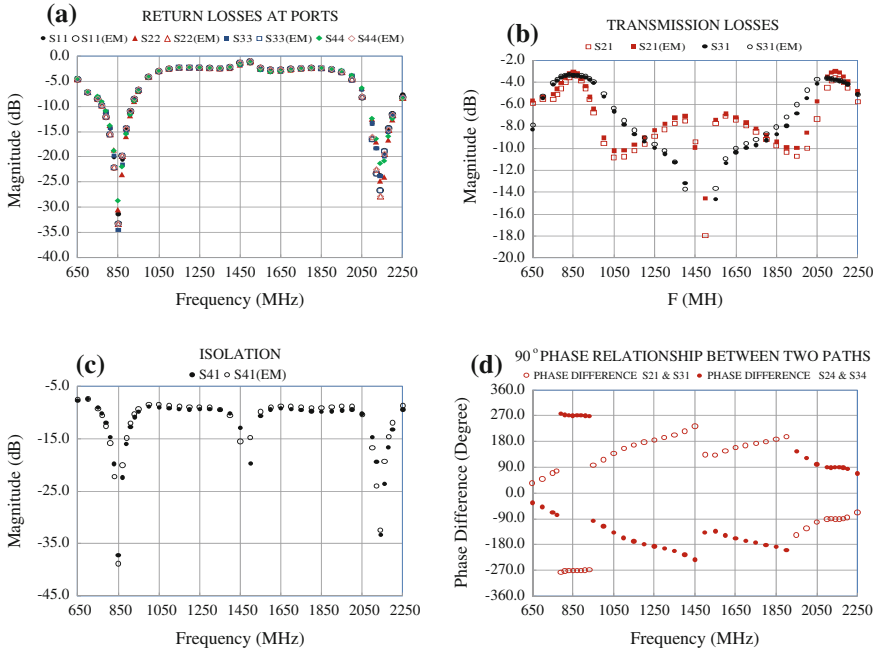


**Fig. 4.14** Measured and simulated results of the 850/2140 MHz dual-band branch-line coupler: **a** return losses at different ports, **b** transmission loss, **c** isolation between two output ports and **d** quadrature-phase relationship between two paths [10]. Reprinted with permission from the John Wiley & Sons, Inc

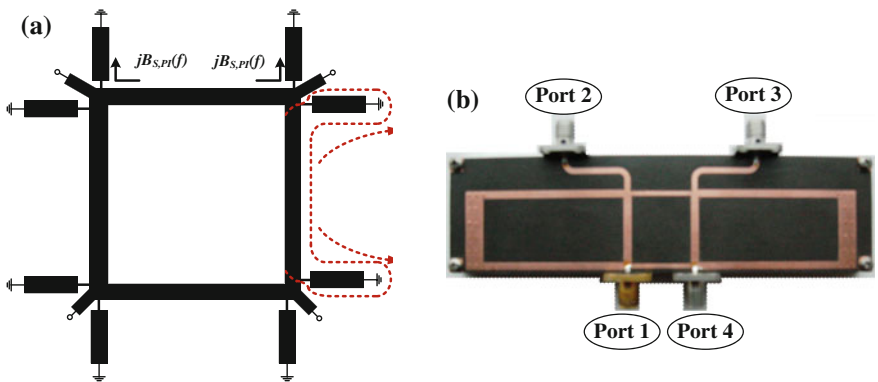


**Fig. 4.15** A dual-band branch-line hybrid coupler designed using an edge-loaded stub. Reprinted with permission from the IEEE

**Table 4.4** Electrical and physical design parameters for 35.35 and 50 Ω branches of a dual-band branch-line hybrid designed using a stub-loaded transmission line at the edges

Electrical design parameter	Electrical design parameter value		Physical design parameter (mm)	Physical design parameter value (mm)	
	35.35 Ω branch	50 Ω branch		35.35 Ω branch	50 Ω branch
$Z_{S,PI}$ (Ω)	38.7	55.3	$w_S$	2.13	1.25
$\theta_{S,PI}$ @ $f_1$	64.6°	64.6°	$l_S$	19.4	19.8
$Z_{P,PI}$ (Ω)	70.6	100.8	$w_P$	0.82	0.38
$\theta_{P,PI}$ @ $f_1$	129.2°	129.2°	$l_P$	40.05	40.93

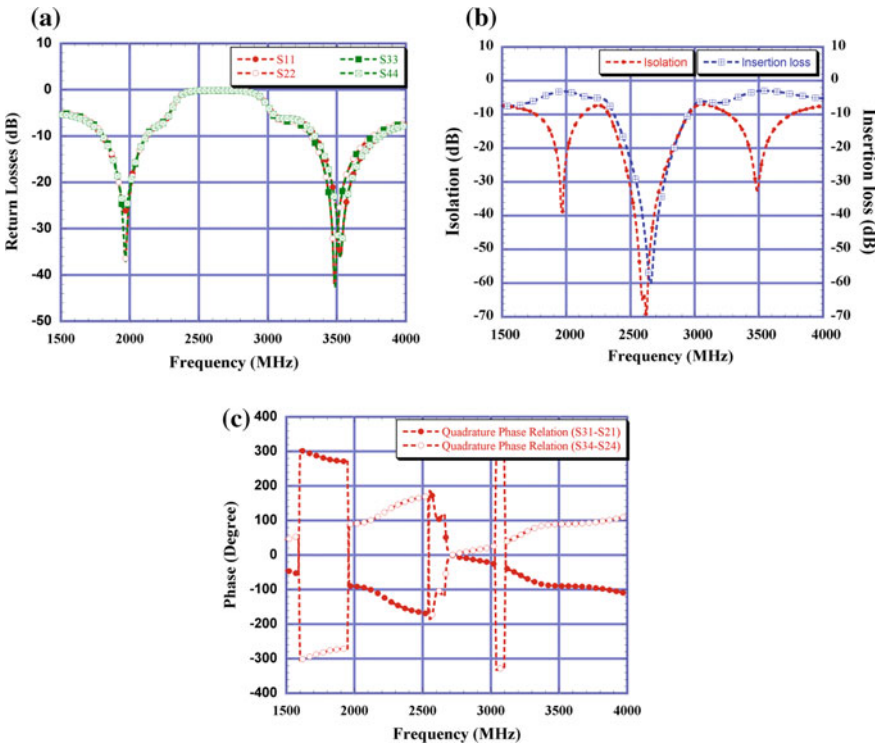


**Fig. 4.16** Measured results of the 1960/3500 MHz dual-band branch-line coupler in terms of **a** reflection, **b** transmission and isolation and **c** quadrature-phase relationship. Reprinted with permission from the John Wiley & Sons, Inc

The fabricated prototype is operating at 1960 and 3500 MHz, which is designed by means of microstrip technology using a substrate RT5870 with a height of 20 mil, dielectric constant of 2.33, and loss tangent of 0.0012.

The design parameters for this 1960/3500 MHz dual-band rat-race coupler are given in Table 4.5.

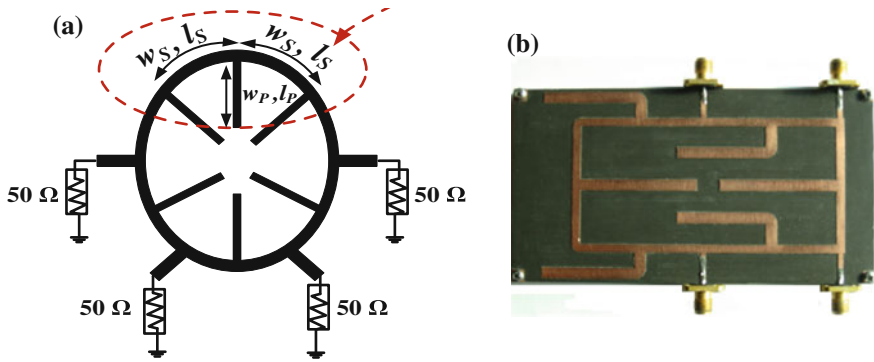


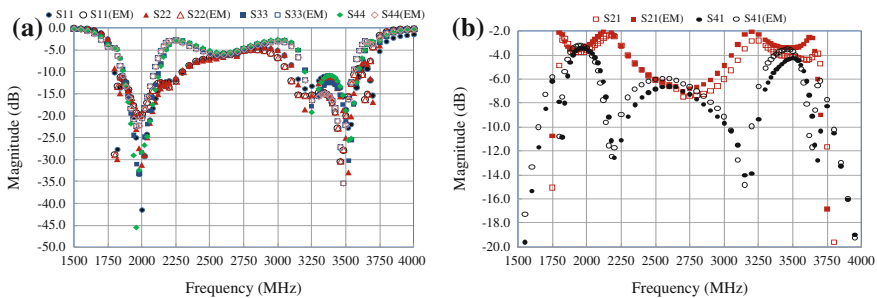
**Fig. 4.17** A dual-band rat-race coupler operating at 190 and 3500 MHz: **a** circuit topology and **b** photograph of fabricated prototype. Reprinted with permission from the John Wiley & Sons, Inc

**Table 4.5** Design parameters for 1960/3500 MHz dual-band rat-race coupler

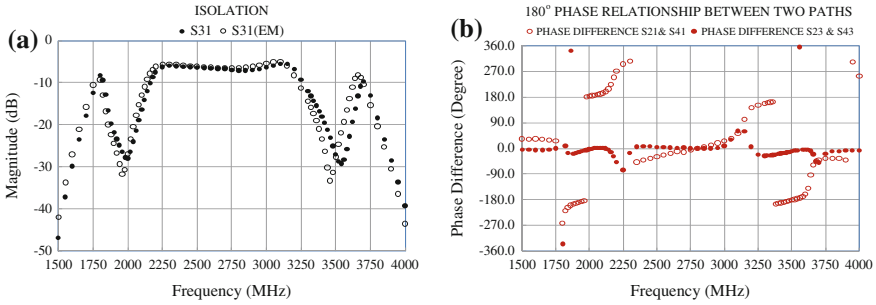
Branch impedance ( $\Omega$ )	Design parameters (mm)	Calculated	Optimized
70.7	Width of unloaded line ( $w_s$ )	2.62	2.5
	Length of unloaded line ( $l_s$ )	19.23	19.35
	Width of open stub ( $w_p$ )	3.79	3.45
	Length of open stub ( $l_p$ )	37.99	37.3

Figure 4.18 shows measured and EM-simulated return and transmission losses at each port of the rat-race coupler as shown in Fig. 4.17b. The insertion loss was less than 3.9 dB over the band of 80 MHz, centered on the two selected frequencies of 1960 and 3500 MHz. The return losses were greater than 16 dB at all ports, and the isolation achieved was better than 20 dB over these bands.

Figure 4.19 shows measured and EM-simulated results for isolation and the 180-degree phase relationship between two transmission paths. One can see from



**Fig. 4.18** Measured and simulated results of the dual-band rat-race coupler in terms of **a** reflection and **b** transmission



**Fig. 4.19** Measured and simulated results of the 1960/3500 MHz dual-band rat-race coupler in terms of **a** isolation between two output ports and **b** 180-degree phase relationship between two paths. Reprinted with permission from the John Wiley & Sons, Inc.

this figure that the isolation achieved was better than 20 dB over both bands of operation.

#### 4.4.3 Multiband Frequency-Dependent Power Dividers

Conventional dual-band hybrid [10, 23] designed using dispersive T- or pi-type structures are generally used for identical response at two frequencies of operation. However, for applications, where the power division requirement is different at different frequencies, such dual-band transformers can be customized to provide uneven power division ratios at two frequencies of operation [7].

Recalling the design methodology of a branch-line coupler for any arbitrary power division  $\alpha$ , the required value of characteristic impedances of a branch-line coupler is given as [24–26]:

$$Z_{T,A} = Z_0 \left( \frac{\alpha}{1 + \alpha} \right)^{0.5}, \quad (4.60a)$$

$$Z_{T,B} = Z_0 (\alpha)^{0.5}, \quad (4.60b)$$

where  $Z_{T,A}$  and  $Z_{T,B}$  are the characteristic impedances of the branches and  $\alpha$  is the respective power division ratio ( $P_A/P_B$ ) between port 2 and port 3 in Fig. 4.20a.

The branch-line hybrid shown in Fig. 4.20a operates at frequency  $f_0$ . In order to extend the operation of this branch-line hybrid at two frequencies  $f_1$  and  $f_2$  with the same power division  $\alpha$  at both the frequencies, a scheme similar to the one described in Sect. 4.3.2 can be used. However, if the circuit is required to operate as a branch-line coupler with two different power division ratios  $\alpha_1$  and  $\alpha_2$  at frequencies  $f_1$  and  $f_2$ , respectively, then the topology of such a hybrid coupler is shown in Fig. 4.20b. In such a topology, each branch of the branch-line hybrid coupler

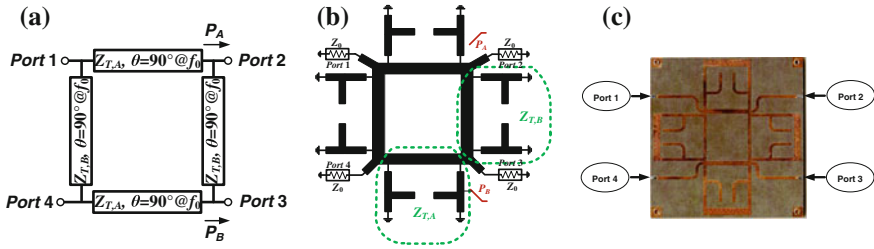


**Fig. 4.20** A branch-line hybrid coupler: **a** topology of single-band unequal and arbitrary power division, **b** topology of dual-band frequency-dependent power division and **c** photograph of dual-band frequency-dependent power division with equal and 3 dB unequal power division ratio at 1960 and 3500 MHz, respectively [27]. Reprinted with permission from the John Wiley & Sons, Inc.

must be replaced by a dual-band quarter-wave transformer with different characteristic impedances at two frequencies of operation, while maintaining quarter-wave electrical length at both the frequencies. As evident from Sect. 4.3.2, pi-type and T-type transformers have frequency-dependent characteristic impedance and electrical length. This frequency dependence can be shaped to achieve a dual-band quarter-wave transformer with different values of characteristic impedances at two frequencies of operation.

However, it has been described in [10–23] and Sects. 4.2.1 and 4.2.3 that in common practice, for a dual-band 90-degree transformer of the same impedance at two frequencies, a simultaneous solution must be sought for the design parameters of the loaded transmission lines and the susceptance values in order to ensure dual-band operation. In such cases, if these stub susceptances are realized by open- and short-circuit transmission lines, there is always a constraint over realizability of these stub susceptance values for a given design parameter of a loaded line [10]. This constraint is in terms of the widths and lengths of the open- and short-circuit transmission lines realizing the stub that can be fabricated with the given fabrication facility [10–23]. Moreover, this becomes more difficult if the 90-degree electrical length is desired along with two different characteristic impedances at two frequencies for applications such as multiband frequency-dependent power dividers.

To solve this problem, one can also utilize a pi- or T-type structure with a multisection stub loading the transmission line for realizing a quarter-wave transformer with two different characteristic impedance values at two different frequencies of operations. The multisection stub-loading technique exhibits greater flexibility and realizability compared with the single-section open and short stub-loading technique. The required values of stub susceptances are realized using multisection stubs, which, in theory, can realize any values of stub susceptances at the two frequencies provided that the frequencies are uncorrelated. Such a dual-band/dual-impedance quarter-wave transmission line is shown in Fig. 4.21a.

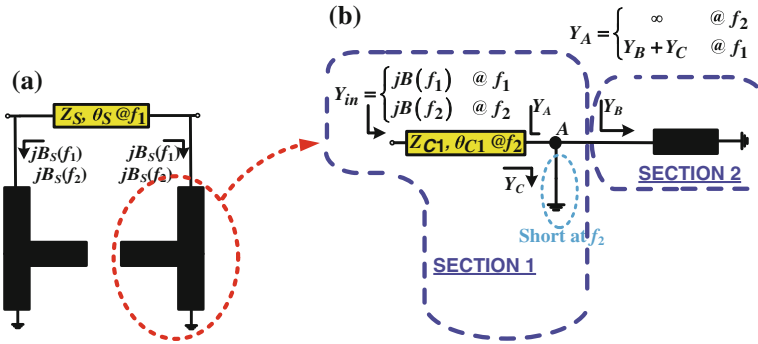


**Fig. 4.21** **a** Proposed schematic of dual-band/dual-impedance quarter-wave transmission line and **b** a multisubsection stub loading the transmission line in a dual-band pi-type structure

This dual-band/dual-impedance quarter-wave transmission line as shown in Fig. 4.21a replaces each branch of the branch-line coupler in Fig. 4.20a as shown in Fig. 4.20b.

The design methodology for such a transformer is divided into two parts. The first part is related to the design of a stub-loaded 2-port structure. In this part, the design parameters of the stub-loaded 2-port structure in Fig. 4.21a are retrieved by solving its corresponding ABCD matrix similar to a pi-type structure analysis. The second part deals with the realization of the stub values loading the transmission line using a multisubsection stub.

In general, using (4.34) and (4.35), the conditions for which a stub-loaded structure as shown in Fig. 4.21a behaves as a dual-band/dual-impedance quarter-wave transformer can be written as

$$Z_T(f) = \begin{cases} Z_S \sin(\theta_S) & @f_1 \\ Z_S \sin(n\theta_S) & @f_2 \end{cases}, \quad (4.61)$$

$$B_S(f) = \begin{cases} (Z_S \tan(\theta_S))^{-1} & @f_1 \\ (Z_S \tan(n\theta_S))^{-1} & @f_2 \end{cases}, \quad (4.62)$$

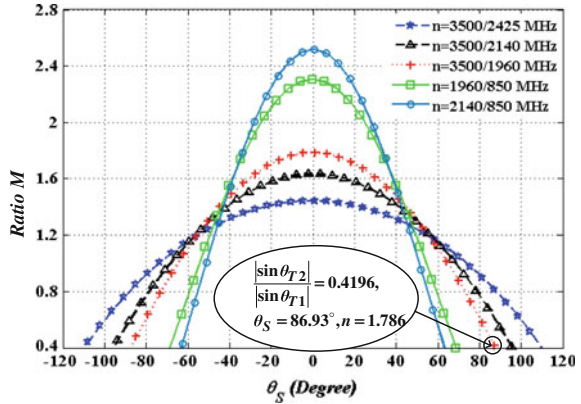
where  $n$  is the frequency ratio  $f_2/f_1$ .

If  $Z_T(f_1)$  and  $Z_T(f_2)$  are the two required characteristic impedances at two frequencies  $f_1$  and  $f_2$ , respectively, then their ratio,  $M$ , can be written as

$$M = \frac{Z_T(f_2)}{Z_T(f_1)} = \left| \frac{\sin(n\theta_S)}{\sin(\theta_S)} \right|. \quad (4.63)$$

Figure 4.20 shows the dependence of the ratio  $M$  over the values of  $\theta_S$  for different values of  $n$  corresponding to various wireless commercial standards [27]. It can be seen from Fig. 4.22 that the maximum value that can be achieved for the

**Fig. 4.22** The range of  $Z_{T1}$  and  $Z_{T2}$  obtained from the proposed methodology for different frequency ratios



ratio  $M$  in (4.63) is decided by the frequency ratio  $n$ . The physical length corresponding to the electrical length  $\theta_S$  is calculated at frequency  $f_1$ .

For given values of  $Z_T(f_1)$ ,  $Z_T(f_2)$ , and  $n$ , Fig. 4.20 can be used to obtain the electrical length  $\theta_S$  of the loaded line. Once the value of  $\theta_S$  is determined,  $Z_S$  can be calculated from (4.61), for a desired value of  $Z_T(f_1)$  or  $Z_T(f_2)$ , which are generally given as the design specification. The design parameter  $B_S$  at the two frequencies  $f_1$  and  $f_2$  is then calculated using (4.62), once  $Z_S$  and  $\theta_S$  are known.

The final step in the design is to realize  $B_S(f_1)$  and  $B_S(f_2)$  using the dual-band multisection stub in Fig. 4.21b.

In Fig. 4.21b, the design of a dual-band/dual-susceptance stub can be divided in two sections, as shown, where the first step is the realization of the required susceptance,  $B(f_2)$ , at the input, which is accomplished as in section 1 of Fig. 4.19b. Here,  $f_1$  is the lower frequency between  $f_1$  and  $f_2$ . Section 1 can be depicted as a transmission-line short circuit at one end at node A. This short circuit can be realized by a 90-degree open-circuit transmission line realized at  $f_2$ , and hence, section 1 can be realized as shown in Fig. 4.19b. Once section 1 is realized, section 2 is designed as an admittance that, when terminating section 1 at node A, emulates susceptance  $B(f_1)$  at the input of section 1. This terminating admittance is denoted as  $Y_B$  in Fig. 4.21b that can further be realized by either an open- or a short-circuit transmission line.

To design section 1 in Fig. 4.21b, if the designer chooses a certain realizable value of  $Z_{C1}$ , in order to achieve the desired input admittance values of  $jB(f_2)$ ,  $\theta_{C1}$  can be expressed as

$$\theta_{C1}(f_2) = \tan^{-1}\left(\frac{-1}{Z_{C1}B(f_2)}\right) \tag{4.64}$$

where  $B(f_2)$  can be positive or negative, depending on the required susceptance value. The value obtained for  $\theta_{C1}$  is considered at  $f_2$ , in order to calculate the physical length. Referring to Fig. 4.21b, once the short circuit at node A is realized



by an open-circuit transmission line of quarter-wavelength at frequency  $f_2$ , adding any further section beyond this point will not affect the input admittance at frequency  $f_2$ . Thus, the value of susceptance  $Y_B$  can be synthesized for frequency  $f_1$ , such that when it terminates section 1, the required susceptance  $jB(f_1)$  can be seen at the input of section 1. This requires synthesis of admittances  $Y_A(f_1)$ ,  $Y_B(f_1)$ , and  $Y_C(f_1)$ , as shown in Fig. 4.21b.  $Y_A(f_1)$  can be obtained by using a standard transmission-line input impedance equation as follows:

$$Y_A(f_1) = \frac{j}{Z_{C1}} \left[ \frac{Z_{C1}B(f_1) - \tan\left(\theta_{C1}(f_2)\frac{f_1}{f_2}\right)}{1 + Z_{C1}B(f_1)\tan\left(\theta_{C1}(f_2)\frac{f_1}{f_2}\right)} \right], \quad (4.65)$$

where  $B(f_1)$  can be positive or negative, depending on the imaginary value of the required complex impedance to be seen at the input of the matching network at frequency  $f_1$ . Since  $Y_A(f_1)$  can be expressed as a parallel combination of  $Y_B(f_1)$  and  $Y_C(f_1)$  at node A in Fig. 4.21b, the following relation holds:

$$Y_B(f_1) = Y_A(f_1) - \frac{j}{Z_{C,OC}} \tan\left(\frac{\pi f_1}{2f_2}\right) \quad (4.66)$$

where the second term on the right-hand side represents  $Y_C(f_1)$ , which is the admittance at the input of the 90-degree transformer in Fig. 4.21b at  $f_1$ .

This synthesized value of  $Y_B(f_1)$  can be realized by an open or short stub of characteristic impedance  $Z_{C2}$  and electrical length  $\theta_{C2}$ . If the designer chooses a certain realizable value for the characteristic impedance of  $Z_{C2}$  for this stub, its electrical length can be given by

$$\theta_{C2}(f_1) = \begin{cases} \tan^{-1}(Z_{C2}\text{imag}(Y_B(f_1))) & \text{stub realized with open-circuit transmission line} \\ \tan^{-1}\left(\frac{-1}{Z_{C2}\text{imag}(Y_B(f_1))}\right) & \text{stub realized with short-circuit transmission line} \end{cases} \quad (4.67)$$

The choice of using an open or short stub and  $Z_{C2}$  in (4.67) depends on the realizability of  $Y_B(f_1)$  with a minimum stub length. The imaginary value of  $Y_B(f_1)$  in (4.67) can be positive or negative, depending on the calculated results in (4.66).

It is worth mentioning that there is no limitation that section 1 of Fig. 4.21b should always be designed for  $f_2$ . Since the two frequencies are assumed to be uncorrelated, section 1 can also be designed for  $f_1$  rather than  $f_2$ , depending on the value of susceptance  $B(f)$  to be realized at a particular frequency. In such a case,  $f_1$  is replaced by  $f_2$  and vice versa in the design Eqs. (4.64)–(4.67). The choice of designing section 1 at  $f_1$  or  $f_2$  depends on the configuration resulting in the overall smaller size of the dual-band stub. This is further demonstrated in the design example, where the value of  $B(f_2)$  is much closer to the short circuit than that of  $B(f_1)$ ; therefore, section 1 is designed to realize  $B(f_2)$  and section 2 is designed to

realize  $B(f_1)$ , in order to achieve an overall smaller size of stub for both input and output matching circuits.

From the application perspective, an uneven branch-line hybrid has been designed to operate at 1960 and 3500 MHz for WCDMA and WiMAX applications. The hybrid provides equal power division in the first frequency, whereas a 3 dB unequal power division is targeted in the second frequency. The photograph of the prototype is shown in Fig. 4.20b.

As a design example, a dual-band branch-line hybrid coupler with an equal power division at  $f_1$  and a 3 dB unequal power division at  $f_2$  is designed and fabricated. For this power division requirement, the values of  $\alpha_1$  and  $\alpha_2$  are chosen as 1 and 0.5, respectively. The corresponding required values of  $Z_{T,A}(f_1)$  and  $Z_{T,A}(f_2)$  are calculated as 35.35 and 28.87  $\Omega$ , respectively, using (4.60a). Similarly, the values of  $Z_{T,B}(f_1)$  and  $Z_{T,B}(f_2)$  are obtained as 50 and 35.35  $\Omega$  using (4.60b).

Table 4.6 gives the design parameters for the dual-band/dual-impedance transformers used in the dual-band uneven branch-line hybrid of Fig. 4.20b.

The fabricated prototype has been measured using a calibrated vector network analyzer (VNA). Figure 4.23 shows EM-simulated and measured results of the return loss and isolation of the fabricated branch-line hybrid.

The measured return losses are higher than 10 dB over a band of 160 MHz symmetrical around 1960 MHz frequency. The corresponding isolation is around 15 dB over a band of 100 MHz symmetrical around 1960 MHz. Similarly, the measured return loss is better than 10 dB over a band 120 MHz symmetrical around 3500 MHz. The corresponding isolation is around 15 dB over a band of 100 MHz symmetrical around 3500 MHz. Because of some fabrication error, there is a slight frequency shift at both the center frequencies resulting in a slightly lower bandwidth symmetric around the two center frequencies of 1960 and 3500 MHz as shown in the zoomed segments of the graph in Fig. 4.23. Hence, if we ignore this symmetry about these center frequencies, the first and second bands have bandwidths of 200 MHz, where the return loss is around 10 dB. Similarly, the isolation

**Table 4.6** Design parameters for the dual-band/dual-impedance transformers

Electrical design parameters	Value		Physical design parameters	Value calculated (mm)		Value optimized (mm)	
	$Z_{T,A}$	$Z_{T,B}$		$Z_{T,A}$	$Z_{T,B}$	$Z_{T,A}$	$Z_{T,B}$
$Z_S$ ( $\Omega$ )	37.13	51.42	$w_S$	2.25	1.4	2.22	1.46
$\theta_S @f_1$ ( $^\circ$ )	72.21	76.51	$l_S$	21.63	23.29	19.18	19.48
$Z_{C1}$ ( $\Omega$ )	50	50	$w_{C1}$	1.47	1.47	1.47	1.47
$Z_{C,OC}$ ( $\Omega$ )	50	50	$w_{C,OC}$	1.47	1.47	1.47	1.47
$Z_{C2}$ ( $\Omega$ )	50	50	$w_{C2}$	1.47	1.47	1.47	1.47
$\theta_{C1}@f_2$ ( $^\circ$ )	42.56	44.15	$l_{C1}$	7.24	7.51	6.9	8.33
$\theta_{OC}@f_2$ ( $^\circ$ )	90	90	$l_{OC}$	15.32	15.32	15.2	15.2
$\theta_{C2}@f_1$ ( $^\circ$ )	39.41	35.27	$l_{C2}$	11.98	10.72	11.81	10.08

**Fig. 4.23** Measured and EM-simulated isolation and return loss of the fabricated branch-line hybrid. Reprinted with permission from the John Wiley & Sons, Inc.

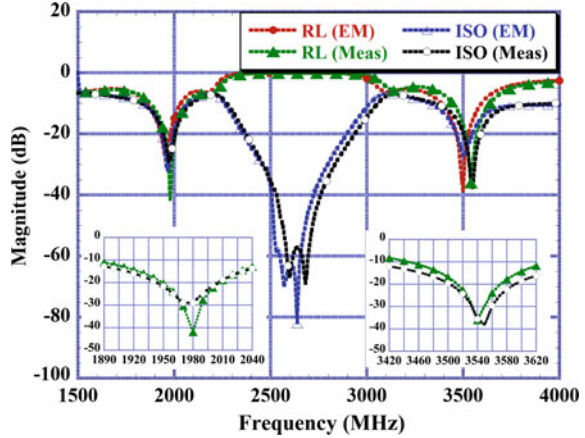
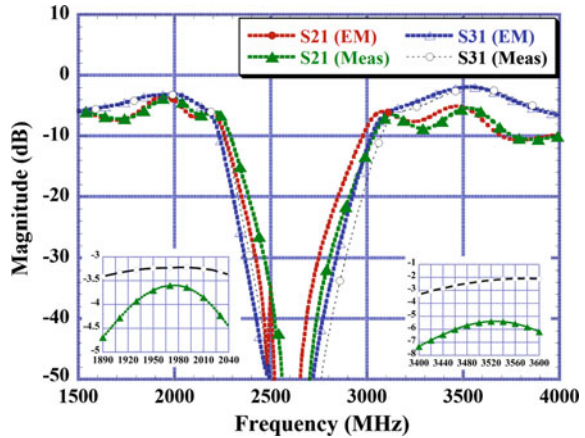


**Fig. 4.24** Measured and EM-simulated insertion loss of the fabricated branch-line hybrid. Reprinted with permission from the John Wiley & Sons, Inc.



is around 15 dB over a frequency range of 120 and 180 MHz at the first and second bands of operation, respectively.

Figure 4.24 shows the EM-simulated and measured results of insertion loss of the fabricated branch-line hybrid. The equal power division is maintained with an error of 1 dB over a frequency range of 120 MHz in the first band, and an unequal 3 dB power division is maintained with 1 dB error over a frequency range of 200 MHz in the second band. This has been demonstrated in a zoomed section of the measured results in Fig. 4.24.

Figure 4.25 shows measured results of the quadrature-phase relationship between split ports of the fabricated branch-line hybrid.

Again, a phase error of around 10° from the quadrature relation has been achieved over the frequency range of 150 and 200 MHz in the first and second bands, respectively, as shown in Fig. 4.25.

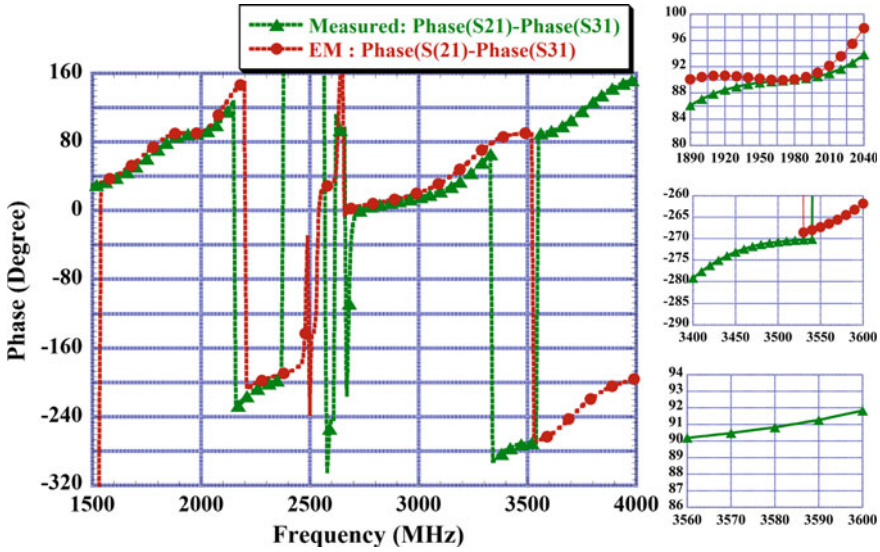


Fig. 4.25 Measured and simulated quadrature-phase performance of the fabricated hybrid. Reprinted with permission from the John Wiley & Sons, Inc.

### 4.5 Planar Slow-Wave Structures and Miniaturization

It can be identified from Figs. 4.5 and 4.6 and Eq. (4.36) that the realizable values of loaded line impedances  $Z_{S,T}$  or  $Z_{S,PI}$  sometimes exist for higher values of electrical lengths (denoted by values of  $p \neq 1$ ). From (4.39), a similar argument is equally valid for the characteristic impedance  $Z_{P,T}$  or  $Z_{P,PI}$  of the stubs that are loading the transmission line. Thus, for some frequency ratios, the circuit can only be realizable with longer lengths of transmission lines and therefore require miniaturization for use in practical applications.

Moreover, the Monzon transformer also utilizes two cascaded transmission lines, and this results in quite a long circuit that occupies a larger space on the board. Periodic loading of the transmission line is one of the easiest and conventional methodologies used for size reduction of the circuit structure [11]. Figure 4.26 shows the circuit topology and photograph of a miniaturized Monzon-based dual-band power divider using a periodic loaded slow-wave structure. The periodic loading of the transmission line results in slow-wave propagation, which has a lower phase velocity than the phase velocity of the substrate [11, 28]. Such periodic loaded lines can achieve higher electrical length with corresponding smaller physical length.

These lines are also referred to as artificial transmission lines that possess similar characteristics as normal transmission lines, such as linear relation of phase velocity

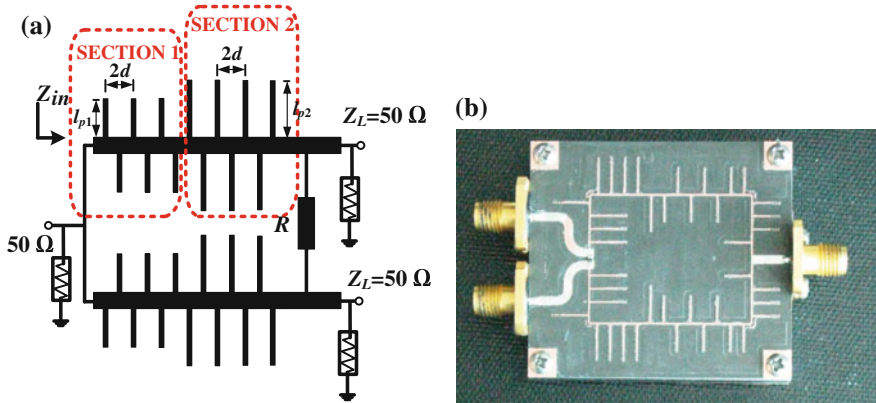


**Fig. 4.26** A design example of miniaturization of a dual-band power divider using periodic loaded slow-wave structure: **a** schematic and **b** photograph. Reprinted with permission from the IEEE

and frequency, and constant characteristic impedance with a nondispersive relationship up to a range of certain frequencies [11].

A simple transmission line section of characteristic impedance  $Z_c$  and phase velocity  $v_p$  is given as in [1, 28]:

$$Z_c = \sqrt{\frac{L}{C}}, \quad v_p = \frac{1}{\sqrt{LC}}, \quad (4.68)$$

where  $L$  and  $C$  are the inductance and capacitance per unit length of the line, respectively.

If we increase the capacitance per unit length in a physically smooth transmission line, it automatically decreases its inductance per unit length. However, if capacitances in the shunt are added at periodic intervals along the length, and the spacing between the added capacitors is small enough compared with the wavelength, it can be anticipated that the line will appear to be electrically smooth with the effective characteristic impedance and the phase velocity given as in [1], [28]:

$$Z_{c,\text{loaded}} = \sqrt{\frac{L}{C + \frac{C_p}{d}}}, \quad (4.69a)$$

$$v_{p,\text{loaded}} = \frac{1}{\sqrt{L(C + \frac{C_p}{d})}}, \quad (4.69b)$$

where  $C_p$  is the periodically loaded capacitance at  $d$  distance apart over the line.  $Z_{c,\text{loaded}}$  and  $Z_c$  are the characteristic impedances of the loaded and unloaded lines, respectively.

Clearly, the effect of periodic loading is the lowering of the effective characteristic impedance and phase velocity. A lowered phase velocity means that an effectively long electrical length can be realized with a shorter physical length. If  $v_{P, \text{loaded}}$  is the phase velocity of the periodically loaded line, then the electrical length,  $\Phi$ , of this line is given by

$$\Phi = l \left( \frac{2\pi f_0}{v_{P, \text{loaded}}} \right), \quad (4.70)$$

where  $l$  is the physical length of the loaded transmission line and  $f_0$  is the frequency of operation.

The phase velocities of the loaded line and the unloaded line can be related through their respective propagation constants  $\beta_0$  and  $k_0$ , and the two phase velocities can be related as

$$v_{P, \text{loaded}} = v_P \left( \frac{k_0}{\beta_0} \right) \quad (4.71)$$

where  $v_{P, \text{loaded}}$  and  $v_P$  are the respective phase velocities of the loaded and unloaded lines. Since both the phase velocity and characteristic impedance of the line are reduced with the periodic loading, it is important to establish a relation of the reduced phase velocity (or increased phase constant) in terms of the reduction in the characteristic impedances.

Equations (4.68)–(4.71) are used to derive this relation, which is given as

$$K = \frac{k_0}{\beta_0} = \frac{Z_{C, \text{loaded}}}{Z_C}. \quad (4.72)$$

For a periodic loaded line to behave as a slow-wave structure, it is necessary that the ratio given by (4.72) is less than one. For a given end value of impedance, it is required to start with a higher impedance unloaded line; consequently, the reduction factor depends on the impedance of this unloaded line. As the characteristic impedance of the unloaded line increases, the reduction factor  $K$  also increases. Using (4.68)–(4.71), the design parameters, such as the distance,  $d$ , of the periodic loading and the capacitance,  $C_P$ , can be expressed in terms of the reduction factor given in (4.72) and the total phase shift required by the loaded line, as in [11]

$$d = \frac{\Phi}{N} \left( \frac{Z_{C, \text{loaded}}}{Z_C} \right) \frac{v_P}{\omega_0}, \quad (4.73)$$

$$C_P = \frac{\Phi}{N\omega_0} \left( \frac{Z_C^2 - Z_{C, \text{loaded}}^2}{Z_C^2 Z_{C, \text{loaded}}^2} \right), \quad (4.74)$$

where  $N$  is the number of periodic sections loaded with the capacitance,  $C_p$ , to achieve the desired electrical length,  $\Phi$ , for the loaded transmission line.

If the capacitance calculated in (4.74) is realized using open-circuit stubs, the following formula can be used, as in [1, 28]:

$$C_p = \frac{1}{\omega_0 Z_{0,\text{stub}}} \tan(k_0 l_{\text{stub}}), \quad (4.75)$$

where  $Z_{0,\text{stub}}$  and  $l_{\text{stub}}$  are the characteristic impedance and physical length of the transmission line used as the stub, respectively.

For dual-band applications, the methodology proposed in Sects. 4.2.2 and 4.3.1 is used to calculate the initial design parameters (characteristic impedance and length) for each impedance transformer in a design of dual-band 2-way Wilkinson power divider. These two impedance transformers in each branch are then miniaturized individually, using (4.72)–(4.75). To achieve a high degree of miniaturization, we load a line of high characteristic impedance (of 120  $\Omega$ ) in each case. Since the required characteristic impedances are different for different impedance transformers as described in Table 4.2, the miniaturization achieved in terms of length of each transformer is different. The value of  $N$ , and hence,  $d$ , is chosen to avoid diffraction (nonlinear phase response with frequency) at the second band, and the corresponding stubs lengths are chosen accordingly, using (4.74) and (4.75).

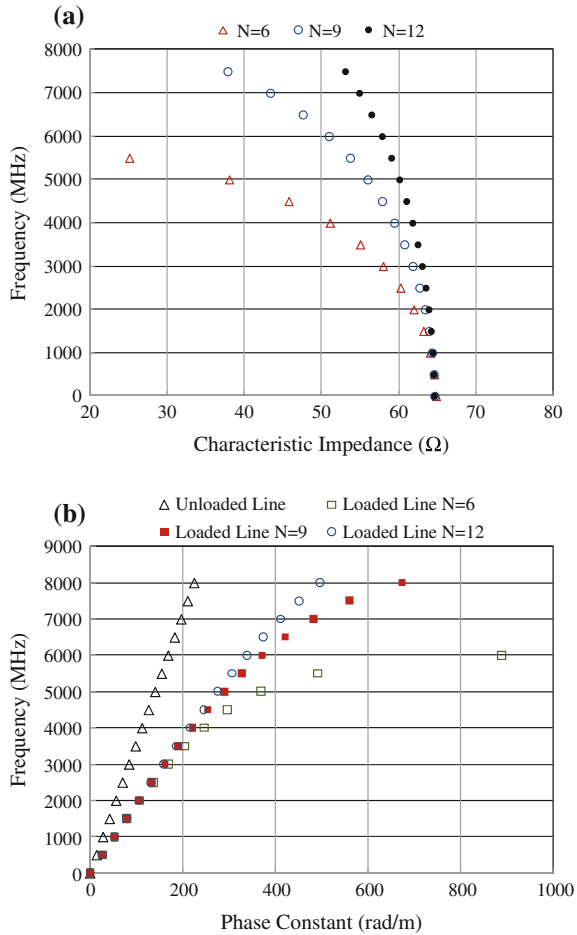
In this case, transmissions-line sections in the Monzon transformer are miniaturized individually by the same periodicity,  $d$ , as shown in Fig. 4.26a. Since the stub lengths,  $l_p$ , and the number of stubs,  $N$ , for different sections are different, sections 1 and 2 have different loaded impedances. The impedance of unloaded lines in Fig. 4.26a are kept at the highest possible value corresponding to the minimum width of the transmission line that can be realized by the given facility in fabrication.

In order to finalize the optimal values of the design parameters for the dual-band design case, it is important to consider the cut-off frequency of the periodic structure designed by stub-loading. Three possible phenomena can determine the first cut-off of the circuit: (1) the variation of impedance with frequency, (2) the periodicity of the structure, and (3) resonance of the open stub. The values of  $N$  (or  $d$ ) and  $C_p$  are, therefore, selected such that one can have the first cut-off far enough from the highest operating frequency. Thus, these effects should be considered while deciding the first cut-off frequency.

Figure 4.26 shows the variation of impedance with different values for  $N$  sections. Figure 4.27 depicts the dispersive characteristic of the periodic structure.

Figure 4.27a, b are plotted using the respective image impedance and effective propagation constant of a unit cell of the periodic structure. This unit cell is similar to the T-type structure given in Fig. 4.4a with an open-circuit transmission line used as the stub for loading. Hence, the effective propagation constant and image impedance of a unit cell in the periodic structure are given by (3.27) and (3.28), respectively. These curves belong to the miniaturized dual-band two-way

**Fig. 4.27** Frequency behavior of a periodic structure: **a** variation of characteristic impedance with frequency and **b** dispersive characteristic of periodic structure



Wilkinson power divider fabricated by means of microstrip technology using a substrate RT5870 with a height of 20 mil, dielectric constant of 2.33, and loss tangent of 0.0012. The design parameters are listed in Table 4.7. Table 4.8 shows the level of miniaturization achieved with this methodology.

The open stub starts presenting a short circuit to the propagation wave as its electrical length approaches 90 degrees with the change in frequency. Thus, as the physical length of the stub is chosen to be high, the corresponding cut-off frequency decreases, for a given phase velocity. This cut-off is given by

$$f_c = \frac{v_{p,stub}}{4l_{stub}}, \tag{4.76}$$

where  $v_{p,stub}$  is the phase velocity of the stub and  $l_{stub}$  is the physical length of the stub.



**Table 4.7** Summary of design parameters for miniaturization

Design parameters (mm)	Section 1		Section 2	
	Calculated	Optimized	Calculated	Optimized
Length of unit cell ( $d$ )	2.35	2.12	2.32	2.12
Width of unloaded line	0.25	0.25	0.25	0.25
No. sections	9	9	11	11
Width of open stubs	0.25	0.25	0.25	0.25
Length of open stubs	5.77	5	3.5	3.23

**Table 4.8** Summary of results in terms of miniaturization

Impedance transformer	Nonminiaturized design	Miniaturized design
Total length of both transformers (mm)	79.2	42.4
Percentage reduction in length (%)	–	46.46
Total circuit area (mm <sup>2</sup> )	65 × 42.31	46.83 × 42.31
Percentage reduction in circuit area (%)	–	27.95

All these three cut-offs should be considered when designing a periodic structure for miniaturization. This nondispersive range of frequency is useful for the miniaturization application since at these frequencies no without introducing higher order modes of the Bloch wave are introduced in the structure [28].

Figure 4.27 and (4.76) are used to choose the optimal values of design parameters  $N$ ,  $d$ , and  $C_p$  (hence, stub length) for the dual-band design case. It is worth mentioning that the number of periodic sections and length of stubs are different for each section of the Monzon transformer because each transformer of different characteristic impedance is miniaturized individually by loading the same value of the high impedance line.

Figures 4.28, 4.29, and 4.30 show some important measured and simulated results of the dual-band power divider based on the Monzon transformer. The

**Fig. 4.28** Simulated and measured results of a miniaturized dual-band power divider based on the Monzon transformer in terms of reflection at each port. Reprinted with permission from the IEEE

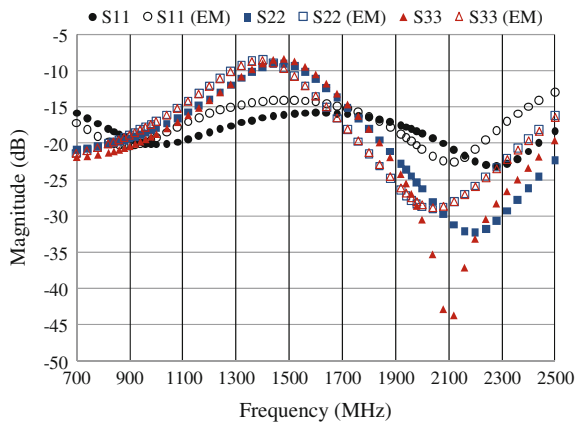


**Fig. 4.29** Simulated and measured results of a miniaturized dual-band power divider based on the Monzon transformer in terms of isolation. Reprinted with permission from the IEEE

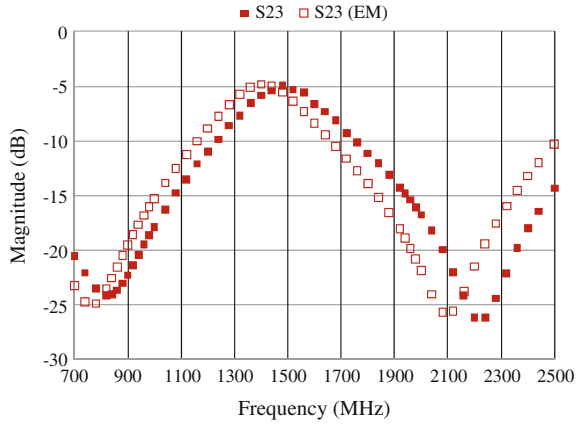
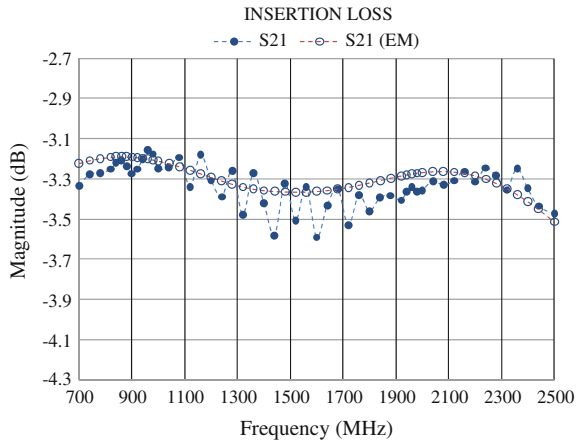


**Fig. 4.30** Simulated and measured responses of a miniaturized dual-band power divider based on the Monzon transformer in terms of transmission between direct ports. Reprinted with permission from the IEEE



insertion loss is less than 3.3 dB over the band of  $\pm 110$  MHz around the two selected frequencies of 850 and 1960 MHz. The return losses were greater than 15 dB at all the ports over the bands. The isolation achieved between the two output ports was better than 15 dB over the bands.

### 4.6 Multiband Filters

With the advent of the upcoming wireless communication requirements such as ultra-wideband, carrier aggregation, and the requirement for multiband RF filters is continuously emerging. In this scenario, multiple passbands or multiple notches are required in order to select multiple frequencies. An alternative strategy is to design reconfigurable/tunable filters that can be customized to operate over a wide range of

frequencies. This section describes the fundamentals of the RF filter design along with the multiband RF filters using the coupling matrix. The section also describes reconfigurable RF filters.

### 4.6.1 Fundamentals of RF Filter Design

Filters are one of the most important RF components that allow signals at a certain range of frequencies to pass while rejecting signals at unwanted frequencies. Based on the frequency response, the RF filters can be generically classified as lowpass, highpass, bandpass, and bandstop filters. However, more specifically, RF filters are classified on the basis of passband and stopband characteristics, e.g., Butterworth, Chebyshev, inverse Chebyshev and elliptic filters. The different choices of passband and stopband characteristics of RF filters depend on the required specifications, such as frequency range, bandwidth, insertion loss, attenuation characteristics, input and output impedances, group delay and transient response.

Two well-known methods to design RF filters are the image parameter method and the insertion loss method. The former is based on the image parameter theory as described in Sect. 4.1. This method does not include any specific passband or stopband characteristic in the design. However, the insertion loss method provides a more accurate solution with specific passband and stopband characteristics based on the type of filter characteristic opted for, such as Butterworth or Chebyshev. Therefore, for RF filter design, the insertion loss method is generally opted for.

In the insertion loss method, a power loss ratio is chosen as a function of frequency with characteristics such as Butterworth and Chebyshev. This can be done by selecting a proper lowpass prototype of lumped elements in the initial stage with the given passband specifications. This prototype is in the form of a ladder network with various series and shunt elements that have particular values depending on the selection of characteristics of Butterworth, Chebyshev, etc. Once a lowpass prototype has been selected, a frequency scaling is required to obtain other characteristics such as highpass, bandpass, and bandstop. Moreover, impedance scaling is also required according to the reference impedance. Finally, the lumped elements of the filters are converted into transmission-line sections, if required, using Richard's transformation and Kuroda's identities.

In the insertion loss method, the filter design is characterized by its insertion loss, obtained by power loss ratio,  $P_{LR}$ , given by [1–3]:

$$P_{LR} = \frac{P_S}{P_L} = \frac{1}{1 - |\Gamma(\omega)|^2}, \quad (4.77)$$

where  $P_S$  is the power available from the source,  $P_L$  is the power delivered to the load, and  $\Gamma(\omega)$  is the reflection coefficient at the load. Therefore, the insertion loss, I.L., is given by

$$I.L = 10 \log P_{LR}. \tag{4.78}$$

Based on specific passband and stopband behavior over frequency, the power loss ratio can be expressed in the form of different functions, resulting in different types of filter prototypes, as described in following section.

*Butterworth filter:* The Butterworth filter is also described as a maximally flat filter that has a flat passband response for given specifications. For a lowpass prototype with Butterworth filter characteristics,  $P_{LR}$  is given by [1–3]:

$$P_{LR} = 1 + p^2 \left( \frac{\omega}{\omega_c} \right)^{2N}, \tag{4.79}$$

where  $\omega_c$  is the cut-off frequency of the filter and  $N$  is the order of the filter. The frequency range of this lowpass filter is from 0 to  $\omega_c$ . For frequencies greater than  $\omega_c$ , the attenuation of the filter increases with the frequency. The term  $p = 1$  corresponds to 3 dB insertion loss at the cut-off frequency,  $\omega_c$ . As the order of the filter,  $N$ , increases, the selectivity of the filter increases, and the Butterworth response looks similar to the plot given in Fig. 4.31.

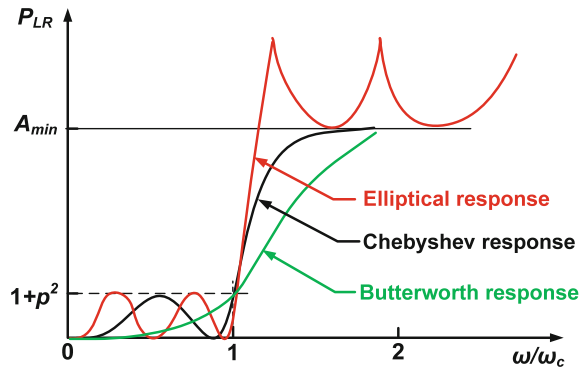
For  $\omega \gg \omega_c$ , the unity term in (4.79) can be neglected and, therefore, one can see that the insertion loss increases at the rate of  $20 N$  dB/decade.

*Chebyshev filter:* The Chebyshev filter response is used where higher roll-off rate of attenuation characteristics are required at the cost of passband loss. The frequency response of the Chebyshev filter is expressed as [1–3]:

$$P_{LR} = 1 + p^2 T_N^2 \left( \frac{\omega}{\omega_c} \right), \tag{4.80}$$

where  $T_N(x)$  is the Chebyshev polynomial, which oscillates between  $\pm 1$  for  $|x| \leq 1$ , creating ripples of amplitude  $1 + p^2$  on the passband response. For a large  $x$ ,  $T_N(x) \sim (1/2)(2x)^N$ . This corresponds to  $\omega \gg \omega_c$ , where,  $P_{LR}$  can be expressed as [1–3]

**Fig. 4.31** Filter responses: Butterworth, Chebyshev and elliptical [1]



$$P_{LR} \approx \frac{p^2}{4} \left( \frac{2\omega}{\omega_c} \right)^{2N}. \tag{4.81}$$

Again, from (4.81), the insertion loss of the Chebyshev filter increases at the rate of  $20 N$  dB/decade as the frequency is far greater than  $\omega_c$ . The insertion loss of the Chebyshev filter is  $(2^{2N})/4$  times greater than that of the Butterworth filter for  $\omega \gg \omega_c$ . Figure 4.31 also shows the Chebyshev response. The magnitude of ripples changes between 1 and  $1 + p^2$  for frequencies less than  $\omega_c$ . The constant term  $p$  decides the amplitude of the ripple on the passband response. It is interesting to note that for a given order of a filter,  $N$ , the Chebyshev filter will have a sharper cut-off compared with the Butterworth filter. Therefore, the applications where higher attenuation is required, Chebyshev filters are preferred at the cost of passband ripple. Butterworth filters have lesser delay distortion, and, therefore, to use them for higher attenuation at stopband, the order of the filter,  $N$ , has to be increased.

*Elliptic function:* This filter characteristic is used where greater selectivity than the Chebyshev function is required. This greater selectivity comes at the expense of ripples present in both passband and stopband as shown in Fig. 4.31. The details of the design in which elliptical filters are used can be found in [29].

### 4.6.2 Lowpass Prototype Design

The lowpass prototype is designed according to the given specification for the normalized frequency and normalized impedances. These standard lowpass prototypes can be used to implement filters with different frequency responses with the help of scaling and frequency transformation. Figure 4.32 shows the topology of a lowpass prototype. The number of reactive elements present in the circuit represents

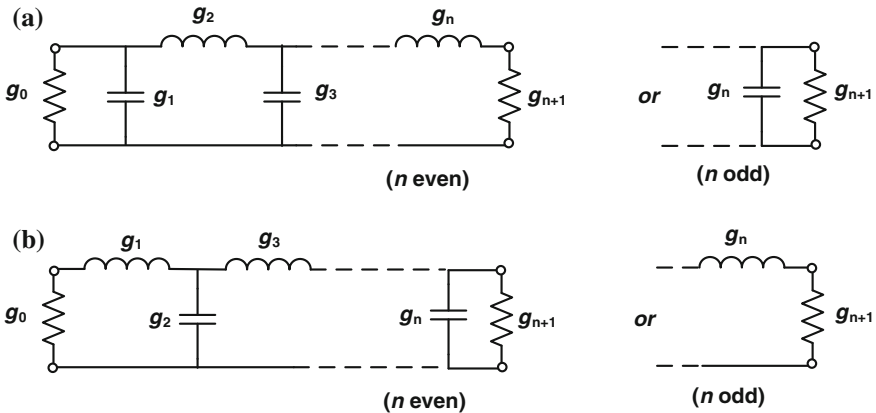


Fig. 4.32 Lowpass prototype of a filter [2]: **a** capacitive load, **b** inductive load

the order of a filter,  $N$ . In Fig. 4.32,  $g_0$  represents the source impedance and  $g_{N+1}$  denotes the load resistance. The elements  $g_1$  to  $g_N$  are the reactive elements of the circuit such that it behaves like a lowpass filter at normalized cut-off frequency  $\omega/\omega_c = 1$ . Following sections will present a set of equations and tables to design a lowpass prototype with the most common filter characteristics, i.e., Butterworth or Chebyshev.

#### 4.6.2.1 Butterworth Filter Response

For the Butterworth response of a filter with normalized cut-off frequency  $\omega/\omega_c = 1$  and insertion loss of 3.01 dB at  $\omega = \omega_c$ , the element values of a lowpass prototype are given by [1–3, 28]:

$$g_0 = 1, \quad (4.82a)$$

$$g_i = 2 \sin\left(\frac{(2i-1)\pi}{2N}\right) \quad \text{for } 1 \leq i \leq N, \quad (4.82b)$$

$$g_{N+1} = 1. \quad (4.82c)$$

The order of the filter is decided according to the specified minimum amount of attenuation needed at stopband frequency. This can be obtained by

$$N \geq \frac{\log(10^{0.1L_{AS}} - 1)}{2 \log(\omega/\omega_c)} \quad (4.83)$$

where  $L_{AS}$  is the minimum stopband attenuation at frequency  $\omega$ . Table 4.9 gives the element values for  $N = 1$ –10.

#### 4.6.2.2 Chebyshev Filter Response

The order for the Chebyshev filter based on the minimum amount of attenuation needed at stopband frequency can be calculated as

$$N \geq \frac{\cosh^{-1} \sqrt{\frac{10^{0.1L_{AS}} - 1}{10^{0.1L_{Ar}} - 1}}}{\cosh^{-1}(\omega/\omega_c)}, \quad (4.84)$$

where  $L_{AS}$  is the minimum stopband attenuation at frequency  $\omega$  and  $L_{Ar}$  is passband ripple. The element values are then calculated as

**Table 4.9** Prototype element values for a lowpass filter prototype with Butterworth characteristics ( $g_0 = 1$ ,  $\omega_c = 1$ ,  $N = 1-10$ ) [1, 4]

$N$	$g_1$	$g_2$	$g_3$	$g_4$	$g_5$	$g_6$	$g_7$	$g_8$	$g_9$	$g_{10}$	$g_{11}$
1	2.0000	1.0000									
2	1.4142	1.4142	1.0000								
3	1.0000	2.0000	1.0000	1.0000							
4	0.7654	1.8478	1.8478	0.7654	1.0000						
5	0.6180	1.6180	2.0000	1.6180	0.6180	1.0000					
6	0.5176	1.4142	1.9318	1.9318	1.4142	0.5176	1.0000				
7	0.4450	1.2470	1.8019	2.0000	1.8019	1.2470	0.4450	1.0000			
8	0.3902	1.1111	1.6629	1.9615	1.9615	1.6629	1.1111	0.3902	1.0000		
9	0.3473	1.0000	1.5321	1.8794	2.0000	1.8794	1.5321	1.0000	0.3473	1.0000	
10	0.3129	0.9080	1.4142	1.7820	1.9754	1.9754	1.7820	1.4142	0.9080	0.3129	1.0000

$$g_1 = \frac{2a_1}{\gamma}, \quad (4.85a)$$

$$g_i = \frac{4a_{i-1}a_i}{b_{i-1}g_{i-1}} \quad \text{for } 1 \leq i \leq N, \quad (4.85b)$$

$$g_{N+1} = \begin{cases} 1 & \text{for } N \text{ odd} \\ \coth^2\left(\frac{\beta}{4}\right) & \text{for } N \text{ even} \end{cases}, \quad (4.85c)$$

where the intermediate parameters  $a_i$ ,  $b_i$ ,  $\beta$ , and  $\gamma$  can be calculated as

$$\beta = \ln\left(\coth\frac{L_{Ar}}{17.37}\right). \quad (4.86a)$$

$$\gamma = \sinh\left(\frac{\beta}{2N}\right). \quad (4.86b)$$

$$a_i = \sin\left[\frac{(2i-1)\pi}{2N}\right] \quad \text{for } 1 \leq i \leq N. \quad (4.86c)$$

$$b_i = \gamma^2 + \sin^2\left(\frac{i\pi}{N}\right) \quad \text{for } 1 \leq i \leq N. \quad (4.86d)$$

Tables 4.10 and 4.11 show element values for normalized lowpass filter prototypes with Chebyshev characteristics. The element values calculated for Chebyshev characteristics with 0.5 dB ripple for different order values from  $N = 1-10$  are listed in Table 4.10. Similarly, Table 4.11 lists the element values for Chebyshev characteristics with 3.0 dB ripple for order values from  $N = 1-10$ . One can note that the load impedance is  $g_{N+1} \neq 1$  for even values of order.

### 4.6.3 Filter Design from Lowpass Prototype (Scaling and Frequency Transformation)

The lowpass prototype values calculated in the Sect. 4.6.2 is for cut-off frequency  $\omega_c = 1$  rad/s and source impedance of  $R_S = 1 \Omega$ . In order to realize filters with standard terminations and particular frequency-selective characteristics (highpass, bandpass, etc.), these element values should be scaled and transformed in terms of impedances and frequency.



**Table 4.10** Prototype element values for lowpass filter prototype with Chebyshev characteristics ( $g_0 = 1$ ,  $\omega_c = 1$ ,  $N = 1-10$ , 0.5 dB ripple) [1, 4].

$N$	$g_1$	$g_2$	$g_3$	$g_4$	$g_5$	$g_6$	$g_7$	$g_8$	$g_9$	$g_{10}$	$g_{11}$
1	0.6986	1.0000									
2	1.4029	0.7071	1.9841								
3	1.5963	1.0967	1.5963	1.0000							
4	1.6703	1.1926	2.3661	0.8419	1.9841						
5	1.7058	1.2296	2.5408	1.2296	1.7058	1.0000					
6	1.7254	1.2479	2.6064	1.3137	2.4758	0.8696	1.9841				
7	1.7372	1.2583	2.6381	1.3444	2.6381	1.2583	1.7372	1.0000			
8	1.7451	1.2647	2.6564	1.3590	2.6964	1.3389	2.5093	0.8796	1.9841		
9	1.7504	1.2690	2.6678	1.3673	2.7239	1.3673	2.6678	1.2690	1.7504	1.0000	
10	1.7543	1.2721	2.6754	1.3725	2.7392	1.3806	2.7231	1.3485	2.5239	0.8842	1.9841

**Table 4.11** Prototype element values for lowpass filter prototype with Chebyshev characteristics ( $g_0 = 1$ ,  $\omega_c = 1$ ,  $N = 1-10$ , 3 dB ripple) [1, 4]

$N$	$g_1$	$g_2$	$g_3$	$g_4$	$g_5$	$g_6$	$g_7$	$g_8$	$g_9$	$g_{10}$	$g_{11}$
1	1.9953	1.0000									
2	3.1013	0.5339	5.8095								
3	3.3487	0.7117	0.3487	1.0000							
4	3.4389	0.7483	4.3471	0.5920	5.8095						
5	3.4817	0.7618	4.5381	0.7618	3.4817	1.0000					
6	3.5045	0.7685	4.6061	0.7929	4.4641	0.6033	5.8095				
7	3.5182	0.7723	4.6386	0.8039	4.6386	0.7723	3.5182	1.0000			
8	3.5277	0.7745	4.6575	0.8089	4.6990	0.8018	4.4990	0.6073	5.8095		
9	3.5340	0.7760	4.6692	0.8118	4.7272	0.8118	4.6692	0.7760	3.5340	1.0000	
10	3.5384	0.7771	4.6768	0.8136	4.7425	0.8164	4.7260	0.8051	4.5142	0.6091	5.8095

### 4.6.3.1 Impedance Transformation

Depending on reference impedance  $R_0$ , the element values of the selected lowpass prototype is multiplied by source resistance  $R_0$ . This scaling can be done using the following expressions [1–3, 28]:

$$L' = R_0 L, \quad (4.87a)$$

$$C' = \frac{C}{R_0}, \quad (4.87b)$$

$$R'_S = R_0, \quad (4.87c)$$

$$R'_L = R_0 R_L, \quad (4.87d)$$

where  $L$ ,  $C$ , and  $R_L$  are calculated from one of the lowpass prototype element values as selected from Tables 4.9, 4.10, and 4.11.

### 4.6.3.2 Frequency Transformation

The element values of lowpass prototype filter as described in Tables 4.9, 4.10, and 4.11 should be scaled in order to design a filter with the cut-off frequency of  $\omega_c$  rad/s and an appropriate frequency transformation is required to change the filter characteristics to the one required (highpass, bandpass, or bandstop etc.).

**Frequency scaling for lowpass filters:** The normalized frequency in series reactance and shunt susceptance is replaced by new element values with equivalent cut-off frequency  $\omega_c$ . This transformation is shown in Fig. 4.33a. The new element values are as follows:

$$L'_k = \frac{L_k}{\omega_c}. \quad (4.88a)$$

$$C'_k = \frac{C_k}{\omega_c}. \quad (4.88b)$$

The element values obtained after both impedance and frequency scaling are

$$L'_k = \frac{R_0 L_k}{\omega_c}. \quad (4.89a)$$

$$C'_k = \frac{C_k}{R_0 \omega_c}. \quad (4.89b)$$

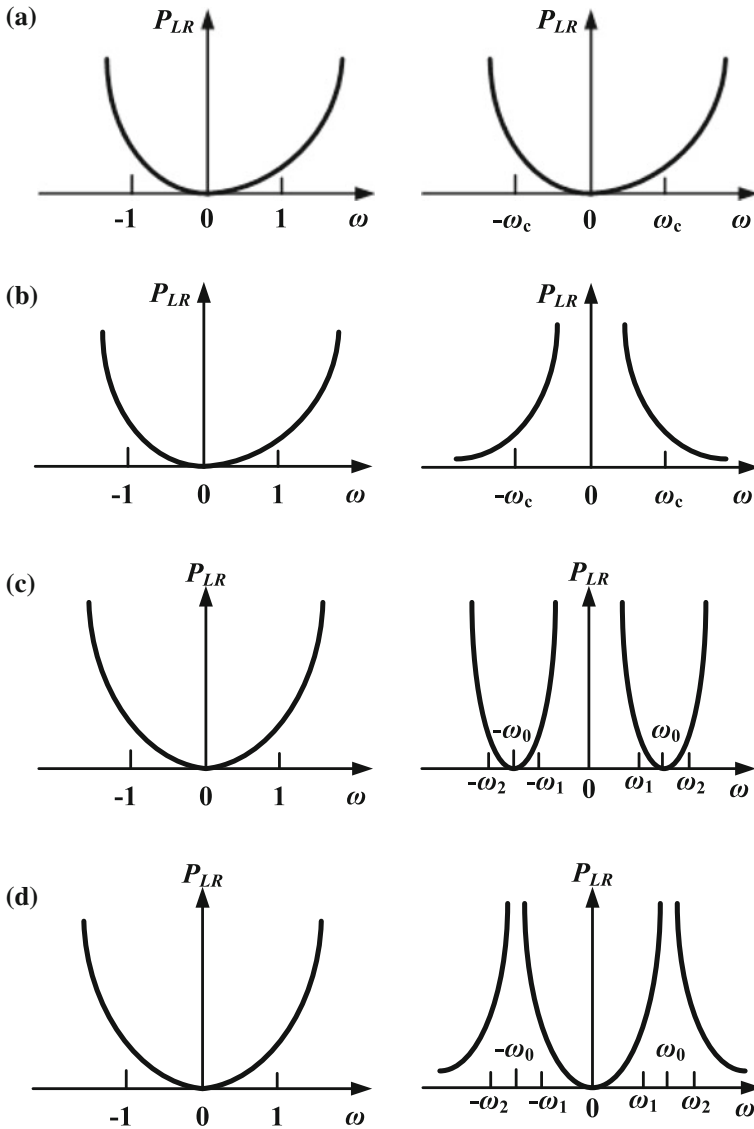


**Fig. 4.33** Frequency transformation from lowpass prototype of cut-off frequency 1 rad/s to **a** lowpass response with cut-off frequency  $\omega_c$ , **b** high-pass response, **c** bandpass response and **d** bandstop response

**Lowpass to highpass transformation:** This transformation needs frequency scaling as shown in Fig. 4.33b. When this transformation is applied to series reactance  $X_k$  and shunt susceptance  $B_k$  of the lowpass prototype elements as shown in Fig. 4.32, one can obtain the following expressions [1–3, 28]:

$$jX_k = -j \frac{\omega_c}{\omega} L_k = \frac{1}{j\omega C'_k}. \quad (4.90a)$$

$$jB_k = -j \frac{\omega_c}{\omega} C_k = \frac{1}{j\omega L'_k}. \quad (4.90b)$$

One can observe that the negative sign in the above scaling converts inductors to capacitors and vice versa. According to (4.90a) and (4.90b), the new component values obtained after frequency scaling are

$$L'_k = \frac{1}{\omega_c C_k}. \quad (4.91a)$$

$$C'_k = \frac{1}{\omega_c L_k}. \quad (4.91b)$$

After applying impedance scaling on (4.91a) and (4.91b), the final element values for highpass filter design are obtained as

$$L'_k = \frac{R_0}{\omega_c C_k}, \quad (4.92a)$$

$$C'_k = \frac{1}{R_0 \omega_c L_k}, \quad (4.92b)$$

where  $C_k$  and  $L_k$  are the elements of the lowpass prototype as obtained from Tables 4.9, 4.10, and 4.11.

**Lowpass to bandpass transformation:** The bandpass transformation requires a frequency variable in the lowpass prototype to be transformed as follows:

$$\omega \rightarrow \frac{1}{\delta} \left( \frac{\omega}{\omega_0} - \frac{\omega_0}{\omega} \right), \quad (4.93)$$

where

$$\delta = \frac{\omega_2 - \omega_1}{\omega_0}; \quad \omega_0 = \sqrt{\omega_1 \omega_2}. \quad (4.94)$$

The term  $\delta$  is the fractional bandwidth with  $\omega_1$  and  $\omega_2$  as the band-edge frequencies and  $\omega_0$  as the center frequency, which can be expressed as the geometric mean of  $\omega_1$  and  $\omega_2$ . This transformation is also represented in Fig. 4.33c. When this transformation is applied to series reactance  $X_k$  of the lowpass prototype elements as shown in Fig. 4.32, one can obtain the following expressions [1–3, 28]:

$$jX_k = j \frac{1}{\delta} \left( \frac{\omega}{\omega_0} - \frac{\omega_0}{\omega} \right) L_k = j \frac{\omega L_k}{\delta \omega_0} - j \frac{\omega_0 L_k}{\delta \omega} = j\omega L'_k - j \frac{1}{\omega C'_k}. \tag{4.95}$$

The above transformation shows that the series inductor in the lowpass prototype element as shown in Fig. 4.34 is converted to a series LC circuit with the following element values:

$$L'_k = \frac{L_k}{\delta \omega_0}. \tag{4.96a}$$

$$C'_k = \frac{\delta}{\omega_0 L_k}. \tag{4.96b}$$

Similarly, when the transformation as expressed in (4.93) is applied to shunt susceptance  $B_k$  of the lowpass prototype elements as shown in Fig. 4.32, one can obtain the following expressions:

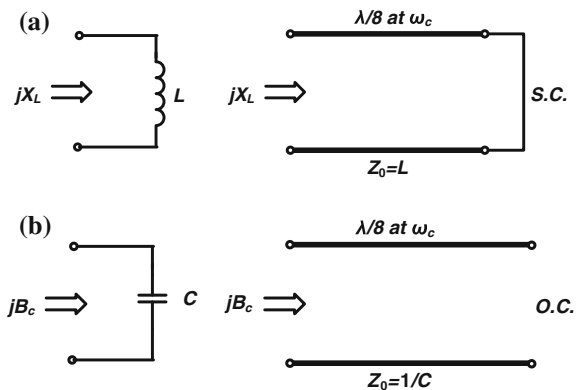
$$jB_k = j \frac{1}{\delta} \left( \frac{\omega}{\omega_0} - \frac{\omega_0}{\omega} \right) C_k = j \frac{\omega C_k}{\delta \omega_0} - j \frac{\omega_0 C_k}{\delta \omega} = j\omega C'_k - j \frac{1}{\omega L'_k} \tag{4.97}$$

The above transformation shows that the shunt capacitor in the lowpass prototype element as shown in Fig. 4.32 is converted to a shunt LC circuit with the following element values:

$$L'_k = \frac{\delta}{\omega_0 C_k}. \tag{4.98a}$$

$$C'_k = \frac{C_k}{\delta \omega_0}. \tag{4.98b}$$

**Fig. 4.34** Transformation of lumped to distributed component using Richard's transformation [1]



The impedance scaling as discussed in Sect. 4.6.3.1 can be applied to the values of (4.96a), (4.96b) and (4.98a), (4.98b) to obtain the final element values of a lumped-element bandpass filter.

**Lowpass to bandstop transformation:** The bandstop transformation requires a frequency transformation inverse of that used in bandpass. Therefore, in order to obtain bandstop transformation, the frequency variable in the lowpass prototype is transformed as follows:

$$\omega \rightarrow -\delta \left( \frac{\omega}{\omega_0} - \frac{\omega_0}{\omega} \right), \quad (4.99)$$

where the term  $\delta$  is the fractional bandwidth with  $\omega_1$  and  $\omega_2$  as the banded frequencies and  $\omega_0$  as the center frequency, which can be expressed as the geometric mean of  $\omega_1$  and  $\omega_2$  as described in (4.94). This transformation is also represented in Fig. 4.33d. When this transformation is applied to the lowpass prototype, the series inductor of the lowpass prototype is converted into shunt  $LC$  circuits whose component values are given by

$$L'_k = \frac{\delta L_k}{\omega_0}. \quad (4.100a)$$

$$C'_k = \frac{1}{\delta \omega_0 L_k}. \quad (4.100b)$$

The shunt capacitor of the lowpass prototype is converted into a series  $LC$  circuit whose component values are given by

$$L'_k = \frac{1}{\Delta \omega_0 C_k}. \quad (4.101a)$$

$$C'_k = \frac{\Delta C_k}{\omega_0}. \quad (4.101b)$$

The impedance scaling as discussed in Sect. 4.6.3.1 can be applied to the values of (4.100a), (4.100b), and (4.110) to obtain the final element values of a lumped-element bandpass filter.

#### 4.6.4 Distributed-Element Filter Realization

The filters as designed in Sect. 4.6.3 are made of lumped elements. These lumped elements, such as capacitors, are limited to a certain frequency range based on their self-resonance frequency (SRF). Therefore, distributed elements are used to realize these component values when intended for high-frequency operation. The following

section describes the transformation of the lumped component into distributed elements for filter design.

#### 4.6.4.1 Richard's Transformation

Richard's transformation is used to realize the lumped elements with open- and short-circuited transmission-line stubs. This transforms the frequency  $\omega$  plane to the  $\Omega$  plane using the following relation [1–3, 28]:

$$\Omega = \tan \beta l = \tan \left( \frac{\omega l}{v_p} \right) \quad (4.102)$$

where  $l$  is the length of the transmission line and  $v_p$  is the phase velocity of the wave traveling in the transmission line. Here, phase velocity is independent of frequency, and length is dependent on frequency. The transformation from  $\omega$  to  $\Omega$  using (4.102) results in repetition of the response with the period of  $\omega l/v_p = 2\pi$ .

The inductor  $L$  in the lumped-element circuit with impedance  $j\omega L$  can be replaced by a short-circuited transmission line with characteristic impedance  $Z_0$  of value  $L$  and electrical length of value  $\beta l$ . The corresponding input impedance of this short-circuit stub is  $jZ_0 \tan(\beta l)$ . Similarly, the susceptance of a capacitor  $j\omega C$  is represented by an open-circuit transmission line with characteristic impedance  $Z_0$  of value  $1/C$  and electrical length of value  $\beta l$ . The input admittance of this open-circuit stub is  $j(1/Z_0) \tan(\beta l)$  as shown in Fig. 4.34.

If  $L$  and  $C$  are obtained for a lowpass prototype with cut-off frequency  $\omega = 1$  rad/s, the equivalent filter transformed using Richard's transformation should have a cut-off frequency of  $\Omega = 1$ . Referring to (4.102), this corresponds to a stub length of  $l = \lambda/8$ . Therefore, if the length is chosen such that  $\lambda$  is calculated at  $\omega_c$ , then using Richard's transform, the filter will have a cut-off frequency  $\omega_c$ .

#### 4.6.4.2 Kuroda Identities

The four Kuroda identities are used along with Richard's transform to implement filter circuits with distributed elements while considering practical realizability. For example, the application of Kuroda identities will physically separate transmission-line stubs, replacing  $L$  and  $C$  in lumped-element filters, and transform series stubs into shunt stubs for practical implementation in planar transmission lines such as microstrips [1–3, 28]. Figure 4.35 shows the four Kuroda identities. The boxes in this figure represent unit elements that are transmission-line sections of characteristic impedances as indicated in the figure and physical length of  $\lambda/8$  at  $\omega_c$ . If the elements of lumped-element filters are replaced by open and short stubs as described in Fig. 4.34, then the corresponding distributed network will contain series as well as shunt stubs.



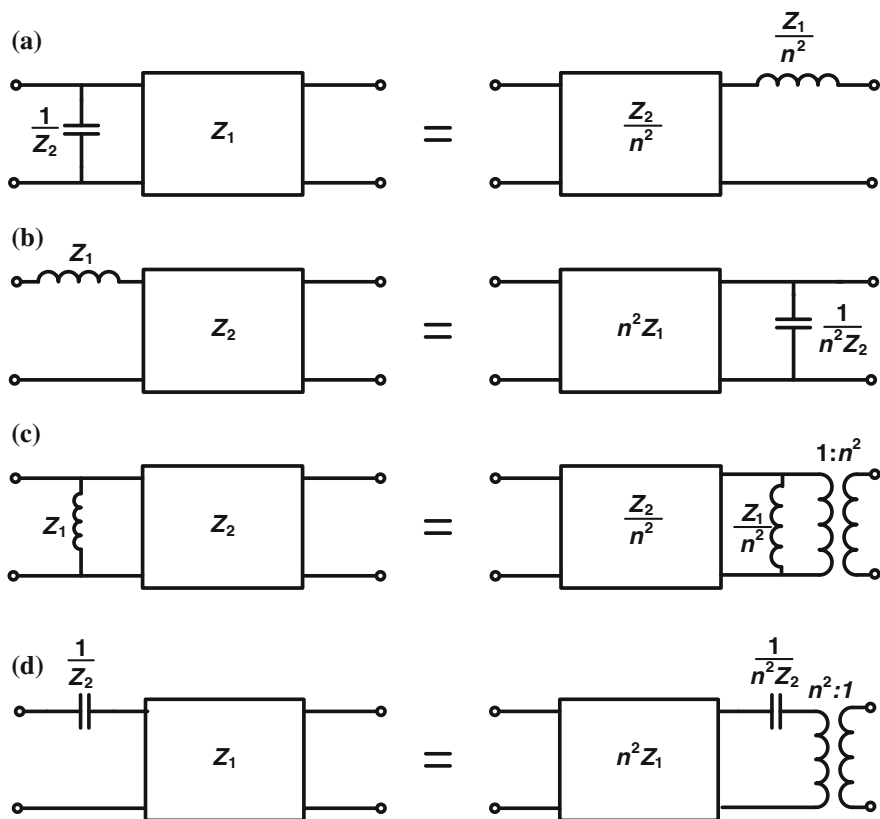


Fig. 4.35 The Kuroda identities [1]

In planar transmission lines such as microstrips, these series stubs are difficult to realize, and therefore they must be converted into shunt stubs. The Kuroda identities as described in Fig. 4.35 convert series elements into shunt elements such that they can be realized using transmission-line-based stubs as described in Fig. 4.34. This is also illustrated in Fig. 4.36. In addition, the unit elements used in Fig. 4.35 separate stubs replacing the lumped components while transforming the lumped filter into the distributed-transmission-line topology.

In practical applications, if a unit element of characteristic impedance  $Z_A$  is inserted in front of a series component realized by a stub as shown in Fig. 4.36a, then, using the Kuroda identity of Fig. 4.35a, one can convert a series stub into a parallel stub as shown in Fig. 4.36b.

The impedance of  $Z_B$  is calculated using the Kuroda identity as represented in Fig. 4.35a. Since the series element in Fig. 4.35a is an inductor, it can be represented by a short-circuit series stub according to the Richard's transformation as shown in Fig. 4.34a. Application of the Kuroda identity of Fig. 4.35a will convert

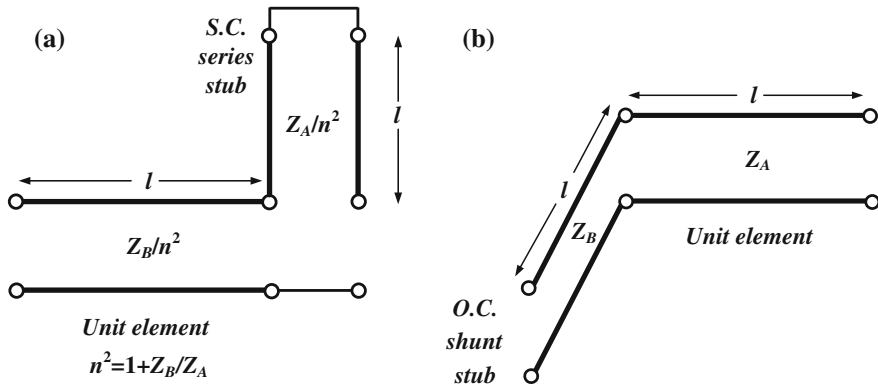


Fig. 4.36 Application of the Kuroda identities [1]

this series inductor into a shunt capacitor represented by an open stub according to Richard’s transformation as shown in Fig. 4.34b. This is shown in Fig. 4.36b.

### 4.6.5 Multiband Lumped-Element Filter Design

The multiband lumped-element filters are very useful for integrated circuit design. Such filters can be further miniaturized by using multilayer ceramic technology such as low-temperature cofired ceramic (LTCC) technology, providing a high level of integration with high reliability. In general, multiband filters can be designed using a parallel combination of different filters. For example, two distinct filters can be combined to achieve dual-band response without interfering with each other as reported in [30]. However, in order to design compact filter topology, it is essential to obtain two different bands of operation from one filter topology where a single set of lumped elements are used [31]. Figure 4.37 shows the schematic of such a dual-band lumped element filter. The LC tank resonator obtained from elements  $L_c$  and  $C_c$  is set to effectively open at a lower passband by selecting its resonance frequency accordingly. This resonator at the second passband will have inductive behavior, which will combine with the inductor  $L_a$  to provide a filter response at the second passband. The element  $C_f$  in Fig. 4.37 will provide additional transmission zeros to improve stopband characteristics.

If the resonators with elements  $L_c$  and  $C_c$  are set to resonate at the center frequency of the first passband frequency  $f_{c1}$ , then the resultant circuit at the first passband is shown in Fig. 4.38a.

This circuit is equivalent to a second-order bandpass filter and the circuit element values can be obtained by choosing the appropriate lowpass filter prototype and applying bandpass transformation as described in the filter synthesis procedure mentioned in Sect. 4.6.3. This will set the component values of  $C_i$ ,  $L_r$ ,  $L_t$ , and  $C_r$ .

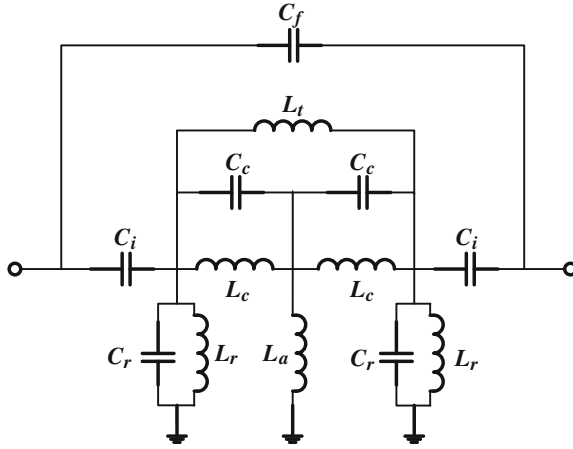


Fig. 4.37 The topology of a dual-band lumped-element bandpass filter [31]

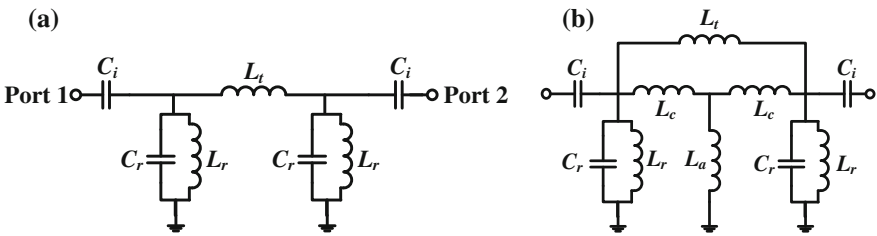


Fig. 4.38 The equivalent of a dual-band filter: **a** lower passband and **b** upper passband [31]

For example, in [31], a Butterworth filter response is chosen with a second-order lowpass prototype element values of  $g_0 = 1$ ,  $g_1 = 1.4142$ ,  $g_2 = 1.4142$ , and  $g_3 = 1$ . For 3 dB fractional bandwidth of 20 % at a center frequency of 2.4 GHz, the element values are calculated as  $C_i = 0.9$  pF,  $L_r = 1.7$  nH,  $L_t = 10.3$  nH, and  $C_r = 2.4$  pF [31]. Figure 4.38b shows the equivalent circuit at second band. It is worth mentioning that  $C_f$  in Fig. 4.37a is not considered yet and will be added for inserting additional transmission zeros after setting the passband responses at both the frequencies. Figure 4.38b shows that the parallel resonators formed by  $L_c$  and  $C_c$ , which has resonance frequency at  $f_{c1}$ , will have an inductive response at the center frequency of the second passband  $f_{c2}$ . This effective inductance is given as

$$L_{\text{eff}} = \frac{L_c}{1 - n^2}, \tag{4.103}$$

where  $n$  is the frequency ratio  $f_{c2}/f_{c1}$ . For a frequency of  $f_{c1} = 2.4$  GHz and  $f_{c2} = 5.2$  GHz, (4.103) gives  $L_{\text{eff}} = -0.27L_c$ . This negative inductance can be

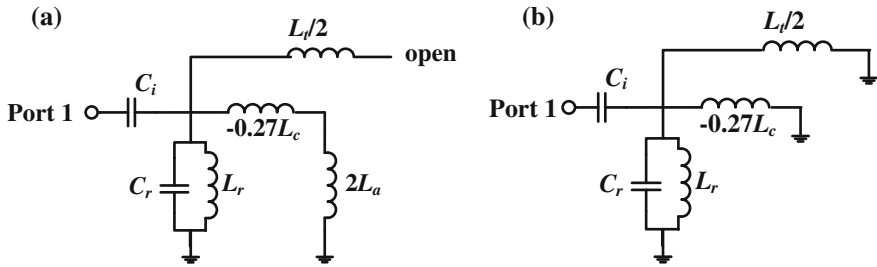


Fig. 4.39 Upper passband equivalent circuit: **a** even mode and **b** odd mode [31]

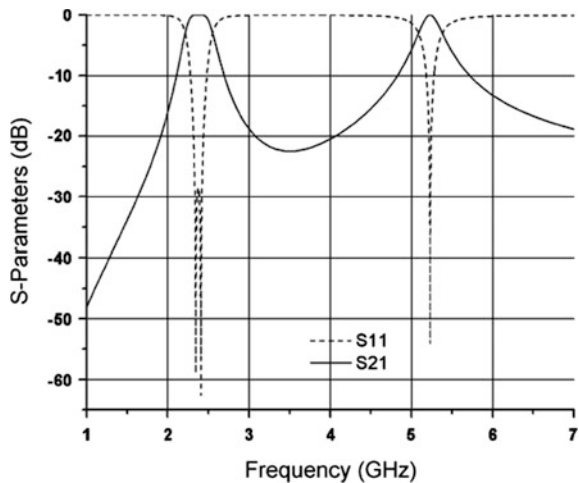
absorbed with the inductor  $L_{-a}$  in a particular case as described in the following discussion. The circuit in Fig. 4.38b can be split along the plane of symmetry by dividing the inductor  $L_a$  into two inductors of values  $2L_a$ . These circuits for even and odd modes are shown in Fig. 4.39.

In the even mode, as shown in Fig. 4.39a, the negative value of  $L_{\text{eff}}$  can be absorbed with  $2L_a$ ; however, in the odd mode, there is no other inductor in the series to the negative inductor for this embedding, as shown in Fig. 4.39b. Therefore, odd-mode resonance is not possible, and only even-mode resonance defines the resonance frequency of the upper passband as

$$f_{c2} = \frac{1}{2\pi \sqrt{\left(Cr + \frac{Ci}{1 + 4\pi^2 f_{c2}^2 Z_0^2 C_i^2}\right) \left(\frac{L_r(2L_a - 0.27L_c)}{L_r + 2L_a - 0.27L_c}\right)}} \tag{4.104}$$

If  $f_{c1}$  is 2.4 GHz and  $C_c$  is set to 1.5 pF, the value of  $L_c$  is calculated as 3 nH. Using (4.104),  $L_a = 0.6$  nH can be computed as described in [31]. Figure 4.40

Fig. 4.40 Dual-bandpass lumped-element filter response using ideal elements without any additional transmission zeros. Reprinted with permission from the IEEE



shows the response of the dual-band lumped-element filter in the absence of  $C_f$ , and therefore without additional transmission zeros.

With the addition of  $C_f$ , the overall  $Y$ -parameter of the circuit is given by

$$\mathbf{Y} = \begin{bmatrix} j\omega C_f + y'_{11} & -j\omega C_f + y'_{12} \\ -j\omega C_f + y'_{21} & j\omega C_f + y'_{22} \end{bmatrix}. \quad (4.105)$$

For transmission zeros, the  $y_{12}$  of the overall  $Y$ -parameter as given by (4.105) is zero. Therefore, the necessary condition is

$$-j\omega C_f + y'_{12} = 0, \quad (4.106)$$

where  $y'_{12}$  is the  $Y$ -parameter of the circuit in Fig. 4.37, which is obtained without  $C_f$ . Equation (4.106) can easily be solved by obtaining the intersection of  $\omega C_f$  with  $-jy'_{12}$ , as shown in Fig. 4.41. The points of intersections give the positions of the transmission zeros.

Two solutions of  $C_f$  that correspond to the values of  $C_{f1} = 0.08$  pF and  $C_{f2} = 0.12$  pF are taken into consideration, and the corresponding transmission zeros added are shown in Fig. 4.42.

#### 4.6.6 Multiband Filter Design Using Coupling Matrix

The transmission-line-based multiband filters can be designed using coupled resonators circuits. In the case of coupled resonators, a coupling matrix of the circuit, which describes the coupling between various resonators, is obtained. The coupled resonators can emulate a frequency-selective transmission response and hence can be used as filters. The coupling matrix is derived from the desired transfer function

**Fig. 4.41** Plot of the  $Y$ -parameter of the circuit in Fig. 4.37a, which is obtained without  $C_f$  and  $\omega C_f$ . Reprinted with permission from the IEEE

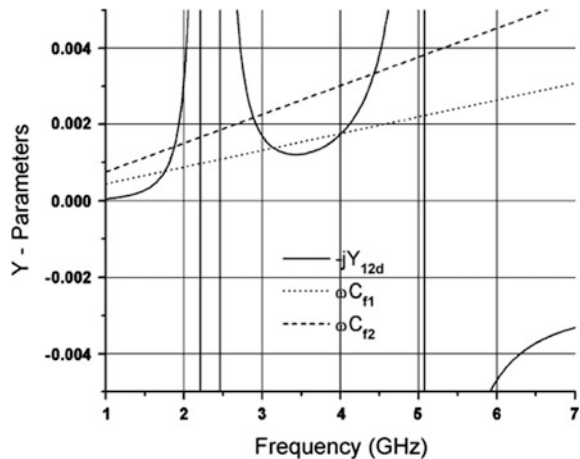
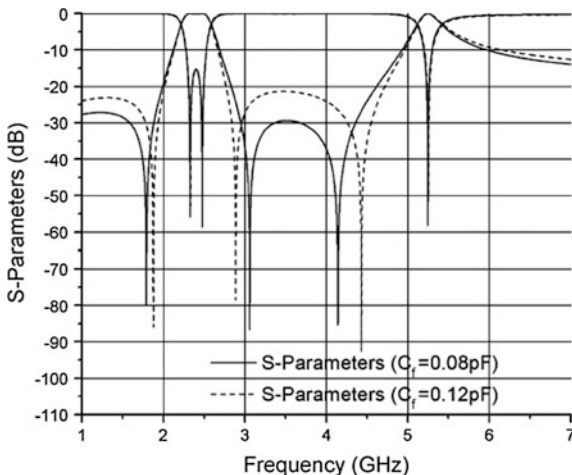


**Fig. 4.42** Plot of the s-parameter of the dual-bandpass lumped-element filter with transmission zeros added to the two different values of capacitor  $C_f$ . Reprinted with permission from the IEEE



of the filter. For single-band filter design, the poles and zeros of the transfer function can be obtained by the filter synthesis procedure as described in Sect. 4.6.3. In such a case, the bandpass transformation as described in Sect. 4.6.3 is useful for single-band bandpass filter design.

However, for dual-band bandpass filter design, a different transformation scheme is used to obtain the dual-band bandpass characteristics. This is described in this section. Nevertheless, the passband and stopband characteristics of the filter depend on the choice of the lowpass prototype in the initial stage. The basic idea of designing multiband filters using this technique is to introduce a transmission zero within the passband of a single-band bandpass filter. Besides providing multiband characteristics, these transmission zeros can sometimes also be used for improving the selectivity of the filter.

Figures 4.43 and 4.44 show the equivalent circuits of magnetically and electrically coupled resonators, respectively [2].

Considering the magnetically coupled resonators in Fig. 4.43 and applying Kirchoff's voltage law in each loop, one can obtain the following expressions:

$$\begin{bmatrix} e_s \\ 0 \\ \vdots \\ 0 \\ 0 \end{bmatrix} = \begin{bmatrix} R_1 + j\omega L_1 + \frac{1}{j\omega C_1} & -j\omega L_{12} & \dots & -j\omega L_{1(n-1)} & -j\omega L_{1n} \\ -j\omega L_{21} & j\omega L_2 + \frac{1}{j\omega C_2} & \dots & -j\omega L_{2(n-1)} & -j\omega L_{2n} \\ \vdots & \vdots & \ddots & \vdots & \vdots \\ -j\omega L_{(n-1)1} & -j\omega L_{(n-1)2} & \dots & j\omega L_{n-1} + \frac{1}{j\omega C_{n-1}} & -j\omega L_{(n-1)n} \\ -j\omega L_{n1} & -j\omega L_{n2} & \dots & -j\omega L_{n(n-1)} & R_n + j\omega L_n + \frac{1}{j\omega C_n} \end{bmatrix} \begin{bmatrix} i_1 \\ i_2 \\ \vdots \\ i_{n-1} \\ i_n \end{bmatrix} \tag{4.107}$$

The expression in (4.107) can also be expressed as  $[Z] \cdot [i] = [e]$ , where  $[Z]$  is the impedance matrix. If all the resonators are assumed to resonate synchronously at  $\omega_0 = 1/\sqrt{LC}$ , implying that all the inductors and capacitors in each resonators are equal, the impedance matrix can be expressed as

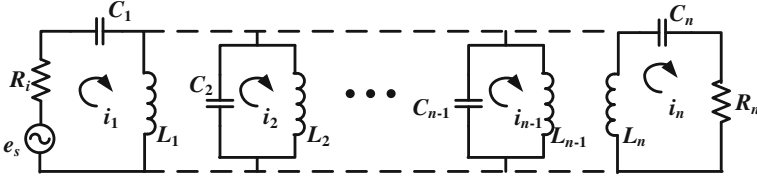


Fig. 4.43 The equivalent circuit of  $n$ -coupled resonators with magnetic coupling [2]

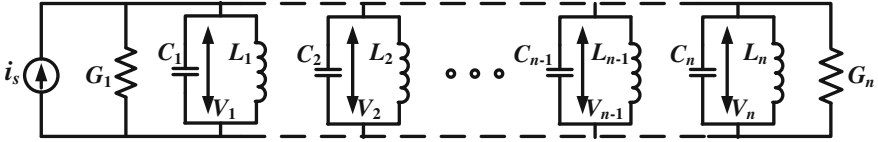


Fig. 4.44 The equivalent circuit of  $n$ -coupled resonators with electrical coupling [2]

$$[\mathbf{Z}] = \omega_0 L \cdot \delta \cdot [\bar{\mathbf{Z}}] \quad (4.108)$$

where  $\delta$  is the fractional bandwidth, and  $[\bar{\mathbf{Z}}]$  is the normalized impedance matrix, given by

$$[\bar{\mathbf{Z}}] = \begin{bmatrix} \frac{R_1}{\omega_0 L \delta} + P & \frac{-j\omega L_{12}}{\omega_0 L \delta} & \cdots & \frac{-j\omega L_{1(n-1)}}{\omega_0 L \delta} & \frac{-j\omega L_{1n}}{\omega_0 L \delta} \\ \frac{-j\omega L_{21}}{\omega_0 L \delta} & P & \cdots & \frac{-j\omega L_{2(n-1)}}{\omega_0 L \delta} & \frac{-j\omega L_{2n}}{\omega_0 L \delta} \\ \vdots & \vdots & \vdots & \vdots & \vdots \\ \frac{-j\omega L_{(n-1)1}}{\omega_0 L \delta} & \frac{-j\omega L_{(n-1)2}}{\omega_0 L \delta} & \cdots & P & \frac{-j\omega L_{(n-1)n}}{\omega_0 L \delta} \\ \frac{-j\omega L_{n1}}{\omega_0 L \delta} & \frac{-j\omega L_{n2}}{\omega_0 L \delta} & \cdots & \frac{-j\omega L_{n(n-1)}}{\omega_0 L \delta} & \frac{R_n}{\omega_0 L \delta} + P \end{bmatrix}. \quad (4.109)$$

and  $P$  is given by

$$P = \frac{j}{\delta} \left( \frac{\omega}{\omega_0} - \frac{\omega_0}{\omega} \right). \quad (4.110)$$

Therefore, one can write (4.107) in a more compact form as

$$[\mathbf{e}] = \omega_0 L \delta [\bar{\mathbf{Z}}] \cdot [\mathbf{i}]. \quad (4.111)$$

If the external quality factor for an  $i$ th resonator is defined as  $Q_{ei} = \omega_0 L / R_i$ , and the coupling coefficient as  $M_{ij} = L_{ij} / L$ , and assuming  $\omega / \omega_0 \approx 1$  for narrow band approximation,  $[\mathbf{Z}]$  is simplified to

$$[\bar{\mathbf{Z}}] = \begin{bmatrix} \frac{1}{q_{e1}} + P & -jm_{12} & \cdots & -jm_{1(n-1)} & -jm_{1n} \\ -jm_{21} & P & \cdots & -jm_{2(n-1)} & -jm_{2n} \\ \vdots & \vdots & \vdots & \vdots & \vdots \\ -jm_{(n-1)1} & -jm_{(n-1)2} & \cdots & P & -jm_{(n-1)n} \\ -jm_{n1} & -jm_{n2} & \cdots & -jm_{n(n-1)} & \frac{1}{q_{en}} + P \end{bmatrix}, \quad (4.112)$$

where  $q_{ei}$  is the scaled external quality factor given by

$$q_{e1} = Q_{ei}\delta \quad (4.113)$$

and  $m_{ij}$  is the normalized coupling coefficient given by

$$m_{ij} = \frac{M_{ij}}{\delta} \quad (4.114)$$

The matrix  $[\bar{\mathbf{Z}}]$  is divided into the following combination of matrices as

$$[\bar{\mathbf{Z}}] = \begin{bmatrix} \frac{1}{q_{e1}} & 0 & \cdots & 0 & 0 \\ 0 & 0 & \cdots & 0 & 0 \\ \vdots & \vdots & \vdots & \vdots & \vdots \\ 0 & 0 & \cdots & 0 & 0 \\ 0 & 0 & \cdots & 0 & \frac{1}{q_{en}} \end{bmatrix} + P \begin{bmatrix} 1 & 0 & \cdots & 0 & 0 \\ 0 & 1 & \cdots & 0 & 0 \\ \vdots & \vdots & \vdots & \vdots & \vdots \\ 0 & 0 & \cdots & 1 & 0 \\ 0 & 0 & \cdots & 0 & 1 \end{bmatrix} - j \begin{bmatrix} m_{11} & m_{12} & \cdots & m_{1(n-1)} & jm_{1n} \\ m_{21} & m_{22} & \cdots & -jm_{2(n-1)} & -jm_{2n} \\ \vdots & \vdots & \vdots & \vdots & \vdots \\ m_{(n-1)1} & m_{(n-1)2} & \cdots & mm_{(n-1)(n-1)} & -jm_{(n-1)n} \\ m_{n1} & m_{n2} & \cdots & m_{n(n-1)} & m_{nn} \end{bmatrix}. \quad (4.115)$$

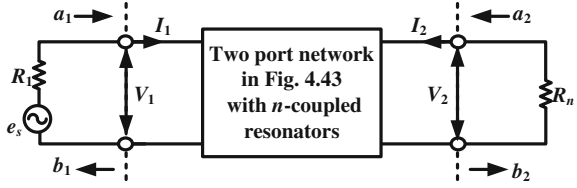
Equation (4.115) can further be written as

$$[\bar{\mathbf{Z}}] = [\mathbf{q}_e] + P[\mathbf{U}] + [\mathbf{m}], \quad (4.116)$$

where  $[\mathbf{m}]$  is a normalized coupling matrix. It is worth mentioning that unlike (4.112), there are diagonal elements present in  $[\mathbf{m}]$  as shown in (4.116). This indicates that the resonators are asynchronously tuned, implying that the resonators can have different self-resonance frequencies.



**Fig. 4.45** The setup for computing s-parameters of  $n$ -coupled resonators



For calculating the s-parameter of the 2-port circuit with  $n$ -coupled resonator as shown in Fig. 4.43, the s-parameter computation setup as shown in Fig. 4.45 can be used.

From Fig. 4.45, one can write  $V_1$  and  $V_2$  as

$$V_1 = e_s - I_1 R_1, \quad (4.117a)$$

$$V_2 = -I_2 R_1, \quad (4.117b)$$

where currents are related to the outer-loop currents shown in Fig. 4.43 as  $I_1 = i_1$  and  $I_2 = -i_2$ . Therefore, the voltage waves  $a_1$  and  $b_1$  are calculated as

$$a_1 = \frac{1}{2} \left( \frac{V_1}{\sqrt{R_1}} + I_1 \sqrt{R_1} \right) = \frac{e_s}{2\sqrt{R_1}}. \quad (4.118a)$$

$$b_1 = \frac{1}{2} \left( \frac{V_1}{\sqrt{R_1}} - I_1 \sqrt{R_1} \right) = \frac{e_s - 2i_1 R_1}{2\sqrt{R_1}}. \quad (4.118b)$$

Moreover,  $a_2 = 0$ , since no excitation is applied to port-2 and  $b_2 = i_n \sqrt{R_n}$ . Therefore, the s-parameters corresponding to transmission and reflection coefficients are calculated using (4.118a), (4.118b), (4.107), and (4.111) as

$$S_{21} = \left. \frac{b_2}{a_1} \right|_{a_2=0} = \frac{2\sqrt{R_1 R_n} i_n}{e_s} = \frac{2\sqrt{R_1 R_n} i_n}{e_s} [\mathbf{Z}]_{n,1}^{-1} = \frac{2\sqrt{R_1 R_n}}{\omega_0 L \delta} [\bar{\mathbf{Z}}]_{n,1}^{-1}, \quad (4.119a)$$

$$S_{11} = \left. \frac{b_1}{a_1} \right|_{a_2=0} = 1 - \frac{2R_1 i_1}{e_s} = 1 - \frac{2R_1 i_1}{e_s} [\mathbf{Z}]_{1,1}^{-1} = 1 - \frac{2R_1}{\omega_0 L \delta} [\bar{\mathbf{Z}}]_{1,1}^{-1}, \quad (4.119b)$$

where  $[\mathbf{Z}]_{n,1}^{-1}$  denotes the  $n$ th row of the first column of the inverse matrix of  $[\mathbf{Z}]$ . The transmission coefficient  $S_{21}$  is approximated with the appropriate filter synthesis scheme, including a suitable lowpass prototype selection, followed by a suitable frequency transformation. For multiband filter design, this transformation is shown in Fig. 4.46 [32].

In Fig. 4.46, the lowpass prototype is selected in the  $\Omega$  domain. This prototype can have characteristics selected from among Chebyshev, Butterworth, and elliptical filters. The following transformation from  $\Omega$  to  $\Omega'$  transforms the frequency

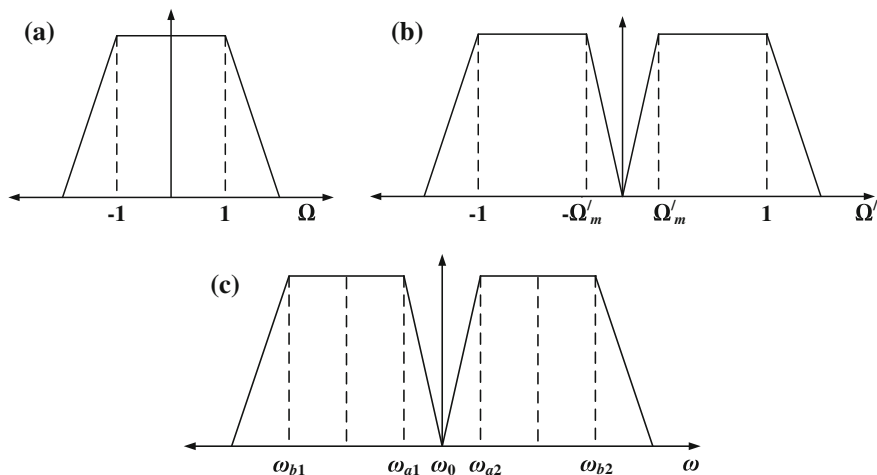


**Fig. 4.46** Frequency transformation for dual-band filter design: frequency response of the filter in the  $\Omega$ ,  $\Omega'$ , and  $\omega$  domains [32]

response of a lowpass prototype as shown in Fig. 4.46a into the frequency response as shown in Fig. 4.46b.

$$j\Omega = \begin{cases} \frac{j\Omega'}{c_1} + \frac{c_2}{j\Omega'} & \text{for } \Omega' > 0 \\ -\left(\frac{j\Omega'}{c_1} + \frac{c_2}{j\Omega'}\right) & \text{for } \Omega' < 0 \end{cases} \quad (4.120)$$

The coefficients  $c_1$  and  $c_2$  are obtained by considering the frequency transformation among the  $\Omega$ ,  $\Omega'$ , and  $\omega$  domains as shown in Fig. 4.46. The values of these coefficients are given by

$$c_1 = 1 - \Omega'_m, \quad (4.121a)$$

$$c_2 = \frac{\Omega'_m}{1 - \Omega'_m}, \quad (4.121b)$$

where  $\Omega'_m$  is given as

$$\Omega'_m = \frac{\omega_{a2} - \omega_{a1}}{\omega_{b2} - \omega_{b1}}. \quad (4.122)$$

The frequency transformation between Fig. 4.46b, c is the conventional band-pass transformation from  $\Omega'$  and  $\omega$  expressed as

$$j\Omega' = \frac{j\omega}{d_1} + \frac{d_2}{j\omega}. \quad (4.123)$$

The unknown variables  $d_1$  and  $d_2$  are given by

$$d_1 = \omega_{b2} - \omega_{b1}. \quad (4.124a)$$

$$d_2 = \frac{\omega_{b1}\omega_{b2}}{\omega_{b2} - \omega_{b1}}. \quad (4.124b)$$

The above frequency transformation can be used to determine the reflection and transmission zeros of dual-passband filters, which can be further used to obtain the transfer functions and coupling matrices for filter implementation. The general expression for power loss ratio is given in (4.80). The reciprocal of this power loss ratio describes the square of the magnitude of the transmission coefficient  $|t(j\Omega)|^2$ , given by

$$|t(j\Omega)|^2 = \frac{1}{1 + p^2 |K_N(j\Omega)|^2}, \quad (4.125)$$

where  $p$  is the ripple factor and  $K_N(j\Omega)$  is the characteristic function that can have a response such as Chebyshev, elliptic. In order to synthesize the filter, the characteristic function is expressed in terms of the rational function of polynomials, which can be expressed in terms of the transmission zeros and poles of the filter as given by

$$K(S) = \frac{F(S)}{P(S)} = \frac{\prod_{i=1}^N (S - S_{zi})}{\prod_{i=1}^N (S - S_{pi})}, \quad (4.126)$$

where  $S = j\Omega$  and  $S_{zi}$  and  $S_{pi}$  are zeros and poles of  $K(S)$ , respectively. Generally, transmission poles are imaginary, but transmission zeros can be imaginary, real, or complex numbers. For elliptic or pseudoelliptic filters, the transmission zeros in the stopband are imaginary, and enhance the frequency selectivity of the filter. The group delay variation in the passband is flattened with the presence of real or complex transmission zeros within the passband. The transmission zeros and poles of Butterworth, Chebyshev, and elliptic filters are all imaginary. Once the rational function as given in (4.126) is selected, the poles and zeros of the lowpass prototype filter is fixed. These poles and zeros are then used to obtain the poles and zeros for the filter shown in Fig. 4.46b. This requires a value of  $\Omega'_m$  that can be calculated using (4.122). These values of poles and zeros of the filter response in Fig. 4.46b are then used to obtain coefficients of polynomials describing the numerator and denominator of the square of the magnitude of the transmission coefficient as described in (4.125).

Since  $|t(j\Omega')|^2 = t(j\Omega')t(-j\Omega')$ , one can determine  $t(j\Omega')$  by considering several conditions as mentioned in [32]. One important condition is selecting the denominator of  $t(j\Omega')$  to be the Hurwitz polynomial, implying that the real parts of the roots are negative [32]. Once  $t(j\Omega')$  is known, it can be compared with the  $S_{21}$  of coupled resonators, as mentioned in (4.119a). Comparing the coefficients results in the computation of values of  $R_1, R_n$ , and unnormalized coupling matrix  $[M]$ . Once the elements of the coupling matrix are known, they can be realized using a stripline as

$$M = \begin{bmatrix} 0 & 0.8302 & 0 & 0 & 0 & 0 & 0 & -0.0851 \\ 0.8301 & 0 & 0.4080 & 0 & 0 & 0 & 0.1053 & 0 \\ 0 & 0.4002 & 0 & 0.4962 & 0 & 0.5076 & 0 & 0 \\ 0 & 0 & 0.4962 & 0 & -0.2294 & 0 & 0 & 0 \\ 0 & 0 & 0 & -0.2294 & 0 & 0.4962 & 0 & 0 \\ 0 & 0 & 0.5076 & 0 & 0.4962 & 0 & 0.4080 & 0 \\ 0 & 0.1053 & 0 & 0 & 0 & 0.4080 & 0 & 0.8302 \\ -0.0851 & 0 & 0 & 0 & 0 & 0 & 0.8302 & 0 \end{bmatrix}$$

$R = 0.5229$

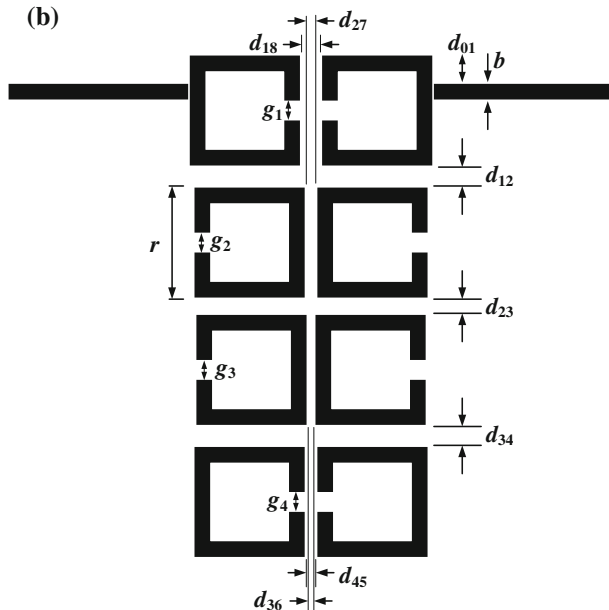


**Fig. 4.47** A dual-band bandpass filter with four poles in each band: **a** coupling matrix and **b** stripline topology using eight open-loop resonators. Reprinted with permission from the IEEE

described in [33]. Figure 4.47a shows the coupling matrix obtained for the dual-band bandpass filter with four poles in each band [33]. Since the coupling coefficients are both positive and negative, an open-loop resonator, which can provide both the electric and magnetic coupling between resonators, is used for realizing the filter with a stripline [33]. The topology of a dual-band bandpass filter with eight open-loop resonators implemented in a stripline is shown in Fig. 4.47b [33]. The tapping position  $d_{01}$  is determined by the external coupling coefficient, and the inter-resonator coupling coefficients determine the distances between two resonators. From Fig. 4.47a, one can see that the diagonal elements are zero in the coupling matrix representing synchronously tuned resonators.

### 4.6.7 Reconfigurable Band Pass Filter Design

For applications such as the ubiquitous multiband/multistandard software-defined radio, it is sometimes beneficial to have operation at only one frequency, while rejecting any transmission in the other bands. Such requirement is essential in ultrawideband (UWB) systems, and reconfigurable bandpass filters are best suited for such applications. In fact, in order to reject some unwanted spurious signals, a notch that can be tuned to suppress undesired signals at a specific frequency is introduced in the passband of the bandpass filter BPF. Thus, for UWB applications, reconfigurable filters are more desirable. The prime design consideration for any reconfigurable BPF is the tuning range of the center frequency, where the variation in bandwidth remains within a specified limit. This is important, because, as the center frequency is tuned, the bandwidth varies. A good design must have control over the variation in the bandwidth as the center frequency is tuned.

In order to design and develop an electronically reconfigurable BPF, active switching or tuning elements—a diode (semiconductor PIN and varactor), RF microelectromechanical systems (MEMS), etc.—are integrated with a passive filtering structure. In fact, RF passive filters developed in a microstrip are well suited for such applications since their planar topology facilitates the integration with active devices [34–36].

Figure 4.48 shows a schematic of a tunable microstrip combline filter [34, 35]. This is a three-pole tunable combline filter, where varactors are used as the active element for electronic tuning. Each resonator has a length shorter than a quarter-wavelength at the center frequency of operation, where one end is shorted as a conventional combline filter, whereas the other end of the resonator is

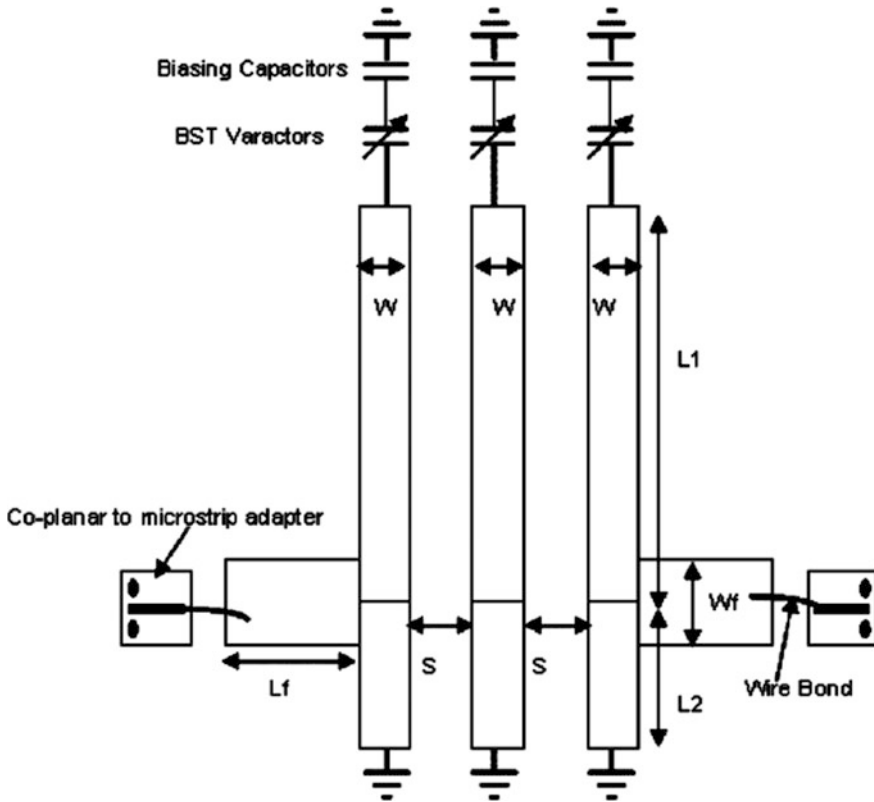


**Fig. 4.48** Schematic of a tunable filter with microstrip-based combline filter topology [35]. Reprinted with permission from the IEEE

connected with a varactor and a biasing capacitor for enabling the tuning of the resonator length.

In order to maintain a constant filter response shape and bandwidth, the coupling coefficient must vary inversely with the tuning frequency and the external  $Q$  must vary directly with the tuning frequency. For this purpose, [36] utilizes step-impedance microstrip resonators in a tunable combline filter topology as shown in Fig. 4.49a. In this topology, lumped inductors are used for input and output coupling networks. By properly choosing the position and value of the lumped inductor, the external  $Q$  can be controlled to satisfy the constant bandwidth requirement. Figure 4.49b shows the  $s$ -parameter response of a tunable combline filter topology as shown in Fig. 4.49a.

In Fig. 4.49b, one can see that the 3 dB passband bandwidth varies less than 3.2 %, while the tuning range is 250 MHz around a center frequency of 2 GHz.

Among recent trends, designers are also looking for bandwidth reconfigurability, while keeping the center frequency constant. In such a case, the filter passband

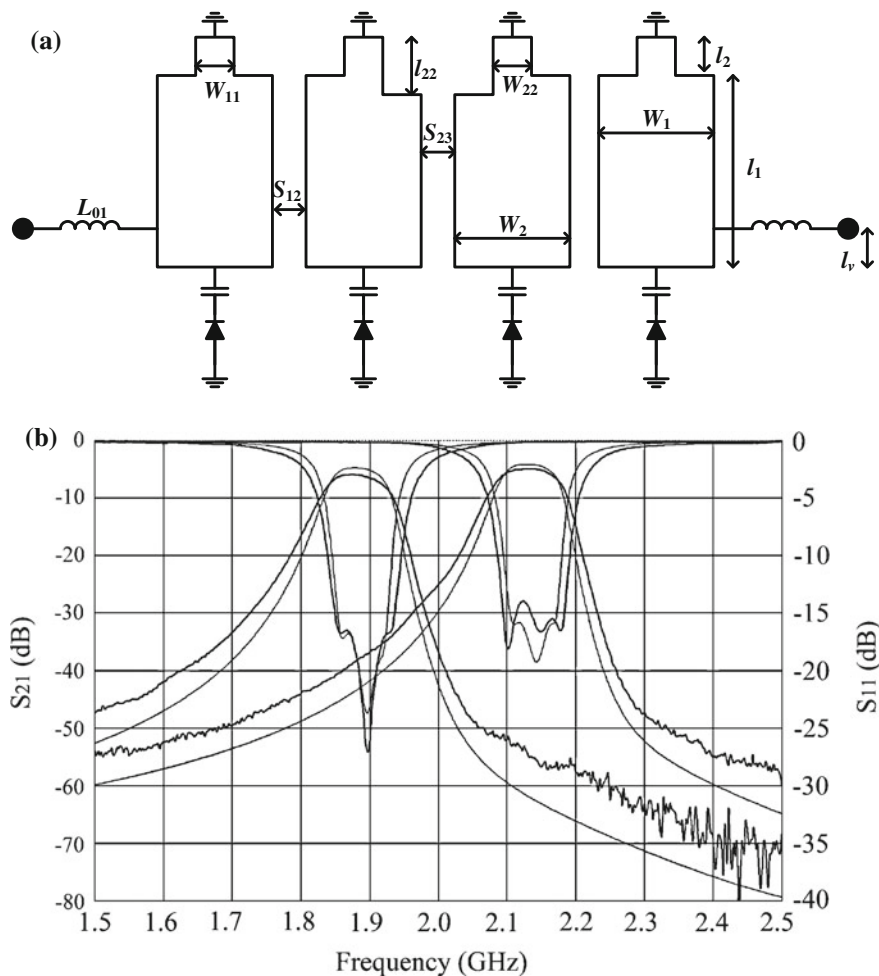


**Fig. 4.49** A tunable bandpass filter using varactor and step-impedance microstrip lines: **a** schematic and **b** measured (*thick lines*) and simulation (*thin lines*) results [36]. Reprinted with permission from the IEEE

bandwidth can be reconfigured between narrow/moderate-band and ultrawideband states [37]. These filters have been put in two categories: signal-interference filter and multiple-mode resonator filters [37].

RF/microwave signal-interference filters are multipath structures, where the signals reaching from different paths interact at the output node. For bandwidth reconfigurable filtering action, these multipath structures are combined with tunable and switchable active elements [37–39]. Figure 4.50 shows the topology of a reconfigurable bandwidth signal-interference bandpass filter using feedforward signal-combination concepts [37, 40].

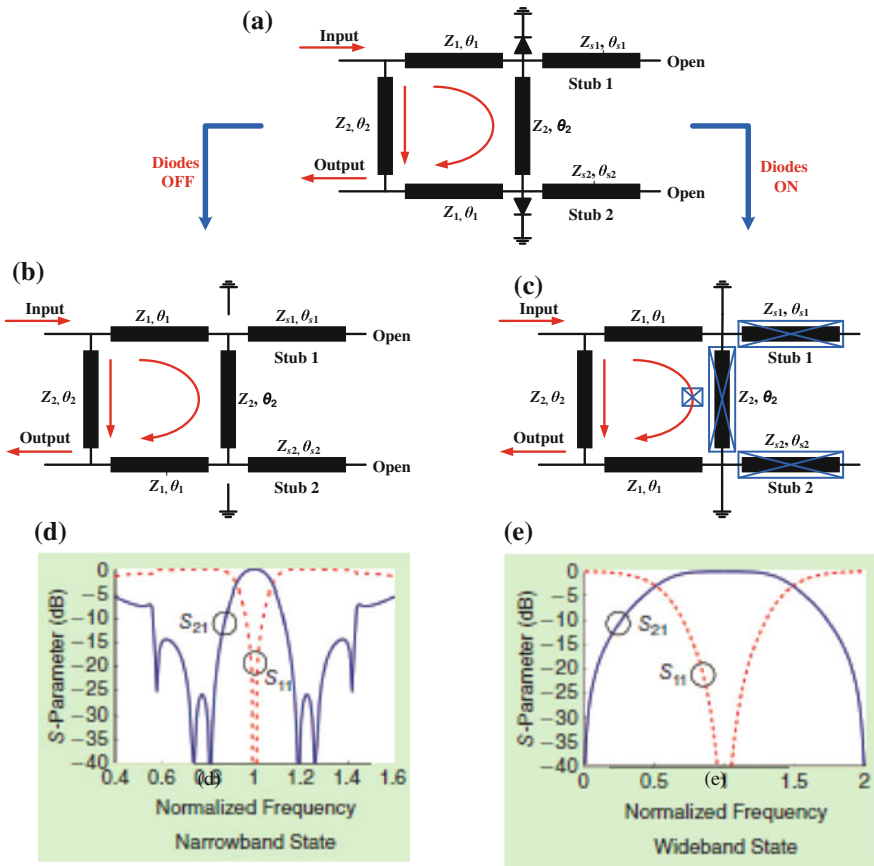
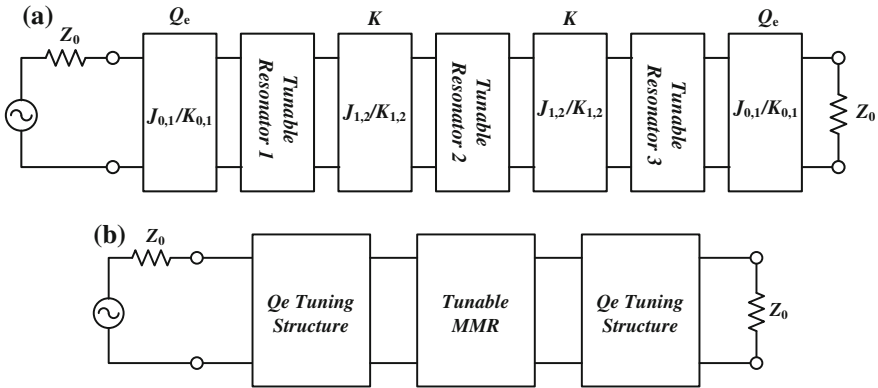


Fig. 4.50 Schematic of a signal-interference reconfigurable bandwidth bandpass filter with operating principle and results [37]. Reprinted with permission from the IEEE

The circuit topology of Fig. 4.50 is obtained by modifying a branch-line directional coupler loaded with open-circuit stubs connected to its coupled and direct ports. The isolated terminal of a branch-line hybrid is used as the output port. Without any diode (when the diode is *off*), this circuit has two paths for the input signal to propagate, where there is a constructive interference in the passband and suppression of signals in the stopband region. Moreover, the diode plays an important role of bandwidth reconfigurability, as shown in Fig. 4.50. The diodes are PIN diodes, which act as short or open when they are *on* and *off*, respectively, using the appropriate bias. When the diodes are switched off, the topology in Fig. 4.50b has two open stubs connected at the coupled and direct ports of the branch-line hybrid. This results in a narrow bandwidth, as shown in Fig. 4.50d.

However, when the diode is *on*, the signal passes directly through the line of characteristic impedance  $Z_2$  and the electrical length  $\theta_2$ , as shown in Fig. 4.50c,





**Fig. 4.51** **a** Topology of the classical third-order coupled resonator tunable bandpass filter and **b** block-diagram of an MMR-based tunable filter architecture with external quality factor  $Q_e$  tuning structures [41]

resulting in a wider bandwidth response as shown in Fig. 4.50e. The values of the bandwidth attained in both the states can be controlled by using design parameters (characteristic impedance and electrical length) of transmission lines in the circuit topology. The passband bandwidth of the wideband state is controlled by the characteristic impedances of the transmission lines forming the branch-line hybrid coupler, whereas the bandwidth of the narrow-band state is selected by the proper selection of stub impedances [37]. Based on the topology shown in Fig. 4.50, [40] reports realization of a microstrip-based switchable-bandwidth bandpass filter prototype centered at 2 GHz with five selectable bandwidth states.

Apart from signal-interference filter topology, as discussed above, the multimode-resonator-based (MMR-based) reconfigurable BPF is quite an effective technique among recent developments in the area of tunable filters. Such a topology provides the option to tune the center frequency in a manner similar to a reconfigurable combline filter besides having passband bandwidth reconfigurable capability. The multiple resonances in the MMR facilitate the tuning of the center frequency without individual control of the resonator and the coupling coefficient among different resonators. In addition to MMR, the external quality factor tuning structure can help in controlling the return loss and the shape factor. Figure 4.51 shows an MMR-based tunable filter architecture along with MMR and external quality factor,  $Q_e$ , tuning structures. Figure 4.52a shows the cross-shaped tunable MMR as reported in [41]. This MMR has three resonant poles and two transmission zeros frequencies. In fact, owing to the symmetry of this MMR, it can be analyzed using even- and odd-mode analysis with equivalent circuits as shown in Fig. 4.52b, c. Therefore, among three resonant poles frequencies,  $f_o$  is obtained from odd-mode analysis, which is controlled by capacitor  $C_1$ , as shown in Fig. 4.52. The other two frequencies  $f_{e1}$  and  $f_{e2}$  are obtained from even-mode analysis, which can be controlled by capacitors  $C_2$  and  $C_3$ , respectively, according to Fig. 4.52c. The two

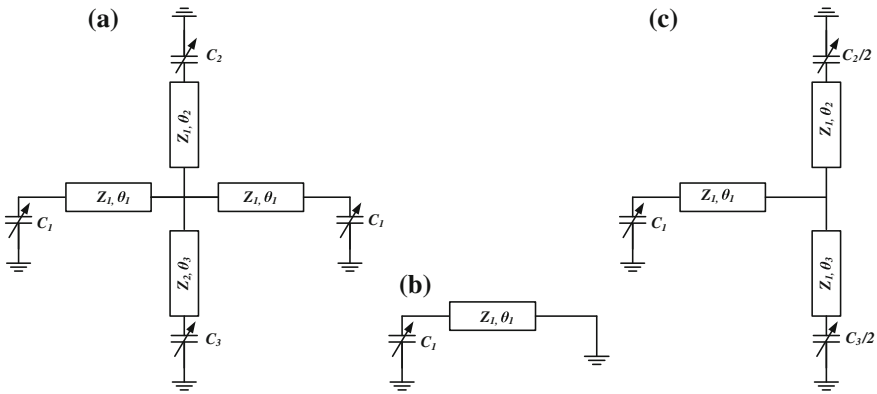


**Fig. 4.52** The cross-shaped tunable MMR [41]: **a** circuit topology, **b** odd-mode equivalent circuit and **c** even-mode equivalent circuit  $Z_1 = 2Z_2$

transmission zeros frequencies  $f_{TZ1}$  and  $f_{TZ2}$  introduced by MMR is obtained by calculating the s-parameter of MMR, as shown in Fig. 4.52a, and enforcing  $S_{21} = 0$ . This will result in an expression showing dependency of frequencies  $f_{TZ1}$  and  $f_{TZ2}$  over the capacitances  $C_2$  and  $C_3$ , respectively [41]. Therefore, in Fig. 4.52a, the  $f_o$  is controlled by  $C_1$ , while  $f_{TZ1}$  and  $f_{TZ2}$  are controlled by  $C_2$  and  $C_3$ , respectively. The other two pole frequencies  $f_{e1}$  and  $f_{e2}$  are controlled by  $C_1$ ,  $C_2$ , and  $C_3$  simultaneously. The transmission zeros are tuned by  $C_2$  and  $C_3$ , and this will also shift the even-mode poles frequencies and hence help in placing out-of-band transmission zeros close to the even-mode poles.

The  $Q_e$  tuning stage is inserted between the termination  $R_0$  and the end resonator as shown in Fig. 4.51a. The theory behind  $Q_e$  tuning is based on realization of the tunable impedance transformer. This impedance transformer will transform the termination  $R_0$  to  $R_{eff}$  based on its transformation ratio  $N$ . The basic schematic of the  $Q_e$  tuning structure and its equivalent is shown in Fig. 4.53, where the resonator is represented by an equivalent LC tank circuit at the center frequency of operation.

If the transformation ratio  $N$  is tunable,  $R_{eff}$  is tunable and hence  $Q_e$  is tunable. An example of the physical realization of the  $Q_e$  tuning stage is shown in Fig. 4.54,

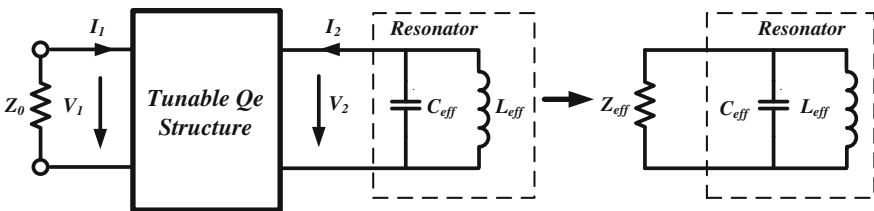


**Fig. 4.53** The  $Q_e$  tuning structure with its equivalent [41]

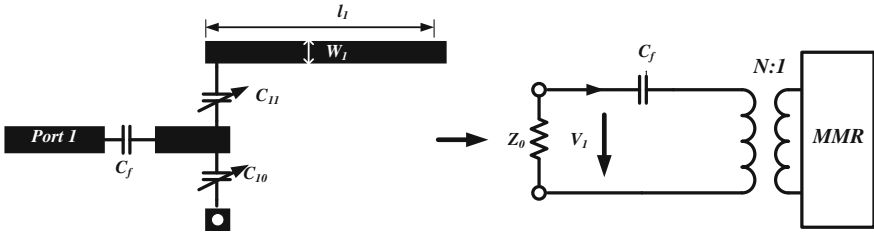


Fig. 4.54 A practical realization of the  $Q_e$  tuning structure with its equivalent [41]

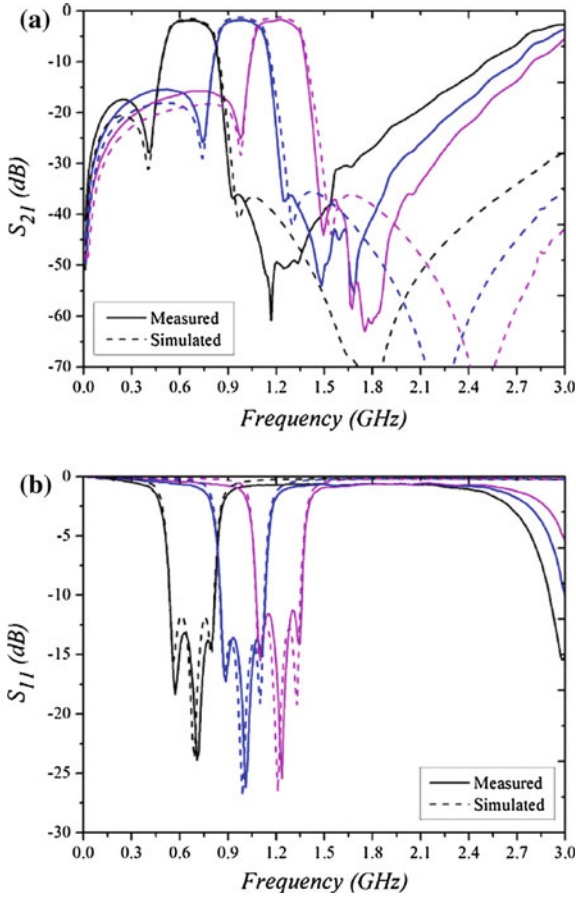
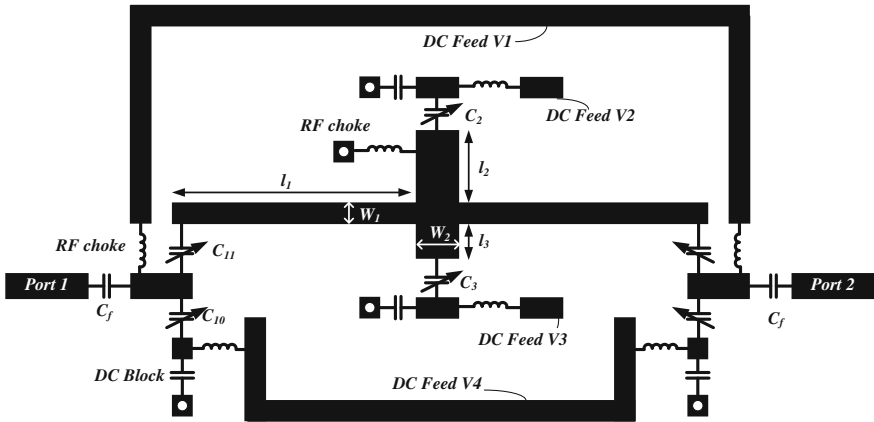
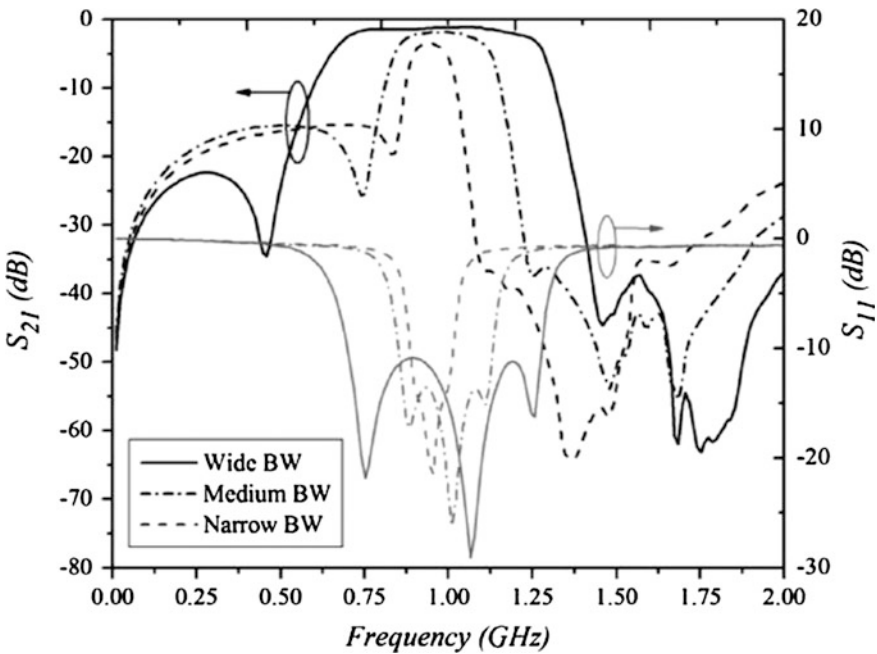


Fig. 4.55 The circuit diagram of a tunable BPF based on a cross-shaped tunable MMR [41]. Reprinted with permission from the IEEE



**Fig. 4.56** Simulated and measured results of a tunable BPF at different tuned values of the center frequency: low frequency:  $V_1 = 1.2$  V,  $V_2 = 10$  V,  $V_3 = 0.5$  V,  $V_4 = 14.5$  V; middle frequency:  $V_1 = 8.2$  V,  $V_2 = 15.8$  V,  $V_3 = 8.9$  V,  $V_4 = 30.3$  V; high frequency:  $V_1 = 12.5$  V,  $V_2 = 21.5$  V,  $V_3 = 14.6$  V,  $V_4 = 46$  V. **a**  $|S_{21}|$  and **b**  $|S_{11}|$  [41]. Reprinted with permission from the IEEE)



**Fig. 4.57** Simulated and measured results of  $|S_{21}|$  for tunable BPF at different tuned values of bandwidth. Wide bandwidth:  $V_1 = 8.3$  V,  $V_2 = 2.1$  V,  $V_3 = 20.5$  V,  $V_4 = 39.5$  V; medium bandwidth:  $V_1 = 8.9$  V,  $V_2 = 8.2$  V,  $V_3 = 15.8$  V,  $V_4 = 30.3$  V; narrow bandwidth:  $V_1 = 9.5$  V,  $V_2 = 10$  V,  $V_3 = 12.9$  V,  $V_4 = 26$  V. Reprinted with permission from the IEEE

where a voltage-divider effect of two varactors  $C_{10}$  and  $C_{11}$  is equivalent to  $N:1$  transformer.

As the odd-mode frequency of the tunable MMR in Fig. 4.52b is allocated at the center of the passband, the  $Q_c$  can be determined from the equivalent circuit of Fig. 4.54. The overall schematic of a tunable BPF is shown in Fig. 4.55, where the varactors  $C_1$  of the MMR (as shown in Fig. 4.52) are replaced by two series varactors  $C_{10}$  and  $C_{11}$ .

The positions between these two varactors  $C_{10}$  and  $C_{11}$  can be used for tapping the input and output ports of the BPF. Since  $C_1$  (shown in Fig. 4.52) is replaced by a series combination of  $C_{10}$  and  $C_{11}$ , their equivalent value determines the odd-mode resonant frequency  $f_o$ . However, the ratio of  $C_{10}$  and  $C_{11}$  controls the  $Q_c$ . Figures 4.56 and 4.57 show the results of the reconfigurable BPF shown in Fig. 4.55 in two different modes of operation.

Figure 4.56a, b shows the mode of operation where the center frequency is tuned to a different frequency range while keeping the bandwidth preserved. Figure 4.57 shows the operation mode, where the passband bandwidth is reconfigured.

## References

1. D.M. Pozar, *Microwave Engineering* (Wiley, New Delhi, 2013)
2. J.-S. Hong, M.J. Lancaster, *Microstrip Filters for RF/Microwave Applications* (Wiley, New York, 2001)
3. P. Jarry, J. Beneat, *Advanced Design Techniques and Realization of Microwave and RF Filters* (IEEE press, Wiley, New York, 2008)
4. G. Matthaei, L. Young, E.M.T. Jones, *Microwave filters, impedance-matching networks, and coupling structures*, Artech House (1985)
5. K. Rawat, M.S. Hashmi, F.M. Ghannouchi, Dual-band RF circuits and components for multi-standard software defined radios. *IEEE Circuit Sys. Mag.* **12**(1), 12–32 (2012)
6. K. Rawat, M.S. Hashmi, F.M. Ghannouchi, Double the band and optimize. *IEEE Microwave Mag.* **13**(2), 69–82 (2012)
7. K. Rawat, F.M. Ghannouchi, A novel dual-band matching technique based on dual-characteristic impedance transformer for dual-band power amplifier design. *IET Microwaves Antennas Propag.* **5**(14), 1720–1729 (2011)
8. H. Zhang, K.J. Chen, A stub tapped branch-line coupler for dual-band operations. *IEEE Microwave Wireless Comp. Lett.* **17**(2), 106–108 (2007)
9. C. Monzon, A small dual-frequency transformer in two sections. *IEEE Trans. Microwave Theory Tech.* **51**, 1157–1161 (2003)
10. K. Rawat, F.M. Ghannouchi, M. Rawat, M.S. Hashmi, Analysis of frequency selective impedance loading of transmission lines for dual band couplers. *Wiley Int. J. RF Microwave Comput.-Aided Eng.* **21**(3), 325–335 (2011)
11. K. Rawat, F.M. Ghannouchi, A design methodology for miniaturized power dividers using periodically loaded slow wave structure with dual band applications. *IEEE Trans. Microwave Theory Tech.* **57**(12, part 2), 3380–3388 (2009)
12. S. Li, B.H. Tang, Y.A. Liu, S.L. Li, C.P. Yu, Y.L. Wu, Miniaturized dual-band matching technique based on coupled-line transformer for dual-band power amplifier design. *Progress Electromagnet. Res.* **131**, 195–210 (2012)

13. Y. Wu, Y. Liu, S. Li, S. Li, A novel high-power amplifier using a generalized coupled-line transformer with inherent DC-block function. *Progress Electromagnet. Res.* **119**, 171–190 (2011)
14. M.J. Park, B. Lee, A dual-band Wilkinson power divider. *IEEE Microwave Wireless Comp. Lett.* **18**(2), 85–87 (2008)
15. E.J. Wilkinson, An N-way hybrid power divider. *IRE Trans. Microw. Theory Tech.* **8**(1), 116–118 (1960)
16. G. Castaldi, V. Fiumara, I.M. Pinto, A dual-band Chebyshev impedance transformer. *Microw. Optical Tech. Lett.* **39**(2), 141–145 (2003)
17. S.J. Orfanidis, A two-section dual-band Chebyshev impedance transformer. *IEEE Microw. Wireless Comp. Lett.* **13**(9), 382–384 (2003)
18. L. Wu, S. Sun, H. Yilmaz, M. Berroth, A dual-frequency Wilkinson power divider. *IEEE Trans. Microw. Theory Tech.* **54**(1), 278–284 (2006)
19. K. Cheng, F. Wong, A new Wilkinson power divider design for dual band application. *IEEE Microwave Wireless Comp. Lett.* **17**(9), 664–666 (2007)
20. A.S.S. Mohra, Compact dual band Wilkinson power divider. *Microw. Optical Tech. Lett.* **50**(6), 1678–1682 (2008)
21. L. Wu, S. Sun, H. Yilmaz, M. Berroth, A dual-frequency Wilkinson power divider. *IEEE Trans. Microwave Theory Tech.* **54**(1), 278–284 (2006)
22. K. Rawat, F.M. Ghannouchi, Design methodology for dual-band Doherty power amplifier with performance enhancement using dual-Band offset lines. *IEEE Trans. Industr. Electron.* **59**(12), 4831–4842 (2012)
23. K.K.M. Cheng, F.L. Wong, A novel approach to the design and implementation of dual-band compact planar 90° branch-line coupler. *IEEE Trans. Microw. Theory Tech.* **52**(11), 2458–2463 (2004)
24. C.L. Hsu, C.W. Chang, J. TsaiKuo, Design of dual band microstrip rat race coupler with circuit miniaturization. in *IEEE MTT-S International Microwave Symposium Digest* (Honolulu, Hawaii, 2007), pp. 177–180s
25. C.L. Hsu, J. Tsai Kuo, C.W. Chang, Miniaturized dual-band hybrid couplers with arbitrary power division ratio. *IEEE Trans. Microw. Theory Tech.* **57**, 149–156 (2009)
26. Y.B. Kim, H.T. Kim, K.S. Kim, J.S. Lim, D. Ahn, A branch line hybrid having arbitrary power division ratio and port impedances, in *Proceedings of Asia Pacific Microwave Conference* (2006), pp. 1–4
27. K. Rawat, M. Rawat, M.S. Hashmi, F.M. Ghannouchi, Dual band branch-line hybrid with distinct power division ratio at two bands. *Wiley Int. J. RF Microwave Comput.-Aided Eng.* **23**(1), 90–98 (2013)
28. R.E. Collin, *Foundation for Microwave Engineering* (IEEE Press Series on Electromagnetic Wave Theory, New York, 1998)
29. J.A.G. Malherbe, *Microwave Transmission Line Filters, Dedham* (Artech House, Mass., 1979)
30. Y.-X. Guo, L.C. Ong, M.Y. W. Chia, B. Luo, Dual-band bandpass filter in LTCC. *IEEE MTT-S Int. Microw. Symp. Dig.* **4**, 2219–2222 (2005)
31. H. Joshi, W.J. Chappell, Dual-band lumped element bandpass filter. *IEEE Trans. Microw. Theory Tech.* **54**(12), 4169–4177 (2006)
32. J. Lee, K. Sarabandi, Synthesizing microwave resonator filters. *IEEE Microwave Mag.* **10**(1), 57–65 (2009)
33. J. Lee, K. Sarabandi, A synthesis method for dual-passband microwave filters. *IEEE Trans. Microw. Theory Tech.* **55**(6), 1163–1170 (2007)
34. J.S. Hong, Reconfigurable planar filters. *IEEE Microw. Mag.* **10**(6), 79–83 (2009)
35. J. Nath, D. Ghosh, J.-P. Maria, A.I. Kingon, W. Fathelbab, P.D. Franzon, M.B. Steer, An electronically tunable microstrip bandpass filter using thin-film barium-strontium-titanate (BST) varactors. *IEEE Trans. Microwave Theory Tech.* **53**(9), 2707–2712 (1982)
36. B.-W. Kim, S.-W. Yun, Varactor-tuned combline bandpass filter using step-impedance microstrip lines. *IEEE Trans. Microwave Theory Tech.* **52**(4), 1279–1283 (2004)

37. R. Gómez-García, M.-A. Sánchez-Soriano, K.W. Tam, Q. Xue, Flexible filters: reconfigurable-bandwidth bandpass planar filters with ultralarge tuning ratio. *IEEE Microw. Magazine* **15**(5), 43–54 (2014)
38. P.W. Wong, I.C. Hunter, A new class of low-loss high-linearity electronically reconfigurable microwave filters. *IEEE Trans. Microwave Theory Tech.* **56**(8), 1945–1953 (2008)
39. D. Segovia-Vargas, O. García-Pérez, V. González-Posadas, F. Aznar-Ballesta, Dual-band tunable recursive active filter. *IEEE Microwave Wireless Compon. Lett.* **21**(2), 92–92 (2011)
40. M.-A. Sánchez-Soriano, R. Gómez-García, G. Torregrosa-Penalva, E. Bronchalo, Reconfigurable-bandwidth bandpass filter within 10–50 %. *IET Microwave Antennas Propagat.* **7**(7), 502–509 (2013)
41. J.-R. Mao, W.-W. Choi, K.-W. Tam, W.Q. Che, Q. Xue, Tunable bandpass filter design based on external quality factor tuning and multiple mode resonators for wideband applications. *IEEE Trans. Microwave Theory Tech.* **61**(7), 2574–2584 (2013)

# Chapter 5

## Multiband Power Amplifier Design

### 5.1 Introduction

This chapter is dedicated to the design techniques involved in multiband power amplifier (PA) design. The chapter starts with a discussion on the various matching techniques for dual-band concurrent operation followed by reconfigurable matching networks. Following the discussion on matching networks, the chapter provides multiband continuous-class and switch-mode PA design examples. Efficiency-enhancement techniques such as the Doherty power amplifier (DPA) and envelope-tracking are also discussed in the perspective of multiband design.

### 5.2 Multiband Power Amplifier Matching

PA design needs a proper matched load to deliver maximum power with optimum DC-to-RF conversion efficiency. On the input side, a conjugate match is preferred to obtain good RF gain and hence best power-added efficiency [1–5]. A proper value of a matched load is predicted either from precise nonlinear device model [3–6] or by using measurement techniques such as load-pull [3–11]. Once the optimum terminations at the input and the output are obtained, the matching networks are used to match a standard load of  $50\ \Omega$  to these optimum terminations at the input and the output. Figure 5.1 shows a typical block diagram of an RF PA circuit with matching networks.

In general, the matching circuit in any amplifier design can be seen as a 2-port network that provides the desired complex input impedance when terminated by a standard load impedance of  $50\ \Omega$ . This complex input impedance is the required value of impedance presented to the device in order to obtain optimal performance in terms of gain, output power, efficiency, etc. [10, 11]. It is worth mentioning that the device in Fig. 5.1 can be unstable and may require an additional compensation



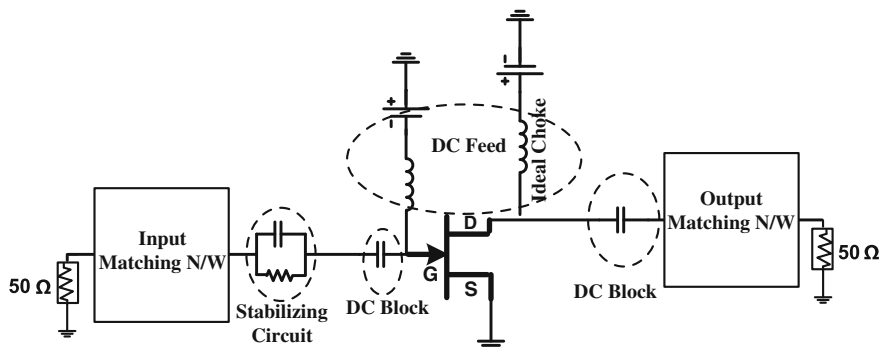


Fig. 5.1 Block diagram of a power amplifier

network to stabilize the transistor as shown in the figure. A detailed analysis on the stability along with the proper methodology of biasing of the transistor is presented in [1, 2]. Moreover, multiband matching can be concurrent or reconfigurable. The concurrent matching technique ensures simultaneous matching at multiple frequencies and hence concurrent operation of the power amplifier at the two frequencies [8–15]. The reconfigurable matching techniques, however, are used in cases where a PA is required to operate at one frequency in one instance, and it is reconfigured to another frequency only when this is required [16, 17].

## 5.2.1 Concurrent Matching Techniques

The concurrent matching network simultaneously ensures matching at multiple frequencies of operation. At low RF frequencies, the lumped-element-based matching network can be used depending on the self-resonance frequency of the lumped components such as inductors and capacitors. At high frequencies, the distributed components, such as transmission-line-based elements, are often used for implementing matching networks.

### 5.2.1.1 Transmission-Line-Based Concurrent Matching Techniques

A PA design using packaged devices may require complex impedances as loads to behave optimally in terms of output power and efficiency. In a multiband operation, these required complex loads can be different at different frequencies of operations. Thus, in general, a dual-band matching network should be able to transform a  $50\ \Omega$  load to two different impedances at two frequencies of operation. Some designs reported in [18, 19] provide the same complex impedances when terminated by a  $50\ \Omega$  load and, therefore, can be used in some specific design problems.

Similarly, some designs utilize transmission-line-based impedance transformers for matching a 50 Ω standard load to real impedances [20, 21] only and hence are not generic, considering that packaged transistors in PA may require complex impedance terminations to behave optimally. Furthermore, the transmission-line-based matching network used for harmonics [22] can also be used for dual-band matching, provided that the resistive components of the required loads are not too high at the two operating frequencies. Matching techniques [23–25] provide the matching of two different complex loads to 50 Ω at two distinct frequencies, provided that this matching can be realized with the practical values of characteristic impedances of transmission lines.

Stub-loaded T-type and pi-type circuits as described in Chap. 3 can also meet the requirements of dual-band matching networks. The dual-band matching network is primarily based on the standard non-50 Ω quarter-wave transformer-matching technique [1] along with some modifications, to realize two distinct reflection coefficients at the two chosen frequencies, in order to achieve dual-band operation. Figure 5.2a shows the topology of this matching network. The key element of this technique is a dual-band/dual-impedance quarter-wave transformer that simultaneously transforms the 50 Ω load seen at the reference plane,  $TT'$  in Fig. 5.2a, to the respective real conductance parts,  $G(f_1)$  and  $G(f_2)$ . These conductances are the real parts of the required complex impedances,  $Y(f_1)$  and  $Y(f_2)$ , to be seen by the active device at frequencies  $f_1$  and  $f_2$ , respectively. In such a technique, the first step in designing the appropriate dual-band impedance transformer is to obtain the required values of the resistive components of  $Y(f_1)$  and  $Y(f_2)$  and then realize the corresponding imaginary parts of the required  $Y(f_1)$  and  $Y(f_2)$  using a dual-band/dual-susceptance stub, as described in Chap. 3.

An alternative dual-band matching topology is shown in Fig. 5.2b. In this scheme, the characteristic impedances of the transformer are synthesized in such a manner that when it is terminated by certain admittances ( $Y_J(f_1)$  and  $Y_J(f_2)$  in Fig. 5.2b) with the real conductive part as 1/50 Ω (represented by  $G_0$  in Fig. 5.2b) at both the frequencies, it will realize the desired input admittances,  $Y(f_1)$  and  $Y(f_2)$ , at the two frequencies, as shown in Fig. 5.2b. In this technique, the first step involves the synthesis of the required values of the characteristic impedances  $Z_{T1}$  and  $Z_{T2}$  at two frequencies  $f_1$  and  $f_2$ , respectively, and the corresponding values of

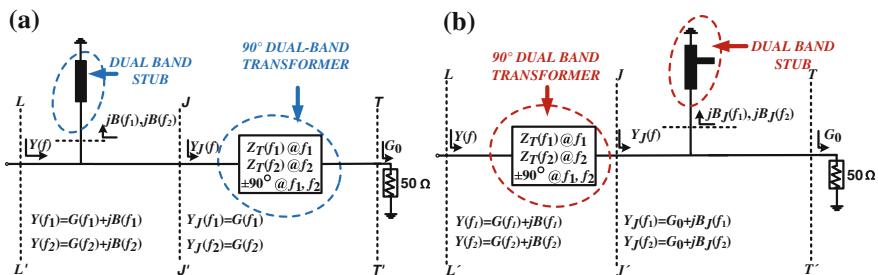


Fig. 5.2 Dual-band matching network design [8, 10]: a topology 1 and b topology 2

the susceptances,  $jB_J(f_1)$  and  $jB_J(f_2)$ , at reference  $JJ'$ . Then the values of these characteristic impedances and susceptances are realized using dual-band components as described in Chap. 3. The value of the junction admittance  $Y_J(f)$  and the required input admittance  $Y(f)$  can be related with a simple impedance inversion relationship of a quarter-wave transformer given by

$$Y_J(f) = \frac{1}{(Z_T(f))^2 Y(f)}; \quad \text{where} \quad Z_T(f) = \begin{cases} Z_{T1} & @f_1 \\ Z_{T2} & @f_2 \end{cases} \quad (5.1)$$

Putting  $Y(f)$  and  $Y_J(f)$  in their complex forms in (5.1), and comparing the real and imaginary parts individually, the susceptance values of the junction admittances (at reference  $JJ'$  in Fig. 5.2b) and the required characteristic impedances of the 90° transformer (impedance inverter) can be synthesized as follows:

$$B_J(f) = \frac{-B(f)G_A(f)}{G(f)} \quad (5.2)$$

$$Z_T(f) = \sqrt{\frac{G_A}{G(f)\sqrt{(G_J(f))^2 + (B_J(f))^2}}} \quad (5.3)$$

Once the required values of  $B_J(f)$  are known from (5.2), these susceptance values are realized using a dual-band/dual-susceptance stub and two different values of characteristic impedances at two frequencies as obtained from (5.3) using a dual-band/dual-impedance quarter-wave transformer. Thus, in both the matching topologies of Fig. 5.2, the design can be divided into two parts: first, designing the dual-band/dual-impedance quarter-wave transformer of two different characteristic impedances at the two frequencies and, second, designing the dual-band/dual-susceptance stub realizing two different susceptances at those desired frequencies. The design scheme for these dual-band transformer and stubs are described in Chap. 3.

One can also think of using such circuits to match the antenna and PA directly. In such a case, the 50 Ω load is replaced by an input admittance of the antenna in Fig. 5.2a, and an additional dual-band/dual-susceptance stub is used to nullify the reactive components in the antenna input impedance as shown in Fig. 5.3a. The resistive component, which is in most cases not 50 Ω, is then matched to the required optimal impedance  $Y(f)$  to be seen by the transistor using a dual-band/dual-impedance quarter-wave transformer.

An alternative solution that does not utilize any additional stub is also shown in Fig. 5.3b. This approach is similar to the one shown in Fig. 5.2b, where the susceptance of the antenna input admittance is absorbed with stub values  $B_J(f_1)$  and  $B_J(f_2)$ , and therefore, the modified values of stubs  $B_T(f_1)$  and  $B_T(f_2)$  are used in Fig. 5.3b. In Fig. 5.3, it has been assumed that the real part of the antenna input impedance, which is mainly composed of radiation resistance and loss resistance, is independent of frequency to some extent. However, for dual-band operation, when

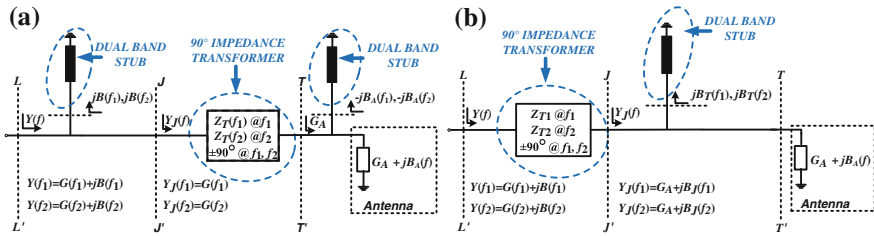


**Fig. 5.3** Dual-band matching network for direct PA and antenna-matching: **a** three sections with two dual-band stubs and **b** two sections with one dual-band stub

the two carrier frequencies are quite apart, this assumption may not be valid and the circuit should match two different complex impedances with both having distinct real and imaginary components. In such a case, the required values of characteristic impedances  $Z_T(f_1)$  and  $Z_T(f_2)$  should be different for Fig. 5.3a, whereas, for Fig. 5.3b, these values of impedances are synthesized differently and Eqs. (5.1)–(5.3) should be modified accordingly.

One more approach to match two arbitrary complex impedances [24] utilizes step-impedance transformers as shown in Fig. 5.4. In Fig. 5.4,  $Y_A(f)$  represents the antenna input admittance and  $Y(f)$  represents the required input admittance of the matching network that a transistor of PA should see in order to behave optimally in terms of efficiency and linearity. The transmission line parameters  $Z_A$ ,  $\theta_A$ ,  $Z_B$ , and  $\theta_B$  are solved by enforcing the following conditions over the impedances  $Z_{in}$  and  $Z_{out}$ :

$$Z_{in}(f_1) = Z_{in}^*(f_2) \tag{5.4a}$$

$$Z_{out}(f_1) = Z_{out}^*(f_2) \tag{5.4b}$$

The operation ‘\*’ represents the conjugate value. Details of this matching technique as shown in Fig. 5.4 are reported in [24]. If the conjugate condition in Fig. 5.4 is not applied, then the design approach will result in transcendental equations that can only be solved by optimization algorithm [24, 25].

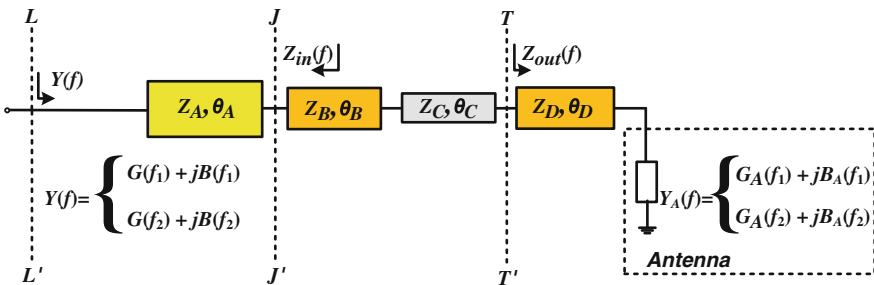


**Fig. 5.4** Dual-band matching network for direct PA and antenna-matching using step-impedance transformers [24]

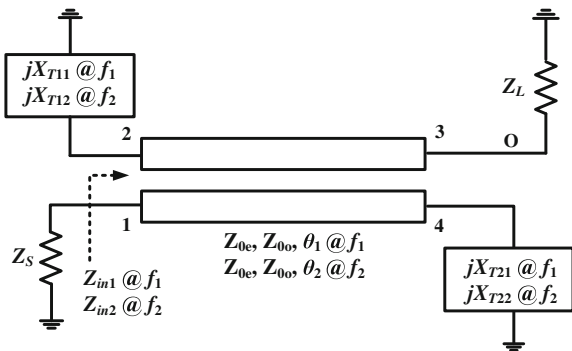
It is worth mentioning that the matching network shown in Fig. 5.4 can also realize two distinct input admittances  $Y(f)$ , for an admittance  $Y_A(f)$  that is the same at  $f_1$  and  $f_2$  and can be purely real [25]. Therefore, such matching networks can also be used for matching a 50  $\Omega$  load directly to the required optimum load obtained from the load-pull.

Similar to the topology given in Fig. 5.4, a 4-port coupled-line structure with proper terminations at its two ports can also be used for a dual-band matching network as proposed in [26]. This topology is shown in Fig. 5.5 [26]. Again, this methodology is quite suitable for direct PA and antenna-matching. However, it can also be used for direct-matching of standard 50  $\Omega$  termination to the optimum load  $Y(f)$  as shown in Fig. 5.5.

For the output matching network of the PA, this load can easily be obtained from the load-pull. In the topology of Fig. 5.5, a 4-port coupled-line is transformed into a 2-port network by terminating two alternative ports with proper admittances. Therefore, the design parameters for such matching networks are the even- and odd-mode characteristic impedances  $Z_{0e}$  and  $Z_{0o}$  and the electrical length  $\theta$  of the coupled-line along with the susceptances  $jB_1$  and  $jB_2$  each at both the frequencies. Depending on the given values of  $Y_A$  and  $Y$  at the two frequencies, the susceptances at the two alternating edges in Fig. 5.5 can be the same.

The key point in the design methodology is the choice of the coupled-line parameters  $Z_{0e}$  and  $Z_{0o}$  and the electrical length  $\theta$ , which can be arbitrarily selected by the designer based on certain electrical constraints as derived in [26], while keeping the physical constraints in mind such as the gap and width between the coupled lines that can be fabricated in the designer’s fabrication facility [27]. Once a proper choice in terms of the coupled-line design parameters is made, the rest of the design parameters in terms of stubs values  $jB_1$  and  $jB_2$  at both the frequencies can be obtained from expressions derived in [26]. It is worth mentioning that the stubs  $jB_1$  and  $jB_2$  are dual-band dual-susceptance stubs and can independently be realized using multisection stubs as discussed in Chap. 3.

**Fig. 5.5** Topology of a dual-band matching network using a coupled-line transformer [26]



**5.2.1.2 Lumped-Element-Based Concurrent Matching Techniques**

The matching networks discussed above utilize transmission-line properties to obtain the required matching. However, the traditional way of designing a lumped matching network based on the filter synthesis technique can also be used in a multiband PA. The key point in such matching networks is to model the frequency-dependent behavior of the required load terminating the matching network as shown in Fig. 5.6a. The task of the matching network is then to transform this load to the standard termination of 50 Ω. For example, in Fig. 5.1, the input impedance  $Z_{in}$  of the PA can be transformed to 50 Ω using this matching network based on filter synthesis. Therefore, for the matching networks shown in Fig. 5.6, the input impedance  $Z_{in}$  of the PA acts as the load for the matching networks in Fig. 5.6. In general, this terminating load is complex, representing the frequency-dependent behavior of this load. Figure 5.6 also shows four different possible load impedances: (a) shunt RC, (b) shunt RL, (c) series RC, and (d) series RL. Based on these four types of complex impedances, typically, four possible configurations for low-pass filter prototypes with unequal terminations are shown in Fig. 5.6.

All component values in Fig. 5.6a–d are normalized with respect to the resistive value of complex impedances. Therefore, each low-pass filter prototype used as a matching network in Fig. 5.6 transforms the impedance level  $r_s$  to 1 with the cut-off frequency of  $\Omega_c = 1$ . The Bode-Fano criterion for optimal matching in terms of the maximum possible bandwidth requires a flat return loss within the matching band [13]. This corresponds to the ideal rectangular insertion-loss characteristics [13], which can be approximated using the equal-ripple function [13]. Therefore, the low-pass filter prototype chosen in Fig. 5.7 should have equal-ripple-type characteristics as described in Sect. 3.5.2.2 of Chap. 3.

However, these filter prototypes used in matching must consider unequal termination at their ends for impedance transformation requirements in the matching problem. The starting point in the dual-band lumped element (DBLE) matching network is similar to filter synthesis, where a suitable low-pass prototype is

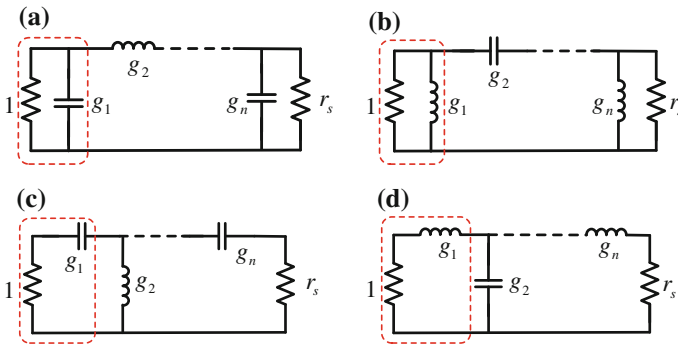


**Fig. 5.6** Low-pass prototype network: **a** shunt RC, **b** shunt RL, **c** series RC and **d** series RL

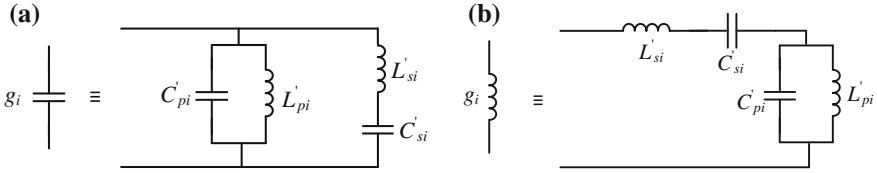


**Fig. 5.7** Element transformation by applying dual-band band-pass transformation [15]: **a** shunt element and **b** series element

selected. In the case of a matching network, the selection of a suitable prototype depends on the type of the terminating load as described in Fig. 5.6. For example, for RC shunt load, the low-pass prototype is selected as shown in Fig. 5.6a. This low-pass prototype with a low-pass response in an  $\Omega$  plane will be converted into a dual-band band-pass response by applying suitable transformations given by [14]:

$$\Omega = b_1 \left( \frac{\omega}{\omega_{01}} - \frac{\omega_{01}}{\omega} \right) - \frac{1}{b_2 \left( \frac{\omega}{\omega_{02}} - \frac{\omega_{02}}{\omega} \right)} \quad (5.5)$$

where  $\Omega$  is the normalized frequency and  $\omega$  is the denormalized frequency. The parameters  $b_1$ ,  $b_2$ ,  $\omega_{01}$ , and  $\omega_{02}$  are the parameters of the DBLE that can be obtained from the upper and lower cut-off frequencies of the two required pass-bands of the dual-band response. These parameters are given by [14, 15]:

$$b_1 = \sqrt{-\frac{n_0}{n_1 n_3}} \quad (5.6a)$$

$$b_2 = \frac{n_1 n_3^2}{n_1 n_2 n_3 - n_1^2 - n_0 n_3^2} \omega_{02} \quad (5.6b)$$

$$\omega_{01} = \sqrt{-\frac{n_0 n_3}{n_1}} \quad (5.6c)$$

$$\omega_{02} = \sqrt{-\frac{n_1}{n_3}} \quad (5.6d)$$

where the intermediate parameters  $n_0$ ,  $n_1$ ,  $n_2$ , and  $n_3$  are obtained from the upper and lower cut-off frequencies of the two required pass-bands of the dual-band response [14].

$$n_0 = \omega_{H1} \omega_{H2} \omega_{L1} \omega_{L2} \quad (5.7a)$$

$$n_1 = \omega_{H1} \omega_{H2} (\omega_{L1} + \omega_{L2}) - \omega_{L1} \omega_{L2} (\omega_{H1} + \omega_{H2}) \quad (5.7b)$$

$$n_2 = \omega_{H1}\omega_{H2} + \omega_{L1}\omega_{L2} - (\omega_{H1} + \omega_{H2})(\omega_{L1} + \omega_{L2}) \tag{5.7c}$$

$$n_3 = (\omega_{L1} + \omega_{L2}) - (\omega_{H1} + \omega_{H2}) \tag{5.7d}$$

The application of the dual-band band-pass transformation of (5.5) will convert the shunt and series elements of the low-pass prototype of Fig. 5.6 to the circuits as shown in Fig. 5.7.

After applying dual-band band-pass transformation, the shunt elements of the low-pass prototype shown in Fig. 5.6a are transformed into a four-element block with a series and shunt LC circuit as shown in Fig. 5.7a. The values of the circuit elements of this four-element block are as follows [14, 15]:

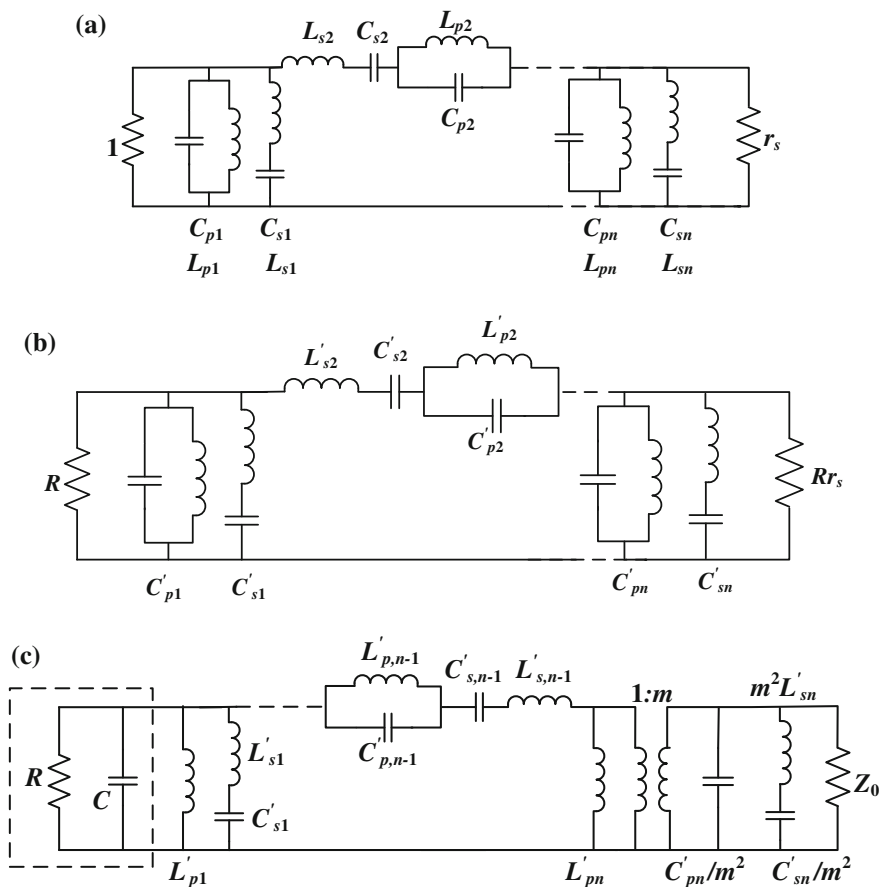


**Fig. 5.8** Various steps in designing a DBLE matching network: **a** a normalized DBLE matching network, **b** a denormalized DBLE matching network after impedance transformation and **c** a DBLE matching network with impedance transformer



$$C_{p,i} = \frac{b_1 g_i}{\omega_{01}} \quad (5.8a)$$

$$L_{p,i} = \frac{1}{b_1 g_i \omega_{01}} \quad (5.8b)$$

$$L_{s,i} = \frac{b_2}{g_i \omega_{02}} \quad (5.8c)$$

$$C_{s,i} = \frac{g_i}{b_2 \omega_{02}} \quad (5.8d)$$

Similarly, the series elements of the low-pass prototype in Fig. 5.6a are transformed into a four-element block with a series and shunt LC circuit as shown in Fig. 5.7b. The values of the circuit elements of this four-element block are as follows [14, 15]:

$$L_{s,i} = \frac{b_1 g_i}{\omega_{01}} \quad (5.9a)$$

$$C_{s,i} = \frac{1}{b_1 g_i \omega_{01}} \quad (5.9b)$$

$$L_{p,i} = \frac{g_i}{b_2 \omega_{02}} \quad (5.9c)$$

$$C_{p,i} = \frac{b_2}{g_i \omega_{02}} \quad (5.9d)$$

Thus, the transformation of each element in Fig. 5.6a according to Fig. 5.7 results in a dual-band band-pass prototype as shown in Fig. 5.8a.

In order to obtain the required shunt RC load in the left-most end of the circuit in Fig. 5.8a, an impedance denormalization is applied, where the denormalization factor is  $R$ , which is the resistance value of the required shunt RC load. The new element values of Fig. 5.8b are as follows [14, 15]:

$$L'_{s,i} = L_{s,i} R \quad (5.10a)$$

$$C'_{s,i} = \frac{C_{s,i}}{R} \quad (5.10b)$$

$$L'_{p,i} = L_{p,i} R \quad (5.10c)$$

$$C'_{p,i} = \frac{C_{p,i}}{R} \quad (5.10d)$$

The value of  $C'_{p,1}$  is included within the load to realize the shunt RC load. Therefore, the first element value  $g_1$  of the low-pass prototype filter is selected such that after all the transformations shown in Fig. 5.8, it will result in  $C'_{p,1}$  equivalent to the capacitance value  $C$  of the shunt RC load. Thus, the first element values of the low-pass prototype filter to be chosen in the initial stage are given by [14, 15]:

$$g_1 = \frac{RC\omega_{01}}{b_1} \tag{5.11}$$

where  $R$  and  $C$  are the elements of the load, which are already known. Therefore, the values of  $g_1$  and the maximum voltage reflection ratio  $|\rho|_{\max}$  can be set in the initial stage. The other element values of low-pass prototype  $g_2, g_3, \dots, g_n$  including the order  $N$ , and the values of  $r_s$ , can be obtained from the Chebyshev function characteristics as described in [13]. The element values of the low-pass prototype following the Chebyshev function characteristics are obtained as [13]

$$g_1 = \frac{2\sin\left(\frac{\pi}{2N}\right)}{x - y} \tag{5.12a}$$

$$g_i g_{i+1} = \frac{4\sin\left(\frac{2i-1}{2N}\pi\right)\sin\left(\frac{2i+1}{2N}\pi\right)}{x^2 + y^2 + \sin^2\left(\frac{i}{N}\pi\right) - 2xy\cos\left(\frac{i}{N}\pi\right)} \quad \text{for } i = 1, 2, \dots, N - 1 \tag{5.12b}$$

$$r_s = \frac{g_n x + y}{g_1 x - y} \quad \text{for } i = 1, 2, \dots, N - 1 \tag{5.13}$$

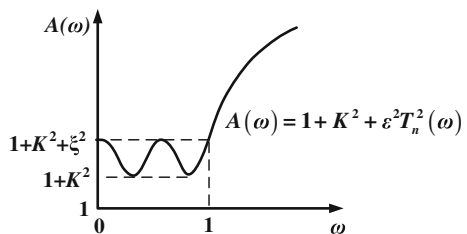
where  $r_s$  has the units of conductance if  $N$  is odd and the units of resistance if  $N$  is even. The constants  $x$  and  $y$  are obtained as [13–15]

$$x = \sinh a \tag{5.14a}$$

$$y = \sinh b \tag{5.14b}$$

where the constants  $a$  and  $b$  are related to the ripple factor  $\epsilon$  and the constant  $K$  appearing in the Chebyshev insertion-loss characteristic as shown in Fig. 5.9. This relation is as follows [13–15]:

**Fig. 5.9** Insertion-loss characteristic of the low-pass prototype defined with the Chebyshev function [13]



$$\sinh^2 na = \frac{1 + K^2}{\varepsilon^2} \tag{5.15a}$$

$$\sinh^2 nb = \frac{K^2}{\varepsilon} \tag{5.15b}$$

Since, the first element  $g_1$  of the low-pass prototype is already known from the characteristics of the load, the Eq. (5.13) can be rearranged as [13]

$$A = \frac{2}{g_1} = \frac{x - y}{\sin \frac{\pi}{2N}} \tag{5.16}$$

Moreover, the minimum value of  $|\rho|_{\max}$  can be achieved if the following condition is satisfied [13]:

$$\frac{\tanh na}{\cosh a} = \frac{\tanh nb}{\cosh b} \tag{5.17}$$

where  $a$  and  $b$  are defined in (5.14a, b). One can simultaneously solve (5.16) and (5.17) to obtain the values of  $a$  and  $b$ . Alternatively, this solution can be obtained graphically as described by Fano and given in Fig. 5.10. Similarly, a graph between  $1/|\rho|_{\max}$  as a function of  $A$  can be plotted as shown in Fig. 5.11.

From Fig. 5.11, one can start the design process by selecting the order of filter  $N$ , for specified values  $A$  and  $1/|\rho|_{\max}$ . The value of  $A$  is specified from the fixed value of the first element  $g_1$ , which depends on the load characteristics. Once the order

**Fig. 5.10** Design curves for a low-pass prototype network with  $N$  elements [13]

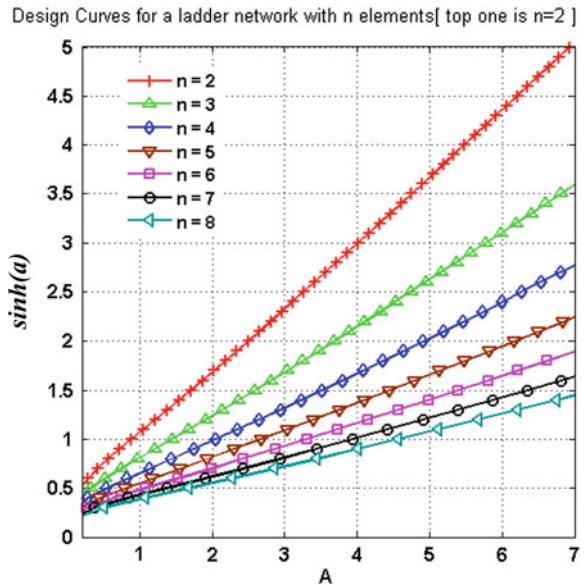
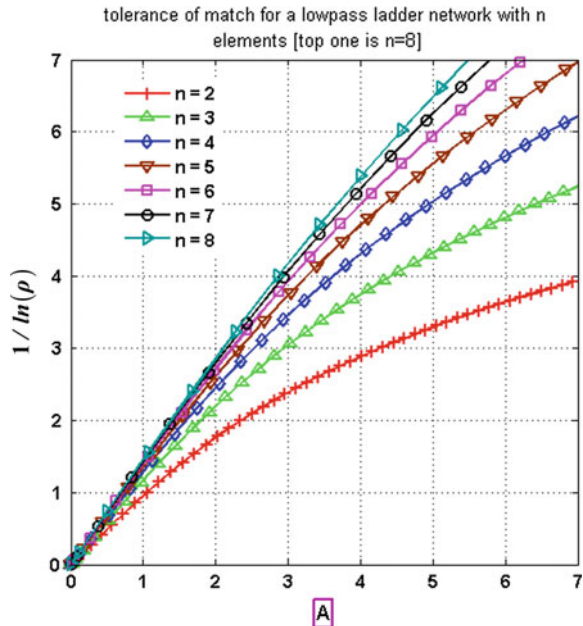


**Fig. 5.11** Tolerance of match for a low-pass prototype network with  $N$  elements [13]



$N$  is finalized, the values of  $x$  can be obtained from Fig. 5.10. After knowing the value of  $x$ , one can calculate  $y$  from (5.16) since  $A$  is already known. The values obtained for  $A$ ,  $x$ ,  $y$ , and  $N$  can be finally used in calculating all the elements of the low-pass prototype of Fig. 5.6a. It should be said that all the possible combinations of the complex terminations in Fig. 5.6 are low-pass. However, for some cases, these loads can be band-pass, where the direct low-pass prototype selection will be difficult. In such cases, the loads with band-pass response can be first converted into low-pass by applying inverse Richard’s transformation and then prototype selection done in later stages. Such a case is discussed in [28].

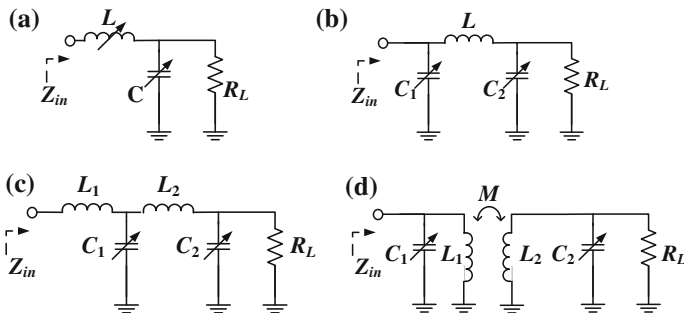
### 5.2.2 Reconfigurable Matching Techniques

Apart from concurrent applications in wireless applications, a wider range of frequencies and variable impedances can be targeted using reconfigurable matching networks. These networks are capable of matching standard  $50 \Omega$  loads to any complex impedance at a particular frequency and can be reconfigured to any other frequency with any other complex impedance. Therefore, a reconfigurable matching network should provide reconfigurability in terms of frequency of operation as well as impedance transformation. Similar to reconfigurable filters as discussed in Chap. 3, the reconfigurable matching network can be obtained by integrating a passive matching network with an active element that can be used for tuning and

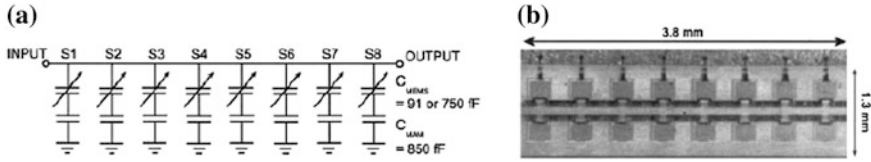
reconfigurability. So far, microelectromechanical (MEMS) and varactor diodes are the most common active elements used in reconfigurable matching networks [16, 17, 29]. Some important specifications for reconfigurable matching networks which are wide range of impedance transformation ratio, wide tuning range, wide range of frequency coverage, low loss and high linearity in case of PA design [17].

Figure 5.12 gives some topologies for reconfigurable matching networks, where variable capacitors can be realized using varactor diodes. Figure 5.12a shows a conventional  $L$ -match. Although this is the simplest form of a matching network, in order to obtain a suitable impedance transformation range it requires a varactor with a very large tuning range [17]. A pi-type network as shown in Fig. 5.12b allows an impedance transformation that can transform standard  $50\ \Omega$  loads to any point over the Smith chart, giving it a wide range of impedance transformation. The ladder structure in Fig. 5.12c provides a higher impedance ratio with a comparatively low  $Q$  of the network [17]. Figure 5.12d shows a transformer-based matching network that suffers from a trade-off between the impedance tuning range and the coupling factor of the coils [17].

It is evident from Chap. 3 that a capacitively loaded transmission acts as a slow-wave structure with changed characteristics in terms of phase velocity and characteristic impedance. In fact, this idea has been used successfully in phase shifters based on the distributed MEMS transmission line (DMTL) model [30]. Such capacitively loaded lines can also be used in reconfigurable matching networks, where  $N$ -digitally-controlled switched MEMS capacitors are used to change the effective phase shift and loaded characteristic impedance. Each MEMS switch provides a different capacitance value in the down-state position (*on* position) and up-state position (*off* position). As more MEMS switches are actuated in the down-state position, the loading of the transmission line increases, which reduces the effective loaded impedance and reduces the phase velocity corresponding to an increase in the effective dielectric constant as described in Sect. 3.4 of Chap. 3. Thus, with more MEMS being actuated, the  $50\ \Omega$  load can be transformed to a much lower input impedance. Figure 5.13 shows a schematic and photograph of a



**Fig. 5.12** Network topologies considered for the implementation of the adaptive matching network: **a** L-type network, **b** pi-type network, **c** two-section L-type network, and **d** transformer-coupled network



**Fig. 5.13** Eight-element reconfigurable matching network: **a** circuit diagram and **b** photograph [16] (reprinted with permission from the John Wiley & Sons, Inc.)

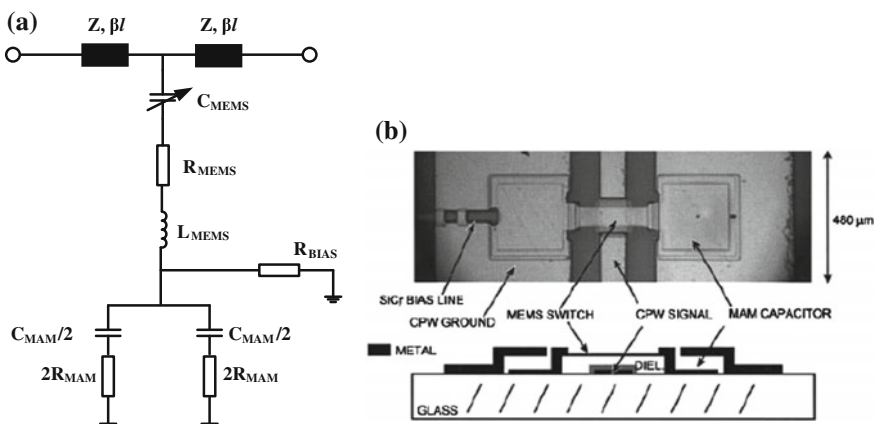
reconfigurable matching network with eight switched MEMS capacitors, which can result in 256 different points in the Smith chart, while the distributed nature of the design ensures broadband frequency coverage [16].

Figure 5.14 shows an equivalent circuit and cross-sectional views of a switched MEMS capacitor. Figure 5.14b shows a photograph of a switched MEMS capacitor.

Switched MEMS capacitors are a combination of capacitive MEMS switches attached to fixed metal-air-metal (MAM) capacitors. These fixed series capacitors can lower the high capacitance ratio of a capacitive MEMS switch, which is typically 30:1 in this case [16]. The highest frequency of operation is limited by the Bragg cut-off frequency of the loaded line, given by

$$f_c = \frac{cZ_L}{\pi s Z_0 \sqrt{\epsilon_{\text{reff}}}} \tag{5.18}$$

where  $\epsilon_{\text{reff}}$  is the effective dielectric constant of the unloaded line, and  $s$  is the period of the loaded structure.  $Z_L$  is the effective characteristic impedance of the loaded line and  $Z_0$  is the characteristic impedance of the unloaded line. The lowest impedance that can be matched to  $50 \Omega$  is dependent on the loading capacitance.



**Fig. 5.14** Switched MEMS capacitors: **a** equivalent circuits and **b** picture and cross-sectional view [16] (reprinted with permission from the John Wiley & Sons, Inc.)

### 5.3 Multiband Power Amplifier Design

The multiband PA requires each component used in the corresponding single-band PA topology to be extended to a multiband operation. A generic block diagram of a PA as shown in Fig. 5.1 typically requires biasing, stability, and matching. The biasing and matching depend on the class of operation. Therefore, for single-band PA design, once these components are finalized based on the class of operation, they are modified for operation in multiple bands. The stability and biasing networks are in general designed to operate as broadband circuits. However, the following section describes the matching networks operating in the dual-band.

#### 5.3.1 Multiband Class-AB Power Amplifier Design

Based on the matching network as discussed in Fig. 5.2a, a 10 W dual-band class-AB PA was designed for Code Division Multiple Access (CDMA) and Worldwide Interoperability for Microwave Access (WiMAX) applications at 1960 and 3500 MHz, respectively [8]. This is shown in Fig. 5.15, where Fig. 5.15b, c show the obtained efficiencies of 59.94 and 55.51 % at 1960 and 3500 MHz, respectively. The gain is higher than 10 dB at saturation for both frequencies. A 10 W GaN HEMT transistor from CREE in Fig. 5.15a is biased at 28 V and 200 mA of drain voltage

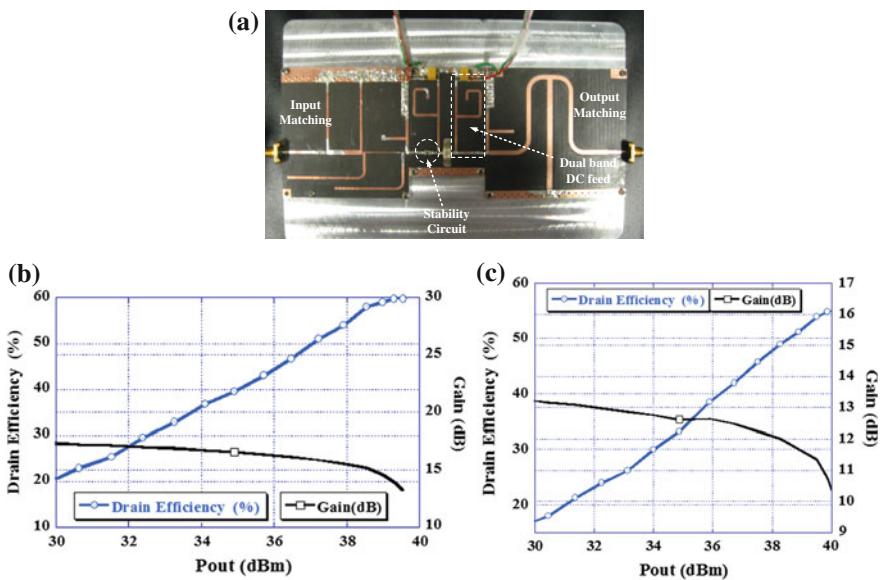


**Fig. 5.15** Design example of a class-AB PA: **a** photograph, **b** performance at 1960 MHz and **c** performance at 3500 MHz

and current, respectively. The transistor is stabilized using a series resistance at the input. Dual-band DC feed lines are used to present an open circuit at two RF frequencies and hence avoid any RF leakage to the bias circuit at the two frequencies of operation. However, an inductor or a small transmission line terminated with a bank of capacitors can also realize an appropriate DC feed [31].

A PA design using a coupled-line-based matching network shown in Fig. 5.5 is presented in [26]. Additionally, a PA based on filter synthesis techniques is presented in [28].

### 5.3.2 Multiband Class-E Power Amplifier

A class-E PA is classified under the switched mode classes of PAs, where the transistor is driven hard enough to act as switch. This is unlike the continuous-class of operation, where the transistor is considered as a current source in defining the mode of operation. Figure 5.16 shows the topology of a class-E PA, where the transistor acts as a switch with a shunt capacitor  $C_s$  present across it and a microstrip-line-based matching network [32, 33].

In a simplified analysis of a class-E PA [34], if the current flowing into the switched capacitor is assumed to be sinusoidal along with the boundary conditions imposed over the switch voltage as described in [35], all the harmonics should be set to open circuit to obtain a class-E operation. If the switching speed of the transistor is  $\omega_s$  at the fundamental frequency, the required output impedance at the fundamental frequency is given by [33, 36, 37]

$$Z_{L,f_0} = \frac{1}{C_s \omega_s} e^{i49^\circ} \tag{5.19}$$

In practice, an open-circuit termination at the second harmonic is sufficient to give a class-E operation [37]. In fact, the output impedance can also be obtained from load-pull [33]. In order to translate the load and source-matching network of

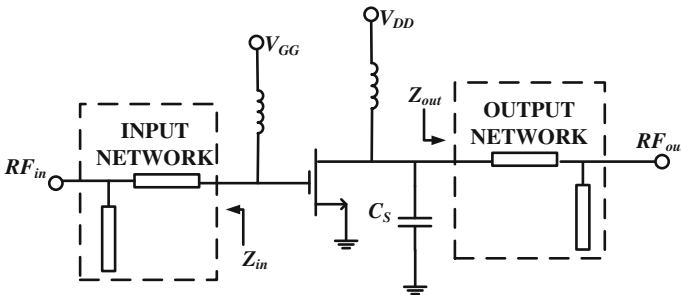


Fig. 5.16 Topology of a class-E PA [33]



class-E PA to a dual-band operation, each transmission-line section of the matching network in Fig. 5.16 should have  $50 \Omega$  characteristic impedance and specific values of electrical length  $\theta_A$  and  $\theta_B$  at two frequencies. As discussed in Chap. 3, stub-loaded transmission-line structures can be used for this purpose. However, as proposed in [33], this section describes the application of composite right/left-handed (CRLH) transmission lines for designing a dual-band matching network. Figure 5.17 shows the schematic of a quasi-lumped CRLH transmission line with one unit cell, where the right-hand (RH) line is an ordinary transmission line and the left-hand (LH) line comprises  $L$  and  $C$  lumped elements in a T-type circuit topology. One can observe from Fig. 5.17 that a lumped-realization LH transmission line is dual of RH transmission line lumped equivalent [38]. Figure 5.17b shows the lumped equivalent of an RH transmission line used in Fig. 5.17a.

From Fig. 5.17, the CRLH line is considered a balanced structure when the series and shunt resonances are equal. If  $\omega_s$  and  $\omega_p$  are the series and shunt resonance frequencies in the CRLH transmission line, then, for the structure in Fig. 5.17a to be balanced, these frequencies should be equal. This results in [38]

$$L_R C_L = L_L C_R \quad (5.20a)$$

$$Z_{0L} = Z_{0R} \quad (5.20b)$$

where  $L_R$ ,  $C_R$ ,  $L_L$ , and  $C_L$  are the inductors and capacitors in the lumped equivalent of RH and LH transmission lines, respectively, as shown in Fig. 5.17.  $Z_{0L}$  and  $Z_{0R}$  are the respective characteristic impedances of the RH and LH transmission lines, given by [33, 38]

$$Z_{0R} = \sqrt{\frac{L_R}{C_R}} \quad (5.21a)$$

$$Z_{0L} = \sqrt{\frac{L_L}{C_L}} \quad (5.21b)$$

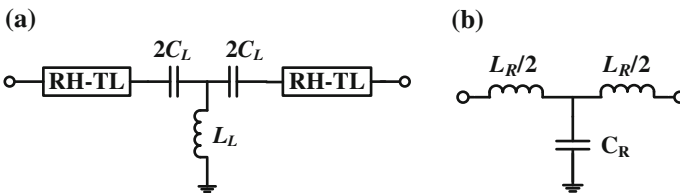


**Fig. 5.17** Schematic of a dual-band transmission line: **a** quasi-lumped equivalent of a CRLH transmission line and **b** a lumped equivalent of an RH transmission line

The effective characteristic impedance of the CRLH lines is given by [33, 38]

$$Z_{0,\text{CRLH}} = Z_{0L} = Z_{0R} \quad (5.22)$$

The values of  $Z_{0L}$ ,  $Z_{0R}$ , and  $Z_{0,\text{CRLH}}$  are usually set at  $50 \Omega$  in practice. In the balanced condition, the phase response of the RH, LH, and CRLH lines is given by [33, 38]

$$\phi_R \approx -P\sqrt{L_R C_R} \quad (5.23a)$$

$$\phi_L \approx Q\sqrt{L_L C_L} \quad (5.23b)$$

$$\phi_C = \phi_R + \phi_L \quad (5.23c)$$

where  $P$  and  $Q$  are given by [33, 38]

$$P = 2\pi N\sqrt{L_R C_R} \quad (5.24a)$$

$$Q = \frac{N}{2\pi}\sqrt{L_L C_L} \quad (5.24b)$$

If the required values of the CRLH transmission line phase shifts are  $-\phi_1$  at  $f_1$  and  $-\phi_2$  at  $f_2$ , then one can write [33, 38]

$$-Pf_1 + \frac{Q}{f_1} \approx -\phi_1 = \phi_C(f_1) \quad (5.25a)$$

$$-Pf_2 + \frac{Q}{f_2} \approx -(n\pi + \phi_2) = \phi_C(f_2) \quad (5.25b)$$

Therefore, for a given  $f_1$  and  $f_2$ , and the required phase shifts in these frequencies,  $P$  and  $Q$  values can be calculated as [38]

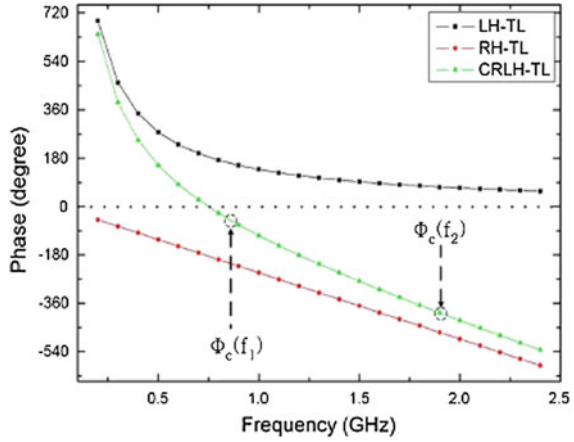
$$P \approx \frac{(n\pi + \phi_2)f_2 - \phi_1 f_1}{f_2^2 - f_1^2} \quad (5.26a)$$

$$Q \approx \frac{\frac{(n\pi + \phi_2)}{f_2} - \frac{\phi_1}{f_1}}{\frac{1}{f_1^2} - \frac{1}{f_2^2}} \quad (5.26b)$$

Figure 5.18 shows the phase response of a CRLH transmission line along with the phase responses of LH and RH transmission lines.

Figure 5.18 also shows that the required phase shifts  $-\phi_1$  at  $f_1$  and  $-\phi_2$  at  $f_2$  are realized with a negative-phase response of the CRLH transmission line.  $P$  and  $Q$  set the required slope of the CRLH transmission line in order to obtain the required phase shifts at  $f_1$  and  $f_2$ . If  $Q < 0$ ,  $P$  and  $Q$  are calculated with a large value of  $n$  in

**Fig. 5.18** Phase responses of LH, RH, and CRLH transmission lines [33] (reprinted with permission from the IEEE)



order to fit the desired phase characteristic. The value  $n$  decides the overall  $N$  numbers of the unit sections of Fig. 5.17 in a CRLH transmission line. For example, the CRLH transmission lines used in [33] to implement a class-E PA uses  $n > 2$ ; however, for  $n = 2$ , the length of an RH transmission line is almost one wavelength at frequency  $f_1$ .

It should be pointed out here that the required phase shifts at the two frequencies can be obtained using the  $N$ -section of the CRLH transmission line. This can be finalized by knowing the cut-off frequencies. The CRLH transmission line has innate LH and RH cut-off frequencies as [38]

$$f_C^{\text{LH}} = \frac{1}{4\pi\sqrt{L_L C_L}} \quad (5.27a)$$

$$f_C^{\text{RH}} = \frac{1}{\pi\sqrt{L_R C_R}} \quad (5.27b)$$

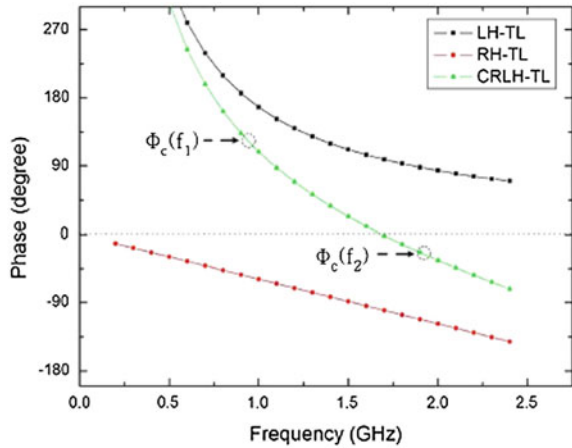
If  $f_C^{\text{LH}} < f_1$ , the design is considered complete; otherwise, one has to perform all the design steps with larger values of  $N$  [37].

The choice of the negative-phase response of the CRLH transmission line to realize the required phases sometimes results in a long physical length of RH transmission lines in Fig. 5.17. An alternative approach is to use a positive-phase region of the CRLH phase response in order to reduce the overall size of the matching network. In such a case, the phase response of the CRLH transmission line can be set as [33]

$$\phi_C(f_1) = \pi - \phi_1 \quad (5.28a)$$

$$\phi_C(f_2) = -(n\pi + \phi_2) \quad (5.28b)$$

**Fig. 5.19** Phase responses of LH, RH, and CRLH transmission lines, where the positive-phase response is used for dual-band design [33] (reprinted with permission from the IEEE)



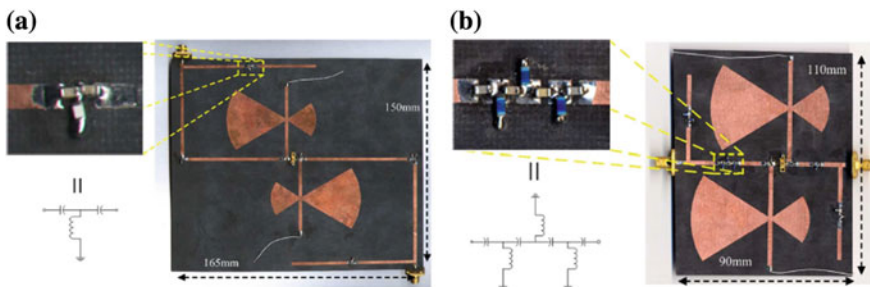
where  $\phi_{C1}(f_1)$  has a positive value since  $\phi_A \leq \pi$  and  $n$  is a positive number. Figure 5.19 shows the phase response of the CRLH transmission line using positive-phase slope characteristics.

One can observe in Fig. 5.18 that the phase response of the CRLH transmission line crosses the  $0^\circ$  phase for  $f < f_1$ , whereas in Fig. 5.19, the CRLH transmission line crosses the  $0^\circ$  phase for  $f > f_1$ .

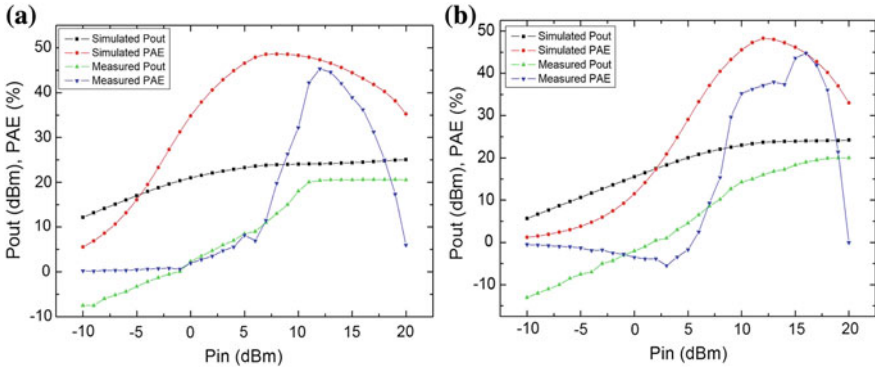
Figure 5.20 shows a photograph of a dual-band class-E PA designed using negative- and positive-phase characteristics of CRLH transmission lines [33].

Figure 5.20a shows that the CRLH transmission line realized by means of the positive phase uses a single section of the LH transmission line developed using the lumped element. Figure 5.20b shows that the CRLH transmission line utilizes two sections of the LH transmission line in a design using its positive phase.

Figure 5.21 shows the output power and power-added efficiency (PAE) of a dual-band class-E PA designed using the negative phase of the CRLH transmission line.



**Fig. 5.20** Photograph of a dual-band class-E PA designed using [33]: **a** negative-phase response of the CRLH line and **b** positive-phase response of the CRLH line (reprinted with permission from the IEEE)



**Fig. 5.21** Output power and PAEs of a dual-band class-E PA using the negative phase of the CRLH transmission line [33]: **a** 836 MHz for simulation, 830 MHz for measurement, and **b** 1.95 GHz for simulation, 1.80 GHz for measurement (reprinted with permission from the IEEE)

One can see from Fig. 5.21 that the maximum PAEs of 45.3 % and 44.7 % is obtained at 830 MHz and 1.80 GHz in measurement, respectively. The corresponding output powers are measured as 20.6 and 19.5 dBm at 830 MHz and 1.80 GHz, respectively. It is worth mentioning that the operating frequencies are referred to the frequency values within the two operating bands where the maximum power is obtained. Therefore, one can see from Fig. 5.21 that there is a discrepancy between the measurement and simulation results for some input powers. This error can be mitigated with the careful post-tuning of the matching sections.

Figure 5.22 shows the output power and PAEs of a dual-band class-E PA designed using the positive phase of the CRLH transmission line.

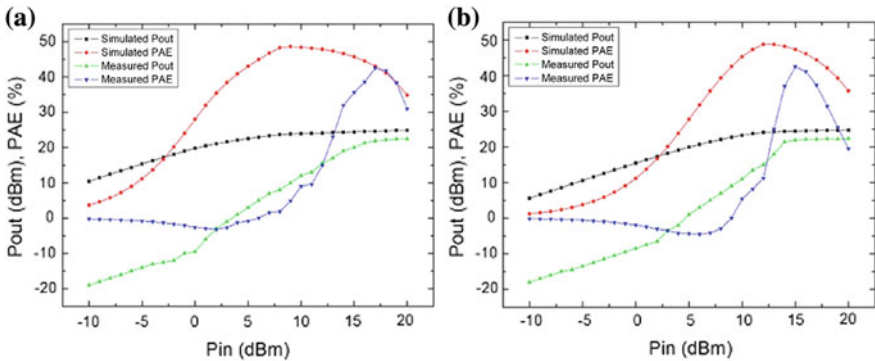


**Fig. 5.22** Output power and PAEs of a dual-band class-E PA using the positive phase of the CRLH transmission line [33]: **a** 836 MHz for simulation, 800 MHz for measurement, and **b** 1.95 GHz for simulation, 1.70 GHz for measurement (reprinted with permission from the IEEE)

From Fig. 5.23, one can observe that the maximum output powers of 22.4 and 22.2 dBm are obtained with maximum PAEs of 42.5 and 42.6 % at 800 MHz and 1.70 GHz, respectively. The details of these designs can be found in [33].

### 5.3.3 Multiband Class-F Power Amplifier

In class-F PAs, the device behaves as a current source with specific harmonic terminations in order to achieve nonoverlapping conditions between drain voltages and currents along with zero power in harmonics. The specific conditions for harmonic termination are that even harmonics should be kept short and odd harmonics kept open. In practice, applying these harmonic matching conditions in the second and third harmonics is sufficient to achieve acceptable class-F waveforms [3]. Figure 5.23 shows an output matching scheme for class-F PA along with its dual-band extension [39]. The circuit topology in Fig. 5.23a shows the appropriate scheme for matching the second and third harmonics along with the fundamental. This scheme is similar to a dual-band multisection stub as discussed in Chap. 3. Transmission line  $TL_A$  along with  $TL_B$ , which is set at length  $l_B = \lambda/4$  at  $3f_0$ , realizes the third harmonic impedance. This will create a short circuit at junction  $P$  in Fig. 5.23a. The length  $l_A$  of transmission line  $TL_A$  is selected to transform this short to open. This can be done by selecting  $l_A = \lambda/4$  at  $3f_0$ .

Similarly, the second harmonic can be controlled using  $TL_C$  and  $TL_D$ . Transmission line  $TL_D$  is set at length  $l_D = \lambda/2$  at  $2f_0$ , which will act as a  $\lambda/4$  transformer at fundamental frequency  $f_0$ . Therefore, choosing length  $l_C$  of transmission line  $TL_C$  as  $5\lambda/6$  at  $2f_0$ , the short at node  $Q$  is transformed to short at the input of the overall matching network at  $2f_0$ . It can be seen from Fig. 5.23a that the short at node  $Q$  is already realized by setting length  $l_D = \lambda/2$  at  $2f_0$ . In addition,

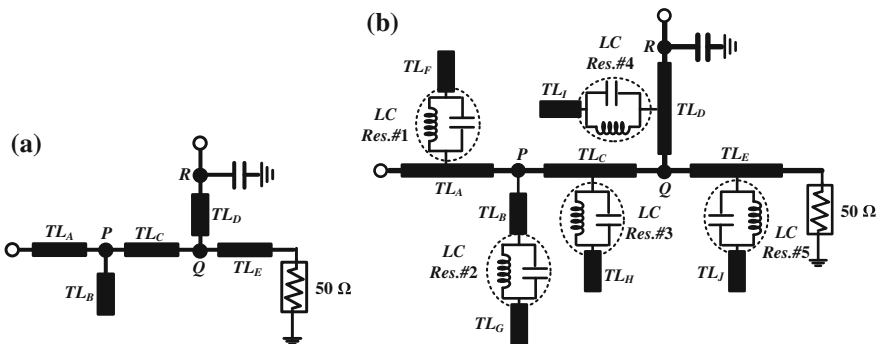


Fig. 5.23 Class-F matching network [39]: a single band and b dual band

transmission line  $TL_D$  is also used as a DC feed, which passes the DC applied at node  $R$  to  $Q$ , but inhibits RF at fundamental frequency  $f_0$  to leak from node  $Q$  to  $R$ . This is because the length of  $TL_D$  is  $\lambda/4$  at  $f_0$ , which transforms the short realized by capacitor  $C_B$  present at node  $R$  to open at node  $Q$ . Therefore, node  $R$  can also be used for applying a DC voltage to the transistor.

It is worth mentioning that in practice, at the device-package plane, the required values of load impedance at harmonics may not be perfectly open or short for a class-F operation. The condition where even harmonics are short and odd harmonics are open should be presented at the device current source plane [34, 40], and this requirement can change at the device's package plane. In such cases,  $l_A$  and  $l_C$  can be modified accordingly [35]. Moreover,  $TL_B$  acts as buffer at  $3f_0$  by realizing short at node  $P$ . This ensures that any further sections that are added beyond node  $P$  do not affect impedance set at  $3f_0$  at the input. Similarly,  $TL_D$  realizes short at  $Q$ , which ensures that any section added further, beyond node  $Q$ , does not affect the impedance realized at the input due to Sects. 5.1 and 5.2. Section 5.3 comprises line  $TL_E$ , which has length  $l_E$  set such that it realizes the required input impedance at fundamental. This requires a response of Sects. 5.1 and 5.2 at fundamental. The matching network in Fig. 5.23a can be transformed into a dual-band class-F matching network as shown in Fig. 5.23b. The matching network shown in Fig. 5.23b can match two fundamental frequencies of the dual-band operation along with the harmonics of each fundamental frequency of the dual-band operation. This is done by sizing all the electrical lengths in Fig. 5.23a for the first fundamental frequency  $f_{0,1}$  and its harmonics, as per the description above.

The additional shunt  $LC$  tank resonators are then added at specific positions to achieve matching for second fundamental frequency  $f_{0,2}$  and its harmonics. For example,  $LC$  resonator #2 attached to transmission  $TL_B$  resonates at  $3f_{0,2}$ , creating open at the end of  $TL_B$ , and therefore changing it to the case similar to the one in Fig. 5.23a. Below the resonance frequency, this shunt resonator will behave inductive and couple  $TL_B$  to  $TL_C$ . If the length of  $TL_C$  is selected appropriately, a combination of  $TL_B$ ,  $TL_C$ , and shunt  $LC$  resonator will imitate a  $\lambda/4$  line at  $3f_{0,1}$ . Therefore, node  $P$  is short circuit for both  $3f_{0,1}$  and  $3f_{0,2}$ . However, resonators #1, 3, 4, and 5 attached to transmission lines  $TL_A$ ,  $TL_C$ ,  $TL_D$ , and  $TL_E$ , respectively, are used to change the phase presented by these transmission lines appropriately at each frequency  $f_{0,1}$  and  $f_{0,2}$  and their corresponding harmonics. For example, resonator #4, attached to  $TL_D$ , resonates at  $2f_{0,2}$ , which will adjust the phase of transmission line  $TL_D$  as  $\lambda/2$  at  $2f_{0,1}$  and  $2f_{0,2}$  with the help of  $TL_I$ . Similarly, resonators #1, 3, and 5 resonate at  $3f_{0,2}$ ,  $2f_{0,2}$ , and  $f_{0,2}$ , respectively. Figure 5.24 shows a photograph and results of a dual-band class-F PA as described in [39].

This PA utilizes a 4 W GaAs MESFET device FLL351ME from Fujitsu [39]. One can see from Fig. 5.24b that peak power is higher than 32 dBm at both the bands, whereas peak drain efficiency is 45 and 61.3 % in the first and second bands, respectively.

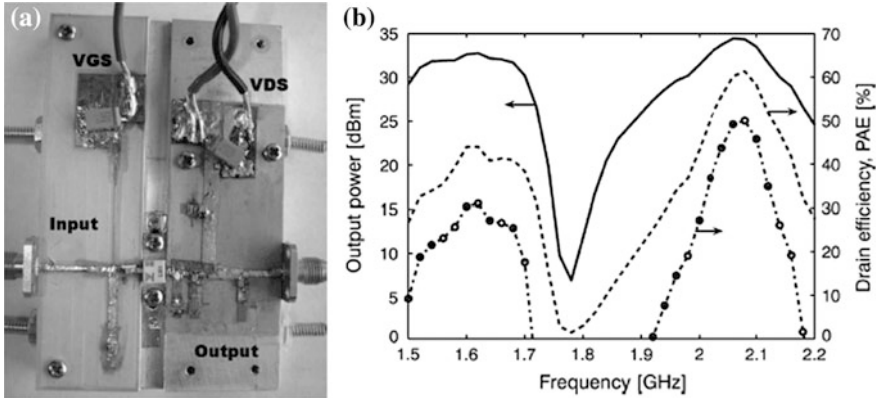


**Fig. 5.24** Dual-band class-F PA [39]: **a** photograph and **b** measured output power (*solid line*), drain (*dashed line*) and power-added (*symbols*) efficiency versus frequency (reprinted with permission from the IEEE)

## 5.4 Multiband Doherty Power Amplifier

The key design specifications of an RF power amplifier are linearity and PAE. The PAE depends on DC-to-RF conversion efficiency (drain efficiency) as well as gain. In the modern context, there is a strong motivation for reducing the carbon footprint from wireless communication by reducing the energy consumed in running base stations [41]. The PA is identified as the most power-hungry component in wireless base stations. Therefore, improving the efficiency of the PA will significantly impact the reduction of power consumption in base stations, resulting in energy-efficient wireless communication. Conventional continuous-class and switch-mode PAs amplify the RF signal with high efficiency when operated at their saturation. For this reason, such PAs operate efficiently at peak power of the input signal.

However, modern communication signals that use complex-modulated envelope-varying signals drive these PAs into the region backed off from saturation. This results in inefficient operation of PAs, leading to loss of power as heat. Moreover, these envelope-varying signals also excite nonlinearity in the PA. In such a case, a special type of PA, which has high efficiency at back-off, is required. One such scheme is the Doherty PA, which utilizes a concept of load modulation to improve efficiency at back-off. The Doherty PA is a combination of two PAs, where the main (also called a carrier) PA, is driven to voltage saturation at back-off, where the input drive is low. This is carried out by presenting the dynamic load to the main PA with the help of an auxiliary (peaking) PA. At back-off, this dynamic load is high enough to drive the main PA at saturation for low output current. However, as the output current increases with the input drive, the load reduces to maintain this peak output voltage up to saturation. Therefore, at back-off as well as saturation, the



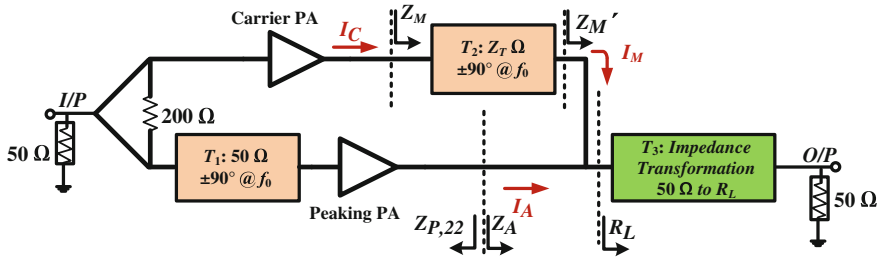


Fig. 5.25 Topology of a Doherty PA

PA is operated with the maximum voltage drive, resulting in a high efficiency region at back-off as well as saturation. A generic schematic of a Doherty PA is shown in Fig. 5.25.

In Fig. 5.25, the input signal is split between the main and auxiliary PAs with a Wilkinson power divider. The main PA is usually biased in the class-B or class-AB mode, whereas the auxiliary PA is biased in the class-C mode. The outputs of the two PAs are combined using a quarter-wave transformer  $T_2$  of characteristic impedance  $Z_T$ . The additional phase shift produced in the main PA because of this transformer is compensated by inserting a  $50\ \Omega$  transmission line  $T_1$  with an additional phase shift of  $90^\circ$  at the input of the auxiliary PA. The common load  $R_L$  is presented at node A by transforming a  $50\ \Omega$  load using a quarter-wave transformer of characteristic impedance  $R_K$  as shown in Fig. 5.25.

In a Doherty PA, the important design parameters are the device size ratio ( $\alpha$ ), the common load  $R_L$ , and the characteristic impedance  $R_T$  of the quarter-wave transformer combining the two PAs in the Doherty PA configuration. The device size ratio  $\alpha$  represents the ratio of the maximum value of the output currents of the auxiliary and main PAs given by

$$\alpha = \frac{|I_{A,\max}|}{|I_{M,\max}|} \quad (5.29)$$

The required value of the input power back-off at which efficiency is the same as saturation is related to the ratio input voltage at saturation and back-off. This is related using load modulation factor  $\beta$  defined as

$$\beta = \frac{V_{\text{in,max}}}{V_{\text{in,BO}}} = 10^{-X/20} \quad (5.30)$$

where  $X$  is the back-off in terms of input power. Figure 5.26 describes the parameters  $\alpha$  and  $\beta$  in terms of the input voltage drive. Figure 5.26a describes an arbitrary value of  $\alpha$ , whereas Fig. 5.26b describes a case of symmetric Doherty PA configuration, where  $\alpha = 1$ .

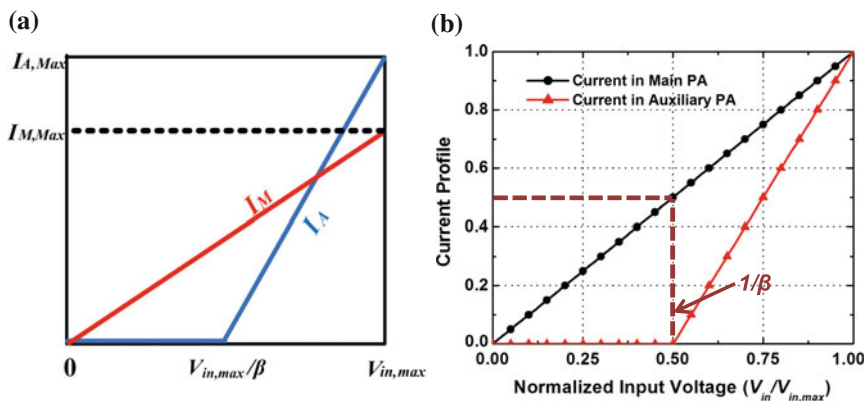


**Fig. 5.26** Output current versus input voltage in a Doherty PA: **a** for arbitrary value of  $\alpha$  and **b** symmetric devices where  $\alpha = 1$

Therefore, in a symmetric Doherty PA configuration, the devices used in the Doherty PA are the same.

The load seen by each PA can be calculated by relating the voltages and currents at the two ports of the quarter-wave transformers using its ABCD parameters. This gives the following loads seen by each PA in the Doherty PA configuration:

$$Z_M = \left( \frac{Z_T}{R_L} - \frac{I_A}{I_M} \right) Z_T \quad (5.31a)$$

$$Z_A = \left( \frac{I_M}{I_A} \right) Z_T \quad (5.31b)$$

The load seen by the main PA at back-off and saturation is given by

$$Z_{M,BO} = \frac{Z_{01}^2}{R_L} = \beta R_{opt} \quad (5.32a)$$

$$Z_{M,sat} = \left( \frac{Z_{01}}{R_L} - \alpha \right) Z_{01} \quad (5.32b)$$

Similarly, the load seen by the auxiliary PA at back-off and saturation is given by

$$Z_{A,BO} = \infty \quad (5.33a)$$

$$Z_{A,sat} = \frac{Z_T}{\alpha} \quad (5.33b)$$

For the cases where the devices are the same and have the optimum load as  $R_{\text{opt}}$ , the maximum output from each PA is ensured if the values of impedance seen by the main and auxiliary PAs at saturation are equal:  $Z_{M,\text{sat}} = Z_{A,\text{sat}} = R_{\text{opt}}$ . This results in the following expression for the design parameters  $Z_T$  and  $R_L$ :

$$Z_T = \alpha R_{\text{opt}} \quad (5.34a)$$

$$R_L = \frac{\alpha^2}{1 + \alpha^2} R_{\text{opt}} \quad (5.34b)$$

For efficiency to be maximum at back-off and saturation, one must ensure  $V_{M,\text{sat}} = V_{M,\text{BO}} = V_{M,\text{Sat}}$ , which results in

$$\beta = 1 + \alpha^2 \quad (5.35)$$

For a symmetric Doherty PA configuration,  $\alpha = 1$ , therefore,  $\beta = 2$  from (5.35). For these values, the other design parameters are calculated as  $Z_T = 2R_{\text{opt}}$  and  $R_L = R_{\text{opt}}/2$ . Figure 5.27a describes the behavior of the load seen by the main and auxiliary PAs for the input voltage drive in the case of a symmetric Doherty PA configuration. Similarly, Fig. 5.27b describes the voltage developed at the output of each PA with the input drive for a symmetric Doherty PA configuration.

The design Eqs. (5.31a, b)–(5.35) for the Doherty PA design are given by assuming an amplifier as a current source with no device parasitic and effect of matching involved. However, in practice, the main and auxiliary PAs utilize devices that are usually matched to  $50 \Omega$ , and device parasitic plays an important role in deciding the Doherty PA's behavior and cannot be neglected. Therefore, in practice, Doherty PA designs use a load combiner that presents a  $100 \Omega$  load at back-off and a  $50 \Omega$  load at saturation, assuming that the devices in the main and auxiliary PAs are matched to  $50 \Omega$  at saturation. This requires a load combiner with  $Z_T = 50 \Omega$ ,

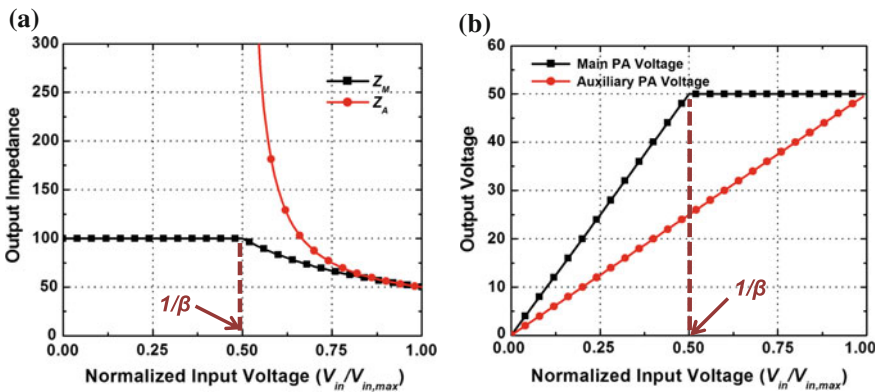


Fig. 5.27 Main and auxiliary PAs: **a** output impedances with respect to the input voltage drive and **b** output voltage with respect to the input voltage drive

$R_L = 25 \Omega$  for  $\alpha = 1$  and  $\beta = 2$ . These design parameters are obtained from (5.34a, b), and (5.35) for improvement at  $X = 6$  dB back-off while using symmetric devices. In such cases,  $50 \Omega$  presented by the load combiner at saturation should transform to  $R_{opt}$ , whereas  $100 \Omega$  presented by the load combiner at back-off should transform to  $2R_{opt}$ . This is only possible if the matching network along with the device parasitic and package response behaves as an impedance transformer with a fixed transformation ratio. In practice this transformation is achieved by using an offset line in the main PA path as shown in Fig. 5.28 [42]. Figure 5.29a shows an example of the load-pull contours shown at back-off power.

The offset line in the main PA path with phase offset  $\Phi_C$  transforms a  $100 \Omega$  load to  $Z_{opt}^*$ , which is the optimum load at back-off power. This optimum load theoretically corresponds to  $2R_{opt}$  at the current source plane as shown in Fig. 5.28. At saturation, the load presented by the load combiner is reduced to  $50 \Omega$ , and the offset line with a characteristic impedance of  $50 \Omega$  in the main PA path will not present effect at saturation provided that there is a proper matching of load. The offset line of phase offset  $\Phi_P$  in the auxiliary PA path ensures that the main PA current  $I_C$  will see an open-circuit condition at the output of the auxiliary PA as described by  $Z_{p,22}$  in Fig. 5.28. This offset line will shift the non-open-circuit condition as described by  $Z'_{p,22}$  in Fig. 5.28 to the open-circuit condition. The operation of this offset line in the main path is described in Fig. 5.29b, where the output impedance of the auxiliary PA in the off condition is shown in the presence and absence of the offset line of phase offset  $\Phi_P$  in the auxiliary PA path.

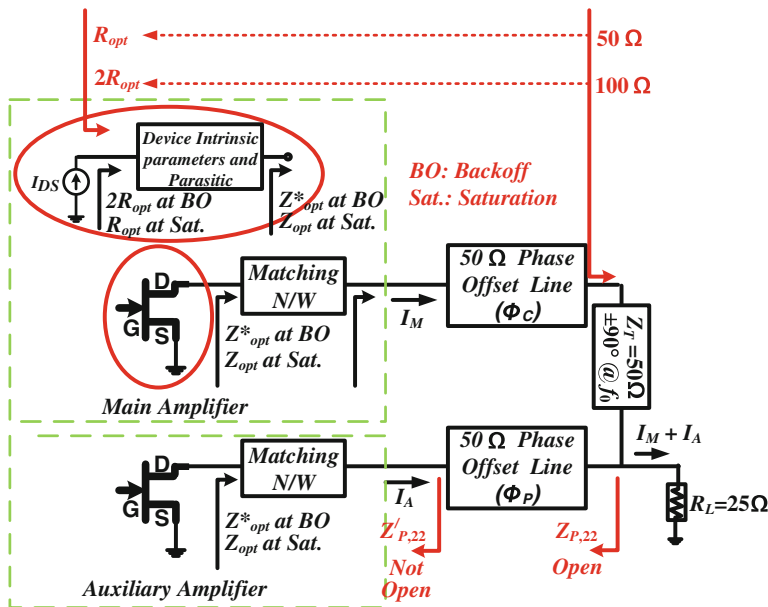


Fig. 5.28 Topology of a Doherty PA with offset lines

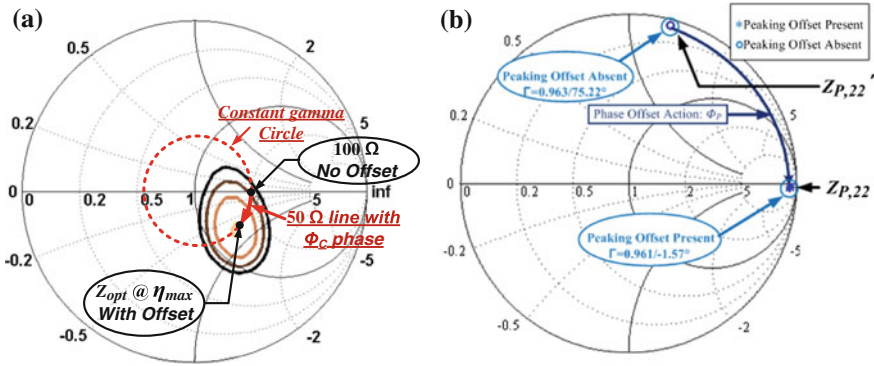


Fig. 5.29 Operation of offset lines: **a** main PA path and **b** auxiliary PA path

In order to extend the single-band operation of a Doherty PA to multiband, each component in a Doherty PA architecture must be replaced using multiband/broadband components. Figure 5.30 shows the dual-band Doherty PA architecture.

One can observe that instead of using a Wilkinson power divider and an input offset line in the auxiliary path as shown in Fig. 5.25, a branch-line coupler can be used. All the components including PAs should be dual-band/broadband. The input offset lines are used to compensate for the offset lines added at the output of the main and auxiliary PAs. However, if these output offset lines in the main and auxiliary paths are the same, then one can avoid the input offset lines.

### 5.4.1 Multiband Doherty Power Amplifier Design

In general, most of the dual-band components as described in Fig. 5.30 are already discussed in Chap. 3. The specifications and performance requirements of each circuit component are similar to its respective single-band configuration, which are readily available in the literature [43–47] and described in the previous section. Figure 5.31 shows the schematic of a proposed dual-band DPA [48, 49]. This configuration utilizes the dual-band components described in Chap. 3.

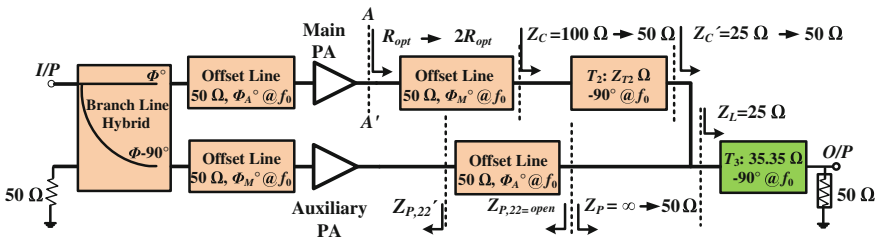


Fig. 5.30 Topology of a dual-band Doherty PA

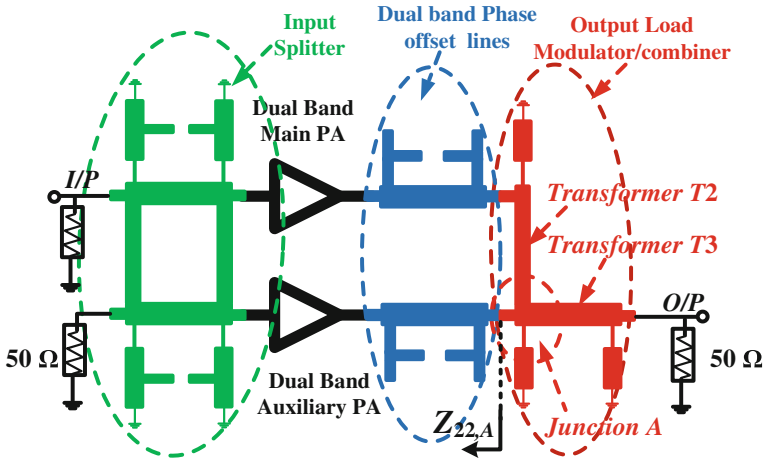
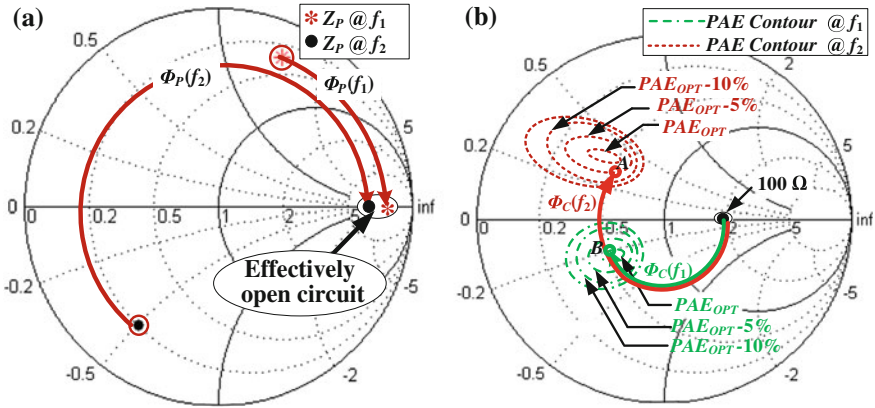


Fig. 5.31 Schematic of a dual-band Doherty PA

The architecture of the dual-band offset line is quite similar to a dual-band/dual-impedance transformer as described in Chap. 3, except that in this particular case, a transmission line of the same characteristic impedance of  $50 \Omega$  and two different electrical lengths at two different frequencies is required. It may be mentioned here that the offset lines at the output of the main and auxiliary PAs are the same, and therefore, no input offset lines are being used. The main PA is a dual-band PA biased at class-AB operation. This involves a dual-band matching topology, in order to match a  $50 \Omega$  load to two arbitrary complex impedances seen by the device at two desired frequencies of operation. Such complex impedances are obtained by a load-pull analysis of a stable GaN-based HEMT device biased for class-AB operation in order to obtain an optimum PAE at saturation.

Once the main PA is designed, the peaking amplifier can be developed: the peaking amplifier is similar to the main amplifier circuit, but biased at class-C operation. After this, a load modulation combiner is designed using a pi-type quarter-wave transformer, which has been described in Chap. 3. For a load modulation factor  $\beta = 2$ , an impedance transformer with a characteristic impedance of  $50 \Omega$  is required and represented as transformer T2 in Fig. 5.31. Accordingly, transformer T3 in Fig. 5.31 has a characteristic impedance of  $35.35 \Omega$ , which transforms a  $50 \Omega$  load to  $R_L = 25 \Omega$  at junction A, as per standard DPA architecture. A corresponding input splitter will be designed as a dual-band branch-line hybrid using pi-type quarter-wave transformers as shown in Fig. 5.31.

The  $50 \Omega$  dual-band phase-offset lines in the carrier and the peaking path as shown in Fig. 5.30 are used to optimize the overall performance of the dual-band DPA. The phase-offset line at the output of the peaking amplifier adjusts the impedance  $Z_A$  in Fig. 5.31 to a high value in order to avoid any power leakage from the carrier to the peaking path. This operation is illustrated in Fig. 5.32a, where a  $50 \Omega$  line shifts the corresponding  $Z_A$  to effectively open-circuit points.



**Fig. 5.32** Operation principle of a dual-band phase-offset line: **a** peaking path and **b** carrier path (reprinted with permission from the IEEE)

Since  $Z_A$  can be different at two frequencies for dual-band applications, the phase shift provided by this line at the two frequencies of the operation is different (represented as  $\Phi_A(f_1)$  and  $\Phi_A(f_2)$  in Fig. 5.32a). Therefore, the design requires a  $50 \Omega$  dual-band phase-offset line with arbitrary phases at the two frequencies. If the impedance  $Z_A$  is effectively open in the back-off (low-power region), then the carrier amplifier will see  $100 \Omega$ , which appears because of the  $50 \Omega$  load transformation by the two quarter-wave transformers of  $50$  and  $35.35 \Omega$  in the load modulation circuit.

When this  $100 \Omega$  load appears at the output of a carrier PA matching network, the offset line in the main path ensures that the optimum impedance corresponding to the optimum PAE will be seen by the device in the main PA at back-off. The operation of such an offset in the main path is shown in Fig. 5.32b, where a  $100 \Omega$  load is shifted to the optimum PAE points (A and B).

Since the optimum load condition also varies with the OPBO [50], a separate load-pull simulation for a main PA along with its matching networks (at the reference plane of the output matching network) is required for the back-off power region, and various PAE contours are plotted as shown in Fig. 5.32b. Each phase-offset line adds corresponding phases in its path; hence, an additional  $50 \Omega$  dual-band phase-offset line is added at the input to compensate for the phase difference in the two paths.

It is worth mentioning that at saturation, the load seen by each main and auxiliary PA is  $50 \Omega$ , and hence, the addition of these  $50 \Omega$  dual-band phase-offset lines will not have any effect at saturation, and the overall matching conditions at saturation for which the main and auxiliary PAs were designed will remain intact. Moreover, it is also evident from Fig. 5.32b that it is not always possible to achieve optimum load (represented as  $PAE_{OPT}$  in Fig. 5.32b) with such phase-offset lines, which depends on the position of the PAE contours in the Smith chart. However, a closest point can be achieved as shown in Fig. 5.32b for the case of frequency  $f_2$ .





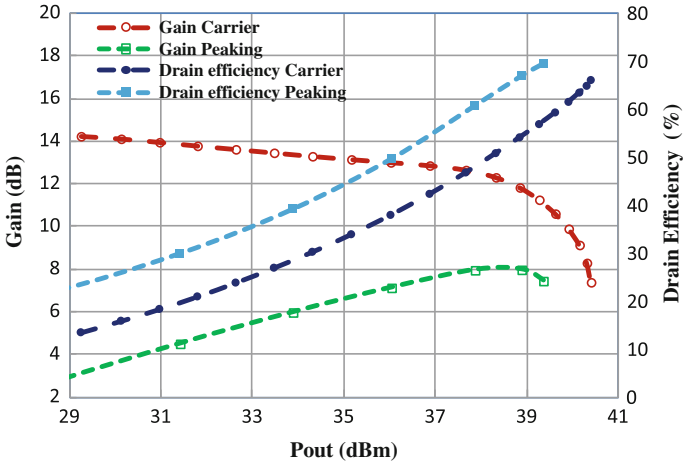


Fig. 5.34 Performance of a carrier and peaking amplifier at 1960 MHz [48] (reprinted with permission from the IEEE)

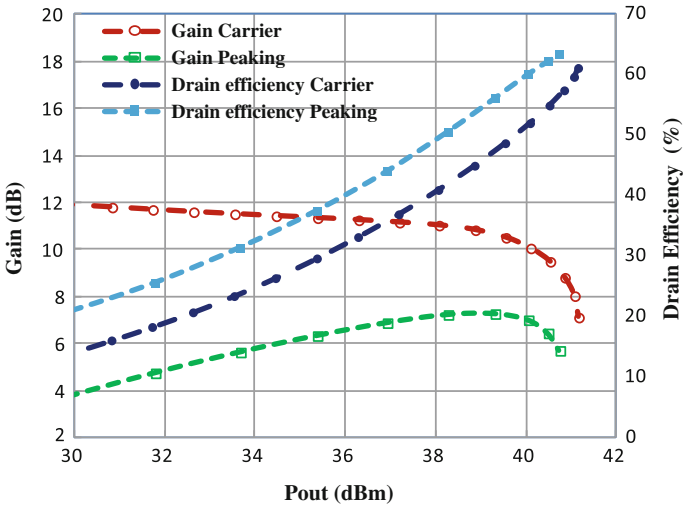


Fig. 5.35 Performance of a carrier and peaking amplifier at 3500 MHz [48] (reprinted with permission from the IEEE)

The peak drain efficiencies of the main PA and auxiliary PAs are 66.1 and 69.5 %, respectively, at 1960 MHz as shown in Fig. 5.34. Similarly, from Fig. 5.35, the peak drain efficiencies of the auxiliary and main PAs can be obtained as 61.1 and 63.4 %, respectively, at 3500 MHz. From these figures, the PAE of the main PA can be calculated as 54 and 49.7 % at 1960 and 3500 MHz, respectively.

Similarly, the PAE of the auxiliary PA is calculated as 49.7 and 48.2 % at 1960 and 3500 MHz, respectively.

It has been discussed in Chap. 3 that the dispersive property of a stub-loaded structure can be used to modify its nonlinear phase response to obtain different electrical lengths (phase shifts) at different frequencies. Therefore, the stub-loaded structure as described in Fig. 3.21 of Chap. 3 is investigated for dual-band phase-offset line applications [48]. The proposed structure is analyzed here to imitate dual-band line characteristics with arbitrary electrical lengths  $\theta_{T1}$  and  $\theta_{T2}$  at  $f_1$  and  $f_2$ , respectively, while the characteristic impedance is  $50 \Omega$  in both the frequencies.

If an arbitrary stub value  $B_S$  loads a transmission line of characteristic impedance  $Z_S$  and electrical length  $\theta_S$ , as shown in Fig. 3.21a, the ABCD parameter of the overall structure can be given by an expression similar to (3.31) in Chap. 3. The respective overall effective electrical length ( $\theta_T$ ) and the characteristic impedance ( $Z_T$ ) of the structure in Fig. 3.21a are given by (3.32) and (3.33). For the convenience of the readers, these expressions are rewritten here as

$$\cos(\theta_T) = \frac{A+D}{2} = \cos\theta_S - B_S Z_S \sin\theta_S \quad (5.36a)$$

$$Z_T = \sqrt{\frac{B}{C}} = Z_S \sqrt{\frac{1}{1 - Z_S^2 B_S^2 + 2Z_S B_S \cot\theta_S}} \quad (5.36b)$$

If  $n$  is the frequency ratio of  $f_1$  and  $f_2$ , where  $f_1$  is the smaller of  $f_1$  and  $f_2$ , (5.36b) can be rearranged as [48]

$$\frac{Z_S^2}{Z_T^2} = 1 - k^2(f_1) + 2k(f_1)\cot\theta_S \quad @f_1 \quad (5.37a)$$

$$\frac{Z_S^2}{Z_T^2} = 1 - k^2(f_2) + 2k(f_2)\cot n\theta_S \quad @f_2 \quad (5.37b)$$

where  $Z_T$  is the effective characteristic impedance at two frequencies and  $k$  is defined as

$$k(f_1) = Z_S B_S(f_1) \quad @f_1 \quad (5.38a)$$

$$k(f_2) = Z_S B_S(f_2) \quad @f_2 \quad (5.38b)$$

Similarly, (5.36a) can be rearranged as

$$k(f_1) \sin(\theta_S) = \cos\theta_S - \cos\theta_{T1} \quad @f_1 \quad (5.39a)$$

$$k(f_2) \sin(n\theta_S) = \cos n\theta_S - \cos\theta_{T2} \quad @f_2 \quad (5.39b)$$

Substituting the corresponding values of  $k$  at  $f_1$  and  $f_2$  from (5.39a) and (5.39b), respectively, in (5.37a) and (5.37b), one can obtain the following simplified relation [48]:

$$Z_S = Z_T \frac{|\sin\theta_{T1}|}{|\sin\theta_S|} \quad @f_1, \quad Z_S = Z_T \frac{|\sin\theta_{T2}|}{|\sin n\theta_S|} \quad @f_2 \quad (5.40)$$

Thus, from (5.39a, b), the following ratio  $M$  can be obtained as

$$M = \frac{|\sin\theta_{T2}|}{|\sin\theta_{T1}|} = \frac{|\sin n\theta_S|}{|\sin\theta_S|} \quad (5.41)$$

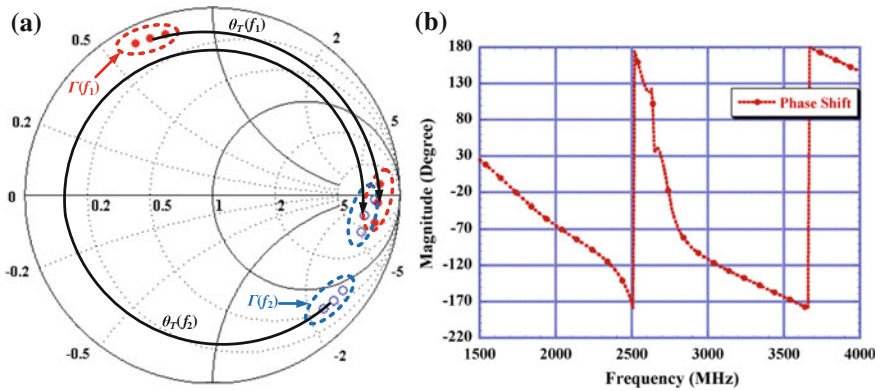
For given values of  $\theta_{T1}$ ,  $\theta_{T2}$ , and  $n$ , (5.40) can be solved analytically or graphically to obtain the electrical length  $\theta_S$  of the loaded line [48]. One can observe that the ratio in (5.41) is the same as the one in (3.63) in Chap. 3. Therefore, Fig. 3.22, showing dependence of the ratio  $M$  over the values of  $\theta_S$  for different values of  $n$  corresponding to various wireless commercial standards, can also be used as the design curves in this case. For given values of  $\theta_{T1}$ ,  $\theta_{T2}$ , and  $n$ , Fig. 3.22 can be used to obtain the electrical length  $\theta_S$  of the loaded line. Once the value of  $\theta_S$  is determined,  $Z_S$  can be calculated from (5.40), for a desired value of  $Z_T$ , which is  $50 \Omega$  in the present case.

Similarly, the value of  $k$  at the two frequencies  $f_1$  and  $f_2$  can be obtained using (5.38a, b). The design parameter  $B_S$  at the two frequencies  $f_1$  and  $f_2$  is then calculated using (5.39a, b), respectively, once  $Z_S$  and  $k$  are known. The final step in the design is to realize  $B_S(f_1)$  and  $B_S(f_2)$  using the dual-band multisection stub of Fig. 3.21b as described in Chap. 3 in the design of a dual-band matching network. Using the design methodology described above, the dual-band offset line can be designed in context to the dual-band Doherty PA operation. Thus, in order to obtain the design specifications for the dual-band offset lines, the graphs similar to Fig. 3.3 are obtained from the simulation of carrier and peaking amplifiers. Figure 5.36 shows the output return loss of the designed peaking amplifier (without any offset line), which is represented as  $\Gamma(f_1)$  and  $\Gamma(f_2)$  at the two frequencies.

It can be seen from Fig. 5.36a that the approximate values of electrical lengths required to bring these impedances to higher values are  $55.84^\circ$  and  $159.68^\circ$  at frequencies  $f_1$  and  $f_2$ , respectively. Figure 5.36b shows the measured phase response of the dual-band phase-offset line. A phase shifts of  $58.87^\circ$  and  $163.2^\circ$  at 1960 and 3500 MHz, respectively, are reported with this phase-offset line.

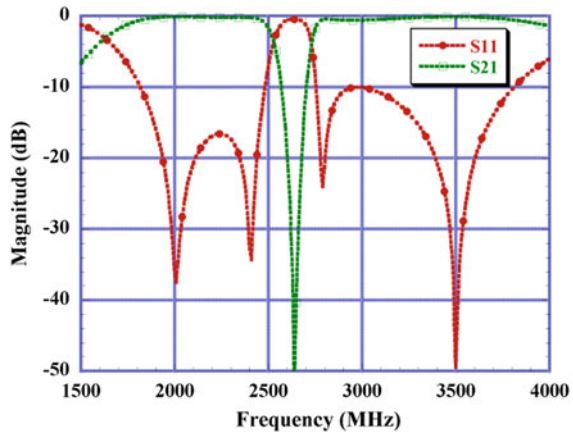
In the presence of this offset line, the required high impedance is achieved at the output of the peaking amplifier at back-off. This fact can also be observed in Fig. 5.36a, where the output impedance of the peaking amplifier is also measured in the presence of this offset line.

Figure 5.37 shows the s-parameters corresponding to the insertion loss and return loss characteristics of this phase-offset line.



**Fig. 5.36** Design specifications and performance of a phase-offset line in the auxiliary PA path **a** in terms of output reflection coefficient of the auxiliary PA and **b** phase response [48] (reprinted with permission from the IEEE)

**Fig. 5.37** S11 and S21 parameters of a dual-band phase-offset line [48] (reprinted with permission from the IEEE)

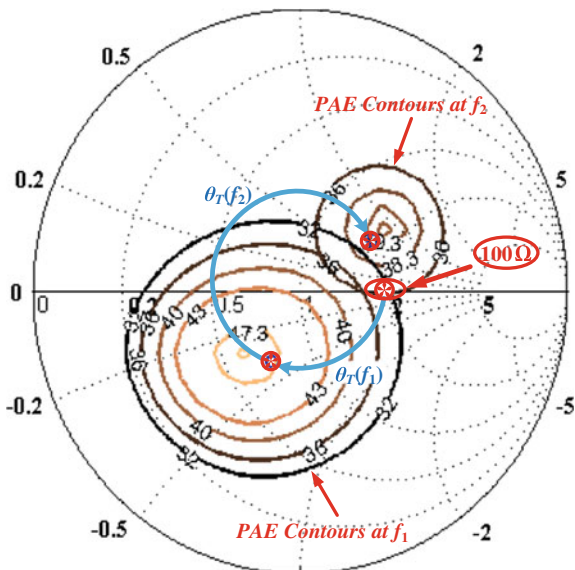


One can see from Fig. 5.37 that the insertion loss is less than 0.12 dB and the return loss is higher than 24 dB at both the frequencies, confirming the characteristic impedance of 50  $\Omega$  for these lines.

Similarly, in order to obtain the required value of phase offset in the carrier path, a load-pull simulation of the main PA including the matching network is done at 6 dB OPBO. These load-pull contours for PAE are plotted in Fig. 5.38. Thus, in order to bring 100  $\Omega$  to these optimum PAE points, dual-band offset lines with arbitrary phases are needed.

In our particular case, when a phase-offset line that is the same as the peaking path is inserted at the output of carrier, it shifts a 100  $\Omega$  load at back-off to the impedances corresponding to reasonable PAEs, i.e., 47.3 and 39.3 %, for the frequencies of 1960 and 3500 MHz as shown in Fig. 3.12. However, in the absence of

**Fig. 5.38** Performance of a carrier amplifier in terms of PAE at OPBO in the presence of phase-offset lines in the carrier path [48] (reprinted with permission from the IEEE)



this offset line, the 100 Ω load lies on the 32 and 38 % PAE contours at frequencies of 1960 and 3500 MHz, respectively. Figure 5.39 shows the effect of these offset lines in the electromagnetic (EM)-based performance of an integrated dual-band DPA at 1960 and 3500 MHz.

From these figures, it can be inferred that the absence of the offset lines at 1960 MHz reduces the efficiency by approximately 9 % at 6 dB back-off. Moreover, at 3500 MHz, the absence of an offset line in the auxiliary PA path reduces efficiency by approximately 7.8 %, whereas the absence of a phase-offset line in the main PA path reduces efficiency by 3.4 % at 6 dB back-off. The reduction of efficiency at back-off in the absence of a main offset line is more prominent at 1960 MHz compared with the operation at 3500 MHz as the PAE

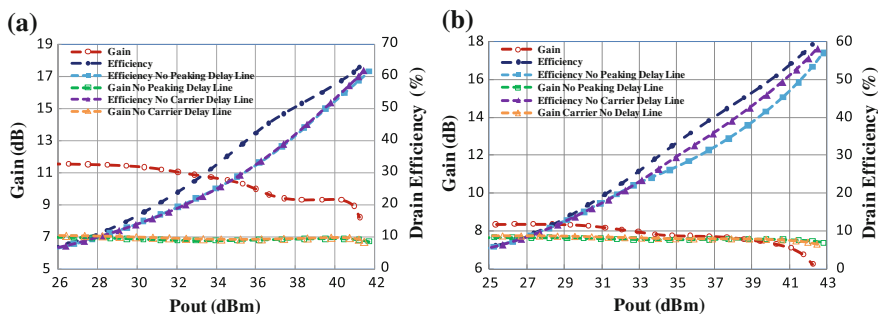


**Fig. 5.39** Effect of phase-offset lines over the performance of the dual-band Doherty amplifier: **a** at 1960 MHz and **b** at 3500 MHz (reprinted with permission from the IEEE)

contours are much closer to  $100\ \Omega$  in the later case as shown in Fig. 5.38. Figure 5.39 also shows the performance improvements in terms of gain in the presence of these offset lines at 1960 and 3500 MHz, respectively.

In order to validate the proposed design architecture and design methodology, each component of the dual-band Doherty PA is fabricated in Rogers RT 5870 board with a dielectric constant of 2.33 and a loss tangent of 0.0012. The substrate thickness is 20 mil. A photograph of an integrated Doherty PA is shown in Fig. 5.40.

The designed dual-band Doherty PA is measured in the presence of continuous-wave (CW) single tones at 1960 and 3500 MHz fed at its input individually. Figure 5.41 shows the performance of a dual-band DPA in comparison with the class-AB balanced-mode operation, at 1960 and 3500 MHz, respectively.

For the operation at 1960 MHz, as shown in Fig. 5.41a, there was an approximately 15.3 % improvement in the drain efficiency compared with the class-AB balanced-mode operation at 6.6 dB back-off. The corresponding PAE improvement is 10.7 %. Figure 5.41b depicts the measured performance of a dual-band DPA in comparison with the class-AB balanced-mode operation, at 3500 MHz. At this frequency, the drain efficiency improvement was around 10.2 % compared with the class-AB balanced-mode operation at 6.7 dB back-off, as shown in Fig. 5.41b. The corresponding PAE improvement is 7.1 % at this back-off.

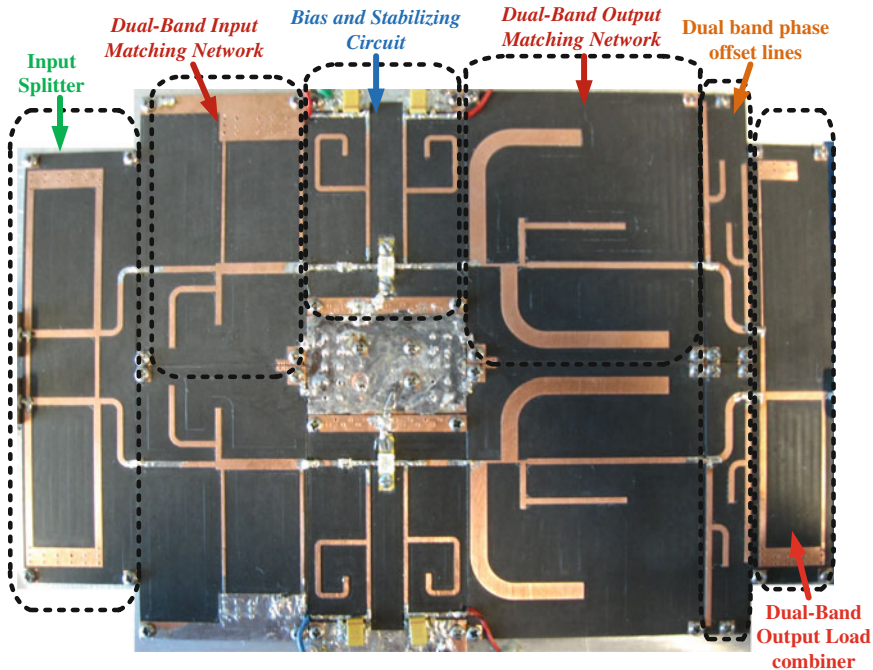


**Fig. 5.40** Photograph of a fabricated dual-band Doherty amplifier [48] (reprinted with permission from the IEEE)

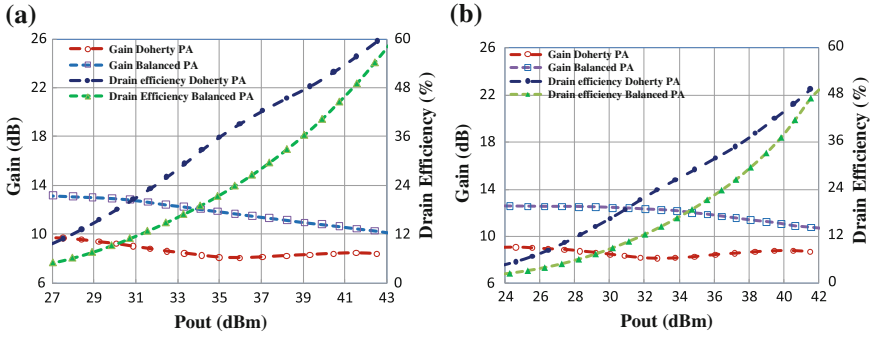


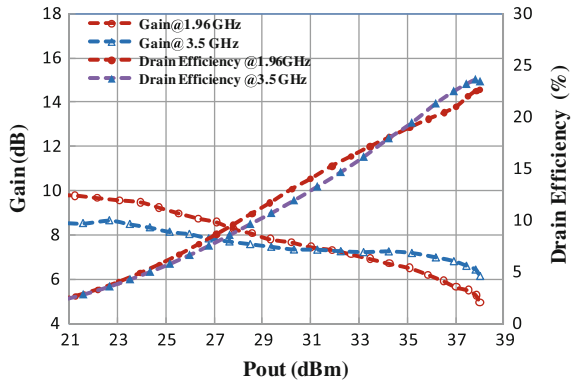
**Fig. 5.41** Measured performance of a dual-band Doherty PA with CW signal at **a** 1960 MHz and **b** 3500 MHz [48] (reprinted with permission from the IEEE)

Although the proposed dual-band DPA design is optimized for individual frequency operation, there is no theoretical limit on the concurrent operation of such a dual-band DPA. Figure 5.42 represents the concurrent operation of the designed dual-band Doherty amplifier.

However, it should be said here that because of the simultaneous power fed at two carrier frequencies, the PA saturates faster; hence, it appears that the PA performs at each frequency as it operates nominally at 3 dB back-off (assuming that both driving signals have equal power levels and that the PA has the same gain at both frequencies), in comparison with its operation when driven by a single-frequency signal. This back-off will be further enhanced if the PA has different gains at the two different frequencies. Figure 5.42 shows that during concurrent operation, the peak drain efficiencies at saturation are 22.5 and 23.4 % at 1960 and 3500 MHz, respectively, whereas the peak PAEs are reported as 15.8 and 17.7 % at 1960 and 3500 MHz, respectively.

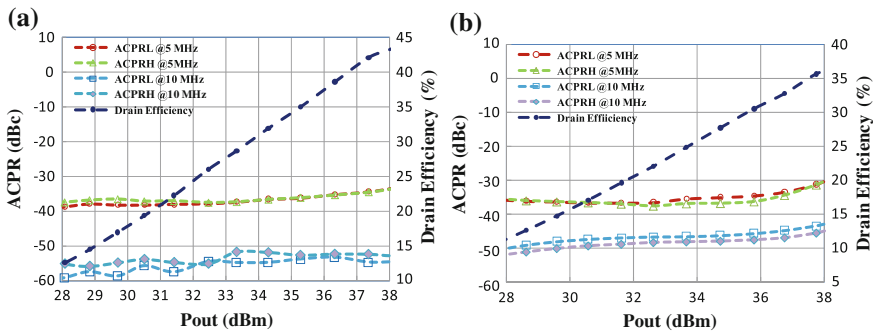
In order to test the designed dual-band DPA in the presence of complex-modulated signals, the output of the designed DPA is measured in the presence of single-carrier WCDMA at 1960 MHz, and a 5 MHz WiMax signal at

**Fig. 5.42** Measured performance of a dual-band Doherty amplifier in the concurrent mode (reprinted with permission from the IEEE) [48]



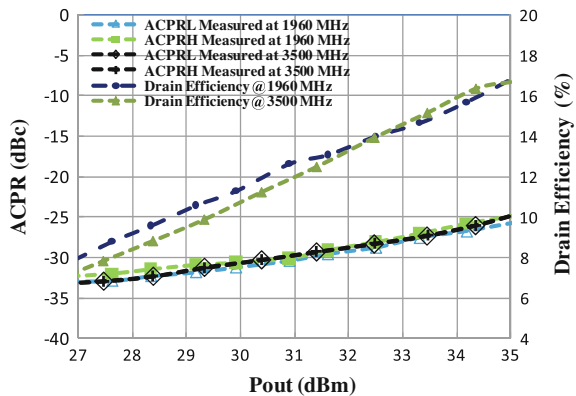
3500 MHz, both having a peak-to-average power ratio of 7 dB. Figure 5.43 shows the average drain efficiency and adjacent channel power ratio (ACPR) measured at 5 MHz and 10 MHz offset and plotted with respect to the average power of complex-modulated signals. This figure also shows a slight difference between the lower side ACPR (ACPRL) and the higher side ACPR (ACPRH), which corresponds to memory effect in the PA. Since the average efficiency depends on the probability density function of the modulated signal, it has slightly different values from the efficiency achieved at back-off in the CW excitation. The ACPRs are higher than  $-34$  and  $-31$  dBc at 1960 and 3500 MHz, respectively. The average efficiencies are 42.1 and 36.8 % at 1960 and 3500 MHz, respectively.

Figure 5.44 shows the average efficiency and ACPR performance in the concurrent mode in the presence of modulated signals at the input. It is clearly evident from this figure that in the concurrent mode, the average efficiency and ACPR performance are poor compared with the individual operations at the respective frequencies.



**Fig. 5.43** Measured average drain efficiency and ACPR with complex-modulated signals: **a** one-carrier WCDMA signal at 1960 MHz and **b** 5 MHz WiMax signal at 3500 MHz [48] (reprinted with permission from the IEEE)

**Fig. 5.44** Measured average drain efficiency and ACPR in concurrent operation with one-carrier WCDMA signal at 1960 MHz and 5 MHz WiMax signal at 3500 MHz [48] (reprinted with permission from the IEEE)





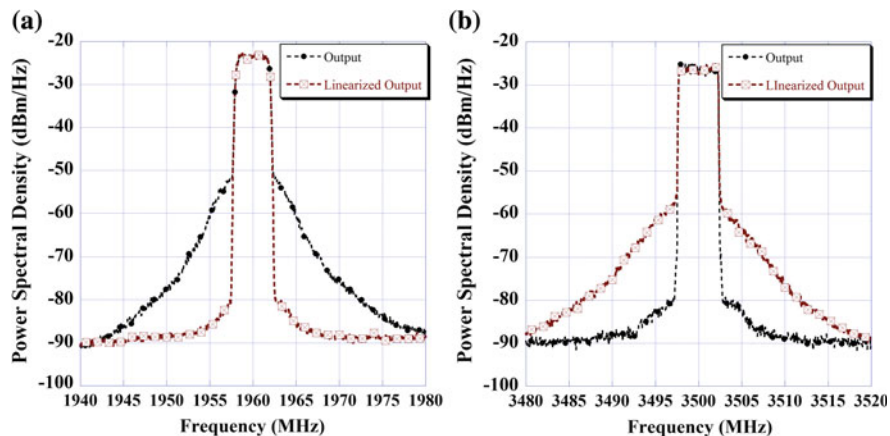


**Fig. 5.45** Output power spectral density of a dual-band Doherty PA measured in the presence and absence of digital predistortion with **a** a WCDMA signal at 1960 MHz and **b** a WiMax signal at 3500 MHz [48] (reprinted with permission from the IEEE)

This is because the DPA saturates faster in simultaneous excitation by the two signals, which also interact and cause lower ACPR performance. The average efficiencies are 16.9 and 16.7 % at 1960 and 3500 MHz, respectively, whereas the ACPR is higher than  $-24.7$  dBc at corresponding frequencies of operation.

In order to validate the use of the designed DPA in conjunction with digital predistortion (DPD), the designed DPA is linearized using the memory-polynomial-based DPD model. Figure 5.45 shows the linearized output of the DPA, in the presence and absence of DPD, at 1960 and 3500 MHz, respectively.

These figures show that the linearized output satisfies the spectral-mask requirements for WCDMA and WiMax signals. With the DPD linearization, there is a corresponding 25 and 20 dB improvement in terms of ACPR at 1960 and 3500 MHz, respectively.

## References

1. G. Gonzalez, *Microwave Transistor Amplifiers: Analysis and Design*, 2nd edn. (Prentice Hall, New Jersey, 1997)
2. T.T. Hà, *Solid State Microwave Amplifier Design* (Wiley, New York, 1981)
3. A. Grebennikov, N. Sokal, M. Franco, *Switchmode RF and Microwave Power Amplifiers*, 2nd ed. (Elsevier, Burlington, 2012)
4. S.C. Cripps, *RF Power Amplifiers for Wireless Communications*, 2nd edn. (Artech House, Boston, 2006)
5. P. Colantonio, F. Giannini, E. Limiti, *High Efficiency RF and Microwave Solid State Power Amplifiers* (Wiley, Great Britain, 2009)
6. P. Roblin, *Nonlinear RF Circuits and Nonlinear Vector Network Analyzers: Interactive Measurement and Design Techniques* (Cambridge University Press, Cambridge, 2011)

7. F.M. Ghannouchi, M.S. Hashmi, *Load Pull Techniques with Applications to Power Amplifier Design* (Springer, London, 2013)
8. K. Rawat, F.M. Ghannouchi, A novel dual-band matching technique based on dual-characteristic impedance transformer for dual-band power amplifier design. *IET Microwaves Antennas Propag.* **5**(14), 1720–1729 (2011)
9. K. Rawat, F.M. Ghannouchi, Load-pull assisted cad design of inverted Doherty Amplifier without quarter-wave transformer, in *25th IEEE Canadian Conference on Electrical and Computer Engineering (CCECE)*, Montreal, Quebec, Canada (2012), pp. 1–4
10. K. Rawat, M.S. Hashmi, F.M. Ghannouchi, Dual-band RF circuits and components for multi-standard software defined radios. *IEEE Circuit Sys. Mag.* **12**(1), 12–32 (2012)
11. K. Rawat, M.S. Hashmi, F.M. Ghannouchi, Double the band and optimize. *IEEE Microwave Mag.* **13**(2), 69–82 (2012)
12. A. Barthwal, G. Ajmera, K. Rawat, A. Basu, S.K. Koul, K. Rawat, Design scheme for dual-band three stage Doherty Power Amplifiers, in *IEEE International Microwave and RF Conference (IMaRC) 2014*, Bangalore, India, Dec 2014, pp. 80–83
13. R. Levy, Explicit formulas for Chebyshev impedance-matching networks, filters and interstages. *Proc. Inst. Electr. Eng.* **111**(6), 1099–1106 (1964)
14. G. Macchiarella, S. Tamiazzo, Design techniques for dual-passband filters. *IEEE Trans. Microw. Theory Tech.* **53**(11), 3265–3271 (2005)
15. Y. Liu, R. Levy, Y. Chen, Optimal dual-band impedance transformers with wide bandwidths for frequency dependent complex loads, in *IEEE MTT-S International Microwave Symposium Digest (IMS)*, 2013, pp. 1–4
16. T. Vähä-Heikkilä, G.M. Rebeiz, A 4–18-GHz reconfigurable RF MEMS matching network for power amplifier applications. *Int. J. RF Microwave Comput. Aided Eng. (RF Appl. MEMS Micromachining)* **14**(4), 356–372 (2004)
17. W.C. Edmund Neo, Y. Lin, X. Liu, L. C.N. de Vreede, L.E. Larson, M. Spirito, M.J. Pelk, K. Buisman, A. Akhnouk, A. de Graauw, L.K. Nanver, Adaptive multi-band multi-mode power amplifier using integrated varactor-based tunable matching networks. *IEEE J. Solid State Circuits* **41**(9), 2166–2176 (2006)
18. Y. Wu, Y. Liu, S. Li, A dual-frequency transformer for complex impedances with two unequal sections. *IEEE Microwave Wirel. Compon. Lett.* **19**(2), 77–79 (2009)
19. M.J. Park, B. Lee, Dual-band design of single-stub impedance matching networks with application to dual-band stubbed T-junctions. *Microwave Opt. Tech. Lett.* **52**(6), 1359–1362 (2010)
20. G. Castaldi, V. Fiumara, I.M. Pinto, A dual-band Chebyshev impedance transformer. *Microwave Opt. Tech. Lett.* **39**(2), 141–145 (2003)
21. S.J. Orfanidis, A two-section dual-band Chebyshev impedance transformer. *IEEE Microwave Wirel. Compon. Lett.* **13**(9), 382–384 (2003)
22. P. Colantonio, F. Giannini, R. Giofrè, A design technique for concurrent dual-band harmonic tuned power amplifier. *IEEE Trans. Microw. Theory Tech.* **56**(11), 2545–2555 (2008)
23. M.L. Chuang, Dual-band impedance transformer using two section shunt stub. *IEEE Trans. Microw. Theory Tech.* **58**(5), 1257–1263 (2010)
24. Y. Wu, Y. Liu, S. Li, C. Yu, X. Liu, A generalized dual-frequency transformer for two arbitrary complex frequency-dependent impedances. *IEEE Microwave Wirel. Compon. Lett.* **19**(12), 792–794 (2009)
25. X. Liu, Y. Liu, S. Li, F. Wu, Y. Wu, A three-section dual-band transformer for frequency-dependent complex load impedance. *IEEE Microwave Wirel. Compon. Lett.* **19**(10), 611–613 (2009)
26. S. Li, B.H. Tang, Y.A. Liu, S.L. Li, C.P. Yu, Y.L. Wu, Miniaturized dual-band matching technique based on coupled line transformer for dual band power amplifiers design. *Prog. Electromagnetics Res.* **131**, 195–210 (2012)
27. K. Rawat, M. Rawat, M.S. Hashmi, F. Falcone, F.M. Ghannouchi, Dual-band phase offset line with required transmission phases at two operational frequencies, in *IEEE MTT-S International Microwave Symposium Digest (MTT)*, 2012, pp. 1–3

28. B. Gowrish, K. Rawat, A. Basu, S.K. Koul, Broad-band matching network using band-pass filter with device parasitic absorption, in *IEEE 82nd Microwave Measurement Conference, Columbus, Ohio*, 2013, pp. 1–4
29. T. Vähä-Heikkilä, G.M. Rebeiz, A 20–50 GHz reconfigurable matching network for power amplifier applications, in *IEEE MTT-S International Microwave Symposium Digest (MTT)*, An Arbor, Michigan (2004), pp. 717–720
30. N.S. Barker, G.M. Rebeiz, Optimization of distributed MEMS transmission line phase shifters—U-band and W-band designs. *IEEE Trans. Microw. Theory Tech.* **48**, 1957–1966 (2000)
31. K. Rawat, B. Gowrish, G. Ajmera, A. Basu, S.K. Koul, Design scheme for broadband Doherty power amplifier using broadband load combiner. *Int. J. RF and Microwave Comput. Aided Eng.* **25**(8), 655–674 (2015)
32. N.O. Sokal, A.D. Sokal, Class E—a new class of high-efficiency tuned single-ended switching power amplifiers. *IEEE J. Solid-State Circuits* **SC-10**(3), 168–176 (1975)
33. S. Hun Ji, C.S. Cho, J.W. Lee, J. Kim, Concurrent dual-band class-E power amplifier using composite right/left-handed transmission lines. *IEEE Trans. Microw. Theory Tech.* **55**(6), 1341–1347 (2007)
34. A. Raffo, F. Scappaviva, G. Vannini, A new approach to microwave power amplifier design based on the experimental characterization of the intrinsic electron-device load line. *IEEE Trans. Microw. Theory Tech.* **57**(7), 1743–1752 (2009)
35. S. Liu, D. Schreurs, Intrinsic class-F RF GaN power amplifier with a commercial transistor based on a modified “hybrid” approach, in *MMIC Workshop*, Dublin, Ireland, Sep 2012, pp. 1–3
36. F.H. Raab, Idealized operation of the class-E tuned power amplifier. *IEEE Trans. Circuits Syst.* **CAS-24**(12), 725–735 (1977)
37. T.B. Mader, Z. Popovic’, The transmission-line high-efficiency class-E amplifier. *IEEE Microw. Guided Wave Lett.* **5**(9), 29–292 (1995)
38. I. Lin, M. Devincintis, C. Caloz, T. Itoh, Arbitrary dual-band components using composite right/left handed transmission lines. *IEEE Trans. Microw. Theory Tech.* **50**(4), 1142–1149 (2004)
39. R. Negra, A. Sadeve, S. Bensmida, F.M. Ghannouchi, Concurrent dual-band class-F load coupling network for applications at 1.7 and 2.14 GHz. *IEEE Trans. Circuit Syst. II Express Briefs* **55**(3), 259–263 (2008)
40. H. Jang, P. Roblin, Z. Xie, Model-based nonlinear embedding for power-amplifier design. *IEEE Trans. Microw. Theory Tech.* **62**(9), 1986–2002 (2014)
41. C. Han, T. Harrold, S. Armour, I. Krikidis, S. Videv, P.M. Grant, H. Haas, J.S. Thompson, I. Ku, C.X. Wang, T.A. Le, M.R. Nakhai, J. Zhang, L. Hanzo, Green radio: radio techniques to enable energy-efficient wireless networks. *IEEE Commun. Mag.* **49**(6), 46–54 (2011)
42. K. Rawat, F.M. Ghannouchi, S. K. Koul, Multiband/broadband techniques in Doherty Power Amplifiers, in *Workshop, IEEE International Microwave and RF Conference (IMARC) 2014*, Bangalore, India, Dec 2014
43. R. Sweeney, Practical magic. *IEEE Microw. Mag.* **9**(2), 73–82 (2008)
44. B. Kim, I. Kim, J. Moon, Advanced Doherty Architecture. *IEEE Microw. Mag.* **11**(5), 72–86 (2010)
45. F.H. Raab, Efficiency of Doherty power-amplifier systems. *IEEE Trans. Broadcast.* **BC-33**(3), 42–50 (1987)
46. B. Kim, J. Kim, I. Kim, J. Cha, The Doherty power amplifier. *IEEE Microw. Mag.* **7**(5), 42–50 (2006)
47. Y. Yang, J. Yi, Y.Y. Woo, B. Kim, Optimum design for linearity and efficiency of a microwave Doherty amplifier using a new load modulation technique. *Microwave J.* **44**(12), 20–36 (2001)
48. K. Rawat, F.M. Ghannouchi, Design methodology for dual-band Doherty power amplifier with performance enhancement using dual-Band offset lines. *IEEE Trans. Industr. Electron.* **59**(12), 4831–4842 (2012)

49. W. Chen, S.A. Bassam, X. Li, Y. Liu, K. Rawat, M. Helou, F.M. Ghannouchi, F. Zhenghe, Design and linearization of concurrent dual-band Doherty power amplifier with frequency-dependent power ranges. *IEEE Trans. Microw. Theory Tech.* **59**(10), 2537–2546 (2011)
50. J.S. Fu, A. Mortazawi, A tunable matching network for power amplifier efficiency enhancement and distortion reduction, in *IEEE International Microwave Symposium Digest*, no. 11, June 2008, , pp. 1151–1154

# Chapter 6

## Digital Techniques for Multiband RF Transmitters

### 6.1 Introduction

This chapter will discuss the nonlinear behavior of concurrent dual-band transmitters first, which is more complicated as compared to conventional single-band transmitter. To account for this phenomenon, multidimension digital predistortion (DPD) techniques are employed to compensate for the nonlinearities in dual-band transmitters including intraband modulation and interband modulation products. To alleviate the burden on the hardware-induced multidimension DPD, low-complexity 2D-modified memory polynomial method and iterative pruning method are also discussed. For hardware implementation, in order to reduce the resource consumption, a subsampling technique for the feedback loop and a hybrid LUT predistortion method are introduced.

### 6.2 Nonlinearities of Multiband Transmitters

With the rapid evolution of communication technologies, mobile communication systems should accommodate multiple standards or multiple modes simultaneously, such as Wideband Code Division Multiple Access (WCDMA), Worldwide Interoperability for Microwave Access (WiMAX), and Carrier Aggregation (CA) applications. In addition, for smooth network migration and upgrades, it is essential to guarantee the backward compatibility of long-term evolution advanced (LTE advanced). Therefore, the radio frequency (RF) front-end in future systems should be able to support multiband operation. In this situation, a multiband transmitter is highly desirable, especially when operating in concurrent mode. Many efforts have recently been carried out to realize concurrent multiband power

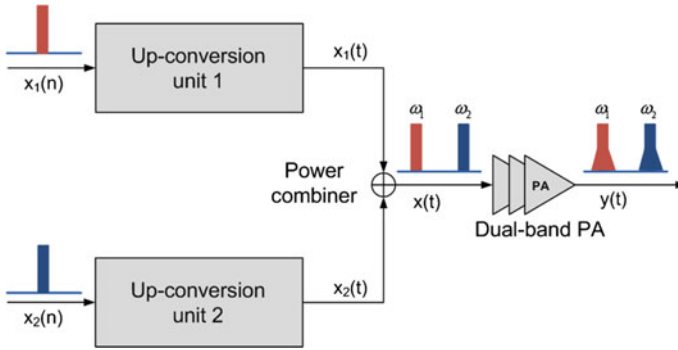


**Fig. 6.1** The basic architecture of the concurrent dual-band transmitter. Reprinted with permission from the IEEE

amplifiers (PAs) [1–3]. Recently, some new techniques to design a Doherty PA that supports concurrent dual-band operation have been proposed using dual-band transformers [4, 5] to enhance the average efficiency. Unfortunately, in concurrent dual-band transmitters, the distortions caused by the transmitter’s nonlinear behavior, which are classified as intermodulation and cross-modulation distortions [6–9], introduce undesired signals at adjacent channels, resulting in degraded adjacent channel power ratio (ACPR) performance (Fig. 6.1).

Figure 6.1 depicts the typical architecture of the concurrent dual-band transmitter, where the two complex baseband signals  $x_1(n)$  and  $x_2(n)$  are modulated and upconverted to their respective RF bands. Then, a wideband power combiner or multiplexer combines the two RF signals together. The final-stage dual-band PA is driven by the combined dual-band signal. Without loss of generality, we can use baseband discrete-time notations for all the signals, and the dual-band input signal can be represented as

$$x(n) = x_1(n)e^{-j\omega nT_s} + x_2(n)e^{j\omega nT_s} \quad (6.1)$$

where  $\omega = \Delta\omega/2$ ,  $\Delta\omega$  is the carrier frequency offset between dual bands, and  $T_s$  is the sampling interval of baseband signals.

The Volterra series is a very general approach to describe the nonlinear relationship of a nonlinear system with memory [10–13]. A simplified form of the Volterra series known as the memory polynomial model, is commonly used. One can also use this model to express the nonlinear behavior of the concurrent dual-band transmitter:

$$y(n) = \sum_{m=0}^{M-1} \sum_{\substack{k=0 \\ k \in \text{even}}}^K a_{(k+1)m} x(n-m) |x(n-m)|^k \quad (6.2)$$

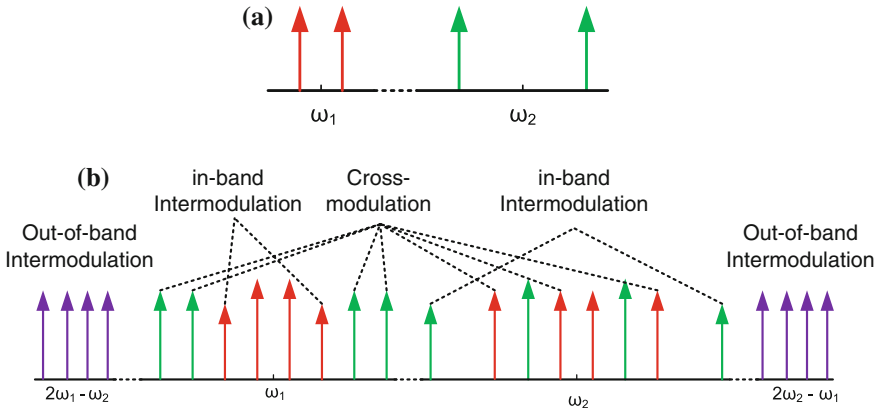


**Fig. 6.2** Power spectrum of the signal at **a** the input and **b** output of a dual-band transmitter. Reprinted with permission from the IEEE

where  $y(n)$  is the complex baseband output of the PA,  $a_{(k+1)m}$  are the model coefficients, and  $K + 1$  and  $M$  are the nonlinearity order and the memory depth, respectively (Fig. 6.2).

The nonlinear behavior of the transmitter is much more noticeable in dual-band systems, in which two modulated signals that are separated in carrier frequencies by  $\Delta\omega$  are transmitted simultaneously. When dealing with dual-band transmitters, the intermodulation products at the transmitter output can be categorized into three major groups [14]. The first group, referred to here as in-band intermodulation, consists of the intermodulation products around each carrier frequency that are solely due to the intermodulation between the signal elements within each band, similar to what it is in single-band transmitters.

The second group, which includes the cross-modulation products, appears within the same frequency range as the in-band intermodulation; however, this distortion is the result of intermodulation products between the signals in both frequency bands. Finally, the last group, which is referred to as out-of-band intermodulation, is the intermodulation products between the two signals in both frequency bands; however, these terms are located at  $\Delta\omega$  away from the lower and upper carrier frequencies. Figure 6.1 shows these three types of intermodulation products for a dual-band transmitter excited with a two-tone signal in each band.

As has been addressed, nonlinearities in the concurrent dual-band transmitter are much more noticeable. To analytically illustrate the fundamental principle of that, we simply model the transmitter with a seventh-order memoryless nonlinearity. Substitution of (6.1) into (6.2) when  $K = 6$  and  $M = 6$  gives

$$\begin{aligned}
y(n) = & \left( a_{10}x_1 + a_{30}x_1|x_1|^2 + 2a_{30}x_1|x_2|^2 \right. \\
& + a_{50}x_1|x_1|^4 + 6a_{50}x_1|x_1|^2|x_2|^2 + 3a_{50}x_1|x_2|^4 \\
& + a_{70}x_1|x_1|^6 + 12a_{70}x_1|x_1|^4|x_2|^2 \\
& \left. + 18a_{70}x_1|x_1|^2|x_2|^4 + 4a_{70}x_1|x_2|^6 \right) e^{-j\omega n T_s} \\
& + \left( a_{10}x_2 + a_{30}x_2|x_2|^2 + 2a_{30}x_2|x_1|^2 \right. \\
& + a_{50}x_2|x_2|^4 + 6a_{50}x_2|x_2|^2|x_1|^2 + 3a_{50}x_2|x_1|^4 \\
& + a_{70}x_2|x_2|^6 + 12a_{70}x_2|x_2|^4|x_1|^2 \\
& \left. + 18a_{70}x_2|x_2|^2|x_1|^4 + 4a_{70}x_2|x_1|^6 \right) e^{j\omega n T_s} \\
& + \left( a_{30}x_1^2x_2^* + 2a_{50}x_1^2|x_1|^2x_2^* + 3a_{50}x_1^2|x_2|^2x_2^* \right. \\
& \left. + 3a_{70}x_1^2|x_1|^2|x_2|^2x_2^* + 3a_{70}x_1^2|x_2|^4x_2^* \right) e^{-j3\omega n T_s} \\
& + \left( a_{30}x_2^2x_1^* + 2a_{50}x_2^2|x_2|^2x_1^* + 3a_{50}x_2^2|x_1|^2x_1^* \right. \\
& \left. + 3a_{70}x_2^2|x_1|^2|x_2|^2x_1^* + 3a_{70}x_2^2|x_1|^4x_1^* \right) e^{j3\omega n T_s} \\
& + \left( a_{50}x_1^3(x_2^*)^2 + 3a_{70}x_1^3|x_1|^2(x_2^*)^2 + 4a_{70}x_1^3|x_2|^2(x_2^*)^2 \right) e^{-j5\omega n T_s} \\
& + \left( a_{50}x_2^3(x_1^*)^2 + 3a_{70}x_2^3|x_2|^2(x_1^*)^2 + 4a_{70}x_2^3|x_1|^2(x_1^*)^2 \right) e^{j5\omega n T_s} \\
& + \left( a_{70}x_1^4(x_2^*)^3 \right) e^{-j7\omega n T_s} + \left( a_{70}x_2^4(x_1^*)^3 \right) e^{j7\omega n T_s}
\end{aligned} \tag{6.3}$$

where  $n$  in  $x_1(n)$  and  $x_2(n)$  are omitted to simplify the notations. Since the frequency offset between the two carrier frequencies is assumed to be large enough, the out-of-band intermodulation components at  $\pm 3\omega$ ,  $\pm 5\omega$ , and  $\pm 7\omega$  are located far away from the lower and upper carrier frequencies and can be filtered out easily. The resultant complex baseband output signals around the carrier frequencies (corresponding to  $-\omega$  and  $\omega$ ) are

$$\begin{aligned}
y_1(n) = & a_{10}x_1 + a_{30}x_1|x_1|^2 + 2a_{30}x_1|x_2|^2 \\
& + a_{50}x_1|x_1|^4 + 6a_{50}x_1|x_1|^2|x_2|^2 + 3a_{50}x_1|x_2|^4 \\
& + a_{70}x_1|x_1|^6 + 12a_{70}x_1|x_1|^4|x_2|^2 \\
& + 18a_{70}x_1|x_1|^2|x_2|^4 + 4a_{70}x_1|x_2|^6
\end{aligned} \tag{6.4a}$$



$$\begin{aligned}
y_2(n) = & a_{10}x_2 + a_{30}x_2|x_2|^2 + 2a_{30}x_2|x_1|^2 \\
& + a_{50}x_2|x_2|^4 + 6a_{50}x_2|x_2|^2|x_1|^2 + 3a_{50}x_2|x_1|^4 \\
& + a_{70}x_2|x_2|^6 + 12a_{70}x_2|x_2|^4|x_1|^2 \\
& + 18a_{70}x_2|x_2|^2|x_1|^4 + 4a_{70}x_2|x_1|^6
\end{aligned} \tag{6.4b}$$

where  $y_1(n)$  and  $y_2(n)$  are the complex baseband output signals of the PA corresponding to each carrier frequency. From (6.4a) and (6.4b), it can be concluded that the output signals around each carrier frequency are relevant to both input signals  $x_1$  and  $x_2$ . This indicates two nonlinear distortion components: the in-band intermodulation (the terms of  $x_1|x_1|^k$  or  $x_2|x_2|^k$ ) and the cross-band modulation (the terms of  $x_1|x_1|^{k-l}|x_2|^l$  or  $x_2|x_2|^{k-l}|x_1|^l$ ,  $l \neq 0$ ). Therefore, the predistortion model for the concurrent dual-band transmitter should properly consider both distortion components.

### 6.3 Two-Dimensional Digital Predistortion (2D-DPD) Technique

To account for the complex nonlinear behavior of concurrent dual-band PAs, many novel DPD techniques have been invented to compensate for the nonlinearities in dual-band PAs [14]. Aidin et al. presents a 2D-DPD architecture that has been developed to compensate for the distortion and nonlinearities of dual-band transmitters. Two independent processing cells are used, where each processing cell is responsible for the compensation of the nonlinearity associated with that particular frequency band. Using this technique, the sampling rate requirements of the digital-to-analog converters (DACs) and analog-to-digital converters (ADCs) in the DPD systems are considerably reduced.

#### 6.3.1 2D-DPD Behavioral Model

Figure 6.3 demonstrates the architecture for dual-band DPD systems [14]. It consists of three major stages: (1) the signal extraction and analysis stage, (2) the processing stage, and (3) the synthesis stage. In the signal extraction and analysis stage, signals at each of the output channels (Chaps. 1 and 2) are downconverted, digitized, and time aligned with the baseband complex input signals ( $z_1$  and  $z_2$ ). In the processing stage, separate processing units are used to construct and identify independent models between the input signals ( $z_1$  and  $z_2$ ) and the output signals for each channel. Next, the input baseband complex signals are predistorted within each processing cell, designated in Fig. 6.3 as C1 and C2. Finally, in the synthesis

stage, the predistorted signals, designated by  $x_1$  and  $x_2$  in Fig. 6.3, are first converted to the analog domain and upconverted to their respective proper carrier frequency and finally combined and passed through the nonlinear transmitter.

Therefore, proper inverse model identification needs to consider both input signals for the DPD linearization technique. Based on these requirements, in this paper, new 2D-DPD technique is proposed and generalized for the nonlinear system with dual complex baseband input signals with  $N$ -th-order nonlinearities and  $M$ -th-order memory depth. The generalized formulation for the output complex signal associated with the each of the input signal is as follows (Fig. 6.3):

$$y_1(n) = \sum_{m=0}^{M-1} \sum_{k=0}^N \sum_{j=0}^k c_{k,j,m}^{(1)} x_1(n-m) |x_1(n-m)|^{k-j} |x_2(n-m)|^j$$

$$y_2(n) = \sum_{m=0}^{M-1} \sum_{k=0}^N \sum_{j=0}^k c_{k,j,m}^{(2)} x_2(n-m) |x_1(n-m)|^{k-j} |x_2(n-m)|^j$$
(6.5)

where  $(c_{k,j,m}^{(1)} \ c_{k,j,m}^{(2)})$  are the coefficients of the proposed model,  $x_1(n-m)$  and  $x_2(n-m)$  are the complex envelope of the input signals of the PA at the carrier frequencies  $\langle \omega_1$  and  $\omega_2 \rangle$ ,  $y_1(n)$  and  $y_2(n)$  are the complex envelopes of the output signals of the PA at the carrier frequencies  $\langle \omega_1$  and  $\omega_2 \rangle$ , and  $||$  is the absolute value of the complex signal. Equation (6.5) can be developed in matrix form as follows:

$$\vec{y}_i = \mathbf{A}_x^{(i)} \vec{C}$$
(6.6)

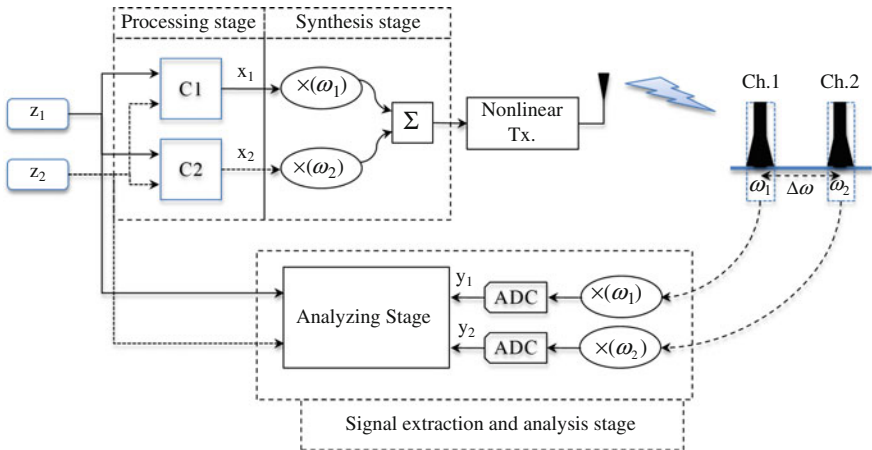


**Fig. 6.3** Block diagram of the proposed dual-cell processing DPD. Reprinted with permission from the IEEE

where

- $\vec{y}_i = [y(n) \dots y(n+L-1)]^T$  is an  $L \times 1$  vector representing the  $L$  samples of output signal at  $i$ th output,
- $\vec{C}$ , as shown in (6.7a), is a  $\frac{1}{2} \times (M \times (N+1)(N+2))$  vector of polynomial coefficients,
- $\mathbf{A}_{\vec{x}}^{(i)}$ , as shown in (6.7a), is an  $L \times \left(\frac{M \times (N+1)(N+2)}{2}\right)$  matrix,
- $\mathbf{b}_{\vec{x}_i}^{(P)}$ , as shown in (6.7c), is an  $L \times \left(\frac{(N+1) \times (N+2)}{2}\right)$  matrix that has its elements extracted from (6.6),
- $\vec{x} = [x(n) \dots x(n+L-1)]^T$  is an  $L \times 1$  vector representing the  $L$  samples of the input signal for each channel.

$$\vec{C} = \left[ c_{0,0,0}^{(i)} c_{1,0,0}^{(i)} c_{1,1,0}^{(i)} \dots c_{i,j,0}^{(i)} \dots c_{N,N,0}^{(i)} \dots c_{N,N,M-1}^{(i)} \right]^T \quad (6.7a)$$

$$\mathbf{A}_{\vec{x}}^{(i)} = \left[ \mathbf{b}_{\vec{x}_i}^{(0)} \quad \dots \quad \mathbf{b}_{\vec{x}_i}^{(P)} \quad \dots \quad \mathbf{b}_{\vec{x}_i}^{(M-1)} \right] \quad (6.7b)$$

$$\mathbf{b}_{\vec{x}_i}^{(p)} = \begin{bmatrix} x_i(n-p) & x_i(n-p)|x_i(n-p)|^{k-j}|x_{ii}(n-p)|^l \dots & x_i(n-p)|x_{ii}(n-p)|^N \\ \vdots & \dots & \vdots \\ \vdots & \dots & \vdots \\ x_i(n-p+L-1) & x_i(n-p+L-1)|x_i(n-p+L-1)|^{k-j}|x_{ii}(n-p+L-1)|^j & x_i(n-p+L-1)|x_{ii}(n-p+L-1)|^N \end{bmatrix} \quad \begin{matrix} i \& \& ii = 1, 2 \\ i \neq ii \end{matrix} \quad (6.7c)$$

In the 2D-DPD technique, approximations of the inverse model coefficients are determined based on the indirect learning approach [14], by swapping the input and output singles in (6.5) and using the least square (LS) algorithm to solve for (6.5). Then, the model coefficients will be used in the  $C1$  and  $C2$  processing blocks to predistorted input signals. The predistorted signals that are the signals at the input of the PA are as follows:

$$\begin{aligned} x_1(n) &= \sum_{m=0}^{M-1} \sum_{k=0}^N \sum_{j=0}^k c_{k,j,m}^{(1)} z_1(n-m) |z_1(n-m)|^{k-j} |z_2(n-m)|^j \\ x_2(n) &= \sum_{m=0}^{M-1} \sum_{k=0}^N \sum_{j=0}^k c_{k,j,m}^{(2)} z_2(n-m) |z_1(n-m)|^{k-j} |z_2(n-m)|^j \end{aligned} \quad (6.8)$$

where  $z_1(n-m)$  and  $z_2(n-m)$  are the complex baseband input signals, and  $x_1(n-m)$  and  $x_2(n-m)$  are the complex baseband predistorted signals.

### 6.3.2 Model Evaluation and Results

As shown in Fig. 6.4, a test bed united by two identical and baseband time-aligned vector signal generators (ESG 4438C), spectrum analyzer (E4440A), 89600 vector signal analysis software, and Matlab has been presented to evaluate the 2D-DPD architecture. The two signal generators act as synthesizers and upconverters of the predistorted baseband signals to their respective RF frequencies where they are combined together using a Wilkinson power combiner. The combined signal drives a wideband preamplifier PA (AR 5S1G4) cascaded with concurrent dual-band Doherty PA. Finally, the output signal is captured by the Agilent PSA E4440A spectrum analyzer and vector signal analyzer (VSA89600). According to the captured input signal and output signal with de-embedding time delay, the reverse model for DPD is derived from (6.5), and thus the predistorted signal can be generated and downloaded into two signal generators for verification, respectively.

To verify the performance of linearization in concurrent mode, one two-carrier and one three-carrier WCDMA signals with peak-to-average power ratio (PAPR) around 10 dB have been simultaneously employed to the dual-band transmitter. The input power at each band is considered so that the same level of output power is observed at each band (Fig. 6.4).

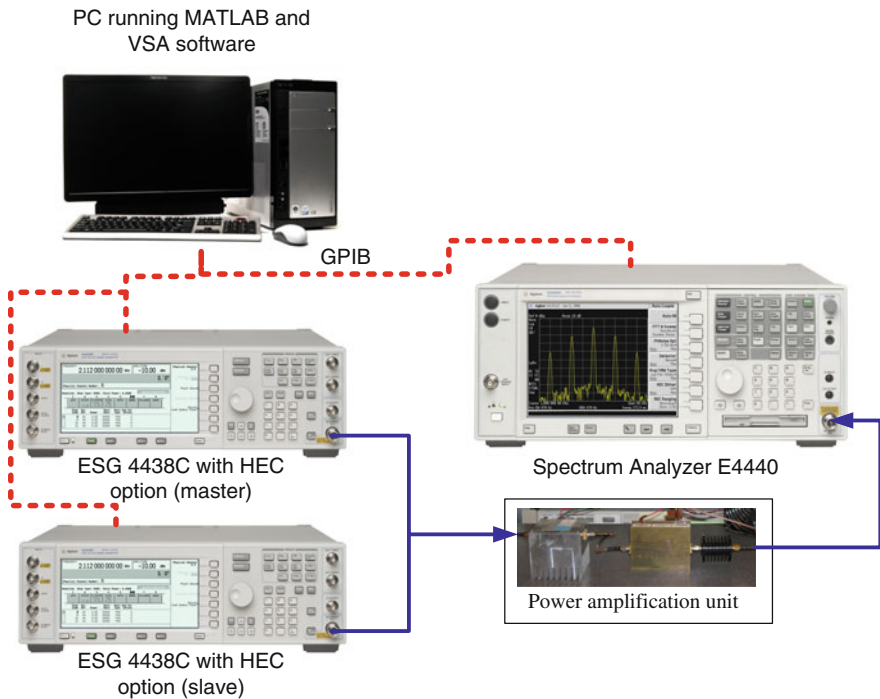
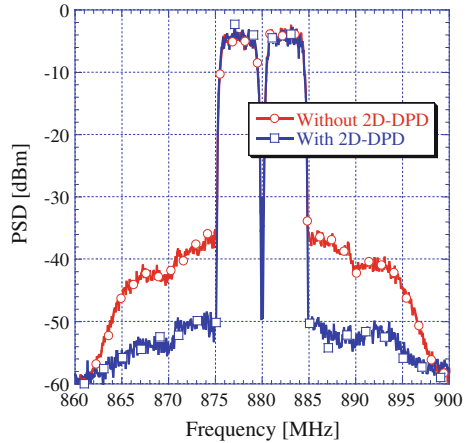


Fig. 6.4 Measurement setup. Reprinted with permission from the IEEE

In this experiment, the nonlinearity of the PA is characterized by nonlinearity order of 5 [ $N = 5$  in (6.1)] and memory depth of 5 [ $M = 5$  in (6.1)]. As shown in Figs. 6.5 and 6.6, two-carrier WCDMA is applied for the lower band, while a 101 three-carrier WCDMA is used for the upper band. Compared with the original signals without DPD in concurrent mode, there is better than 10 dB ACPR improvement in dual bands. The detailed ACPR performance measurement of linearization technique has been presented in Table 6.1 (Figs. 6.5 and 6.6; Table 6.1).

**Fig. 6.5** Measured output spectrum with and without DPD in the lower band. Reprinted with permission from the IEEE



**Fig. 6.6** Measured output spectrum with and without DPD in the upper band. Reprinted with permission from the IEEE

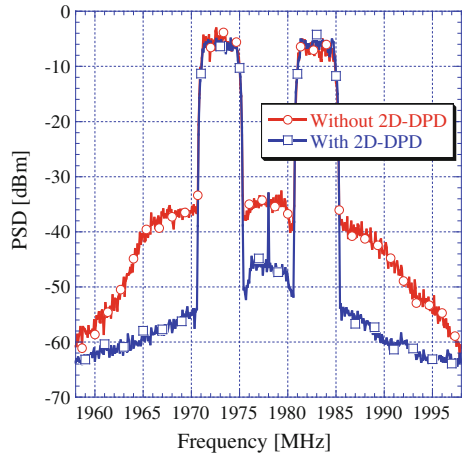


**Table 6.1** The linearization performance of concurrent dual-band Doherty PA

Freq. (MHz)	Signal	ACPR at 5 Mz offset (dBc)		ACPR at 10 MHz offset (dBc)	
		w/o DPD	w DPD	w/o DPD	w DPD
880	2-carrier 11-WCDMA	-34.01	-46.00	-38.29	-49.44
1978	3-carrier 101-WCDMA	-31.57	-49.90	-41.36	-54.10

## 6.4 Low-Complexity 2D-DPD Techniques

### 6.4.1 2D-Modified Memory Polynomial (2D-MMP) Model

#### 6.4.1.1 2D-MMP Behavioral Model

As known, using two independent conventional memory polynomials (MPs) for each band is not proper to compensate for nonlinear distortion in the concurrent dual-band transmitter, since the cross-band modulation effects are not considered. On the other hand, the prior 2D-DPD model shows quite high complexity, where three summations are required and the total number of coefficients is very large.

In order to achieve the same linearization accuracy as the 2D-DPD model with a low complexity like the conventional MPs, Liu et al. presents a 2D-MMP model for the concurrent dual-band transmitter [17]. The general form of the 2D-MMP model is as follows:

$$y_1(n) = \sum_{m=0}^{M-1} \sum_{k=0}^K h_{km}^{(1)} x_1(n-m) \times \left| |x_1(n-m)| + jc_{k+1}^{(1)} |x_2(n-m)| \right|^k \quad (6.9a)$$

$$y_2(n) = \sum_{m=0}^{M-1} \sum_{k=0}^K h_{km}^{(2)} x_2(n-m) \times \left| |x_2(n-m)| + jc_{k+1}^{(2)} |x_1(n-m)| \right|^k \quad (6.9b)$$

where  $i = 1, 2$  are indexes used to indicate variables at lower band (LB) and upper band (UB),  $h_{km}^{(i)}$  ( $i = 1, 2$ ) are the model coefficients,  $c_{k+1}^{(i)}$  ( $i = 1, 2$ ) are defined as the  $(k + 1)$ -th-order envelope-coupling factors between  $x_1(n)$  and  $x_2(n)$  for LB and UB. Specifically,  $c_{k+1}^{(i)}$  have real numbers and are significant for the modeling.

To theoretically illustrate the validity of the developed model, we simply consider the first-order memory depth ( $M = 1$ ) and the seventh-order nonlinearity ( $K = 6$ ) in (6.9a) and (6.9b) with odd-order nonlinearity terms. By straight mathematical manipulations when  $k = 0, 2, 4, 6$  and  $M = 1$ , (6.9a) and (6.9b) can be rewritten as

$$\begin{aligned} y_1(n) = & h_{00}^{(1)} x_1 + h_{20}^{(1)} x_1 |x_1|^2 + h_{20}^{(1)} \left( c_3^{(1)} \right)^2 x_1 |x_2|^2 \\ & + h_{40}^{(1)} x_1 |x_1|^4 + 2h_{40}^{(1)} \left( c_5^{(1)} \right)^2 x_1 |x_1|^2 |x_2|^2 + h_{40}^{(1)} \left( c_5^{(1)} \right)^4 x_1 |x_2|^4 \\ & + h_{60}^{(1)} x_1 |x_1|^6 + 3h_{60}^{(1)} \left( c_7^{(1)} \right)^2 x_1 |x_1|^4 |x_2|^2 \\ & + 3h_{60}^{(1)} \left( c_7^{(1)} \right)^4 x_1 |x_1|^2 |x_2|^4 + h_{60}^{(1)} \left( c_7^{(1)} \right)^6 x_1 |x_2|^6 \end{aligned} \quad (6.10a)$$

$$\begin{aligned}
y_2(n) = & h_{00}^{(2)} x_2 + h_{20}^{(2)} x_2 |x_2|^2 + h_{20}^{(2)} \left( c_3^{(2)} \right)^2 x_2 |x_1|^2 \\
& + h_{40}^{(2)} x_2 |x_2|^4 + 2h_{40}^{(2)} \left( c_5^{(2)} \right)^2 x_2 |x_2|^2 |x_1|^2 + h_{40}^{(2)} \left( c_5^{(2)} \right)^4 x_2 |x_1|^4 \\
& + h_{60}^{(2)} x_2 |x_2|^6 + 3h_{60}^{(2)} \left( c_7^{(2)} \right)^2 x_2 |x_2|^4 |x_1|^2 \\
& + 3h_{60}^{(2)} \left( c_7^{(2)} \right)^4 x_2 |x_2|^2 |x_1|^4 + h_{60}^{(2)} \left( c_7^{(2)} \right)^6 x_2 |x_1|^6
\end{aligned} \tag{6.10b}$$

where  $n$  in  $x_1(n)$  and  $x_2(n)$  are omitted again to simplify the notations. The expressions in (6.10a) and (6.10b) indicate that the proposed 2D-MMP model also includes both the in-band intermodulation and the cross-band modulation products, which ensures that the 2D-MMP model is an appropriate approach for predistortion of the concurrent dual-band transmitter.

However, we may notice that the general form of 2D-MMP in (6.9a) and (6.9b) is not quite applicable, because the  $(k+1)$ -th-order envelope-coupling factors  $c_{k+1}^{(i)}$  are defined along with different nonlinearity orders  $k$ . This will increase the extraction burden of the general form of the 2D-MMP model. In order to further simplify the 2D-MMP model, we can conduct the detailed analysis for  $c_{k+1}^{(i)}$  as follows and an efficient representation for  $c_{k+1}^{(i)}$  will be given.

For preliminary analysis, we only consider the odd-order nonlinearity in (6.9a) and (6.9b) (i.e., only allow even  $k$ ), because in complex baseband, the even-order nonlinearities are not so significant and are usually ignored (later on, we can further generalize the conclusion by including both even-order and odd-order nonlinearities to obtain better model performance). In theory, by comparing the terms between (6.4a), (6.4b) and (6.10a), (6.10b) for each band, the following relations should be satisfied:

$$\begin{cases} a_{30}^{(i)} = h_{20}^{(i)}, \\ 2a_{30}^{(i)} = h_{20}^{(i)} \left( c_3^{(i)} \right)^2 \\ a_{50}^{(i)} = h_{40}^{(i)}, 3a_{50}^{(i)} = h_{40}^{(i)} \left( c_5^{(i)} \right)^2, 3a_{50}^{(i)} = h_{40}^{(i)} \left( c_5^{(i)} \right)^4 \\ a_{70}^{(i)} = h_{60}^{(i)}, 4a_{70}^{(i)} = h_{60}^{(i)} \left( c_7^{(i)} \right)^2, \\ 6a_{70}^{(i)} = h_{60}^{(i)} \left( c_7^{(i)} \right)^4, 4a_{70}^{(i)} = h_{60}^{(i)} \left( c_7^{(i)} \right)^6 \end{cases} \tag{6.11}$$

where  $i = 1, 2$ , again. From (6.11), one can obtain the constraints for  $c_{k+1}^{(i)}$  as follows:

$$\begin{cases}
\left(c_3^{(i)}\right)^2 = 2 \\
\left(c_5^{(i)}\right)^2 = 3, \left(c_5^{(i)}\right)^4 = 3, \left(c_5^{(i)}\right)^2 = 1 \\
\left(c_7^{(i)}\right)^2 = 4, \left(c_7^{(i)}\right)^4 = 6, \left(c_7^{(i)}\right)^6 = 4, \\
\left(c_7^{(i)}\right)^2 = 3/2, \left(c_7^{(i)}\right)^4 = 1, \left(c_7^{(i)}\right)^2 = 2/3
\end{cases} \quad (6.12)$$

Then, by directly calculating each equation in (6.12), the following values of  $c_{k+1}^{(i)}$  for each order should be satisfied:

$$\begin{cases}
c_3^{(i)} = 1.414 \\
c_5^{(i)} = 1.732, c_5^{(i)} = 1.316, c_5^{(i)} = 1 \\
c_7^{(i)} = 2, c_7^{(i)} = 1.565, c_7^{(i)} = 1.260, \\
c_7^{(i)} = 1.225, c_7^{(i)} = 1, c_7^{(i)} = 0.816
\end{cases} \quad (6.13)$$

Here, only positive numbers of  $c_{k+1}^{(i)}$  are reserved, because the negative ones have the same meanings as the positive ones in the 2D-MMP model. In other words,  $c_{k+1}^{(i)}$  and their inverse number  $-c_{k+1}^{(i)}$  perform identically in the 2D-MMP model. So, only considering the positive numbers is enough. The results in (6.13) show that the third-order envelope-coupling factors (when  $k = 2$ ) can be exactly determined as  $c_3^{(i)} = 1.414$  ( $i = 1, 2$ ) for each band. However, for the other orders, envelope-coupling factors (when  $k \neq 2$ , e.g.,  $c_5^{(i)}$  and  $c_7^{(i)}$ ), (6.13) give inconsistent values. It shows that we cannot theoretically determine a unique value of  $c_{k+1}^{(i)}$  at each other order when  $k \neq 2$ . Despite this, one can still assume that there exists a specific value of  $c_{k+1}^{(i)}$  at each band that can accommodate all the other orders ( $k \neq 2$ ). Here, we purposely generalize  $c_{k+1}^{(i)}$  at each band as one *generalized envelope-coupling factor* for all the other orders ( $k \neq 2$ ), i.e.,  $c_{k+1}^{(i)}$  are redefined as  $c_g^{(i)}$  for all the other orders ( $k \neq 2$ ). In summary, the envelope-coupling factors  $c_{k+1}^{(i)}$  are generalized in the following efficient way:

$$c_{k+1}^{(i)} = \begin{cases} 1.414, & \text{when } k = 2 \\ c_g^{(i)}, & \text{when } k \neq 2 \end{cases}, \quad i = 1, 2 \quad (6.14)$$

where  $c_g^{(i)}$  ( $i = 1, 2$ ) are the two generalized envelope-coupling factors at each band for all the other orders when  $k \neq 2$ .



With regard to the general form of the 2D-MMP model in (6.9a) and (6.9b), on the one hand, generalizing  $c_{k+1}^{(i)}$  as (6.14) gives the 2D-MMP model a more simplified form, ultimately decreasing the complexity in the model's identification. On the other hand, although this kind of generalization will take away some of the generality of the model, the performance of the 2D-MMP model is still maintained.

In preparation for the model's identification, we further present the following analysis to give the value range of  $c_g^{(i)}$ . Notably,  $c_g^{(i)}$  are obtained by generalizing all the other orders of  $k \neq 2$ . More specifically, in the above analysis,  $c_g^{(i)}$  should accommodate both the fifth-order ( $k = 4$ ) and the seventh-order ( $k = 6$ ) nonlinearities. Following (6.13), we have the value ranges of  $[1, 1.732]$  for  $c_5^{(i)}$  and  $[0.816, 2]$  for  $c_7^{(i)}$ . In most cases, since a seventh-order nonlinearity analysis is already enough for behavioral modeling and linearization, it is believed that  $c_g^{(i)}$  is located in the range determined by the union of the above two value ranges, i.e.,  $c_g^{(i)} \in [0.816, 2]$ . Without loss of generality, the value range can be chosen as

$$c_g^{(i)} \in [0.8, 2] \quad (6.15)$$

Notably, the above analysis only considers the odd-order nonlinearities in the 2D-MMP model. Usually, in practical applications, one can further consider the even-order terms [i.e., allow odd  $k$  in (6.9a) and (6.9b)] for better generality.

For the general case, when both even-order and odd-order nonlinearities are included in the 2D-MMP model, definitions of (6.14) and (6.15) are still valid. Specifically, although the value range of (6.15) is only derived based on the odd-order nonlinearity analysis, we still maintain it for the general case when including both even-order and odd-order nonlinearities in the 2D-MMP model. This is because the odd-order nonlinearities are really far more important than the even-order nonlinearities in practice. Thus, the value range of (6.15) is already enough for the determination of  $c_g^{(i)}$ , in fact, without loss of the model's performance.

It should be also noticed that although the above analysis for  $c_g^{(i)}$  is only for the memoryless nonlinear model, the conclusion is still valid for the memory cases. This is because the same relations like that between (6.4a), (6.4b) and (6.10a), (6.10b) can also be obtained for the memory terms when the PA is with memory. As a result, we can still reach the relations like (6.11)–(6.13). Finally, the definition of (6.14) and the value range for  $c_g^{(i)}$  in (6.15) are still achievable for the memory cases.

Recalling (6.9a), (6.9b) and (6.14), the identification of the 2D-MMP model follows two steps. First, the exact value of  $c_g^{(i)}$  at each band is determined from the value range of (6.15) in advance, which actually makes  $c_{k+1}^{(i)}$  in (6.9a) and (6.9b) determined based on (6.14). Second, for the given values of  $c_{k+1}^{(i)}$ , the LS algorithm is used to extract model coefficients  $h_{km}^{(i)}$ .

In the first step,  $c_g^{(i)}$  are determined based on the normalized mean square error (NMSE) criterion of a postdistortion process, using a *binary search algorithm*. The starting point of the postdistortion process is that PA's postdistorter can be treated to be identical to the predistorter according to the  $p$ -th-order inverse theory. At each band, for a given value in the range of (6.15) that is assigned to  $c_g^{(i)}$ , the postdistorter is identified using LS algorithm by swapping the input and output signals in (6.9a) and (6.9b). After that, apply the postdistorter to the output signals of the PA to give

$$\begin{aligned} u_1(n) &= F_{\text{post}}^{(1)}(y_1(n), y_2(n)) \\ u_2(n) &= F_{\text{post}}^{(2)}(y_2(n), y_1(n)) \end{aligned} \quad (6.16)$$

where  $F_{\text{post}}^{(i)}(\cdot)$  ( $i = 1, 2$ ) are the 2D-MMP postdistorters at each band,  $u_i(n)$  are the complex baseband postdistorted signals, and  $y_i(n)$  are the complex baseband output signals of the PA.

Based on the NMSE criterion of the postdistortion process, we employ the following binary search algorithm to search the value of  $c_g^{(i)}$  from the range of (6.12), which can avoid a general sweep search process and reduce the computational complexity. Figure 6.7 shows the flow chart of the binary search algorithm, and  $c_g^{(1)}$  of LB and  $c_g^{(2)}$  of UB are searched separately using the algorithm in practice. Taking any of them, ( $c_g^{(1)}$  or  $c_g^{(2)}$ ), for example, in this algorithm, two critical parameters are defined as  $c_{\text{left}}$  and  $c_{\text{right}}$ , which are initialized to be the two boundaries of (6.15). A step-size constant is initialized as  $\Delta c = (c_{\text{right}} - c_{\text{left}})/2$ , and another critical parameter  $c_{\text{middle}}$  is initialized to be  $c_{\text{middle}} = (c_{\text{right}} + c_{\text{left}})/2$ . For initialization, make the assignment of  $c_g^{(i)} = c_{\text{middle}}$  and identify the 2D-MMP postdistorter for each band, to give the NMSE results, which are named  $\text{NMSE}_{\text{post-middle}}^{(i)}$  ( $i = 1, 2$ ). Then, the algorithm goes into the iteration. At each iteration,  $\Delta c$ ,  $c_{\text{left}}$ , and  $c_{\text{right}}$  are updated at first (Fig. 6.7)

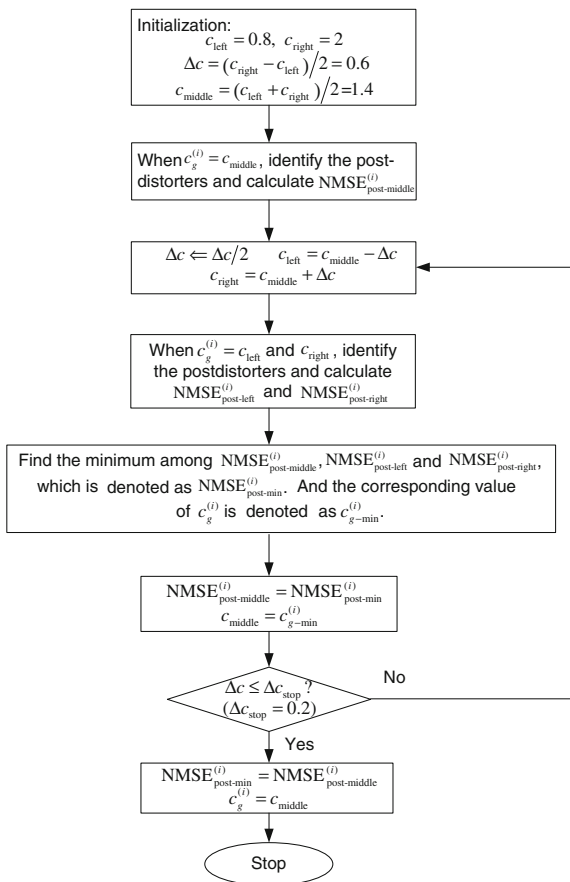
$$\Delta c \Leftarrow \frac{\Delta c}{2} \quad (6.17)$$

$$c_{\text{left}} = c_{\text{middle}} - \Delta c \quad (6.18)$$

$$c_{\text{right}} = c_{\text{middle}} + \Delta c \quad (6.19)$$

Similarly, the corresponding NMSEs when, respectively, assigning  $c_{\text{left}}$  and  $c_{\text{right}}$  to  $c_g^{(i)}$  in the 2D-MMP model are named as  $\text{NMSE}_{\text{post-left}}^{(i)}$  and  $\text{NMSE}_{\text{post-right}}^{(i)}$ . After comparing the three NMSEs ( $\text{NMSE}_{\text{post-middle}}^{(i)}$ ,  $\text{NMSE}_{\text{post-left}}^{(i)}$  and  $\text{NMSE}_{\text{post-right}}^{(i)}$ ), the minimum one is assigned to  $\text{NMSE}_{\text{post-middle}}^{(i)}$ , and the corresponding value of  $c_g^{(i)}$  is assigned to  $c_{\text{middle}}$ . Subsequently, the algorithm goes to the next iteration.

**Fig. 6.7** Flow chart of the binary search algorithm to determine  $c_g^{(i)}$ . Reprinted with permission from the IEEE



Finally, if the stop condition  $\Delta c \leq \Delta c_{\text{stop}}$  is satisfied,  $c_{\text{middle}}$  is returned to  $c_g^{(i)}$ , which is just the exact value for  $c_g^{(i)}$  determined by the binary search algorithm, and  $\text{NMSE}_{\text{post-middle}}^{(i)}$  is returned to be the minimized NMSE value as  $\text{NMSE}_{\text{post-min}}^{(i)}$ . Here, the stop condition is set to be  $\Delta c \leq 0.2$  ( $\Delta c_{\text{stop}} = 0.2$ ). Empirically, it is already enough to achieve a high linearization performance of the 2D-MMP model. In all of our simulations and experimental demonstrations, we found that further decreasing  $\Delta c$  to find a more precise  $c_g^{(i)}$  does not significantly improve the post-distortion accuracy and the final linearization performance much more.

Till now,  $c_g^{(i)}$  at each band have been determined using the binary search algorithm. In the second step of the model's identification, following the definition of  $c_{k+1}^{(i)}$  in (6.14), the model coefficients  $h_{km}^{(i)}$  can be easily extracted using the LS algorithm. Based on the indirect learning architecture, the predistortion model

coefficients using the 2D-MMP model can be obtained by swapping the input and output signals in (6.9a) and (6.9b).

#### 6.4.1.2 Model Evaluation and Results

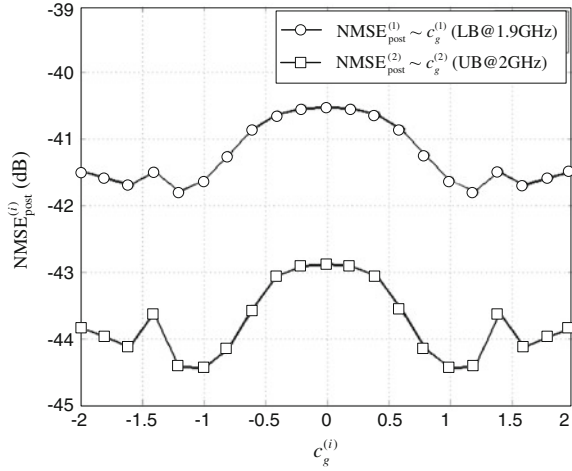
The 2D-MMP model was further evaluated using the 2D-DPD measurement setup. In order to validate the robustness of the proposed 2D-MMP model, we tested two types of PAs: (1) a 5-W laterly diffused metal oxide semiconductor (LDMOS) class-AB PA, which can operate in a wide range of frequency band and was concurrently driven by a two-carrier WCDMA signal at 1.9 GHz (LB) and a single-carrier WCDMA signal at 2 GHz (UB); and (2) a 10 W dual-band Doherty PA built using the SiC MESFET (CREE, CRF24010). The dual-band excitation signal, exhibiting more significant frequency spacing (more than 1 GHz), is constructed using a two-carrier WCDMA signal at 880 MHz (LB) and a three-carrier WCDMA 101 (with the middle carrier off) signal at 1.96 GHz (UB).

In the experiments, the output signals of the PA were captured in two steps by respectively setting the central frequency of VSA 89600 software to LB and UB. After timing the alignment for the output signals with their corresponding baseband input signals at each band, the DPD coefficients were identified. For the dual-band class-AB PA, a nonlinearity order of five ( $K = 4$ ) and a memory depth of four ( $M = 4$ ) were chosen. While for the dual-band Doherty PA, we chose  $K = 4$  and  $M = 5$ .

The first step for the implementation of the 2D-MMP technique is to determine the exact value of  $c_g^{(i)}$  using the binary search algorithm based on the postdistortion process. In the experiments, before employing the binary search algorithm, in order to show a global view about the relations between  $\text{NMSE}_{\text{post}}^{(i)}$  and  $c_g^{(i)}$ , we purposely swept  $c_g^{(i)}$  from  $-2$  to  $2$  with a step size of  $0.2$ , and for each value that was assigned to  $c_g^{(i)}$ , the postdistorter for each band was identified to give the corresponding  $\text{NMSE}_{\text{post}}^{(i)}$  value. For instance, the results of the dual-band class-AB PA are presented in 0 for LB (1.9 GHz) and UB (2 GHz). One can see that the curves are symmetrical, about  $c_g^{(i)} = 0$ , which agree with the previous analysis. Specifically, it is shown that  $c_g^{(i)}$  that minimizes  $\text{NMSE}_{\text{post}}^{(i)}$  is indeed located in the range of (6.15). Similarly, for the dual-band Doherty PA, we also obtained similar relations like those in Fig. 6.8.

Once  $c_g^{(i)}$  were determined for each band, the coefficients of the 2D-MMP model were identified based on the indirect learning architecture using the LS algorithm. For comparison, we also give the results using two independent MPs and the 2D-DPD technique. Figure 6.9 shows the measured spectra of the PA output at LB (1.9 GHz) and UB (2 GHz) before and after linearization, for the dual-band class-AB PA, and Fig. 6.10 is that for the dual-band Doherty PA at LB (880 MHz) and UB (1.96 GHz). It can be noticed that using two independent MPs only provides

**Fig. 6.8** Relations between  $NMSE_{\text{post}}^{(i)}$  and  $c_g^{(i)}$  in the postdistortion process (for the dual-band class-AB PA). Reprinted with permission from the IEEE



quite limited linearization performances, while the proposed 2D-MMP model offers almost the same linearization accuracy as the 2D-DPD model (Table 6.2).

The detailed results of ACPRs at 5 MHz offset and the NMSEs between the output signals of the PAs and the original input signals are also summarized in Table 6.2 for both PAs. It is also shown that the 2D-MMP model can achieve comparable linearization performances in the dual bands as the 2D-DPD model. Less than -52 dBc ACPRs for the dual-band class-AB PA and less than -50 dBc ACPRs for the dual-band Doherty PA are feasible. The NMSE results between the 2D-MMP model and the 2D-DPD model in the DPD applications are also comparable linearization performances. For more details, Table 6.2 also presents the number of coefficients of different models used in the DPD linearization. One can see that the 2D-MMP model requires much fewer coefficients than the 2D-DPD model. Only 41 and 51 coefficients were required in the 2D-MMP model for the dual-band class-AB PA and the dual-band Doherty PA. However, to compensate for the same nonlinearity order and memory depth, the 2D-DPD model required 120 and 150 coefficients for each PA, respectively. This indicates significant

**Table 6.2** Comparison of linearization performances and model complexity for concurrent dual-band PAs

	Concurrent dual-band class-AB PA (1.9 GHz/2 GHz)			Concurrent dual-band Doherty PA (880 MHz /1.96 GHz)		
	NMSE of LB/UB (dB)	ACPR at 5 MHz of LB/UB (dBc)	Num. of coefficients	NMSE of LB/UB (dB)	ACPR at 5 MHz of LB/UB (dBc)	Num. of coefficients
w/o DPD	-21.97/-20.69	-42.48/-41.20	-	-17.38/-19.10	-36.05/-31.88	-
w/two indep. MPs	-26.57/-28.05	-47.38/-41.73	40	-24.63/-19.92	-36.71/-32.47	50
w/2D-DPD	-40.55/-39.86	-52.58/-56.82	120	-39.32/-34.59	-50.95/-52.61	150
w/2D-MMP	-40.12/-39.50	-52.06/-56.20	41	-38.16/-34.72	-50.78/-52.54	51

reduction of run-time complexity in a real system when using the 2D-MMP model. In summary, the comparison results illustrate that the 2D-MMP model outperforms the technique that uses two independent MPs, in terms of performance, and the 2D-DPD model, in terms of complexity (Figs. 6.9 and 6.10; Table 6.3).

### 6.4.1.3 Complexity Comparison

It should be noticed that there are only two summations in the 2D-MMP model for each band. This gives it the same model complexity as the conventional MP DPDs. For comparison, Table 6.4 summarizes the complexity information of both the 2D-MMP model and the 2D-DPD model, for a nonlinearity order of  $K + 1$  and a

**Fig. 6.9** Measured spectra of the output of the dual-band class-AB PA at **a** LB (1.9 GHz) and **b** UB (2 GHz) before and after linearization. Reprinted with permission from the IEEE

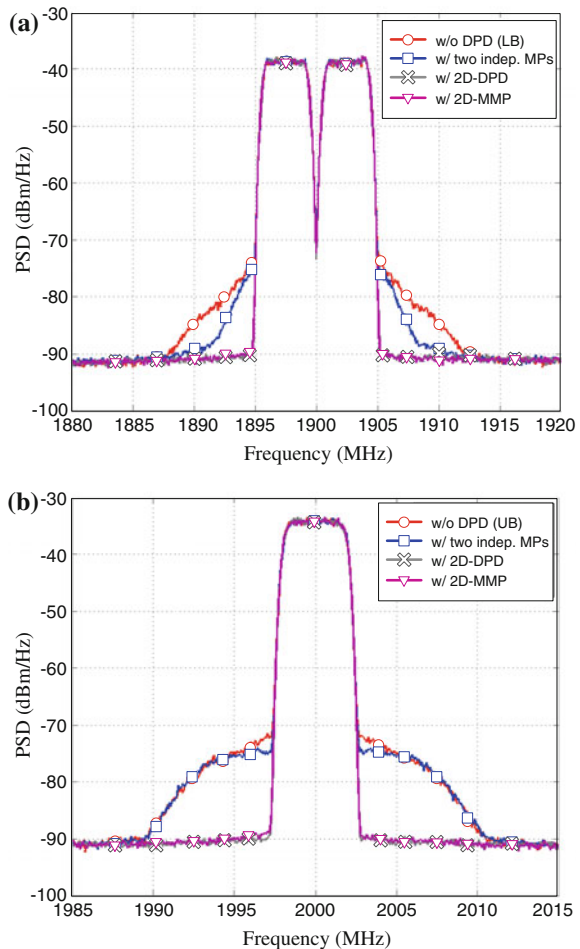


**Fig. 6.10** Measured spectra of the output of the dual-band Doherty PA at **a** LB (880 MHz) and **b** UB (1.96 GHz) before and after linearization. Reprinted with permission from the IEEE

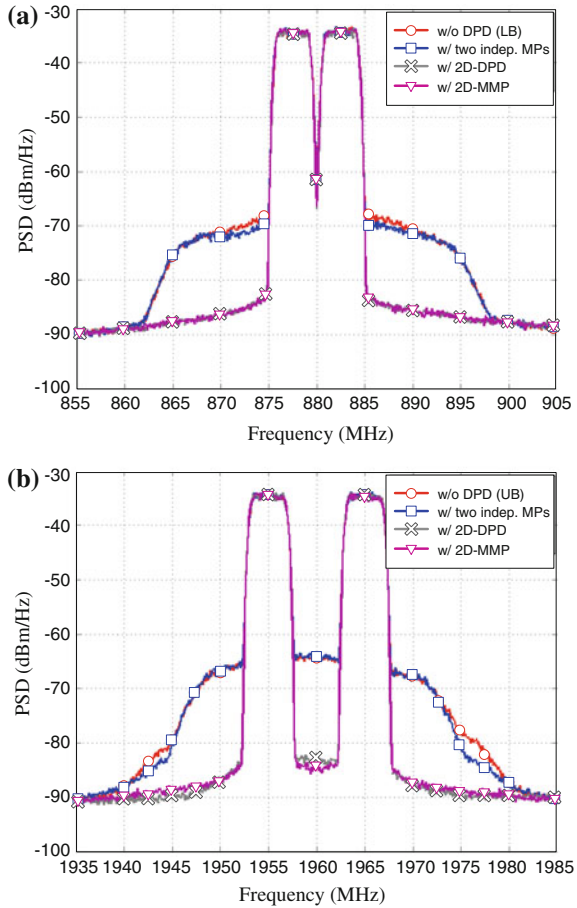


**Table 6.3** Comparison of linearization performances and model complexity for concurrent dual-band PAs

	Concurrent dual-band class-AB PA (1.9 GHz/2 GHz)			Concurrent dual-band Doherty PA (880 MHz/1.96 GHz)		
	NMSE of LB/UB (dB)	ACPR at 5 MHz of LB/UB (dBc)	Num. of coefficients	NMSE of LB/UB (dB)	ACPR at 5 MHz of LB/UB (dBc)	Num. of coefficients
w/o DPD	-21.97/-20.69	-42.48/-41.20	-	-17.38/-19.10	-36.05/-31.88	-
w/two indep. MPs	-26.57/-28.05	-47.38/-41.73	40	-24.63/-19.92	-36.71/-32.47	50
w/2D-DPD	-40.55/-39.86	-52.58/-56.82	120	-39.32/-34.59	-50.95/-52.61	150
w/2D-MMP	-40.12/-39.50	-52.06/-56.20	41	-38.16/-34.72	-50.78/-52.54	51

**Table 6.4** Comparison of complexity between 2D-MMP and 2D-DPD

	2D-MMP	2D-DPD
Number of complex-valued coefficients	$2M(K+1)+1$	$M(K+1)(K+2)$
Number of matrix inversion in model's identification	12	4
Matrix size	$L \times (M(K+1))$	$L \times (M(K+1)(K+2)/2)$

memory depth of  $M$ . Specifically, in the 2D-MMP model, since  $c_g^{(1)}$  and  $c_g^{(2)}$  are real numbers, we equivalently consider them as one complex-valued coefficient. Therefore, the total number of complex-valued coefficients in the 2D-MMP model for both bands is  $2M(K+1)+1$ . However, the total number of complex-valued coefficients in the 2D-DPD model is  $M(K+1)(K+2)$ . This shows that the complexity of the 2D-MMP model is almost  $(K+2)/2$  times less than that of the 2D-DPD model (Table 6.4).

Furthermore, the computational complexity in the model's identification is also assessed in terms of number of matrix inversion. Generally, most previous works have revealed that at least two or three LS iterations are required to obtain the converged DPD, when using the indirect learning architecture. Taking the two LS iterations for instance, the 2D-DPD model requires at least four matrix inversions (two for LB and two for UB), and the matrix size is  $L \times (M(K+1)(K+2)/2)$ , where  $L$  is again the sample length. In the 2D-MMP model, the binary search algorithm also requires some matrix inversions in the postdistortion process. According to Fig. 6.2, until the stop condition  $\Delta c \leq 0.2$  is satisfied, ten matrix inversions (five for LB and five for UB) are required. One must notice that once  $c_g^{(i)}$  is determined, the predistorter of the first LS iteration is already obtained for this given  $c_g^{(i)}$ . So, it only needs one more LS iteration for each band to obtain the converged 2D-MMP predistorter. In total, 12 matrix inversions are required for the 2D-MMP model, but the matrix size is much lower, i.e.,  $L \times (M(K+1))$ . Normally, an appropriate way to represent the total computational complexity in the model's identification can be defined as a product of the number of the matrix inversions and the matrix size. Since usually at least a fifth-order nonlinear compensation is required in practice, i.e.,  $K \geq 4$ , we have

$$12L(M(K+1)) \leq 4L \left( \frac{M(K+1)(K+2)}{2} \right) \quad (6.20)$$

This illustrates that the total computational complexity when identifying the 2D-MMP model is still not higher than that when identifying the 2D-DPD model.



### 6.4.2 Adaptive Pruning Method for 2D-DPD

#### 6.4.2.1 Adaptive Pruning Algorithm

There are many strategies to prune an MP model based on data analysis, such as the all possible (AP) test, stepwise methods, and optimal methods, the feasibility of which are dependent on conditions. The error variation ranking (EVR) pruning method is, therefore, proposed with the objective of identifying better models with a moderate amount of computations. The process is illustrated in Fig. 6.11, and the details of each step are described in the following.

During the initialization, four vectors are defined and denoted as  $\mathbf{P}$ ,  $\mathbf{B}$ ,  $\mathbf{R}$ , and  $\mathbf{V}$ , respectively.  $\mathbf{P}$  is the vector for all remaining bases,  $\mathbf{B}$  is the buffer,  $\mathbf{R}$  is a vector for all pruned bases, and  $\mathbf{V}$  is a vector for the NMSE variation caused by removing each basis, corresponding to the elements in  $\mathbf{R}$ . Obviously,  $\mathbf{P}$  and  $\mathbf{R}$  complement each other: when a basis is pruned away from  $\mathbf{P}$ , it is moved to  $\mathbf{R}$ .  $\mathbf{P}$  and  $\mathbf{B}$  are both initialized with all potential bases:

$$\mathbf{P} = \mathbf{B} = [u_1, u_2, \dots, u_{km}, \dots, u_l] \tag{6.21}$$

where  $u_{km}$  denotes the MP basis with nonlinear order  $k$  and memory depth  $m$ , whose basis function is  $u_{km}(n)$ . Both  $\mathbf{R}$  and  $\mathbf{V}$  are defined as blank vectors.

After initialization, the bases in  $\mathbf{P}$  are removed one by one in order, until there is only one base in  $\mathbf{P}$ . In each iteration, the last basis in  $\mathbf{P}$  is moved to  $\mathbf{R}$ , as

$$\mathbf{R} = [\mathbf{R}, \mathbf{P}(\text{end})] \tag{6.22}$$

$$\mathbf{P} = \mathbf{P}(1 : \text{end} - 1) \tag{6.23}$$

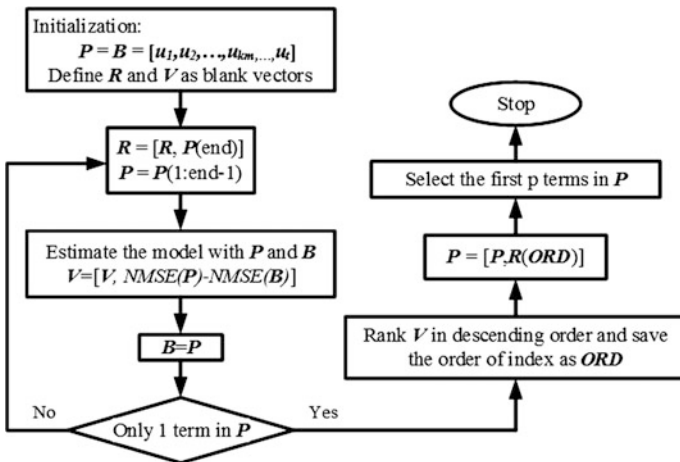


Fig. 6.11 Flow chart of the pruning algorithm. Reprinted with permission from the IEEE

where  $P(\text{end})$  is the last basis of vector  $\mathbf{P}$ , and  $P(1 : \text{end} - 1)$  is all bases in  $\mathbf{P}$  except the last one. The two models built with the bases in  $\mathbf{P}$  and  $\mathbf{R}$  are then estimated, and the difference of their NMSEs is calculated and added to vector  $\mathbf{V}$ :

$$\mathbf{V} = [\mathbf{V}, \text{NMSE}(\mathbf{P}) - \text{NMSE}(\mathbf{B})] \quad (6.24)$$

where  $\text{NMSE}(\mathbf{P})$  and  $\text{NMSE}(\mathbf{B})$  are the NMSEs of the model estimated with  $\mathbf{P}$  and  $\mathbf{B}$ , respectively.

At the end of each loop,  $\mathbf{P}$  is buffered to  $\mathbf{B}$ :

$$\mathbf{B} = \mathbf{P} \quad (6.25)$$

The bases in  $\mathbf{R}$  can then be ranked in descending order in line with the significance of its corresponding element in  $\mathbf{V}$ , denoting its importance in the whole model, and moved back to  $\mathbf{P}$ . Afterward,  $\mathbf{P}$  is organized as

$$P(j) = \begin{cases} P(1), j = 1 \\ P(\text{ORD}_v(j - 1)), 2 \leq j \leq t \end{cases} \quad (6.26)$$

where  $\text{ORD}_v(j - 1)$  is the index of the  $(j - 1)$ th basis in  $\mathbf{V}$  after ranking. Finally, the first  $p$  bases of  $\mathbf{P}$  are selected as a trade-off between complexity and performance.

#### 6.4.2.2 Application to Concurrent Dual-Band PAs

In practice, the 2D models are much more complex than the 1D models, so it is more desirable to simplify them. In this section, an experiment is performed to prove that the new algorithm can simplify the 2D-DPD model effectively and guarantees the performance when linearizing concurrent dual-band transmitter.

The device under test (DUT) is a concurrent dual-band PA based on CREE CGH 40010 transistor, which is a 10 W GaN HEMT. The PA is designed to work at 1.9 and 2.6 GHz for 4G communication, and its saturation output power could reach 11 W under concurrent dual-band CW stimulus. Two LTE signals are used to drive the DUT, which have 15 and 10 MHz bandwidth, respectively. Signals on both the bands are clipped into PAPR 7 dB. While operating, the PA has 30.3 and 30.5 dBm output power on each band, which is 33.4 dBm in total. ACPRs in higher and lower bands before DPD are  $-32.51$  dBc and  $-34.05$  dBc, respectively (Fig. 6.12; Table 6.5).

When the pruning algorithm is performed on a 2D-DPD model, each band model is pruned to eight basis functions, limiting the acceptable NMSE of the inverse model to not larger than  $-37$  dB. The basis functions of the final model are listed in Fig. 6.5. Most of the final basis functions are static terms. Only four of the 16 terms are about memory effects. The comparison of the performance is depicted in 0. The pruned 2D-DPD model has similar performance as a 2D-MMP does, but with much less computational complexity.

**Fig. 6.12** Measured spectrum of the PA output **a** UB and **b** LB. Reprinted with permission from the IEEE

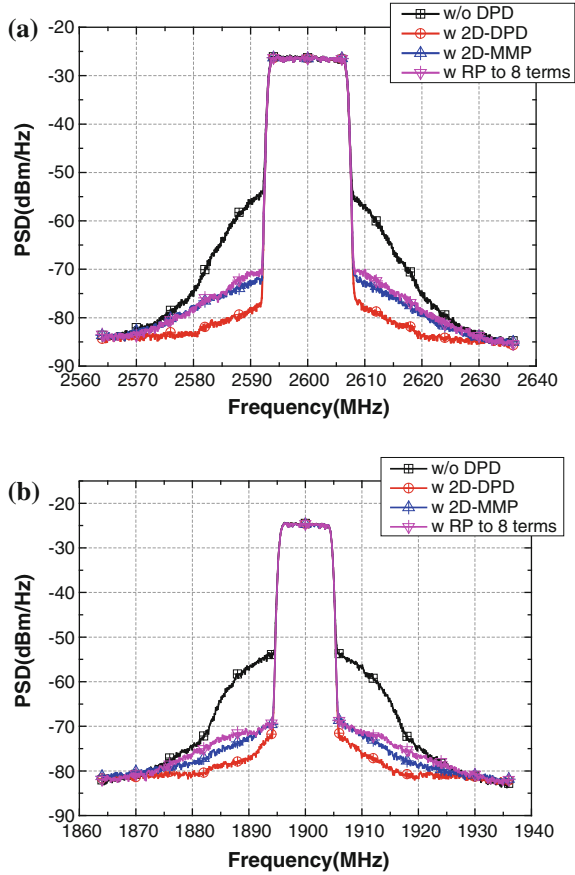


**Table 6.5** Final terms in each band after pruning

Band	Final terms
UB	$x_1(n), x_1(n) x_1(n) , x_1(n) x_1(n) ^2, x_1(n) x_1(n)  x_2(n) ,$ $x_1(n) x_2(n) , x_1(n) x_2(n) ^2, x_1(n-1), x_1(n-1) x_1(n-1) $
LB	$x_2(n), x_2(n) x_2(n) , x_2(n) x_2(n) ^2, x_2(n) x_2(n)  x_1(n) ,$ $x_2(n) x_1(n) , x_2(n) x_1(n) ^2, x_2(n-1), x_2(n-1) x_1(n-1) ^2$

### 6.4.2.3 Comparison of Different Adaptive Pruning Methods

The three adaptive pruning methods are also compared on 2D-DPD model when used in modeling the concurrent dual-band PA. The pruning processing is implemented by sweeping NMSEs of the model versus the number of basis that remains. To quantify the difference between the methods, we limit the acceptable NMSEs of

**Table 6.6** Complexity and performance of different DPD models

		Number of coefficients	Number of FLOPs	NMSE <sub>MOD</sub> (dB)	ACPR (dBc)	NMSE <sub>PA</sub> (dB)
w/o DPD	UB	N.A.	N.A.	N.A.	-33.4	-22.8
	LB	N.A.	N.A.	N.A.	-31.5	-24.9
2D-DPD ( $M, N$ ) = (3, 4)	UB	45	406	-40.4	-52.2	-36.2
	LB	45	406	-39.2	-48.7	-36.5
2D-MMP ( $M, K$ ) = (3, 4)	UB	16	168	-38.9	-47.7	-37.1
	LB	16	168	-38.2	-46.9	-37.7
PRUNED 2D-DPD	UB	8	92	-37.2	-46.6	-36.9
	LB	8	92	-38.4	-46.5	-37.7

the models to not larger than  $-38$  dB. Then, the numbers of the selected basis functions are listed in Table 6.6. As shown, the proposed method prunes the 2D-DPD model to not more than ten terms, much fewer than the others (Table 6.6).

## 6.5 Digital Techniques for Multiband Transmitters with Hardware Impairments

### 6.5.1 Time-Misalignment Tolerant (TMT) Behavioral Model

#### 6.5.1.1 2D-TMT Model Concept

A typical concurrent dual-band transmitter with dual-band observation feedback loops is shown in Fig. 6.13, where  $x_1(nT), x_2(nT), y_1(nT)$  and  $y_2(nT)$ , present the sampled signals before and after the PA, and the time delays in each branch of the transmitter and feedback receiver are marked as  $\Delta t_1^T, \Delta t_2^T, \Delta t_1^R$  and  $\Delta t_2^R$ . Hence, construct the combined input  $x(nT)$  and output  $y(nT)$  as shown below:

$$x(nT) = x_1(nT + \Delta t_1^T)e^{j\omega_1 nT} + x_2(nT + \Delta t_2^T)e^{j\omega_2 nT} \quad (6.27)$$

$$y(nT) = y_1(nT - \Delta t_1^R)e^{j\omega_1 nT} + y_2(nT - \Delta t_2^R)e^{j\omega_2 nT} \quad (6.28)$$

where  $\omega_1$  and  $\omega_2$  are the carrier frequencies of the two bands, and  $T$  is the sampling interval. Here, it is important to mention that  $\Delta t_1^T, \Delta t_2^T, \Delta t_1^R$  and  $\Delta t_2^R$ , are not necessary multiples of  $T$  and can be fractions of  $T$ . Later on, this will allow the mitigation of mismatches of both integral and fractal delays (Fig. 6.13).

To avoid the estimation error of the delays, we can align the sampled output signal with the corresponding input, and express the input to the PA as

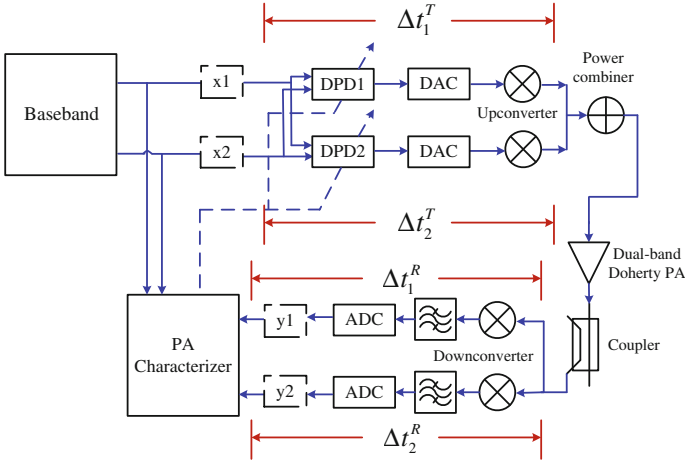


**Fig. 6.13** Typical concurrent dual-band transmitters. Reprinted with permission from the IEEE

$$x(nT) = x_1(nT)e^{jw_1nT} + x_2(nT + \Delta t_2^T - \Delta t_1^T)e^{jw_2nT} \quad (6.29)$$

Express  $x_1(nT)$ ,  $x_2(nT)$ , and  $x_2(nT + \Delta t_2^T - \Delta t_1^T)$  as  $x_1[n]$ ,  $x_2[n]$ , and  $\tilde{x}_2[n]$ , respectively. Thus, the format of the expression (6.31) becomes similar to the one in reported in [14]. Hence, a delay-mismatch-tolerant 2D-DPD model can be derived. By expanding  $|\tilde{x}[n]|$  as a linear interpolation of the amplitude of its neighboring  $L$  samples, i.e.,

$$|\tilde{x}_2[n]| = \sum_{l=-L}^L a_l |x_2[n-l]| \quad (6.30)$$

and substituting it into 2D-DPD models,  $y_1[n]$  is derived as

$$y_1[n] = \sum_{m=0}^M \sum_{k=0}^{N-1} \sum_{j=0}^k c_{k,j,m}^{(1)} x_1[n-m] \times |x_1[n-m]|^{k-j} \left\{ \sum_{l=-L}^L a_l |x_2[n-m-l]| \right\}^j \quad (6.31)$$

where  $c_{k,j,m}^{(1)}$  is the coefficients of the model,  $M$  is the memory depth, and  $N$  is the nonlinearity order. Expand the expression in braces on the right side; a new delay-mismatch-tolerant model is obtained as shown below:

$$\begin{aligned}
y_1[n] = & \sum_{m=0}^M \sum_{k=0}^{N-1} \sum_{j=0}^k \sum_{p_{-(L-1)}=0}^j \cdots \sum_{p_L=0}^{p_{L-1}} c_{m,k,j,p_{-(L-1)},\dots,p_L}^{(1)} x_1[n-m] \\
& \times |x_1[n-m]|^{k-j} |x_2[n-m+L]|^{j-p_{-(L-1)}} \\
& |x_2[n-m+L-1]|^{p_{-(L-1)}-p_{-(L-2)}} \cdots |x_2[n-m-L]|^{p_{L-1}-p_L}
\end{aligned} \quad (6.32)$$

To reduce the complexity of the model and keep only meaningful terms in the expression (6.32), the cross-terms effects between different memory depths could be ignored in systems such as PAs, where memory effects are secondary effects to a static nonlinear behavior, as pointed out and used in [11]. Consequently, the expression of the 2D-TMT-MP model can be further simplified as follows:

$$y_1[n] = \sum_{m=0}^M \sum_{k=0}^{N-1} \sum_{j=0}^k \sum_{l=-L}^L c_{k,j,m}^{(1)} x_1[n-m] \times |x_1[n-m]|^{k-j} |x_2[n-m-l]|^j \quad (6.33)$$

In this expression, there are  $2L$  redundant terms in each iteration at  $j = 0$ . Thus, we can further simplify the expression by merging the redundant terms and derive the final expression of 2D-TMT-MP model, as (6.36) presents.

$$\begin{aligned}
y_1[n] = & \sum_{m=0}^M \sum_{k=0}^{N-1} \alpha_{k,m}^{(1)} x_1[n-m] |x_1[n-m]|^k \\
& + \sum_{m=0}^M \sum_{k=1}^{N-1} \sum_{j=1}^k \sum_{l=-L}^L \beta_{m,k,j,l}^{(1)} x_1[n-m] |x_1[n-m]|^{k-j} |x_2[n-m-l]|^j
\end{aligned} \quad (6.34)$$

This model consists of two parts: the first is the traditional single-band MP model, and the second includes all the required cross-terms. The model degrades to a conventional 2D-DPD model as  $L = 0$ . At first glance, the proposed model (6.34) has some resemblance to the 2D extension of the generalized memory polynomials (GMP), expressed as (6.35) [12]. However, 2D-TMT-MP can outperform 2D-GMP in terms of robustness and complexity. A detailed comparison will be shown in the following experiments.

$$\begin{aligned}
y_1[n] = & \sum_{m=0}^{M_a} \sum_{k=0}^{N_a-1} \sum_{j=0}^k a_{m,k,j} x_1[n-m] |x_1[n-m]|^{k-j} |x_2[n-m]|^j \\
& + \sum_{m=0}^{M_b} \sum_{k=1}^{N_b-1} \sum_{j=0}^k \sum_{l=1}^{L_b} b_{m,k,j,l} x_1[n-m] |x_1[n-m-l]|^{k-j} |x_2[n-m-l]|^j \\
& + \sum_{m=0}^{M_c} \sum_{k=1}^{N_c-1} \sum_{j=0}^k \sum_{l=1}^{L_c} c_{m,k,j,l} x_1[n-m] |x_1[n-m+l]|^{k-j} |x_2[n-m+l]|^j
\end{aligned} \quad (6.35)$$

### 6.5.1.2 Model Evaluation and Results

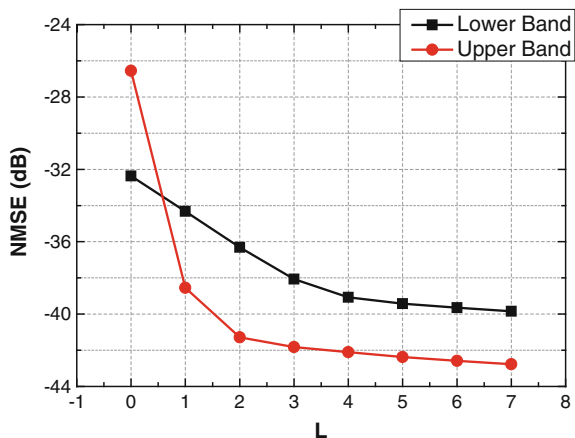
A class-AB PA prototype based on 33 W GaN transistor (DX02033) developed by Dynax Inc. was used to fulfill the dual-band transmitter. The PA supports a frequency range of 1.8–2.7 GHz. The two carrier frequencies were selected at 2.1 and 2.4 GHz, and the baseband signals were a 10 MHz bandwidth LTE-A signal and a 15 MHz LTE-A signal for the upper and lower bands, respectively. The signals both use the sample rates of 92.16 MSPS and exhibit a PAPR of 7.5 dB.

Figure 6.14 depicts the achieved NMSEs while extracting the forward model using 2D-TMT-MP with various  $L$ . Here, in order to verify the model capability in characterizing PA nonlinearities and tolerating the time-misalignment errors, a time misalignment of 4.87 samples (i.e., 52.84 ns) was set on purpose in Matlab. One can conclude from Fig. 6.14 that a higher  $L$  leads to a higher accuracy in the forward modeling. And the curves converge just as the threshold  $L$  approaches the time misalignment (Fig. 6.14).

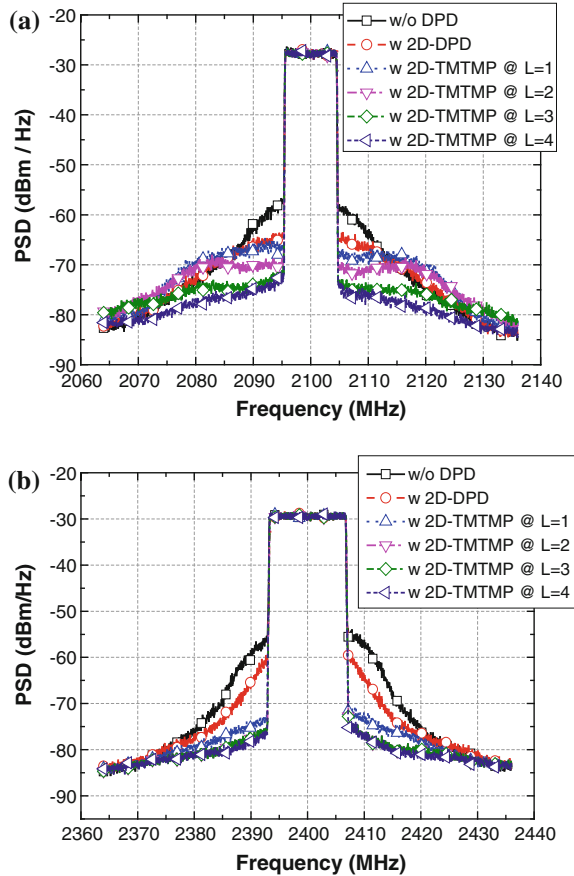
To further validate 2D-TMT-MPs' potential in DPD technique, the models are also utilized as predistorters in a concurrent dual-band transmitter with 4.87 samples misaligned as before. The overall system outputs before and after DPD processing are depicted in Fig. 6.15. As Fig. 6.15 shows, the ACPR is obviously compressed after using the 2D-TMT-MP model with relative high  $L$ , which indicates that the 2D-TMT-MP exhibits an excellent performance as time misalignment existed between the two frequency bands. Detailed NMSEs and ACPRs are listed in Table 6.7 and Fig. 6.16, which shows that, using 2D-TMT-MP with  $L = 4$ , an ACPR improvement of better than 10 dB is achieved compared with 2D-DPD.

To validate the robustness of the proposed model for various scenarios, it was tested with different time misalignments that existed between the two bands. The 2D-DPD model and 2D-GMP expressed as (6.37) are used as reference

**Fig. 6.14** NMSE comparison when 2D-TMT-MPs with different  $L$ . Reprinted with permission from the IEEE



**Fig. 6.15** Comparison of the DUT output spectrum after the DPD process with a 2D-TMT-MP model at different  $L$  when 4.87 samples misalign between the two bands. **a** The lower band (LB); **b** The upper band (UB). Reprinted with permission from the IEEE



linearization examples, and the time misalignment between the two bands is swept from minus five samples to five samples with a step of 0.25 samples. Here, without DPD, the two bands are with ACPRs of  $-33.0/-32.9$  dBc and  $-36.2/-36.0$  dBc, respectively. To give a fair comparison, the worst ACPR performance of the upper band's left/right adjacent channel and the lower band's left/right adjacent channel is selected as the final ACPR and depicted in 0. At the same time, the parameter settings and NMSEs when the polynomials are used as postinverse models are listed in Table 6.8. It can be observed that the 2D-TMT-MP model could even outperform the 2D-GMP model with fewer coefficients, although they both consider the cross-terms of different delays. In the case of one to two samples misalignment, the 2D-TMT-MP model can handle the time delay easily without performance sacrifice, while the 2D-DPD and 2D-GMP models have encountered obvious linearity degradation (Fig. 6.16; Tables 6.7 and 6.8).



**Fig. 6.16** The best ACPR of the upper band's left/right adjacent channel and the lower band's left/right adjacent channel versus different time misalignments. Reprinted with permission from the IEEE

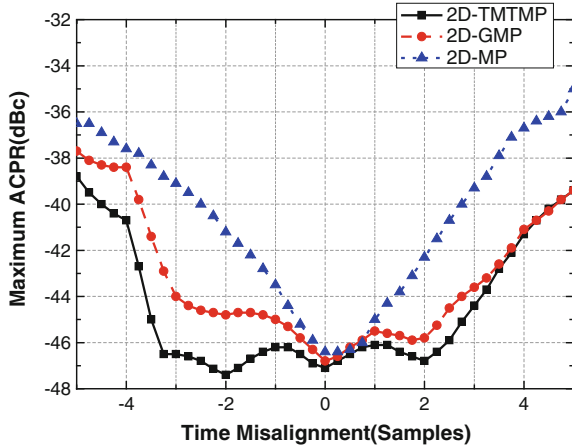


**Table 6.7** NMSEs and ACPRs of 2D-TMT-MP versus model dimensions when 4.87 samples misalign between the two bands

Model dimensions ( $M, N, L$ )	NMSE (dB)		ACPR (dBc)		Number of coefficients
	Lower band	Upper band	Lower band	Upper band	
w/o DPD	N/A	N/A	-34.2/-36.2	-34.1/-32.4	N/A
(4, 5, 0)	-32.4	-26.5	-38.3/-38.8	-39.5/-38.8	75
(4, 5, 1)	-34.3	-38.5	-39.0/-40.5	-46.8/-46.8	175
(4, 5, 2)	-36.3	-41.3	-42.4/-43.1	-49.5/-49.0	275
(4, 5, 3)	-38.1	-41.8	-46.5/-47.1	-49.9/-49.5	375
(4, 5, 4)	-39.8	-39.2	-49.9/-48.2	-49.9/-49.6	475

**Table 6.8** Performance comparison of three models

Model	Parameters settings	LB/UB NMSE(dB) @-2 samples TM	Number of coefficients
2D-TMT-MP (Eq. 6.8)	$L = 1, M = 3, N = 5$	-44.0/-44.5	140
2D-GMP (Eq. 6.9a, 6.9b)	$L_B = L_C = 1, M_A = M_B = M_C = 3$ $N_A = N_B = N_C = 5$	-42.4/-41.3	172
2D-DPD (Eq. 6.8)	$L = 0, M = 3, N = 5$	-29.7/-38.0	60

## 6.5.2 Phase-Compensated Behavioral Model

### 6.5.2.1 Phase-Aligned Pruned Voterra Model

The previous multiband DPD cells only account for the main amplitude modulation to amplitude modulation (AM/AM) and amplitude modulation to phase modulation

(AM/PM) dynamic behavior of the multiband PA, where the output of each band relies on the compound amplitude of the input-signal complex envelope, and the memory effects are incorporated only in the envelope amplitude. However, the effect of the instantaneous or past-phase information from the other bands is not considered. In the case of multiband transmitters, this problem is more obvious. However, not much work on multiband transmitters has accounted for the phase difference variation across the wideband frequency interval between multiple signals driving the transmitter. Therefore, the impact of the phase distortion as well as the dynamic amplitude distortion across three bands should be investigated, and their impact on the accuracy of linearization has to be validated in a concurrent triband transmitter.

The simplified Volterra model can be expressed as follows:

$$y(n) = y_s(n) + y_d(n) \quad (6.36)$$

The baseband static function for the triband case is given as

$$\begin{aligned} \tilde{y}_{s,q}(n) &= \sum_{p=0}^{N-1} \sum_{s=0}^p \sum_{k=0}^s h_{p,s,k}^{(q)} \tilde{x}_q(n) \\ &\quad \times |\tilde{x}_q(n)|^{p-s} |\tilde{x}_j(n)|^{s-k} |\tilde{x}_l(n)|^k \end{aligned} \quad (6.37)$$

where  $h_{p,s,k}^{(q)}$  is the set of baseband coefficients of the static part around angular frequency  $\omega_q$ , and  $q, j, l \in \{1, 2, 3\}$ , where  $q \neq j \neq l$ .

To compensate for the phase distortion in broadband system, a newly dynamic function is derived as [20]

$$\begin{aligned} \tilde{y}_{d,q}(n) &= \sum_{g=1}^6 \sum_{i_1=0}^{M_1-1} \sum_{i_2=i_1+1}^{M_2-1} \sum_{i_3=i_2+1}^{M_3-1} \psi_{g,i_1,i_2,i_3}^{(q)}(\tilde{x}_q(n), \tilde{x}_j(n), \tilde{x}_l(n)) \\ &\quad \times \sum_{p=0}^{N-5} \sum_{s=0}^p \sum_{k=0}^s h_{p,s,k,g}(i_1, i_2, i_3) F_{p,s,k,i_1}(\tilde{x}_q(n), \tilde{x}_j(n), \tilde{x}_l(n)) \end{aligned} \quad (6.38)$$

where  $F_{p,s,k,i_1}(\tilde{x}_q(n), \tilde{x}_j(n), \tilde{x}_l(n))$  is the compound envelope function given by

$$\begin{aligned} &F_{p,s,k,i_1}(\tilde{x}_q(n), \tilde{x}_j(n), \tilde{x}_l(n)) \\ &= |\tilde{x}_q(n - i_1)|^{p-s} |\tilde{x}_j(n - i_1)|^{s-k} |\tilde{x}_l(n - i_1)|^k \end{aligned} \quad (6.39)$$

and  $\psi_{g,i_1,i_2,i_3}^{(q)}(\tilde{x}_q(n), \tilde{x}_j(n), \tilde{x}_l(n))$  is given by

$$\begin{aligned}
\psi_{1,i_1,i_2,i_3}^{(q)} &= \tilde{x}_q^3(n-i_1)\tilde{x}_q^*(n-i_2)\tilde{x}_q^*(n-i_3) \\
\psi_{2,i_1,i_2,i_3}^{(q)} &= \tilde{x}_q^2(n-i_1)\tilde{x}_j(n-i_1)\tilde{x}_q^*(n-i_2)\tilde{x}_j^*(n-i_3) \\
\psi_{3,i_1,i_2,i_3}^{(q)} &= \tilde{x}_q^2(n-i_1)\tilde{x}_l(n-i_1)\tilde{x}_q^*(n-i_2)\tilde{x}_l^*(n-i_3) \\
\psi_{4,i_1,i_2,i_3}^{(q)} &= \tilde{x}_q(n-i_1)\tilde{x}_j(n-i_1)\tilde{x}_l(n-i_1) \\
&\quad \times \tilde{x}_j^*(n-i_2)\tilde{x}_l^*(n-i_3) \\
\psi_{5,i_1,i_2,i_3}^{(q)} &= \tilde{x}_q(n-i_1)\tilde{x}_j^2(n-i_1)\tilde{x}_j^*(n-i_2)\tilde{x}_j^*(n-i_3) \\
\psi_{5,i_1,i_2,i_3}^{(q)} &= \tilde{x}_q(n-i_1)\tilde{x}_l^2(n-i_1)\tilde{x}_l^*(n-i_2)\tilde{x}_l^*(n-i_3)
\end{aligned}$$

It is seen from these equations that accurate representation of the multiband transmitter output requires past information on the compound amplitude of the complex envelopes of the multi-input signals, as well as past information on the phase differences between the complex envelopes of the input signals as analytically derived. This derivation indicates that the previously reported model in [21], which only depends on the compound amplitude of the input signals and neglects any phase information on the input signals, is incapable of giving an accurate and true representation of the full dynamics of the multiband transmitter and hinders the full capacity of the model.

### 6.5.2.2 Model Evaluation and Results

The phase-aligned pruned Volterra DPD is linear with respect to its coefficients. Under the assumption of stationarity, if the coefficients are extracted with respect to a minimum mean or square error criterion, a single global minimum can be achieved. Therefore, direct linear-system identification algorithms, e.g., LS or recursive LS, can be used for estimating the model coefficients, which are defined as linear weighting of the nonlinear signals.

The transmitter hardware consists of three vector signal generators (VSGs) responsible for digital baseband-to-analog RF upconversion. A two-carrier LTE signal of 8 MHz bandwidth and 9.4 dB PAPR was sent at the lower 1.842 GHz frequency band; a one-carrier LTE signal of 5 MHz bandwidth and 9.5 dB PAPR at 1.96 GHz middle-frequency band; and a three-carrier LTE signal with a middle off-carrier, of 14 MHz total bandwidth and 9.7 dB PAPR at the upper frequency band 2.14 GHz. All three signals had a baseband sampling frequency of 92.16 MHz. Connections between the generators and an external clock generator are made to allow the synchronization of the transmitted bandpass signals. Figure 6.17 shows the power spectral density (PSD) of the multicarrier linearized LTE signals centered at the lower, middle, and upper frequency bands, respectively, for both the 3D-triband DPD and the proposed DPD. It can be seen that the phase-aligned pruned model outperforms the other methods.

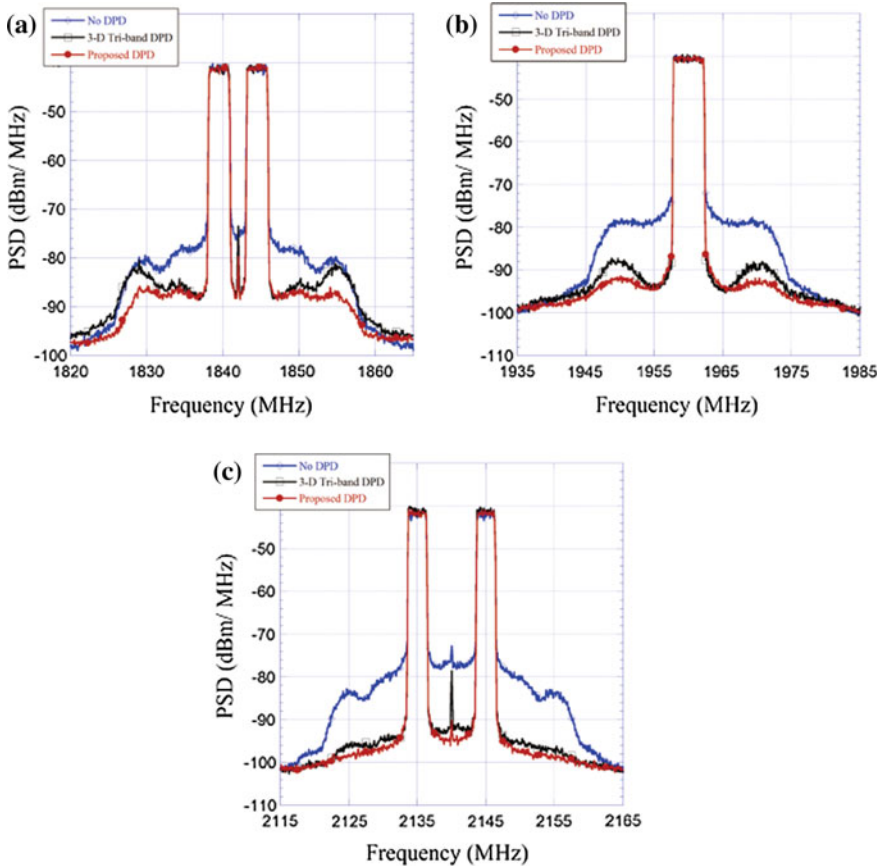


**Fig. 6.17** Linearization results of phase-aligned 3D-DPD. Reprinted with permission from the IEEE

## 6.6 Hardware Implementation for 2D-DPD with Subsampling Technique

### 6.6.1 Subsampling Feedback Architecture

Subsampling, or bandpass sampling, is a technique of sampling the band-limited RF signal at a rate much lower than the Nyquist rate. The subsampling technique has been considered a flexible solution for reconfigurable radio receivers, particularly in multistandard applications. As multistandard transceivers are becoming more and more ubiquitous in the cellular industry, the need for more flexible

topologies with fewer RF components and lower power consumption is greater now than ever before (Fig. 6.18).

As known, dual-band nonlinear devices will produce intermodulation, cross-modulation, and harmonic products caused by the two fundamental signals. In order to obtain samples from the output of the dual-band system, dual-branch or dual-band downconverter is conventionally needed in the feedback loop, which increases the complexity and power consumption of the DPD linearization block. Substituting the dual-band or dual-branch receiver feedback loop of the linearization topology with a subsampling receiver architecture reduces the complexity of the system. However, the different intermodulation, cross-modulation, and harmonic products make choosing the sampling frequency, which is intended to avoid any overlap between the downconverted desired signals and their intermodulation and cross-modulation products, a complex task. Therefore, it is imperative to develop an algorithm to select the sampling frequency so that it takes into account all the possible frequencies such that the target signals will not be interfered with.

Concurrent multiband receiver architectures traditionally require a bandpass filter, downconversion stage, and ADC for the translation of each RF frequency to baseband. Using subsampling with a high-speed ADC allows the elimination of all these components; however, the user needs to make sure the signals do not overlap in the subsampled spectral domain. Sampling multibands at the same time also eliminates the time delay between different band paths caused by the filters. Figure 6.18 displays the dual-band predistortion architecture with a subsampling feedback loop [22]. After subsampling of the PA output, the desired frequency bands are digitally filtered and downsampled to acquire their respective baseband waveforms.

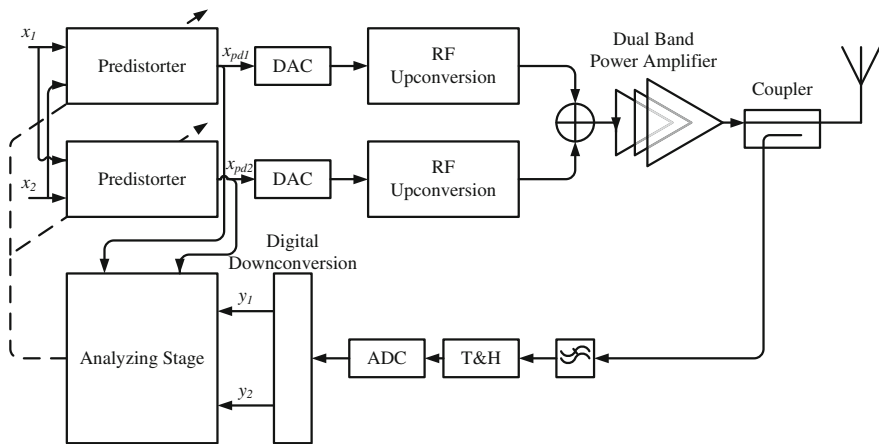


**Fig. 6.18** Dual-band digital predistortion with subsampled feedback loop. Reprinted with permission from the IEEE

### 6.6.2 Subsampling Frequencies Selection

Sampling the band-limited RF signal at frequency rates much lower than the Nyquist rate (but higher than signal bandwidth) folds the RF signal to the lower frequencies, where these replicates of the RF signal at baseband or intermediate frequencies can be used to reconstruct the baseband signal. To make sure that there is no aliasing between the replicas, the subsampling rate should be chosen in the following range:

$$\frac{2f_U}{n} \leq f_s \leq \frac{2f_L}{n-1} \quad \text{where } 1 \leq n \leq \left\lfloor \frac{f_U}{B} \right\rfloor \tag{6.40}$$

$$f_s \geq 2 \times B \quad \text{Nyquist rate}$$

where  $f_L$  and  $f_U$  are the lower and upper frequencies of the band-limited RF signal,  $B = f_U - f_L$  is the signal bandwidth, and  $n$  is an integer value.

The subsampling frequency range in (6.40) is valid for single-band RF signal. Extending it for the dual-band signals requires major modification and further analysis. Considering two RF signals at carrier frequencies of  $f_1$  and  $f_2$ , with their respective bandwidths  $B_1$  and  $B_2$  as shown in Fig. 6.19, the subsampling frequency,  $f_s$ , must be chosen to ensure that the two signals do not overlap in the subsampled domain. Following the universal subsampling formula for sampling the multiband signals, there exist eight possible replica orders. Following the neighbor and boundary constraints, an iterative process is used to find all the valid subsampling frequencies for the two fundamental frequencies (Fig. 6.19).

The intermodulation, cross-modulation, and harmonics generated by the fundamental signals are not required for the predistortion application. A relaxed version of the algorithm in the previous section can be used, where the unwanted signals' only restriction is not to overlap with the fundamental tones. For Fig. 6.19 and setting  $n_1 = n_2 = n$ , the modified formula from (6.40) is as follows:

$$f_1 + nf_s \leq f_2 < f_1 + (n + 1)f_s \tag{6.41}$$

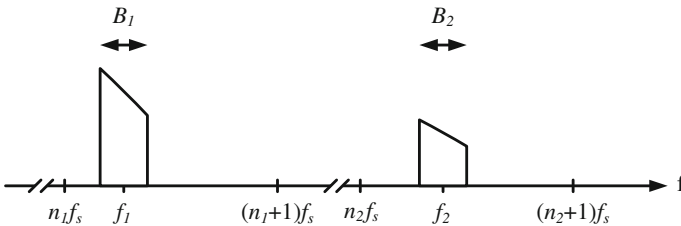


**Fig. 6.19** Truncated frequency axis of two signal bands at their RF frequencies. Reprinted with permission from the IEEE

where  $n = \left\lfloor \frac{f_2 - f_1}{f_s} \right\rfloor = \left\lfloor \frac{\Delta f}{f_s} \right\rfloor$ . The maximum value of  $n$  can be constrained by the following formula:

$$n_{\max} = \left\lfloor \frac{\Delta f - \frac{\sum B}{2}}{\sum B} \right\rfloor \quad (6.42)$$

To find the sampling frequency upper bound, the bandwidths of the two frequencies must not overlap each other. Thus, the following upper bound constraint must hold:

$$f_1 + nf_s + \frac{B_1}{2} < f_2 - \frac{B_2}{2} \quad (6.43)$$

Rearranging (6.43), the upper sampling frequency bound can be found as

$$f_s < \frac{(f_2 - f_1) - \frac{(B_1 + B_2)}{2}}{n} \quad (6.44)$$

Similarly, the sampling frequency lower bound can be computed from the following equation:

$$f_1 + (n + 1)f_s - \frac{B_1}{2} > f_2 + \frac{B_2}{2} \quad (6.45)$$

resulting in

$$f_s > \frac{(f_2 - f_1) + \frac{(B_1 + B_2)}{2}}{n + 1} \quad (6.46)$$

To account for the image frequency,  $-f_1$  must be considered, and Eqs. (6.43)–(6.47) can be repeated with  $\Delta f = f_2 + f_1$ . The final result is having a vector of valid ranges for  $f_2 - f_1$  and  $f_2 + f_1$ , where the valid frequencies are the ones equal to the intersection of each set  $(f_2 - f_1)$  and  $(f_2 + f_1)$ .

The final step to establish the valid sampling frequencies  $F$  is to perform an intersection of all the valid subsampling frequencies as follows:

$$F = F_{db} \cap F_{\text{imd}} \cap F_{\text{cmd}} \cap F_{\text{hmd}} \quad (6.47)$$

where  $F_{db}$  is the valid subsampling frequencies for the fundamental signals,  $F_{\text{imd}}$  is the complete set of frequencies for the intermodulation distortion case,  $F_{\text{cmd}}$  is the complete set of frequencies for the cross-modulation case, and  $F_{\text{hmd}}$  is the complete set of frequencies for the harmonic distortion case.

### 6.6.3 Experimental Evaluation

The experimental setup of the dual-band linearization architecture in Fig. 6.18 is developed as presented in Fig. 6.20. The nonlinear DUT is a Doherty-based concurrent dual-band PA using Cree CRF24010 transistors operating at 880 MHz and 1978 MHz frequency bands [5]. Two independent WCDMA signals are downloaded into the two baseband time-aligned Agilent E4438C vector signal generators, and upconverted to the desired lower and upper RF frequencies. These two signals are combined using the broadband Wilkinson power combiner and fed the Doherty-based concurrent dual-band PA. A coupler is used at the output of the PA to capture the signal for the feedback loop of the system in Fig. 6.18.

The feedback loop is based on subsampling technique using the ADC development kit and logic signal analyzer. It consists of the time-interleaved 800 MSPS ADC development board from SP Devices. The ADC was connected to an Agilent 16901A logic analyzer mainframe to allow triggering and deep memory depth capture. After capturing the signal, the data is filtered around the signal bands of interest, then digitally downconverted to baseband signals for linearization processing. A separate Agilent signal generator was also required to supply the ADC development board with the necessary sampling frequency clock, and all signal generators were phase locked with a reference clock (Figs. 6.20 and 6.21).

Figure 6.21a shows the output spectrum of the PA under test, captured using a spectrum analyzer. Compared with the simulation results, there is an extra term  $p$  component, which is a seventh-order intermodulation product at 436 MHz. The power differences, and the fact that terms  $i$  component and  $j$  component are not visible is due to the design of the PA output-matching network.

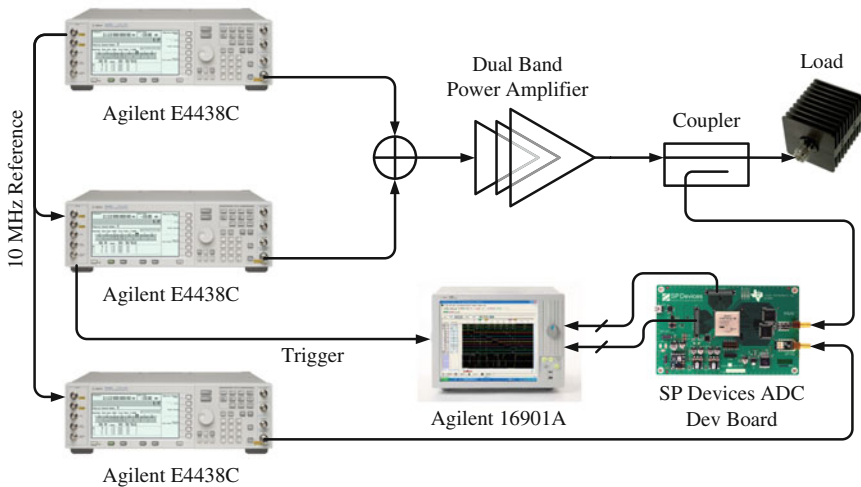


**Fig. 6.20** Experimental setup for dual-band linearization architecture. Reprinted with permission from the IEEE



**Fig. 6.21** Spectra of the captured signal using an ADC operating at 619.8 MHz. Reprinted with permission from the IEEE

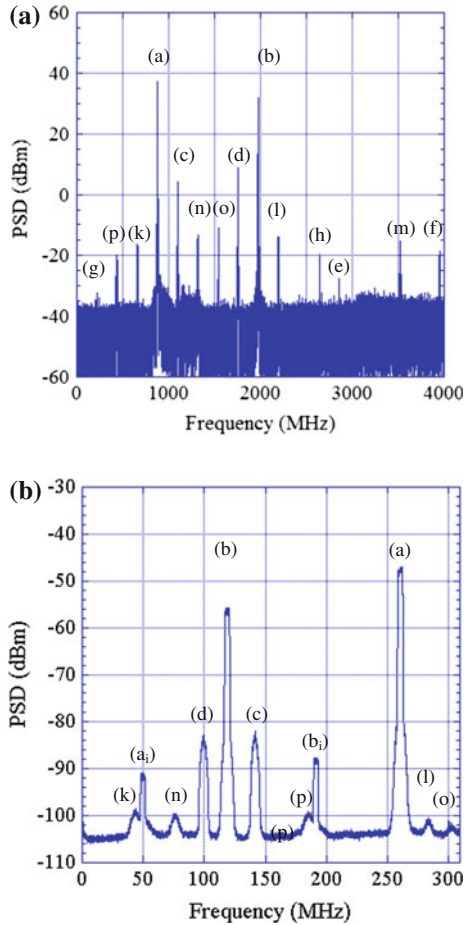


Figure 6.21b shows the digitized signal captured from the PA under test by the ADC and logic analyzer using a sampling frequency of 619.8 MHz. Compared with the simulation results, the distinct 5 MHz attenuated fundamental signals that exist at 49.7 MHz ( $a_i$ ) and 191.3 MHz ( $b_i$ ) are caused by bandwidth mismatch effects in the ADC time-interleaved architecture. Since there was no track-and-hold (T&H) in the validation measurement setup, there is a significant power difference between the power levels of the two fundamental frequencies. This can be compensated by including a proper T&H into the final solution. Furthermore, there is an extra term at 183.8 MHz that is caused by the extra term  $p$  at 436 MHz.

The fundamental signals are bandpass filtered in Matlab, and digitally down-converted to baseband for dual-band predistortion processing. Processing the signals captured by the subsampling-based feedback loop and predistorting the input signals based on linearization block, the spectrum of the output signals with and without linearization are shown in Fig. 6.22a, b. Using the dual-band linearization

architecture, one can significantly compensate for the in-band and out-of-band distortions and bandwidth regrowth to reduce the interference within the adjacent channels. The only drawback of the subsampling-based system is the higher noise level due to the noise folding caused by the subsampling process, which is shown by the raised noise floor at the PA output. However, this is negligible compared with the improvement achieved in distortion compensations.

The better evaluation of in-band and out-of-band signal quality with and without linearization is by measuring the NMSE and the ACPR as shown in Fig. 6.22. The measurement results in Table 6.9 show that having performed linearization, the

**Fig. 6.22** Predistortion results for **a** 880 MHz and **b** 1978 MHz using concurrent dual-band predistortion with subsampling feedback loop. Reprinted with permission from the IEEE

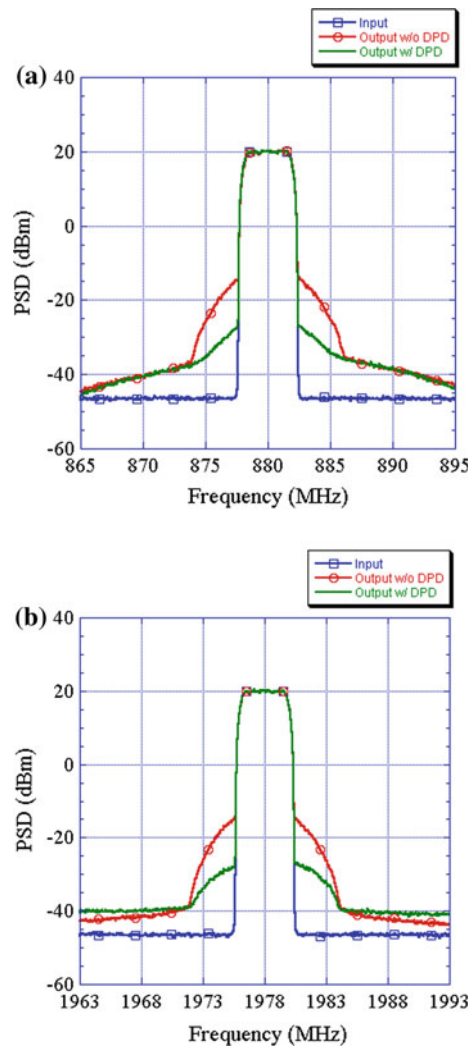


**Table 6.9** Results of predistortion with subsampling feedback loop

Signal	NMSE (dB)	Adjacent channel power ratio	
		Lower (dBc)	Upper (dBc)
880 MHz no DPD	-26.4	40.1	39.3
880 MHz w/DPD	-39.5	51.6	50.6
1978 MHz no DPD	-29.8	40.2	40.2
1978 MHz w/DPD	-41.0	51.1	50.0

in-band signal quality (NMSE) is improved by more than 10 dB and the out-of-band distortion compensation (ACPR) is around 10 dB for the lower band and for the upper band (Table 6.9).

## References

1. A. Cidronali, N. Giovannelli, I. Magrini, G. Manes, Compact concurrent dual-band power amplifier for 1.9 GHz WCDMA and 3.5 GHz OFDM wireless systems, in *Proceedings of 38th European Microwave Conference*, EuMC 2008, pp. 1545–1548
2. R. Negra, A. Sadeve, S. Bensmida, F.M. Ghannouchi, Concurrent dual-band class-F load coupling network for applications at 1.7 and 2.14 GHz. *IEEE Trans. Circ. Syst. II: Exp Briefs* **55**(3), 259–263 (2008)
3. P. Colantonio, F. Giannini, R. Giofre, L. Piazzon, A design technique for concurrent dual-band harmonic tuned power amplifier. *IEEE Trans. Microw. Theory Tech.* **56**(11), 2545–2555 (2008)
4. X. Li, W. Chen, Z. Zhang, Z. Feng, X. Tang, K. Mouthaan, A concurrent dual-band Doherty power amplifier, in *Asia-Pacific Microwave Conference*, Yokohama, Japan, Dec. 2010
5. W.H. Chen, S.A. Bassam, X. Li, Y. Liu, M. Helaoui, K. Rawat, F.M. Ghannouchi, Z. Feng, Design and linearization of concurrent dual-band doherty power amplifier with frequency-dependent power ranges. *IEEE Trans. Microw. Theory Tech.* **59**(10), 2537–2546 (2011)
6. S.A. Bassam, Advanced signal processing techniques for impairments compensation and linearization of SISO and MIMO Transmitters, *Doctor Dissertation*, University of Calgary, 2010
7. A. Cidronali, I. Magrini, R. Fagotti, G. Manes, A new approach for concurrent dual-band IF digital predistortion: system design and analysis, in *Workshop on Integrated Nonlinear Microwave and Millimeter-Wave Circuits* (INMMINC), Malaga, Spain, 24–25 Nov. 2008, pp. 127–130
8. P. Rblin, Suk Keun Myoung, D. Chaillot, Young Gi Kin, A. Fathimulla, J. Strahler, S. Bibyk, Frequency-selective predistortion linearization of RF power amplifiers. *IEEE Trans. Microw. Theory Tech.* **56**(1), 65–76 (2008)
9. S.A. Bassam, M. Helaoui, F.M. Ghannouchi, BER performance assessment of linearized MIMO transmitters in presence of RF crosstalk,” in *Proceedings of IEEE Radio and Wireless Symposium*, RWS 2010, New Orleans, LA, pp. 10–14
10. J. Kim, K. Konstantinou, Digital predistortion of wideband signals based on power amplifier model with memory. *Electron. Lett.* **37**(23), 1417–1418 (2001)
11. L. Ding, G.T. Zhou, D.R. Morgan, Z. Ma, J.S. Kenney, J. Kim, C.R. Giardina, A robust digital baseband predistorter constructed using memory polynomials. *IEEE Trans. Commun.* **52**(1), 159–165 (2004)

12. A. Zhu, P.J. Draxler, J.J. Yan, T.J. Brazil, D.F. Kimball, P.M. Asbeck, Open-loop digital predistorter for RF power amplifiers using dynamic deviation reduction-based Volterra series. *IEEE Trans. Microw. Theory Tech.* **56**(7), 1524–1534 (2008)
13. Y. Park, R. Melville, R.C. Frye, M. Chen, J.S. Kenney, Dual-band transmitters using digitally predistorted frequency multipliers for reconfigurable radios. *IEEE Trans. Microw. Theory Tech.* **53**(1), 115–122 (2006)
14. S.A. Bassam, M. Helaoui, Fadhel M. Ghannouchi, 2-D digital predistortion (2-D-DPD) architecture for concurrent dual-band transmitters. *IEEE Trans. Microw. Theory Tech.* **59**(10), 2547–2554 (2011)
15. S.A. Bassam, W. Chen, M. Helaoui, Fadhel M. Ghannouchi, Z. Feng, Linearization of concurrent dual-band power amplifier based on 2D-DPD technique. *IEEE Microw. Wireless Compon. Lett.* **21**(12), 685–687 (2011)
16. S.A. Bassam, A. Kwan, W. Chen, M. Helaoui, Fadhel M. Ghannouchi, Subsampling feedback loop applicable to concurrent dual-band linearization architecture. *IEEE Trans. Microw. Theory Tech.* **60**(6), 1990–1999 (2012)
17. Y.-J. Liu, W. Chen, J. Zhou, B.-H. Zhou, F.M. Ghannouchi, Digital predistortion for concurrent dual-band transmitters using 2D modified memory polynomial. *IEEE Trans. Microwave Theory Technol.* **61**(1), 281–290 (2013)
18. S.A. Bassam, W. Chen, M. Helaoui, F.M. Ghannouchi, Transmitter architecture for CA. *IEEE Microwave Mag.* **14**, 78–86, (2013)
19. S. Zhang, W. Chen, Y. Liu, F.M. Ghannouchi, A time misalignment tolerant 2D-memory polynomials predistorter for concurrent dual-band power amplifiers. *IEEE Microwave Wirel. Compon. Lett.* **23**(9), 501–503 (2013)
20. M. Younes, A. Kwan, M. Rawat, F.M. Ghannouchi, Linearization of concurrent tri-band transmitters using 3-D phase-aligned pruned volterra model. *IEEE Trans. Microw. Theory Tech.* **61**(12), 4569–4578 (2013)
21. M. Younes, A. Kwan, M. Rawat, F.M. Ghannouchi, Three-dimensional digital predistorter for concurrent tri-band power amplifier linearization, in *IEEE MTT-S International Microwave Symposium Digital*, Seattle, WA, USA, pp. 1–4 (2013)
22. S.A. Bassam, A. Kwan, W. Chen, M. Helaoui, F.M. Ghannouchi, Subsampling feedback loop applicable to concurrent dual-band linearization architecture. *IEEE Trans. Microwave Theory Technol.* **60**(6), 1990–1999 (2012)